

Gain Efficient Waveguide Optical Amplifiers for Si Microphotonics

by

Sajan Saini

B.Sc. Honors Physics
McGill University, 1995

M.Sc. Condensed Matter Physics
McGill University, 1997

Submitted to the Department of Materials Science and Engineering in Partial Fulfillment
of the Requirements for the Degree of

Doctor of Philosophy in Electronic, Photonic And Magnetic Materials
at the
Massachusetts Institute of Technology

September 2004

© 2004 Massachusetts Institute of Technology. All rights reserved.

Signature of Author: _____

Department of Materials Science and Engineering

July 26th, 2004.

Certified by: _____

Lionel C. Kimerling

Thomas Lord Professor of Materials Science and Engineering

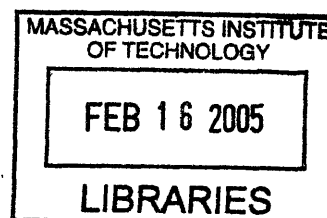
Thesis Supervisor

Accepted by: _____

Carl V. Thompson II

Stavros Salapatas Professor of Materials Science and Engineering

Chair, Departmental Committee on Graduate Students



ARCHIVES

Gain Efficient Waveguide Optical Amplifiers for Si Microphotonics

by

Sajan Saini

B.Sc. Honors Physics

McGill University, 1995

M.Sc. Condensed Matter Physics

McGill University, 1997

Submitted to the Department of Materials Science and Engineering in Partial Fulfillment
of the Requirements for the Degree of

Doctor of Philosophy in Electronic, Photonic And Magnetic Materials
at the
Massachusetts Institute of Technology

September 2004

© 2004 Massachusetts Institute of Technology. All rights reserved.

Signature of Author: _____

Department of Materials Science and Engineering

July 26th, 2004.

Certified by: _____

Lionel C. Kimerling

Thomas Lord Professor of Materials Science and Engineering

Thesis Supervisor

Accepted by: _____

Carl V. Thompson II

Stavros Salapatas Professor of Materials Science and Engineering

Chair, Departmental Committee on Graduate Students

Gain Efficient Waveguide Optical Amplifiers for Si Microphotonics

by

Sajan Saini

Submitted to the Department of Materials Science and Engineering on July 29, 2004, in Partial Fulfillment of the Requirements for the Degree of Doctor of Philosophy in Electronic, Photonic and Magnetic Materials

ABSTRACT

Si Microphotonics is a micron-scale planar processing technology compatible with the fabrication tools of Si Microelectronics. The first demonstration of an integrated set of microphotonic devices replicating the function of an entire fiber optic link, dubbed a Planar Lightwave Circuit (PLC), is being developed to solve the Integrated Circuit (IC) interconnection bottleneck problem: the project proposes replacing time delaying metal interconnects with optical interconnects, i.e. a PLC integrated onto the IC chip. This work requires the development of compact micron-scale analogs to fiber optic link device elements. In this thesis, we take example from commercially available Erbium Doped Waveguide Amplifiers (EDWAs), to investigate the use of high Er concentration doped materials and device design optimization to create gain efficient Waveguide Optical Amplifiers (WOA) in the PLC, at 1.55 μm light.

We develop a waveguide index difference Δn scaling methodology with which to optimally design a WOA into as small a planar footprint as possible and using as little optical pump power as required. We observe that device gain efficiency and footprint have a power-law dependence, summarized in a cumulative Figure-of-Merit, of $\Delta n^{2.6}$. This strong improvement in WOA performance is dependent on the requirement of strip waveguide propagation losses < 0.2 dB/cm, a requirement demonstrated in SiON waveguides. We conclude that a 10 mW-powered 3 dB or 30 dB gain WOA can be fit into a $425 \times 425 \mu\text{m}^2$ or $3 \times 3 \text{ mm}^2$ footprint, respectively, using an SiON $\Delta n = 0.155$ Er-doped strip waveguide. The impact of Δn scaling shows the WOA to be feasible for dense PLCs and low cost planar EDWAs.

We examined Er_2O_3 as a materials candidate for ultra-high Er-based gain. We reported the first infrared photoluminescence PL study of Er_2O_3 and found a 7 ms lifetime at 4 K, attributed to a metastable FCC or HCP phase. We showed the thermodynamically stable BCC crystal phase has PL emission lines at 1537 nm and 1550 nm, and metastable FCC and HCP crystal phases result in PL emission lines at 1542 nm and 1533 nm. Upconversion coefficient measurements on the BCC phase and 7 ms lifetime metastable phase gave values of 10^{-17} and $10^{-18} \text{ cm}^3/\text{s}$, respectively. Comparison of room temperature absorption versus 4 K PL of Er_2O_3 and an $\text{SiO}_2:\text{Er}$ reference showed the BCC phase to be the dominant volume fraction. The calculated WOA power requirements for 3 dB gain in the metastable phase were found to be 450 mW.

We examined SiON and Si₃N₄ for high index difference ($\Delta n=0.1-0.7$) Er host materials. Samples were grown by sputtering, and we investigated the optical materials quality of this process by studying sputtered SiO₂:Er; we report a record co-sputtered SiO₂:Er room temperature lifetime of 14 ms. PL versus heat treatment results strongly indicate the nitride environment of Si₃N₄ favors a higher Er solubility and lower cooperative upconversion than the oxide environment of SiO₂. We measure a 2.4 ms radiative lifetime in co-sputtered Si₃N₄:Er, $\sim 4\times$ smaller than radiative lifetime reports in ion implanted Si₃N₄:Er PL samples; we attribute this enhancement to an optimized Er ligand field from the sputter process. We report the first $\lambda_p=488$ nm pump absorption cross-section σ_{pump} and upconversion C_{24} measurements in SiON:Er ($\sigma_{\text{pump}}=2.2\times 10^{-15}$ cm², $C_{24}=4\times 10^{-18}$ cm³/s) and Si₃N₄:Er ($\sigma_{\text{pump}}=9.2\times 10^{-16}$ cm², $C_{24}=1.5\times 10^{-18}$ cm³/s), showing a $\sim 10^6\times$ enhancement in σ_{pump} and $\sim 2.5-6.6\times$ decrease in C_{24} , as compared to SiO₂:Er. We conclude the nitride environment favors both Er optical and solubility properties; optical gain measurement results indicate a 14 dB/cm and 23 dB/cm gain (for 1.55 μm light) in SiON:Er and Si₃N₄:Er, respectively.

We investigated and present results on two additional optical confinement methods involving resonance, in order to increase Er-doped WOA gain efficiency and decrease footprint, at a given Δn . Using an SiON case study ($\Delta n=0.155$). We study ring resonators as an example of longitudinal resonant confinement and present a model to describe sub-lasing threshold gain. We conclude such Resonant-WOAs (R-WOAs) can give up to a 120 \times enhancement in 3-dB gain efficiency and 18 \times decrease in footprint, at $\Delta n=0.155$. We model the performance of an Er-doped ring laser and theoretically predict up to 20 μW output power for 8 mW optical pump power. Design calculations for a ring resonator application as an integrated photo-detector de-multiplexer are also presented.

Our second resonance study modeled light propagation in an Er-doped “defect” layer clad by a Photonic Crystal (PC), as an example of transverse resonant confinement. We present two device designs using this confinement principle: design (i) is based purely on PC confinement of both signal and pump optical modes, design (ii) is a hybrid structure confining signal mode by total internal reflection and pump mode by PC. Both designs break with the co-propagation pump scheme to explore uniform resonant pumping. The PC-WOAs yields a 5.2 \times decrease in footprint, and PC-WOA design (ii) shows an optimal 3-dB gain efficiency 1.13 \times lower than the $\Delta n=0.155$ WOA. We grew PC-WOA design (i) by sputtering for testing of the uniform resonant pump-coupling scheme, and confirmed the structure’s optical cavity characteristics by reflectivity measurements.

The results of this thesis show optically pumped amplifiers are an appropriate and highly efficient device element for an insulator-based Si Microphotonics materials platform; within which the Er atom maintains its role as a 1.55 μm gain center and shows strong enhancement capability, despite upconversion limitations, by the adopting of nitride-rich host environments.

Thesis Supervisor: Lionel C. Kimerling

Title: Thomas Lord Professor of Materials Science and Engineering

Table of Contents

Table of Contents	4
List of Figures	8
List of Tables	17
Acknowledgments	21
Chapter 1: Introduction to the EDWA, Photonics, and the Planar Lightwave Circuit	23
1.1 Er-Doped Amplifiers	24
1.2 Thesis Study: Er-doped Microphotonic Amplifier	25
1.3 Thesis Study: Materials for the Microphotonic Amplifier	27
1.4 Thesis Study: Resonant Techniques for Gain Efficiency and Footprint Enhancement	29
1.5 Review: Photonics and the Confined Propagation of Light	31
1.6 Review: The Need for Amplification in Communications	35
1.7 Review: Microphotonics	38
1.7.1 Silicon Microelectronics & A Seemingly Unrelated Problem	38
1.7.2 Silicon Microphotonics: an Optical and Electronic Convergence	41
1.8 Review: Si Microphotonics and the Planar Lightwave Circuit	43
Chapter 2: Optical Shrink: the Effect of Transverse Confinement in High Δn Waveguide Amplifiers	46
2.1 Chapter Abstract	47
2.2 Introduction	48
2.2.1 Optical Shrink for the Optically Pumped Amplifier	48
2.2.2 An Adjustable Refractive Index Materials Host and An Adjustable Optical Dopant	51
2.2.3 Areal Gain and the HIC-WOA	54
2.2.4 This Work: A Computer Simulation Study of Optical Shrink	56
2.3 Amplifier Physics	56
2.3.1 Amplification Background	56
2.3.2 Optical Shrink as a Power Trajectory Path	60
2.3.3 Discussion: The Meaning of a Noise Figure	62
2.4 Results and Discussion 1: Amplifier Scaling Principles	64

2.4.1 HIC Scaling Principle 1: Gain Efficiency	65
2.4.2 HIC Scaling Principle 2: Device Footprint	76
4.4.3 HIC Scaling Principle 3: the Independence of Amplified Spontaneous Emission	77
2.5 Results and Discussion 2: The Effect of L_g in Optical Shrink and Amplifier Design Rules	78
2.6 Synthesis of Scaling Principles.....	81
2.6.1 Methodology.....	81
2.6.2 Figure of Merit.....	82
2.7 Conclusion: Transverse Optical Confinement for the WOA.....	83
Chapter 3: High Er Concentration Materials Systems for Si Microphotonic Amplifiers	87
3.1 Chapter Abstract	88
3.2 Introduction.....	88
3.2.1 The Small Interaction Cross-Section of the Er Atom.....	88
3.2.2 Cooperative upconversion and Its Influence on Er_2O_3	94
3.2.3 This Work	96
3.3 Experimental Details	96
3.4 Reference Sample Studies	100
2.4.1 Characterization of Er-Doped Corning Glass	100
2.4.2 Characterization of Er_2O_3 Commercial Powder.....	106
3.5 Sputtered Er_2O_3 Thin Films: Results and Discussion	108
3.5.1 Low Temperature Study Reveals Three Optical Centers	109
3.5.2 Energy Migration and the Rapid Quench of the 7 ms Optical Center	113
3.5.3 Absorption Versus Luminescence	114
3.5.4 Er_2O_3 Powder: Confirming the BCC Phase.....	115
3.5.5 Optical Center Volume Fractions and Crystal Phases	116
3.5.6 The Effect of Annealing on Recrystallization	118
3.5.7 Cooperative upconversion in Sputtered Er_2O_3	121
3.5.8 Population Inversion Calculation	125
3.6 Chapter Conclusion	126
Chapter 4: Adjustable Refractive Index Materials for Er-doped Si Microphotonic Amplifiers.....	128

4.1	Chapter Abstract	129
4.2	Introduction.....	130
4.3	Experimental Procedure	134
4.4	Results & Discussion.....	136
4.4.1	Photoluminescence: Room Temperature Data	136
4.4.2	Photoluminescence: Thermal Activation	143
4.4.3	Photoluminescence: Temperature=4 K Data.....	147
4.4.4	Photoluminescence: Process Map	149
4.4.5	Materials Loss Measurements	150
4.4.6	AFM Results.....	151
4.4.7	Optical Pump Absorption Cross-Section Measurement	153
4.4.8	Cooperative Upconversion Measurement.....	160
4.4.9	VSL Gain Measurements.....	164
4.5	Conclusions.....	173
Chapter 5: the Effect of Longitudinal Confinement in Ring Resonator		
Waveguide Amplifiers		
5.1	Chapter Abstract	177
5.2	Introduction.....	179
5.2.1	The Ring Resonator.....	179
5.2.2	Er-Doped Ring Resonators	181
5.3	Theoretical Background.....	185
5.3.1	Relating Power within the Ring Resonator to the Waveguide Bus (the Modified Purcell Factor)	185
5.3.2	Regimes of Coupling: Under-, Over- and Critical.....	189
5.4	Applications	198
5.4.1	Rings for a WDM Laser Light Source	198
5.4.2	Optical Amplifier	211
5.5	Conclusion	229
Chapter 6: the Effect of Transverse Resonant Confinement in Photonic		
Band Gap Waveguide Amplifiers.....		
6.1	Chapter Abstract	232
6.2	Introduction.....	233
6.3	Theoretical Background.....	235

6.4	Results	249
6.4.1	Device Physics and WDM Applicability	249
6.4.2	Device Performance	270
6.5	Conclusion	276
Chapter 7: Looking to the Light: Si Microphotonic Amplifier		
Conclusions and Suggestions for Future Work		279
7.1	Er Waveguide Optical Amplifiers for Microphotronics	280
7.2	Future Work in the SiON–Si₃N₄:Er Systems	280
7.3	The Impact of Optical Shrink.....	281
7.4	The Influence of Resonance on Gain Enhancement	282
7.5	Photonic Crystal Methods	284
7.6	Light Sources at Wavelengths \neq 1.55 μm.....	284
Appendix 1: Modal Confinement & Turning Loss		287

List of Figures

- Fig. 1.1.1. (a) Transmission of light through glass over the ages[]. The 20th century insight into optical impurities being the cause for high absorption led to (b) the dramatic decrease of materials absorption at $\lambda=1.55 \mu\text{m}$ []. The erbium emission spectrum is overlaid, demonstrating erbium's unique role as an amplifying transition for long-haul fiber optic communications. 33
- Fig. 1.1.2. The Optical Communications Roadmap[37], charting the power law rise of communication transmission rate (in units of bit/s) over time. The introduction of optical fiber networks and WDM-based networks contributed disruptive advances in the communications trends, as a function of time. (ETDM stands for Electronic Time Domain Multiplexing, the electrical form for carrying multiple communication signals []). 34
- Fig. 1.1.3. The impact of fiber optics on telecommunications. Map of the submarine and trans-continental long haul fiber optic links, circa 2001 []. 36
- Fig. 1.1.4. (a) Cross-talk between WDM channels A and B after amplification through an EDFA []. (b) The atomic three-level system of the Er atom [13]. 37
- Fig. 1.1.5. Moore's Law, representing the unprecedented power law improvement of circuit performance/cost ratio as a function of decreasing lithography wavelength []. 39
- Fig. 1.1.6. Trend in global interconnect (1 cm length) propagation delay with technology linewidth and time, for traditional aluminum metal and SiO₂ insulator; projected copper and low dielectric material; and projected optical waveguide technologies[37]. 40
- Fig. 1.1.7. The Planar Lightwave Circuit[38], comprised of a transceiver interface and optical layer. The optical amplifier is an all-optical device, distributed across the optical layer for in-line power-budget maintenance. 43
- Fig. 2.1. Dimensional scaling for high gain planar HIC-WOAs (dB/cm²). (a) Serpentine structure, minimizing areal extent with straight-line waveguide segments. (b) Coil structure, optimally packing a planar area with curved waveguides. Nearest neighbor waveguide distance p is the larger of (i) radius r for 0.042 dB/cm turning loss[44] or (ii) decay length d corresponding to a 40 dB drop in evanescent cladding field intensity. In limit (i), magnitude of p is turning loss limited; in limit (ii) p is evanescent wave leakage limited. w is the waveguide width. Table 2.6 lists the equations relating WOA footprint size F to WOA length L_g . 54
- Fig. 2.2. Optical amplification in a three-level system. Signal photons (wave-like arrows) at wavelength λ_s undergo multiplication by stimulated emission W_{21} . Phonons mediate the rapid "fast nonradiative" de-excitation rate $N_3 \rightarrow N_2$. 57

- Fig. 2.3. Effect of co-propagating pump and spontaneous emission on power distribution along a WOA. L_{\max} is defined in Table 1. (Data plotted for upconversion-free case study; power profile $P_s(z)$ for case study with upconversion is additionally plotted.) 59
- Fig. 2.4. Performance Map 1: $\lambda=1.55 \mu\text{m}$ Optical Amplification Regimes for Fig. 3 (upconversion-free) case study. The four operating regimes are quantitatively partitioned as a function of pump and signal power (mW). The inter-related effect of Δn and L_g determines the spatial extent of Regimes I-IV in Fig. 2.3, and the path of a “power trajectory” in this figure. The power trajectory represents $P_p(z)$ and $P_s(z)$ at local z positions along the Propagation Direction axis of Fig. 2.3. 60
- Fig. 2.5. (a) Noise Figure versus radiative lifetime, using the Optical Shrink case study with variable τ_r . (b) Case study simulation of power and gain profiles, with modification to a constant pump profile. 62
- Fig. 2.6. $\lambda_s=1.55 \mu\text{m}$ wavelength mode profile in single mode cut-off WOA cross-section area, for $\Delta n=0.5, 2.0$. The shaded areas show that the same modal fraction is confined within the core of a single mode cut-off waveguide, regardless of Δn . For higher Δn , decreasing A_{core} thus implies an increase in flux density ϕ_s, ϕ_p within the WOA core. 65
- Fig. 2.7. (a) Plot of power and gain profiles using case study parameter with modification of index difference to value $\Delta n=0.06$. (b) Comparison of signal power $P_s(z)$ and gain $\gamma(z)$ profiles for $\Delta n=0.06$ case versus $\Delta n=0.5$ case study. 69
- Fig. 2.8. (a) Device Gain for case study versus Pump Power (upconversion-free data) shows an increase in slope (i.e. gain efficiency) with increasing Δn . (b) Performance Map 2: plot of gain efficiency versus Δn . This data does not include the simulation of scattering transmission loss. 71
- Fig. 2.9. Plot of power and gain profiles (upconversion-free case study) for a series of pump powers (a) $P_p=0.2 \text{ mW}$ (below population inversion), (b) $P_p=0.8 \text{ mW}$ (linear regime of gain from Fig. 2.8.a) and (c) $P_p=2 \text{ mW}$ (approaching gain saturation of the device). 72
- Fig. 2.10. HIC Scaling Principle 1 for Microphotonics. Simulation is for SiON:Er single mode cut-off waveguide ($\Delta n=0.155$) with $L_g=2 \text{ cm}$. All other parameters same as case study; simulation performed with upconversion and no propagation loss. (a) Device Gain versus Pump Power shows an increase in slope (i.e. gain efficiency) with increasing Δn . (b) Plot of gain efficiency versus Δn . 75
- Fig. 2.11. Performance Map 3: Plot of Serpentine (solid) and Coil (dotted) footprints versus Δn . Shown are footprints for constant device lengths ($L_{\text{gain}}=1 \text{ cm}, 1\text{m}$) and constant device gain ($\gamma_d=3 \text{ dB}, 27 \text{ dB}$). Comparison of Serpentine and Coil structures for $L_{\text{gain}}=1 \text{ cm}$ shows that while comparable for small Δn , the Coil structure packs with a smaller footprint area at higher Δn , and

thus is the structure providing higher Areal Gain. Formulas to compute F are given in Table 2.6. 77

Fig. 2.12. Performance Map 4: (right axis) output signal-to-noise ratio versus Δn ; (left axis) P_s , P_{ASE+} versus Δn . (Data calculated for upconversion-free case study.) 78

Fig. 2.13. Plot of signal profile using upconversion-free case study with different L_g . For different L_g , ASE causes a divergence in P_s profile; L_{max} is not a constant. 79

Fig. 2.14. Performance Map 5: Plot of Optimal Device Lengths versus Δn , for three different P_p , determined from numerical simulation, in the presence of no scattering transmission loss (upconversion-free case). 80

Fig. 2.15. Figure of Merit versus Δn , for (upconversion-free) case study. 83

Fig. 3.1. (a) The atomic transition energy levels for Er[15], with labeling describing N_1 , N_2 , σ_{12} and σ_{21} . Spin-orbit coupling within the Er 4f-electron shell lifts a total angular momentum degeneracy of the shell, resulting in 4f-shell excited state $^4I_{13/2}$, $^4I_{11/2}$, $^4I_{9/2}$, etc. Local crystal field symmetry causes further Stark level splitting of spin-orbit states into meV-broadened manifolds. At room temperature, thermalizing phonons increase N_2 population energy higher into the $^4I_{13/2}$ manifold, resulting in hot line spontaneous emission, blue-shifted with respect to the dominant $^4I_{13/2} \rightarrow ^4I_{15/2}$ transition. (b) Schematic illustration of the intuitive interpretation of an absorption cross-section area σ_{12} . 89

Fig. 3.2. The cooperative upconversion effect is a two-step non-radiative resonant energy transfer (phenomenologically represented by coefficients C_{24} , C_{37}) between nearest neighbor Er atoms, resulting in the non-radiative de-excitation of 3 Er atoms from the first excited state for every 1 Er atom emitting green radiation at $\lambda \sim 560$ nm. 94

Fig. 3.3. Schematic of RF magnetron sputter machine, purchased from Kurt J. Lesker Company. The sputter machine can simultaneously sputter from three targets. RF sputter guns enable sputtering of metals (such as Er), semiconductors (such as Si) or dielectric insulators (such as SiO_2 and Si_3N_4). Three gas lines deliver Ar gas directly below each gun for Ar-sputtering; one gas ring disperses Ar/ O_2 (10% O_2) gas above the guns for oxygen reactive sputtering. 96

Fig. 3.4. Cross-section TEM of annealed Er_2O_3 thin film shows large grained complete crystallization. 97

Fig. 3.5. (a) The spectral responsivity of the Hamamatsu photomultiplier tube, as measured prior to installation in May, 2001. (b) Lifetime plots overlaying mechanical chopper temporal skew and 980 nm luminescence from Er-doped commercial glass. Lifetimes less than 100 μs cannot be temporally resolved. 98

- Fig. 3.6. (a) PL profile of Sample 7 at different temperatures, normalized to peak intensity. (b) 1 Å high resolution scan of Sample 7 PL at 4 K. High resolution scan reveals 1537 nm peak to be dominant intensity and therefore dominant ${}^4I_{13/2} \rightarrow {}^4I_{15/2}$ transition. 100
- Fig. 3.7. (a) Room temperature wide-range (visible to IR) PL profile of Sample 7. (b) Magnification of room temperature PL profiles in visible and 980 nm ranges. 102
- Fig. 3.8. (a) Gaussian function fits to room temperature PL profile of Corning Sample 7. (b) Room temperature Boltzman factor versus activation energy E_a , quantifying thermal population of hot line emission ($\lambda=1493$ nm) state. The experimental data in red overlaps the ratio of fitted $I(\lambda=1537$ nm)/ $I(\lambda=1493$ nm) from the measurement in (a), at $E(\lambda=1493$ nm)- $E(\lambda=1493$ nm)=23 meV. 103
- Fig. 3.9. (a) Single exponential fit of 4 K PL intensity decay (at $\lambda=1537$ nm) at 30 mW pump excitation power. (b) Inset: plot of fitted 4 K lifetime versus pump power (at $\lambda=1537$ nm). Outset: plot of 1/lifetime versus pump power; slope determines cooperative upconversion coefficient. 105
- Fig. 3.10. (a) 4 K PL profile of Er_2O_3 powder. (b) 4 K lifetime decay of $\lambda=1549.5$ nm PL peak. 107
- Figure 3.11. 4 K PL profile of Er_2O_3 powder in the visible spectrum. 108
- Fig. 3.12. (a) Plot of spectrally integrated PL versus temperature for $t=1$ hour anneals. (b) Plot of spectrally integrated PL versus time for $T=1050^\circ\text{C}$ anneals. Samples were annealed in a Rapid Thermal Anneal furnace under forming gas ambient. 108
- Fig. 3.13. Photoluminescence of Er_2O_3 films at different temperatures. All spectral profiles are normalized with respect to their peak intensities (in order to plot all the profiles within one graph). 109
- Fig. 3.14. (a) Peak intensity versus temperature at $\lambda=1533, 1537, 1542$ nm. (b) Visible PL emission from Er_2O_3 at 4K, consistent with the results of Kasuya et al.[71]. 111
- Fig. 3.15. Room temperature absorption versus luminescence for (a) an Er_2O_3 thin film and (b) the Er-doped Corning reference (Sample 7). 114
- Fig. 3.16. Overlap of room temperature PL profile for Er_2O_3 powder and sputtered thin film. The overlap indicates the 1537 nm optical center in sputtered Er_2O_3 corresponds to the BCC crystal phase commonly seen in the powder sample. 115
- Fig. 3.17. (a) 4 K Photoluminescence of Er_2O_3 thin film as-sputtered, after a low temperature anneal and after a hybrid low + high temperature anneal. Inset: comparison of PL intensity of 30 s RTA annealed sample versus hybrid low + high temperature anneal sample. Corresponding X-ray diffraction

- scans: (b) as-sputtered Er_2O_3 thin film, (c) low temperature 650 °C anneal, and (d) high temperature 1050 °C anneal. 117
- Fig. 3.18. Transmission electron microscopy of (a) as-sputtered Er_2O_3 thin film, (b) low temperature 650 °C anneal, and (c) rapid thermal anneal at 1050 °C. 119
- Fig. 3.19. Deviation in calculation of excited state population N_2 in the presence of cooperative upconversion, using an exact solution versus an iterative solution, (a) for Corning reference Sample 7, and (b) for sputtered Er_2O_3 . (Using an assumed cooperative upconversion coefficient of $10^{17} \text{ cm}^3/\text{s}$ for both case (a) and (b).) 121
- Fig. 3.20. 4 K cooperative upconversion coefficient calculation for Er_2O_3 FCC phase (1542 nm PL peak). Plot of $1/(\text{lifetime})$ versus pump power. Fitted linear slope derives an approximate value for the cooperative upconversion coefficient. Inset: plot of lifetime at 4 K as a function of Ar-ion pump power. 123
- Fig. 4.1 (a) Adjustable control of refractive index for reactively sputtered SiON films, as a function of Ar/ O_2 (10% O_2) gas flow rate[99]. 134
- Fig. 4.2. Room temperature PL scans from visible to IR (500-1700 nm) of as-sputtered (lower plot) and $T=1000^\circ\text{C}$ (for $t=1$ hour) annealed (upper plot) thin films of (a) $\text{SiO}_2:\text{Er}$ (b) $\text{SiON}:\text{Er}$, reactively sputtered, (c) $\text{SiON}:\text{Er}$, co-sputtered, and (d) $\text{Si}_3\text{N}_4:\text{Er}$. Data in the visible spectral range has been magnified by factors listed. All data has been renormalized with respect to Er concentration, film thickness, and luminescence extraction efficiency. 136
- Fig. 4.3. Normalized plots of Er IR emission in the four samples. The plots are staggered and overlaid with 2 nm resolution PL scans. The negligible change in peak linewidth indicates inhomogeneous broadening. 140
- Fig. 4.4. X-ray diffraction scan of $T=1000^\circ\text{C}$ ($t=1$ hour) annealed $\text{Si}_3\text{N}_4:\text{Er}$ sample, grown by PECVD and sputtering. The emergence of a short-range order around $2\theta=15^\circ$ may correspond with the formation nanocrystals of some other form of an Er-sensitizer. (Data courtesy Jifeng Liu.) 141
- Fig. 4.5. Photoluminescence (PL), normalized to peak intensity, from sputtered $\text{SiO}_2:\text{Er}$, $\text{SiON}:\text{Er}$ and $\text{Si}_3\text{N}_4:\text{Er}$. Peak position is at 1533 nm. (b) Plot of PL peak intensity versus annealing temperature for $\text{SiO}_2:\text{Er}$ and $\text{Si}_3\text{N}_4:\text{Er}$ samples. The lines are B-spline curves meant to guide the eye. 143
- Fig. 4.6. 4K PL spectral of samples, overlaid with 2 nm resolution scans. The negligible change in linewidth confirms inhomogeneous broadening. 147
- Fig. 4.7. Process Map for $T=1000^\circ\text{C}$ ($t=1$ hour) annealed sputter samples. (a) Measure of Er clustering process in different hosts. (b) Measure of Er cooperative upconversion process in different hosts. The lines are spline curves meant to guide the eye. 149

Fig. 4.8. AFM. (a) Si ₃ N ₄ :Er, as-sputtered (b) SiON:Er reactive, as-sputtered (c) and (e) SiON:Er co-sputter, as-sputtered (d) and (f) SiON:Er co-sputter, annealed.	152
Fig. 4.9. Optical pump cross-section σ_p measurements determined from plotting PL risetime versus pump photon flux, for (a) the Corning reference sample, (b) SiO ₂ :Er, (c) SiON:Er, (d) Si ₃ N ₄ :Er. (Data acquired courtesy of Jae Hyung Yi and Dr. Luca Dal Negro, MIT.)	154
Fig. 4.10. Possible formation of nanocrystals in annealed SiON and Si ₃ N ₄ .	158
Fig. 4.11. PL peak intensity at $\lambda=1533$ nm versus $\lambda=985$ nm for (a) SiON:Er and (c) Si ₃ N ₄ :Er. Correlation plots identifying the upconversion process for (b) SiON:Er and (d) Si ₃ N ₄ :Er. (Data collected courtesy Jae Hyung Li.)	161
Fig. 4.12. Upconversion coefficient C_{24} simulation fits to PL emission decay data for ($P_p:90$ mW \rightarrow 0 mW at $t=0$) (a) SiON:Er and (c) Si ₃ N ₄ :Er. As comparison, the approximation technique for measuring C_{24} in chapter 3 is also plotted for (b) SiON:Er and (d) Si ₃ N ₄ :Er.	162
Fig. 4.13. Schematic diagram of VSL set-up, depicted in a sideways (as opposed to overhead optical pump) profile. (Image courtesy Dr. Luca Dal Negro, MIT.)	165
Fig. 4.14. Variable Stripe Length method for measuring Amplified Spontaneous Emission[100] from SiON:Er (co-sputtered). Results show a decrease in modal loss as a function of pump power. (Data acquired courtesy Dr. L. Dal Negro.)	169
Fig. 4.15. Variable Stripe Length method for measuring Amplified Spontaneous Emission[100] from Si ₃ N ₄ :Er. Results show a decrease in modal loss as a function of pump power. (Data acquired courtesy Dr. L. Dal Negro.)	171
Fig. 5.1. (a) Schematic diagram showing the fundamental elements of a (traveling wave) ring resonator WDM de-multiplexer. (b) Comparison with a Fabry-Perot standing wave resonator.	179
Fig. 5.2. Schematic of out-of-plane coupling between waveguide bus and ring resonator.	181
Fig. 5.3. Schematic illustration of transfer of incident power $ s_i ^2$ from waveguide bus to ring resonator power $ A ^2$, through field coupling coefficient κ . $ s_i ^2$ is the transmitted power continuing in the waveguide bus after coupling.	185
Fig. 5.4. Equivalence between a traveling-wave ring resonator and standing wave resonator cavity. Transmitted power downstream from the ring (open arrow-head in (a)) is equivalent to the reflected power from a resonator cavity (open arrow-head in (b)).	189
Figure 5.5. Reflection diagram reproduced from [110], plotting $\text{Im}(\Gamma)$ versus $\text{Re}(\Gamma)$.	191
Figure 5.6. Undercoupling.	194
Figure 5.7. Critical coupling.	194

- Fig. 5.8. Overcoupling. 195
- Figure 5.9. (a) Plot of s_t versus $1/\tau_o$, for a fixed $1/\tau_e$. Using SiON case study parameters. (b) P_{ring} versus Q_e shows optimal power transfer at critical coupling $Q_e=Q_o$. 197
- Figure 5.10. (a) Lasing threshold calculation for the SiON case study, in units of threshold pump power $P_{p,th}$. (b) Magnification of upconversion case from (a), in units of threshold pump power flux $\phi_{p,th}$. Right axis in both plots show the fraction threshold population inversion $\Delta N_{th}/N$ corresponding to $P_{p,th}$, $\phi_{p,th}$. 201
- Fig. 5.11. Coupling strength of waveguide bus to resonator. Plot of Q_e and coupling efficiency η versus gap δ . Extrapolate δ required for given Q_e . The derivation of these plots is shown in Appendix 2. (Calculation performed by Daniel Sparacin, MIT.) 204
- Fig. 5.12. (a) Signal power versus pump power inside the resonator, with and without upconversion. (b) Magnification of (a), showing abrupt change in quantum efficiency above and below lasing threshold. (c) Signal power versus pump power outside the resonator, with and without upconversion, shows a lower slope and a higher lasing threshold for the upconversion case. (d) Coupling of optical pump from the waveguide bus into the ring laser clamps to a constant value above lasing threshold. 207
- Figure 5.13. Ring resonator Fabry-Perot mode locations for SiON case study, overlapped with Er PL emission profile from SiON:Er. 211
- Fig. 5.14. Property Map 1. Areal footprint of a ring resonator, whose radius is radiative loss-limited ($\alpha_{rad}=0.1$ dB/cm), as a function of Δn . An effective path length $L_{eff}=1$ cm (or 100 μm) corresponds to a total quality factor $Q=36\ 500$ (or 360). 212
- Fig. 5.15. (a) Analytic calculation of enhancement in small signal transmission versus reflectivity, in a VC SOA. (b) Simulation of power inside the resonant cavity, using (5.35), of the VC SOA reported in [119]. 216
- Fig. 5.16. (a) Analytic calculation of enhancement in small signal gain for transmission past the R-WOA. (b) Plot of Fig. 5.17.d for case when incident signal is shut off; we recover the ring laser L-I curve from section 5.4.1. 219
- Fig. 5.17. (a) Device gain, signal and noise power in waveguide bus for $Q_e=7\times 10^3$. (b) Signal and noise power inside R-WOA for $Q_e=7\times 10^3$. (c) Device gain, signal and noise power in waveguide bus for $Q_e=1\times 10^4$. (d) Signal and noise power inside R-WOA for $Q_e=1\times 10^4$. 220
- Fig. 5.18. Ring Amplifier Property Map 2 & 3: for ring amplifiers giving a 3 dB output gain, (a) Gain Efficiency (3 dB/ P_p) versus Q_e and (b) Transmission Enhancement for $P_s=1, 10\ \mu W$, versus Q_e . 222

- Fig. 5.19. (a) Current Si Microphotonic designs for efficient coupling of dielectric materials-based optical interconnects to a semiconductor-based photo-detector. (b) The WDM Ring Detector design. 226
- Fig. 6.1. (a) Transverse-resonant optical pump scheme will give uniform power profile along z-direction of propagation. (b) A Projection Band Diagram of the case study for this chapter. Pertinent PBG features are labeled. 234
- Fig. 6.2. (a) Reflectivity spectra for a Bragg reflector at three different angles of incidence (from ambient free space). (b) The spectra of (a) viewed as linear trajectories on a Photonic Crystal projection band diagram. 236
- Fig. 6.3. Confinement inside a resonant cavity (a) with refractive index less than Photonic Crystal layer n_2 , and (b) with refractive index greater than Photonic Crystal layer n_2 . 243
- Fig. 6.4. Case (i): TM and TE mode projection band diagram for $\text{Si}_3\text{N}_4/\text{SiO}_2$ Photonic Crystal. 247
- Fig. 6.5. Case (ii): TM and TE mode projection band diagram for $\text{Si}/\text{Si}_3\text{N}_4$ Photonic Crystal. 247
- Fig. 6.6. Case (iii): TM and TE mode projection band diagram for Si/SiO_2 Photonic Crystal. 248
- Fig. 6.7. Schematic diagram of 1-D PBG with an $\text{SiO}_2:\text{Er}$ defect layer. The structure was grown with 6 Bragg reflector Si/SiO_2 pairs of thickness $\lambda_s/4n$, in order to minimize λ_s transmission loss in the propagation direction. 249
- Fig. 6.8. Spectral profile of Er emission overlaid with PBG defect state band structure. ω and β variables are plotted in units normalized to $2\pi c/L$ and $2\pi/L$, respectively. 250
- Fig. 6.9. (a) Projection Band Diagram for the designed PC-WOA structure. (b)-(e) plot spatial distribution of TE modes as labeled for given (ω, β) values from (a). Plots (b)-(e) were computed for a finite PC-WOA composed of 3 Bragg Reflectors cladding the $\text{SiO}_2:\text{Er}$ defect layer on either side (the sputter-deposited structure is composed of 6 Bragg Reflectors cladding either side). The fraction of power confined within the PC-WOA core for these spatial modes are listed in Table 6.1. 252
- Fig. 6.10. (a) Schematic diagram of a Si_3N_4 60° prism coupler atop the PC-WOA. (b) The coupling effect of a Si_3N_4 prism coupler, as understood on the Projection Band Diagram. 255
- Fig. 6.11. (a) Plot of defect layer dispersion bands at λ_s and λ_p for the choice of three different defect layer thicknesses. (b) and (c) are magnifications of (a) around the λ_s and λ_p frequency regions, respectively. 258
- Fig. 6.12. (a) Spectral Reflectivity at angle corresponding to λ_s propagation, for different number Si/SiO_2 Bragg Reflector stacks. (b) Reflectivity and propagation loss α_p versus number Si/SiO_2 Bragg Reflector stacks, at λ_s . 261

- Fig. 6.13. (a) Re-plotting of defect bands 1 and 3 from Fig. 6.9.a (without low/high dielectric bands) and (b) the first derivative of (a), defined as the group velocity. 263
- Fig. 6.14. (a) Dispersion relation for SiON case study (end of chapter 2) in one-dimension, show band structure for index-guided propagating modes. (b) Band structure curvature versus frequency ω for index-guided and PBG-guided propagating modes. Magnification of two local regions shows the curvature at frequency corresponding to λ_s for (c) index-guided band structure and (d) PBG-guided bandstructure. 265
- Fig. 6.15. Secondary Electron Mass (SEM) micrographs of the sputtered 1-D PC-WOA test structure, (a) as-deposited and (b) with magnification; (c) after $t=1$ hour, $T=1000^\circ\text{C}$ anneal and (d) with magnification. 268
- Fig. 6.16. (a) Reflectivity plot of sputtered PC-WOA, showing good agreement between experimental structure versus theoretical design, for both defect layer standing wave state (shown as higher spectral resolution in (b)) and Bragg Reflector stop-band. 270
- Fig. 6.17. (a) Plot of optical powers (left axis) and gain profile (right axis) versus position z within the $L_g=2$ cm PC-WOA, yielding an output device gain of 3 dB for $P_s=10$ μW input signal power (constant pump power profile within the resonant cavity, $P_{p(\text{in})}=0.425$ mW). For the same device, plot of device gain versus pump power (b) inside the PC-WOA, $P_{p(\text{in})}$ and (c) outside the PC-WOA, $P_{p(\text{out})}$. We observe that $P_{p(\text{out})}=32$ mW corresponds to the $P_{p(\text{in})}=0.425$ mW cavity pump power profile. (d) Plot of $P_{p(\text{in})}$ versus $P_{p(\text{out})}$, demonstrating the PC-WOA to be a highly under-coupled device. 272
- Fig. 6.18. (a) Schematic for hybrid PC-WOA, comprised of a higher refractive index defect layer which guides propagating modes of λ_s by total internal reflection confinement, and λ_p by both total internal reflection confinement and PBG resonant confinement. (b) Projection Band Diagram for this structure 276

List of Tables

Table 1.1. Performance summary of a characteristic long-haul EDFA and SOA, summarized from [5].	38
Table 2.1. Definitions table for all notation used in this chapter.	50
Table 2.2. Collection of rare-earth IR-emitting optical dopants (ODs), listing their PL peak's (~gain peak) wavelength.	53
Table 2.3. Case study device parameter and control variable values used to generate Figs. 4.4-4.11. (NA means Not Applicable; the SiON case study was presented as a function of pump power P_p , and not at one particular P_p .)	55
Table 2.4. Gain Efficiency (upconversion-free case study) in the presence of loss, and optimization by reduction of amplifier length L_g .	73
Table 2.5. Order of magnitude pump powers sufficient to achieve population inversion in WOAs for index differences $\geq \Delta n_{\min}$.	81
Table 2.6. Design Rules: summary of scaling equations for interpolating arbitrary device parameters and performance functions from Performance Maps 1-6 (using upconversion-free case study, $\alpha_s = \alpha_p = 0$ dB/cm).	84
Table 3.1. Summary of Er-doped glass samples donated by Corning Inc. to the Kimerling Research Group, MIT University. Listed are the doped Er concentrations N_{doped} . Corning certifies $N_{\text{doped}}/N_{\text{active}} \cong 1$ for all samples.	101
Table 3.2. Lifetime measurement summary of Corning Sample 7.	106
Table 3.3. Assignment of 4 K lifetime, 4 K cooperative upconversion coefficient, apparent density and crystal phases of Er_2O_3 thin films. Cooperative upconversion coefficient and density could not be computed for the 1533 nm phase.	110
Table 3.4. Summary of small signal gain and gain efficiency calculations.	126
Table 4.1. Deposition parameters for the four sputtered samples. Also listed are measured refractive indices by thin film ellipsometry ($\lambda=633$ nm), refractive index measurement (for samples with an index higher than thermal oxide) by a prism coupler ($\lambda=1555$ nm), and measured Rutherford Back Scattering (RBS) Er concentrations.	137
Table 4.2. Deposition time and deposited film thickness (measured by profilometry), estimate of normal incidence pump power transmission coefficient (at $\lambda=488$ nm) into films (using $\lambda=633$ nm measured index values from Table 4.1), luminescence extraction efficiency ($\lambda=1533$ nm), and PL peak intensity enhancement or T=1000°C annealed (t=1hour) versus as-sputtered sample.	139

Table 4.3. List of lifetimes (at 4K and room temperature) for SiO ₂ :Er, SiON:Er (reactive), SiON:Er (co-sputter) and Si ₃ N ₄ :Er samples, as-sputtered and after a T=1000°C anneal (for t=1 hour).	142
Table 4.4. Listing T _{anneal} , T _{thres} , T _{melt} for the four study samples.	145
Table 4.5. Loss measurements of propagating slab modes in Er-free films	150
Table 4.6. Refractive index, 4 K and room temperature lifetime data, and Rutherford Back-Scattering(RBS) Er concentration measurements, for SiO ₂ :Er, SiON:Er and Si ₃ N ₄ :Er. ‘CVD SiO ₂ ’ refers to a CVD grown SiO ₂ :Er sample donated by Corning, Inc. The Er concentration for the CVD sample is a nominally prepared composition as determined by Corning manufacturers.	157
Table 5.1. Summary of device parameters used for ring laser and amplifier.	199
Table 5.2. Summary of lasing threshold and quantum efficiencies (with and without upconversion), both inside and outside the ring laser.	209
Table 5.3. Summary of ring laser device dimension and specifications. Designs implanted in lithography mask <i>MASK Amplifier H-tree</i> (see chapter 2 introduction image).	210
Table 5.4. Data transmission limit due to resonant confinement.	213
Table 5.5. Nominally assigned values to device parameters for (5.35) in order to approximate gain performance of a III-V VC SOA.	217
Table 5.6. Summary of detector design.	229
Table 6.1. Summary of transverse-resonant propagating mode group and effect refractive indices, and mode angle θ_m ; coupling angle into the resonant states from ambient free space (θ_{air}) and an ambient Si ₃ N ₄ prism coupler ($\theta_{Si_3N_4}$).	255
Table 6.2. Summary of propagation loss as a function of the number of Bragg Reflector pairs (cladding a defect layer below and above) reveals that the exponential sensitivity of α_p on R requires a minimum of 8 Si/SiO ₂ Bragg Reflector pairs in order to decrease propagation loss to ~0.3 dB/cm.	261
Table 6.3. Summary of effective refractive index, group refractive index and Free Spectral Range at two pump wavelengths $\lambda_p=488, 980$ nm and signal wavelength $\lambda_s=1537$ nm.	262
Table 6.4. List of band curvature, dispersion coefficient, and temporal pulse broadening Δt at 100 Gbit/s and 10 Gbit/s, for an index-guided versus PBG-guided WOA (Microphotonic length scale $L_g=1$ cm).	266
Table 6.5. Materials dispersion: the decrease in refractive index for both Si and SiO ₂ with increasing wavelength. We observe a larger change in refractive index for Si over this wavelength range, than for SiO ₂ .	267
Table 6.6. Summary of Er absorption Q_{Er} versus external coupling Q_e . α_{Er} has been taken at $z=L_g$, the location in the PC-WOA at which population inversion	

ΔN is lowest (for a constant pump $P_{p(in)}=0.425$ mW power profile), and thus absorption at $\lambda_p=980, 488$ nm is highest. 273

“Education is the kindling of a flame, not the filling of a vessel.”

–Socrates

“Success is the most knowledge from the least exploration... The art of research is primarily creative problem definition and secondarily execution. Go to it!”

–email from Prof. L.C. Kimerling (6/21/01)

“Remember, 90% of the task is framing the problem such that new knowledge can be found as a foundation for the next problem. Think small, but be relentless in demanding closure every two weeks. These are my expectations.”

–email from Prof. L.C. Kimerling (6/22/01)

“I guess you’ll graduate when you’ll see the 3 dB light at the end of the tunnel!”

–Dr. J. Michel

“Talk while you’re walking.”

–Frank Minna, “Motherless Brooklyn”
by Jonathan Lethem

“Work is worship.”

–a Hindu Holy Man, Fall 2003

Acknowledgments

It's first light in the homeland of my family, and I'm sitting here halfway around the world, one week after my final defense... I came to MIT in 1997, and it's been a good, challenging time. No regrets.

I'm completely in gratitude to Professor Lionel C. (I never learned what the C stood for) Kimerling, Fearless Leader of EMAT and the best possible man I could have worked for. Kim taught me leadership, communication, efficient scientific investigation, how to make a stand and say where it's at; the wisdom to listen, and his kind compassion on one heart-breaking day gave me courage to stay my course. Thank you, boss.

And then there's Jurgen, who by my account is my second thesis advisor. Jurgen can achieve anything in the lab, and his daily guidance showed me how to be an experimentalist and get the job done. His immense kindness and good will gave me a resource of comfort I can't fully express. Jurgen's door was always open, and I learned a lot from listening to him. Thank you.

I spent my first two years in MIT transitioning through Leslie Kolodziejski's group before finding my home with Kim. My thanks to Leslie, I appreciate the time, the good work learning MBE and that fantastic group at Lincoln Labs: Katie Hall, Joe Donnelly, Sam Choi and Bob Bailey—the coolest III-V processor I ever met. Alexei (Lex) Erchak and Steve Patterson made the office place sane. You guys are champs.

EMAT has been a group of people who made coming in to work fun and inspiring, every day. Thomas Chen (my Er predecessor), Andy Luan, Kevin Chen, Michal Lipson, Desmond Lim, Aimee Smith, Anand Reddy and Kevin Kidoo Lee welcomed me into Kim's enclave and put me at ease. I have fond memories of Andy and Kidoo. I couldn't have achieved my experimental work without Jessica Sandland and Anat Eshed's sputtering collaboration, it was great fun and I'm glad to have known them. Xiaoman Duan collaborated with me and gave me sweet-hearted advice when I needed it. Anu Agarwal was a post-doc who felt like a big sister, thank you Ji. Kazumi Wada was the soft-spoken leader who welcomed me into the group with Kim and helped me develop many ideas. Mindy Baughman, our administrative assistant extraordinaire, kept the office going like a live wire; it's been a blast talking Lit & movies. Dan "The Man" Sparacin, Douglas "Might of the Midwest" Cannon, Dave Danielson, Victor Nguyen, Donghwan Ahn, Trisha Montalbo, Shoji Akiyama, Yasha Yi, Luca Dal Negro, Jae Hyung Yi, Jifeng Liu, Ching-Yin Hong, Mike Stolfi and Nok have been great collaborators; some of you even better friends. Luca Dal Negro is a powerhouse Carnot engine who along with Jae Hyung helped me realize the important optical gain work of this thesis. Donghwan, Shoji and Trisha have been the best possible office-mates. Dan, Dave and Douglas make you want to hang out and have good times even after 5PM. My special thanks to Milos Popovic, super-cool ring resonator expert, the incomparable Prof. Hermann Haus, and my thesis committee—Prof. Gene Fitzgerald (you've been there guiding me past all the highs and lows), Prof. Sam Allen (thank you for your good will and making kinetics make sense) and Prof. Rajeev Ram (thank you for your diligence)—whose contributions helped raise the standard of this work.

At MIT I also explored my other great interest, fiction and literature. You'd be surprised what treasures MIT has hidden amongst its engineering and Media Lab buildings. I took a fiction-writing program, memorably instructed by people like Anita Desai and the heart-warming Steven Alter... but it was in the spring of 2000 when I took a detective fiction class and I met my literary guru, Prof. David Thorburn. Prof. Thorburn introduced me to the Shakespearean Prof. Donaldson, the far-reaching, ahead-of-his-time brilliance of Prof. Henry Jenkins and the powerhouse intellectual community of CMS... but for me in the end, all roads come back to Prof. Thorburn and continue again from there. Alongside Kim, Prof. Thorburn was a guiding mentor for me in these years. Thanks, Sir.

My friends. You guys made it fun 24/7, no matter how oppressive MIT felt. I came to this town knowing only G-dog and Matt, and today there's Gianni & Christy Taraschi, Lisa McGill & Matt Borthwick, Jamileh Jemison, Manish Deopura & Rupa Das, Rohan Oberoi & Karolina Minda, Zachi Avrahami & Keren Hamel, Sean & Suzanne George, Alexei Erchak & Lauren, Rohit & Anu Prasankumar, Rajappa Tadipalli, Asha Balakrishnan, Kate Jackson and m'main man, Mr. Vikas Mehta. Beyond MIT have stood the core trinity: Balbir Basra, Norman Landry and Lap-Lung Chiu... Geez, almost everyone's married! Ah guys, it's been awesome, it is awesome, it will continue to be awesome. There are no endings, only mortgages and baby-making... Purnima Sahgal has been my big sister away from home, and you're a spiritual inspiration to follow, P-didi! Aparna, it was great fun. Against all the change, it's a small sweet thing I remember fondly. John Matthew's Harvard-Wellesley SAATH gang, the Aswin Punathambekar-led CMS crowd and the always-cheerful Prof. Tuli Bannerjee completed the picture. A shout-out to Philip Tan and the Assassins' Guild: pick the blue pill.

My family. I can't put into words how much it meant to me that they came for my final defense. Mummy and Daddy, Amita and Aruna, I love you all so much. My brother-in-laws Sanjeev Ahuja and Deepak Chadda added to the family and helped bring four little people into the world who make me proud: Deeksha, Aneesha, Roohi and my little hobbit, Neil. Ok guys, got the message—will find you a Mami soon, I promise! My uncle Jindi Mama and my bald-headed cousin Shabad are the other two family members I am closely tied to, wish you guys could've come to the defense.

I'd like to acknowledge Peter Parker and the hard-luck super-heroic struggle. Great powers bring great responsibility, Amen. (Million Year..., best store in town.)

Life is full of ups and downs. Maybe I saw that with imbalance during the MIT years, but my Mom and Dad were always there to cheer me on. This has been as long and as hard for me as it has been for them. Finally done with academia, I'm at a point where I find everything they ever said about life, was on the money. And with work being the worship of our existence, my parents are the hard-working heroes of my life. I dedicate this Ph.D. thesis to Rama Saini and Baldev Raj Saini. I love you both.

And I'm outta here. Namaste.

Chapter 1:

Introduction to the EDWA, Photonics, and the Planar Lightwave Circuit



Optical components used in first rare earth ion doped fiber amplifier, reproduced from [1]. From top to bottom, the elements are a laser cavity, a fiber laser shaped in a helical form, a flashtube and an 18 cm scale. Reference: Snitzer et al[2].

“... I wanted to do something in optics... when I was young I took electromagnetic theory in the Physics department in Seoul National University... it made me really want to study, before that I was just...” –Donghwan Ahn (Ph.D. student, EMAT), fellow 13-4153 office-mate and mp3-man.

“I like this, somehow... it’s very stimulating.” –Dr. L. Dal Negro (Post-Doctoral Associate, EMAT), optics guru.

“You remind me of that donkey from Winnie the Pooh, you know the one?... He’s always depressed!” –Dr. Anuradha Agarwal’s (Research Associate, EMAT) observation during an XPS measurement, three years ago.

1.1 Er-Doped Amplifiers

The Er-Doped Fiber Amplifier (EDFA) and Er-Doped Waveguide Amplifier (EDWA) are devices which deliver optical gain in the neighborhood of $\lambda_s=1.55 \mu\text{m}$ light, by means of stimulated emission between a three-level energy system within the Er atom. The EDFA has been the workhorse component[1] of modern (fiber optic) telecommunications for the last twenty years, performing typical $\sim 10^3\times$ optical amplification of pulse-encoded light signals, after characteristic distances of 100 km transmission through optical fiber.

It is because of the EDFA device that fiber optic signals can propagate for thousands of miles, running trans-continental or sub-marine lengths (see Fig. 1.1.3). The EDFA enabled the practical applicability of long-distance, or long haul, telecommunications, giving rise to the high data rate (10 Gbit/s and rising) global communications market driven by internet applications today.

The EDFA is a waveguiding optical fiber, with a higher numerical aperture or waveguide core/cladding index difference[3] than typical fiber, whose waveguide core has been co-doped with Er. Given the insulator materials (typically SiO_2 majority constituent) used to make ultra-low transmission loss optical fibers[1], the EDFA is an optically pumped amplifier, where the Er atoms are energized into higher excited states and made available for net gain (i.e. population inversion[4]), by a pumping wavelength λ_p of energy higher than the $\sim 1.55 \mu\text{m}$ signal wavelength λ_s . Typical pump schemes involve co-propagating or counter-propagating the waveguiding pump and signal wavelengths.

The EDWA is a recently commercialized[5] planar technology version of the EDFA, designed to take advantage of the planar processing technologies developed in the semiconductor industry, in order to create smaller sized (principally by increasing Er doping), lower-cost Er-based optical amplifiers. The EDWA is currently sold as a rib or ridge waveguide[6], somewhat limiting its physical compactness. Academic research into Er-doped planar waveguides[7][8] has thus far limited itself to rib waveguide structures as well. This is because the optical gain from ms radiative lifetime Er is prohibitively low, resulting in concentration-limited (see chapter 3 for details) gain coefficients around 3 dB/cm. For an Er-doped amplifier to provide net gain, waveguiding losses must be considerably smaller than 3 dB/cm. The ultra-low loss properties of optical fibers and confinement geometry of ridge waveguides provide low waveguide losses satisfying this requirement.

1.2 Thesis Study: Er-doped Microphotonic Amplifier

This thesis continues planar processing research studies into Er-doped waveguide amplifiers by looking at Er emission and optical gain performance in high refractive index Erbium Oxide (Er_2O_3), Silicon Oxynitride (SiON) and Silicon Nitride (Si_3N_4) materials. Given recent advances in engineering low propagation loss strip SiON waveguides[9] using semiconductor processing tools, we explore the implications of planar processing to maximize optical gain, maximize amplifier gain efficiency, and minimize amplifier size.

The specific need for a low power, small (areal) footprint planar optical amplifier is detailed in section 1.7. To briefly summarize, Si Microelectronics has reached a communications bottleneck, where as a result of chip complexity, electronic data rates on

an integrated circuit are beginning to be limited by resistive and capacitive (RC) delays in the metalization lines carrying signal information. A proposed solution is to replace these metal interconnects with optical interconnects: micron-scale densely integrated waveguides, free of such RC delays. The basic structure of such an optical interconnect architecture is called the Planar Lightwave Circuit (PLC). Optical waveguides within a PLC are envisioned to have core/cladding refractive index differences on the order of $\Delta n=0.1-0.7$. Such magnitude index differences enable the processing of single mode waveguide structures with turning radii and characteristic device feature size on the order to 50-500 μm . Thus, a PLC constrained to $\Delta n=0.1-0.7$ will have micron-scale size features, enabling this architecture be (potentially monolithically) integrated onto an existing layer of metal interconnects in an integrated circuit.

The micron-scale waveguiding devices requisite for the optical interconnect application PLC, are more generally referred to as microphotonic devices. Specifically, our research group's concerns to create such devices for the Si Microelectronics interconnect problem, restricts the class of materials we work with, to Si processing compatible materials. This restricted materials class of micron-scale waveguide devices are thus referred to as Si Microphotonics. Our research goal is to extend the EDWA-initiated work in planar Er-doped amplifiers, to a Si Microphotonic amplifier.

The materials constraint for a Si Microphotonic amplifier must be the choice of a materials system compatible with Si processing and the Si substrate. For devices designed to operate at carrier frequencies about 1.55 μm , there are currently two options for optical amplification: III-V based InGaAsP materials or the Er atom. While the Er atom is Si processing compatible, the III-V elements are lifetime killers for Si

Microelectronics. Hence our choice for exploring a Si Microphotonic amplifier is based on the Er-doped optically pumped waveguide.

In order to (i) maximize gain per unit pump power and (ii) minimize footprint for such an optically pumped amplifier in a densely integrated PLC, we did a design study (chapter 2) to systematically map the influence of index difference Δn on these two performance criteria. Provided waveguide scattering loss can be kept to minimal values of ~ 0.2 dB/cm (a benchmark which has been met in the SiON materials system), we map the strong power-law influence of Δn on Si Microphotonic Waveguide Optical Amplifiers (WOAs), in comparison to the EDFA or EDWA.

1.3 Thesis Study: Materials for the Microphotonic Amplifier

The micron-scale dimensions of microphotronics requires our investigating new materials systems within which optical gain can be maximized per unit length and per unit pump power. There are two classes of Er-based Si Microphotonic-compatible amplifying materials we investigated, (i) erbium oxide (Er_2O_3), an ultra-high Er-doped host material ($\sim 10^{22}$ Er/cm³) with refractive index $n=1.87$, and (ii) silicon oxynitride (SiON) and silicon nitride (Si_3N_4), with refractive indices $n=1.6$ and 2.2 , respectively. When clad with a silicon oxide (SiO_2) cladding (index $n=1.445$), these materials form waveguides with index differences of (i) $\Delta n=0.425$ and (ii) $\Delta n=0.155$ and $\Delta n=0.755$, respectively.

Prior work in our group demonstrated the considerable glass chemistry difficulty of inhibiting atomic clustering of Er atoms when co-doped into SiO_2 by CVD[10]. The most promising options for doping Er atoms at high light-emitting concentrations with

minimal atomic clustering were by either ion implantation[11] or a form of PVD[12,13]. For the work in this thesis we have investigated Er co-doping into dielectric hosts by the PVD process of sputtering. In order to access the possibility of maximizing optical gain from the Er-based transition, we have also investigated Erbium Oxide (Er_2O_3) as a limiting example of ultra-high Er concentrations within a dielectric host.

Er_2O_3 is a material compatible with Si processing cleanroom facilities. There is only one reported photoluminescence (PL) study in the literature, done in the visible PL range. In chapter 3 we present an infrared PL study of Er_2O_3 , reporting both room temperature and low temperature (4 Kelvin – 20 Kelvin) emission and lifetime measurements. Transmission Electron Microscopy and X-ray diffraction studies are presented as well to relate PL emission spectra with different structural phases, and measurements are done to quantify an Er gain-limiting process known as cooperative upconversion. We then theoretically evaluate the optical gain potential of this material, based on its measured lifetime and upconversion values.

Er-doped SiON and Si_3N_4 materials are a priori our most promising Er-based optical gain systems, potentially having minimal cooperative upconversion. As detailed in both chapters 3 and 4, cooperative upconversion is an Er-Er interaction process which significantly increases with Er concentrations above 10^{20} cm^{-3} . In chapter 4 we explore Er PL emission in these two host materials. While there are preliminary experimental reports of gain measurement in Er ion-implanted SiON, there has been no systematic characterization done of SiON:Er and Si_3N_4 :Er lifetimes, interaction cross-sections and upconversion coefficients. We performed measurements on all these optical parameters and combined them to test optical gain prediction using a three-level atomic transition

model that incorporates upconversion. The resulting optical gain prediction was compared against experimentally measured results. Secondly, there has been very little literature published on Er co-sputtered Si_4N_4 films, and none for SiON films. Our materials deposition is done by the sputtering process, and we report on this process' ability to grow optical gain quality material, in contrast to the predominantly favored Er-doping process of ion-implantation.

1.4 Thesis Study: Resonant Techniques for Gain Efficiency and Footprint Enhancement

In order to further enhance our performance metrics of gain efficiency and planar device footprint, we initiate two new studies attempting to take advantage of resonant confinement principles. We present the theoretical analysis of these two approaches and some preliminary results.

In chapter 5 we study the influence of resonant confinement along the signal and pump propagation direction (longitudinal resonant confinement), on WOA gain per unit length, gain efficiency and footprint. Using as a reference comparison, recently published results showing similar gain enhancement for III-V materials-based Vertical Cavity Semiconductor Optical Amplifiers (VCSOAs), we present a two-level laser differential equation model, modified to account for the effect of confined signal enhancement inside a resonant cavity. We compare our model's predictions with III-V reported results, and apply the model to quantify the photon build-up inside a particular type of Er-doped resonant structure, the ring resonator. We discuss the difference in resonance confinement on pump wavelengths for VCSOA versus ring resonators, and how this difference affects device gain efficiency. Simulations of device gain and applicability to

broadband gain are discussed. Simulation results are also presented on the first attempt to create an Er-doped ring resonator laser. The Er-doped ring laser and the Er-doped Resonant-WOA (R-WOA) are currently being processed for experimental testing.

In chapter 6 we present our second approach to enhancing WOA gain efficiency: transverse resonant confinement. We design a one-dimensional photonic crystal to resonantly confine, within a defect layer, both optical pump and signal wavelengths, as propagating modes of light. This confinement principle builds on research activities over the last ten years investigating the optics physics of Photonic Band Gaps[14], and recent studies leading to commercialization efforts in Photonic Crystal fibers[15]: fibers which guide light not by the principle of total internal reflection (as in fiber optics), but rather the principle of omnidirectional reflectivity. We extend these ideas to explore the influence of omnidirectional reflectivity, which chapter 6 describes in more details as a form of resonant confinement, on optical pumping of an Er-doped waveguide core. This form of (transverse) resonant confinement should yield an enhancement in gain efficiency, while eliminating the sub-lasing threshold constraint of longitudinal resonant confinement. We model gain of such a device and report on its gain efficiency. We present two Photonic Crystal PC-WOA models; (i) model 1 allows feasible testing of our optical pump confinement principle, and (ii) model 2 is a hybrid structure based on both total internal reflection and Photonic Band Gap confinement, resulting in a PC-WOA that can take optimal advantage of transverse resonant confinement. We grow model 1 by sputtering and present some preliminary SEM and reflectivity results on the device. Further amplifier testing of this device will be carried on by our research group.

Together with the materials investigation and theoretical design Property Maps presented in this work, this thesis explores and defines the device impact and materials constraints of microphotonic scale Si processing-compatible EDWAs, as a function of two variables: device gain efficiency and device footprint.

The layout of each chapter in this thesis is like a journal publication, containing a Chapter Abstract, Introduction, Experimental Background, Discussion and Conclusion section. Our cumulative results and suggestions for future work are summarized in chapter 7.

The remainder of this chapter presents an historical aside reviewing the relevance of EDFAs in telecommunications and the convergence of optics and electronics giving rise to interest in developing micron-scale photonics and their PLC applications to problems such as the Interconnect Bottleneck.

1.5 Review: Photonics and the Confined Propagation of Light

Photonics is the technology of light waveguiding and light signal processing. The foundation of Photonics rests on three cornerstone discoveries of the 20th century: (i) the invention of the laser, (ii) the invention of low loss optical fiber, and (iii) the invention of semiconductor optical devices. This chapter gives a brief overview of the origin of Photonics, the impact of Er-doped optical amplifiers in developing fiber optic networks, and the role of Er-doped waveguide amplifiers explored by this thesis work, in the emerging technology of Silicon Microphotonics.

Photonics is the modern name for a field of materials research and device technology deriving its origin from Snell's Law and the Principle of Total Internal

Reflection. Snell's Law is the application of Fermat's Principle[16], minimizing the optical path length travelled by light in two media of refractive indices n_1 and n_2 . Fermat's Principle equivalently implies that the form of Snell's Law,

$$n_1 \sin \theta_1 = n_2 \sin \theta_2 \quad (1)$$

is an expression for the conservation of the speed of light in both media n_1 and n_2 .

For $n_2 > n_1$, the Principle of Total Internal Reflection defines a critical angle θ_c for light to remain trapped within media n_2 ¹

$$\theta_c = \sin^{-1} \left(\frac{n_1}{n_2} \right). \quad (2)$$

The discovery of light confinement by total internal reflection remained a scientific curiosity until the development of electromagnetic theory in the 19th century[17] and a leap in the processing of ultra-pure materials in the 20th century. John Tyndall's experiments of guiding light through flowing water in 1870[16] and James Clerk Maxwell's development of electromagnetic theory gave rise to the insight of propagating states of light arising due to optical confinement in two spatial dimensions—guiding light to travel as a series of discretely-defined propagation states along the third remaining spatial dimension. An early application of light-guides was in the form of guided microwave radiation along hollow metal waveguides[18].

We will refer throughout this thesis to total internal reflection confined light-guiding in dielectric materials as Index-guiding. Chapter 6 will present a novel amplifier

¹ Leading to popular explanations for the optical glimmering quality of high refractive index materials, such as diamonds, in ambient air.

design based on an alternate confinement principle, which we will refer to as Photonic Crystal-guiding.

The first index-guiding application of micron length scale light came with the invention of the fiberscope in 1956 by O'Brien and Kapany of American Optical Company and Imperial College of London, respectively. By 1966, a landmark paper[19] by Kao and Hockam proposed the possibility of using optical fibers as a medium for guiding high transmission rate communication signals, provided optical fiber materials loss could be reduced to values below 20 decibels (dB) per kilometer (km).

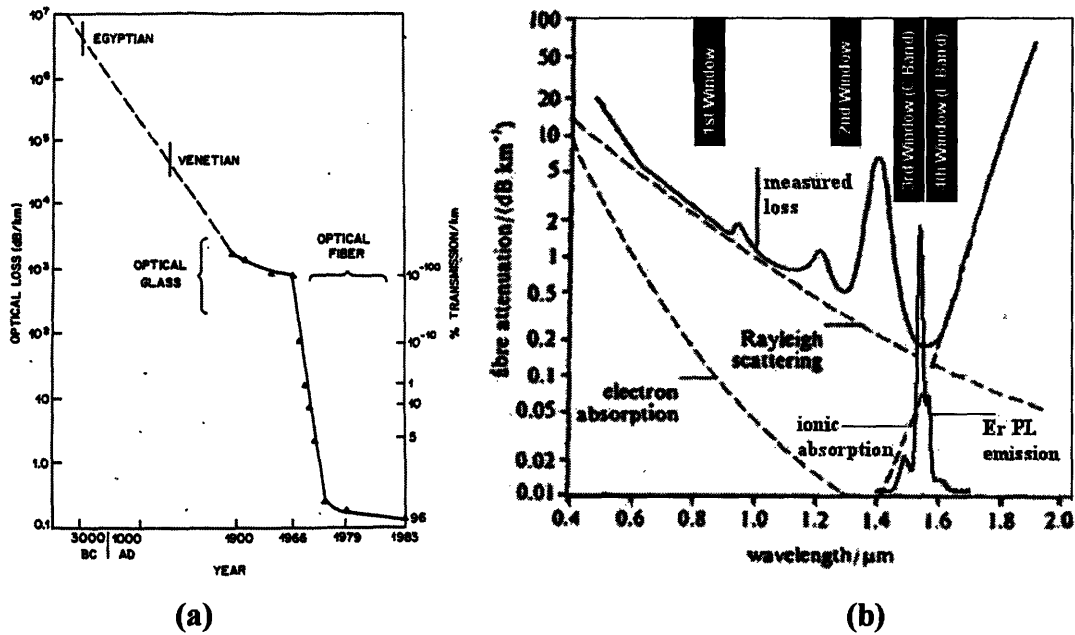


Fig. 1.1.1. (a) Transmission of light through glass over the ages[20]. The 20th century insight into optical impurities being the cause for high absorption led to (b) the dramatic decrease of materials absorption at $\lambda=1.55 \mu\text{m}$ [21]. The erbium emission spectrum is overlaid, demonstrating erbium's unique role as an amplifying transition for long-haul fiber optic communications.

In 1970, theory became reality: Maurer, Keck and Schultz of Corning Glass Works demonstrated ultra-low loss light-guiding optical fiber by growing an ultra-pure

silicon oxide (SiO₂) based glass by modified Chemical Vapor Deposition[22]. The ability to propagate micron length scale light with a transmission loss of <1 dB/km was a landmark achievement (see Fig. 1.1.1.a) in transmission properties of light through matter, and for SiO₂-based glass systems the transmission minima was observed to occur at wavelength $\lambda=1.55$ microns (μm) (see Fig. 1.1.1.b).

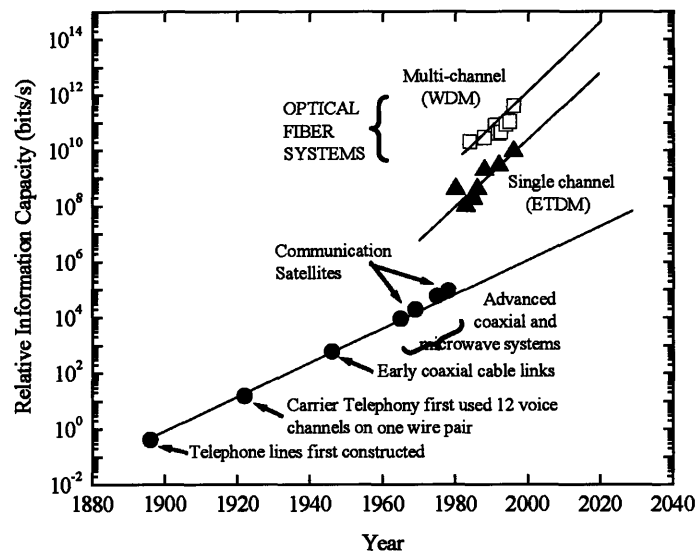


Fig. 1.1.2. The Optical Communications Roadmap[37], charting the power law rise of communication transmission rate (in units of bit/s) over time. The introduction of optical fiber networks and WDM-based networks contributed disruptive advances in the communications trends, as a function of time. (ETDM stands for Electronic Time Domain Multiplexing, the electrical form for carrying multiple communication signals[23]).

The Communications Roadmap[24] of Fig. 1.1.2 charts the performance of communication systems, accounting for development in device innovation and subsequent refinements in both materials processing and device design. We observe that the growth capacity of modern telephone systems has increased at a remarkable semi-logarithmic rate with time as coaxial cable, microwave and satellite platforms were

incorporated to sustain user demand for higher transmission bandwidth. However, the introduction of ultra-low loss optical fiber, or fiber optics, contributed a disruptive step[25] to the evolution of communication systems, due to the critical fact that the 1.55 μm propagating light corresponds to a carrier frequency of 2×10^{14} Hz—10 000 times faster than the highest radio frequencies being used. Fiber optic communications thus enabled a $>10^4 \times$ increase in data communication rates. However, the deployment of such a high transmission rate fiber-based platform could not be implemented for global communications, until the invention of the Erbium-Doped Fiber Amplifier (EDFA).

1.6 Review: The Need for Amplification in Communications

The concept of a travelling wave optical amplifier was proposed by Geusic and Scovil[26] in 1962 and first demonstrated by Elias Snitzer[2] at the American Optical Company in 1964. But it wasn't until the invention of optical fiber networks, the first generation of photonic devices, that a high demand application for such a device became apparent.

Optical fiber networks were built by telecommunications companies as a high bandwidth alternative to resistive-capacitive (RC) delay limited copper telephone lines[27], but their transmission distance was limited to 50-100 km. With III-V light sources and photodiode detectors, a feasible fiber optic link (made up of a light source, modulator, optical fiber transmission line, and photodiode detector) could only tolerate a 25-40 dB loss in transmitted signal power, corresponding to fiber lengths of 50-100 km. A light amplifier was needed which could selectively boost power to the 1.55 μm carrier signal, and the Er emission profile inside glass hosts[28] produced a suitable spectral

addition, the ms-scale long lifetime of the Er atom, in comparison to the ~ 1 Gbit/s (corresponding to a pulse period of ~ 0.5 ns) signal transmission rate, washes out time-dependent effects of gain modulation between neighbor WDM channels[32]: there is $\ll 1$ dB intersymbol interference between EDFA-amplified WDM channels (see Fig. 1.1.4.a).

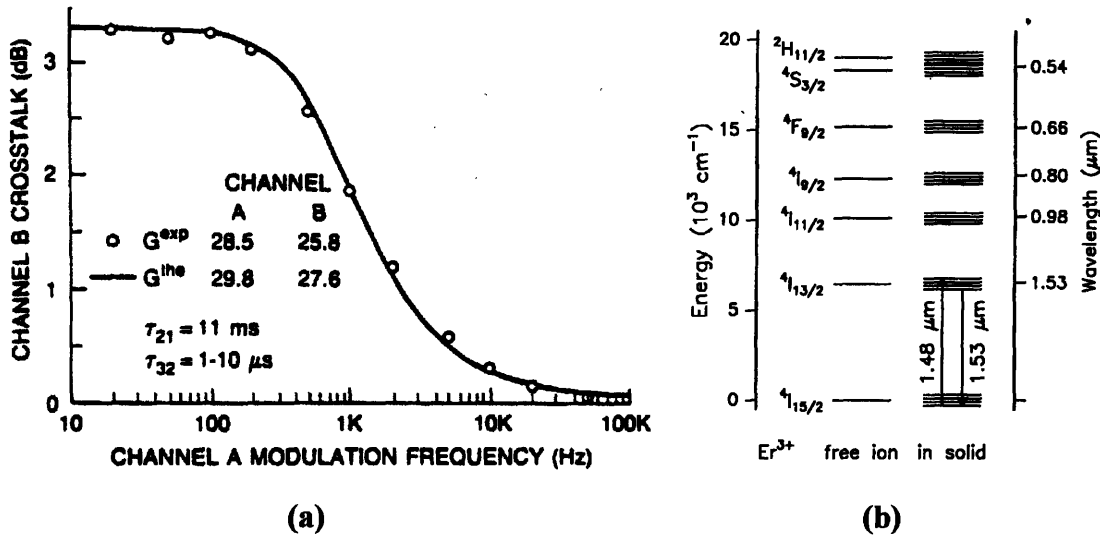


Fig. 1.1.4. (a) Cross-talk between WDM channels A and B after amplification through an EDFA[33]. (b) The atomic three-level system of the Er atom[13].

While Semiconductor Optical Amplifiers (SOAs) have risen in the last ten years as a competitive long-haul amplifier[32] which can supply 25-40 dB gain, the ns-scale SOA lifetime implies significant WDM channel interference by means of gain modulation at 1 Gbit/s. Secondly, the ms-lifetime of the EDFA also results in a lower Noise Figure than the SOA. The Noise Figure is a measure of the additional decrease in signal-to-noise ratio after amplification (see chapter 2 for detailed discussion of Noise Figure). Table 1.1 lists some characteristic performance numbers for an EDFA versus an SOA, as reported in the literature, giving a rough illustration of the EDFA's performance advantage over the SOA, but at the considerable cost of having a significantly larger

amplifier length, and hence a larger device footprint when integrated into a fiber optic link.

	EDFA	SOA
High Gain Linewidth	~30 nm	~30 nm
Gain	30 dB	20 dB
Amplifier Length	10 m	1 mm
Noise Figure	4 dB	6.5 dB
WDM gain modulation	$\ll 1$ dB	~1 dB

Table 1.1. Performance summary of a characteristic long-haul EDFA and SOA, summarized from [5].

Lastly, the IC compatibility of the optically pumped three-level (see Fig. 1.1.4.b) Er system, allows for this material to be imported into a Si Microelectronics fab. This critical processing access makes the final case for our decision to explore Er amplification in this work, as applicability to Si-based micron-scale photonics.

1.7 Review: Microphotonics

Microphotonics is the planar reduction of a macroscopic fiber optic link, made up of discretely mated photonic devices, into a micron-scale integrated link (or lightwave circuit), made up of continuously mated photonic devices. The inspiration and potential first application of microphotonics comes from Si Microelectronics, and we make a brief aside to explain the guiding principle and potential application of this technology.

1.7.1 Silicon Microelectronics & A Seemingly Unrelated Problem

The invention of integrated electronic devices by Kilby and Noyce in 1959[34], has culminated today in a \$250 billion semiconductor industry, transforming modern

society. The guiding principle of Si Microelectronics is the development of a rational design[35] approach towards creating an electronic circuit: a design approach that creates device functionality by selectively modifying a host environment. The two methods applying this design approach are (i) dopant delivery and (ii) lithography. Dopant delivery mimics a macroscopic electronic board's material-diverse circuits, as devices comprised of a common host material with different types or different spatial distributions of electronic dopants. Lithography mimics a macroscopic electronic board's architecture by localizing devices as discrete elements while at the same time monolithically integrating them by patterned metal interconnection lines.

The lithography principal for circuit design underlies a fundamental paradigm that characterizes microelectronics was an economy of scale technology: circuit size and circuit chip density scale with lithography wavelength. The impact of microelectronics as an economy of scale technology is aptly summarized by Moore's Law (see Fig. 1.1.5).

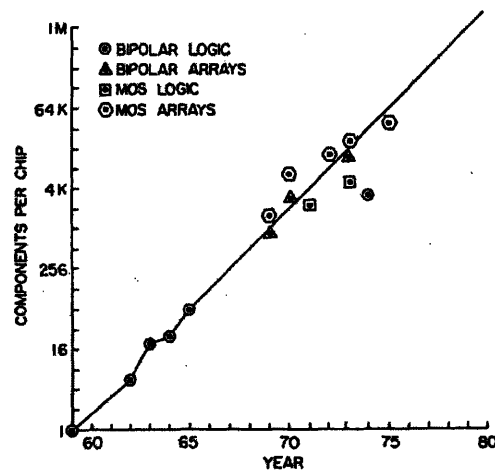


Fig. 1.1.5. Moore's Law, representing the unprecedented power law improvement of circuit performance/cost ratio as a function of decreasing lithography wavelength[36].

The invention of a high quality thermal oxide and Field Effect Transistors has resulted in the modern Integrated Circuit (IC) industry. With Moore's Law as a development roadmap, higher functionality, greater speed and lower cost have fuelled the proliferation of microelectronic applications, while working with the same basic set of Si-compatible materials and unit processes, thus resulting in an unprecedented performance/cost ratio for technology development.

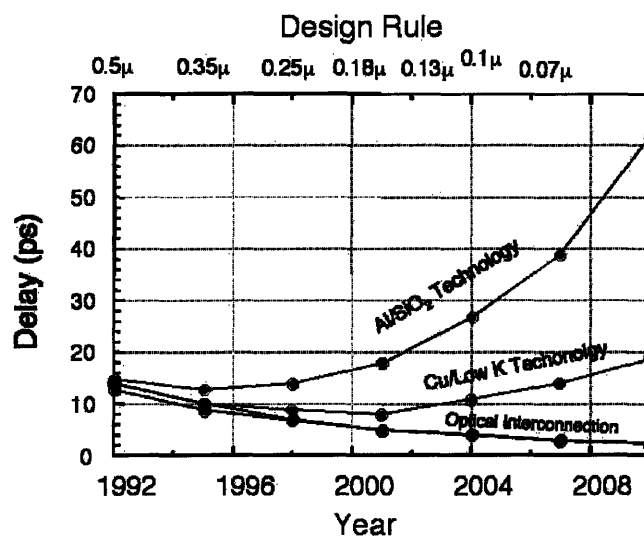


Fig. 1.1.6. Trend in global interconnect (1 cm length) propagation delay with technology linewidth and time, for traditional aluminum metal and SiO₂ insulator; projected copper and low dielectric material; and projected optical waveguide technologies[37].

In the next decade, the Roadmap for Si Microelectronics[37] has defined the technological limits to IC computation to be the metalization lines (also known as interconnects) connecting computation sectors on an IC chip. The increase in line resistance and parasitic capacitance, as a result of interconnect miniaturization and line densification, respectively, contributes an RC delay (see Fig. 1.1.6) to global interconnects (the longest ~1 cm metalization lines). Alternative materials solutions, such

as the use of lower resistance copper lines and lower dielectric constant films to embed the interconnects within, reduce this line delay, and it is a current point of debate as to whether alternate material-solutions ensure a line delay reduction rate satisfying the exponential Moore's Law-required performance/cost ratio trend.

A solution to this Interconnection Bottleneck problem has been suggested which radically breaks with the materials limitations due to electronic signal transfer, by following the telecommunications industry's lead: replace copper with fiber optic—or in this case, an optical waveguide.

1.7.2 Silicon Microphotonics: an Optical and Electronic Convergence

The optical network today is made up of discrete photonic devices interconnected by fiber splices, reminiscent of pre-IC electronic systems. While WDM technologies promise as high as Tbit/s transmission along long haul fiber optic links, transmission within cities suffers a significant drop due to an insufficient metropolitan area fiber optic architecture. This reduction in transmission rate due to a return to electronic technology within the city creates a Transmission Bottleneck between the urban user and the Long Haul backbone.

If photonic device processing can be re-invented as an economy of scale technology, the performance/cost ratio will radically increase, potentially making photonics a viable technology to build metropolitan fiber optic architectures for. And this could possibly open the path for Fiber To The Home and the once much-anticipated delivery of ultra-high transmission bandwidth, as an office-space or household commodity, for audio-visual intensive internet-driven applications.

The goal of microphotronics is therefore to re-design photonics as a planar substrate lithography-based technology. In particular, Si Microphotronics[25] attempts to leverage the same basic set of Si-compatible materials and unit processes used in microelectronics, and in doing so to try to optimise the performance/cost ratio of technology development.

Given the potential for the immediate transfer of a Si-CMOS compatible microphotonic link to a cleanroom fabrication facility, the first practical application of a microphotonic link has been envisioned to be an optical waveguide solution to the Interconnect Bottleneck problem[37]. By replacing the IC chip's global interconnects with optical waveguides and a light source/modulator/detector interface (which transduces chip electronic signals to optical pulse encoded signals and back), such a microphotonic link, dubbed an optical interconnect, has been theoretically predicted to solve the Interconnect Bottleneck (see Fig. 1.1.6).

The design inspiration for Si Microphotronics and this first-case application is a convergence of the problems and solutions created by microelectronic and photonic technologies. The microelectronic Interconnection Bottleneck computation problem may be solved by a microphotonic communications technology, where the design of this microphotronics technology is inspired by the microelectronic IC circuit rational design, and which may in turn relieve the Transmission Bottleneck communications problem of long haul photonics. Si Microphotronics takes advantage of this collaboration between IC computation technology and Telecom communication technology in the form of an optical interconnect, or more generally, a Planar Lightwave Circuit (PLC). The goal of this thesis work is to create a Si-compatible microphotonic amplifier for the PLC, and we

have chosen the Er atom as our optical center for designing this amplifier, seeking to take advantage of its (i) low optical noise, (ii) 1 Gbit/s WDM compatibility, and (iii) ability to leverage mature Si Microelectronics fabrication tools and processing recipes in order to sustain an optimal performance/cost ratio for microphotronics development.

1.8 Review: Si Microphotronics and the Planar Lightwave Circuit

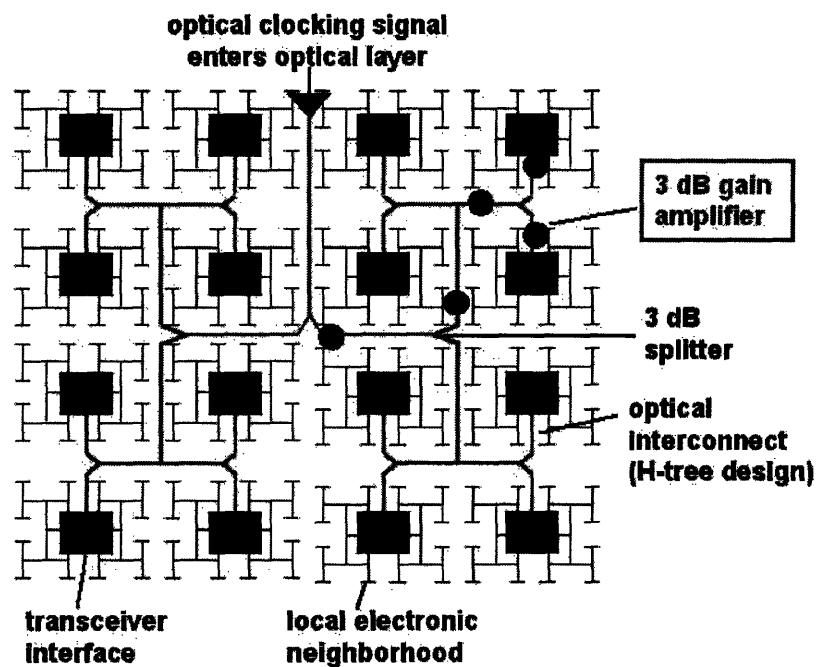


Fig. 1.1.7. The Planar Lightwave Circuit[38], comprised of a transceiver interface and optical layer. The optical amplifier is an all-optical device, distributed across the optical layer for in-line power-budget maintenance.

Fig. 1.1.7 shows the layout of a Planar Lightwave Circuit (PLC), designed to overlay above an IC chip, as replacement for the chip's global interconnect level. The layout is designed as a conventional 'H-tree' architecture, splitting an incoming signal to any number of local electronic neighborhoods on the IC chip. This particular example represents a design for carrying an optical clocking signal[38,39] across the IC chip.

The PLC is comprised of two architecture elements: (i) a transceiver interface and (ii) an optical layer. The transceiver interface contains light sources, optical modulators and photo-detectors, i.e. all the photonics devices involved in the transducing of electronic to optical signal and signal encoding. The optical layer is comprised of waveguides, WDM add/drop multiplexers, and amplifiers, i.e. all the photonic devices involving light-guiding, optical signal processing and power budget maintenance.

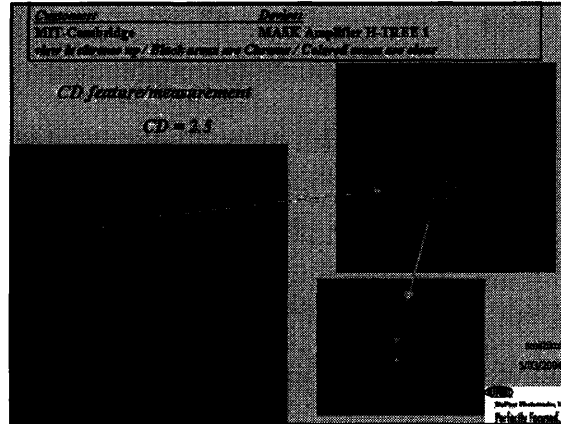
The H-tree architecture demonstrates that any basic PLC design involves the splitting of incoming signals (by perhaps a 50% power drop at each split) an arbitrary number of times before reaching the transceiver interface at the local electronic neighborhood. An optical amplifier will be an important device for maintaining the power budget in the optical layer, and a minimal benchmark requirement for a microphotonic PLC will be 3 dB (i.e. boosting signal power by 2×) gain per microphotonic amplifier.

The integration of a PLC as optical interconnects on an IC chip requires deposition of a waveguide core material (with refractive index n_2) onto the global interconnect level of a Chemical Mechanical Polished IC chip surface. Research by our group into poly-silicon waveguides[40] ($n_2=3.478$ at $\lambda=1.55 \mu\text{m}$) concluded significant transmission losses of 15 dB/cm[41] due to either materials absorption at poly-Si grain boundaries or high waveguide transmission loss due to scattering from rough waveguide core surfaces[42]. A more feasible materials choice was decided to be the integration of Si-CMOS compatible dielectric materials with lower refractive indices ($n_2=1.6-2.2$ at $\lambda=1.55 \mu\text{m}$) and higher melting point temperatures than Si. Such dielectric materials can be deposited by either Chemical Vapor Deposition (CVD) or Physical Vapor Deposition

(PVD) techniques as amorphous waveguide cores with low materials absorption. The current work in our group is actively exploring silicon nitride (Si_3N_4) and silicon oxynitride (SiON) dielectric materials for waveguide core materials by CVD[9] and sputtering[43]. The advantage of a PVD process such as sputtering is the minimization of substrate temperature during deposition, allowing for the possibility to monolithically integrate SiON-based optical interconnects by direct deposition onto an IC chip, without disturbing the original microelectronics thermal budget design for the chip.

Further, the creation of a micron scale PLC rests intrinsically on the ability to design single mode waveguide structures that fit within hundreds of μm square areas or less. Such high optical confinement can only be achieved with waveguides designed for index differences of $\Delta n = n_2 - n_1 = 0.1 - 1.0$. Silicon, silicon nitride and silicon oxynitride waveguide cores (n_2), hermetically sealed within a deposited silicon oxide cladding (n_1), are CMOS-compatible materials that meet these high Δn requirements.

Chapter 2: Optical Shrink: the Effect of Transverse Confinement in High Δn Waveguide Amplifiers



Specifications sheet for level 1 of lithography mask *MASK Amplifier H-TREE*, showing the coil/serpentine, variable length, and ring resonator waveguides which will experimentally test the computer simulation results of chapters 2 & 5.

“Dear Mr. Saini:

I thought of a simple way to explain why the confinement of the radiation does not improve the noise performance. The critical angle limits the transverse component of the k-vectors of the radiation within a wave-guide to some value $k_{sub} T$... The bigger the waveguide, the less radiation is captured. The number of atoms increases at the same rate as the captured radiation decreases.”

-email from Prof. H. Haus, which changed the last third of publication IEEE JLT 21(10), 2368-2376 (2003).

2.1 Chapter Abstract

Chapters 3-4 study Er_2O_3 and the $\text{Si}_3\text{N}_4 \leftrightarrow \text{SiON:Er}$ materials system as our candidates for a Si microphotonic optical amplifier. Independent of these material gain (dB/cm) results, we carried out three studies into the possibility of enhancing the SiON:Er material gain, per unit optical pump power. The results of these studies constitute chapters 2, 5 and 6. As a common reference for these three chapters, we studied the gain (as a function of pump power) performance of a characteristic ~ 3 dB/cm Er-based material gain.

3 dB/cm gains correspond to prohibitively large device lengths, on the order 10^4 μm , in order to create devices that meet our 3 dB gain/device benchmark for PLC application (chapter 1). To access the device feasibility of $\text{Si}_3\text{N}_4 \leftrightarrow \text{SiON:Er}$ for a microphotonic PLC, we developed a scaling methodology that we call Optical Shrink, to study optically pumped waveguide amplifiers, as a function core/cladding index contrast and amplifier length. Our study extends the gain efficiency versus index contrast studies of commercial EDFAs ($\Delta n \sim 0.06$) [18], to index difference magnitudes characteristic of Si Microphotronics ($\Delta n \sim 0.1-0.7$). Our study concludes that increasing index contrast for fixed amplifier length results in two crucial advantages: (i) increase in device gain efficiency, and (ii) decrease in areal footprint of a planar structure. Increasing index contrast is observed to have no effect on the output noise figure. A figure of merit summarizing these advantages demonstrates the powerful role of index contrast as an enabler for improving amplifier device feasibility. We studied amplifier lengths for fixed index contrast and conclude the presence of Amplified Spontaneous Emission sets an upper limit on amplifier length, in order to optimize device gain efficiency. We

summarize our amplification study of index contrast and amplifier length into a set of design rules that use the performance maps to determine optimum amplifier length, footprint and pump power, for a given index contrast and Er-doped lifetime. Using the Er-doped Waveguide Amplifier as a simulation case study for these design rules, we conclude an optical amplifier with >3 dB/cm gain, powered by a single 10 mW pump source, can be integrated into a PLC within a $425 \times 425 \mu\text{m}^2$ area. The $\text{Si}_3\text{N}_4 \leftrightarrow \text{SiON:Er}$ system is therefore feasible for device integration into microphotonic PLCs. However, the results of this study are critically dependent on the processing of ultra-low loss <0.2 dB/cm waveguides. We created a lithography mask and optimized materials calibration to experimentally test our case study and the Optical Shrink performance maps. We conclude that the lithographic and etch chemistry challenge of processing <0.2 dB/cm loss waveguides is the final requirement for experimentally demonstrating the results of our study. This design rule approach helped us develop a set of empirical equations that can be used to for first-order approximations of microphotonic amplifier performance, as a function of index contrast and device size. We conclude with a list of these equations.

2.2 Introduction

2.2.1 Optical Shrink for the Optically Pumped Amplifier

The Erbium Doped Fiber Amplifier, the workhorse component of long haul telecommunications, is an optically pumped three-level atomic transition system. To optically pump EDFA fibers, a pump wavelength λ_p must be injected into the optical fiber in parallel with the signal wavelength λ_s . The resulting overlap of pump and signal electromagnetic field distributions within the Er-doped fiber core provides the region of optical gain.

In shrinking an EDFA down to microphotonic length scales, we sought to investigate the two physical factors characteristic of an optically pumped amplifier's device physics,

(i) Optical Confinement: an optically confined profile for the pump rate, dependent on the refractive index difference Δn between waveguide core and cladding, and dependent on the waveguide core dimensions, and

(ii) Co-propagation: a pump power distribution that injects pump energy in parallel with the signal photons (this is termed the 'co-propagation' of λ_p and λ_s in EDFA physical modeling).

Optical confinement and co-propagation have an inter-related dependence on index difference Δn and device length Δz ; we investigate how this dependence can be extrapolated in order to optimally design power efficient planar waveguides, within a minimal two-dimensional (lithographically patterned) footprint.

(To clarify nomenclature, index difference is defined as $\Delta n = n_{\text{core}} - n_{\text{cladding}}$, and index contrast is defined as $\Delta n / n_{\text{cladding}}$. We will use these two terms interchangeably.)

This chapter presents our simulations for studying the effect of what we call *Optical Shrink* (which we define as the increase of Δn and decrease of Δz) on optical confinement and co-propagation, as we transform fiber-scale EDFA device performance into microphotonic scale Waveguide Optical Amplifier (WOA) performance. Our conclusion is that the planar design platform of microphotonic reveals a strong influence primarily of Δn , and secondarily of Δz , on:

Device Parameters	
Δn	index difference= $n_{\text{core}}-n_{\text{cladding}}$
A_{core}	waveguide core cross-section area= $\text{width} \times \text{height}$
N	optical dopant concentration
τ_r	optical dopant radiative lifetime $\propto 1/\sigma_{21}$
τ_{nr}	optical dopant nonradiative lifetime (due to host: waveguide core)
σ_{ij}	optical dopant interaction cross-section, energy level $i \rightarrow j$
$1/\tau$	total de-excitation rate= $(1/\tau_r + 1/\tau_{nr})$
η	luminescence efficiency= τ/τ_r
C_{ij}	upconversion coefficient between levels $i \rightarrow j$
Γ_s, Γ_p	overlap integral of signal, pump mode with optical dopant-doped core
L_g	amplifier length
L_g^*	optimal amplifier length
F	WOA areal footprint
α_s, α_p	signal, pump transmission loss

Table 2.1. Definitions table for all notation used in this chapter.

(1) WOA device performance scaling: device gain efficiency increases with Δn

and can be optimized with Δz ; and

(2) WOA device size scaling: device areal footprint decreases with Δn .

The influence of these two scaling advantages allows us to improve the PLC integration of SiON:Er-based WOAs: for a given optical gain per unit length, we can optimize the device operation, per unit pump power and per unit planar area. This is the optical engineering design goal of chapters 2, 5 and 6: to optimize PLC integration of a

Control Variables	
$h\nu_p, h\nu_s$	pump and signal photon energy
$P_p, P_p(z)$	input pump power, pump power profile ($0 < z < L_g$)
$\phi_p(z)$	pump flux profile= $\Gamma_p P_p(z)/A_{core}/h\nu_p$
$P_s, P_s(z)$	input signal power, signal power profile
$\phi_s(z)$	signal flux profile= $\Gamma_s P_s(z)/A_{core}/h\nu_s$
W_{13}	optical pump rate= $\phi_p \sigma_{13}$
W_{21}	stimulated emission rate= $\phi_s \sigma_{21} + \phi_{ASE} \sigma_{ASE,21} + \phi_{ASE} \sigma_{ASE,21}$
W_{12}	absorption rate= $\phi_s \sigma_{12} + \phi_{ASE} \sigma_{ASE,12} + \phi_{ASE} \sigma_{ASE,12}$

Table 4.1, continued.

WOA with respect to pump energy and physical area.

The key parameters describing materials selection and device performance for our simulation modeling are index difference Δn , radiative τ_r and nonradiative τ_{nr} lifetimes, pump P_p and signal P_s powers, and amplifier length Δz —which we rename here as L_g (the ‘g’ subscript refers to length of gain medium). Table 2.1 (shown on these pages) gives a list of all relevant parameters with detailed definitions.

2.2.2 An Adjustable Refractive Index Materials Host and An Adjustable

Optical Dopant

While lightly doped silica, phosphate or chalcogenide glasses have been used as the Er-doped waveguide cores for EDFAs, our proposed SiON materials system for microphotonic scale index differences ($\Delta n=0.1-1.0$) is silicon oxynitride (SiON), a

Performance Functions	
$N_2(z),$ $N_1(z)$	
$\gamma(z)$	Local signal gain profile $\equiv N_2(z)\sigma_{21} - N_1(z)\sigma_{12}$
P_o	output signal power $= P_s(z=L_g)$
γ_d	device gain $= 10\log(P_o/P_s)$
γ_{eff}	gain efficiency $\equiv d(\gamma_d)/dP_p$
γ_A	Areal gain $= \gamma_d L_g / F$
P_{ASE+}	output noise: forward amplified spontaneous emission
SNR_o	output signal-to-noise ratio $= P_o/P_{ASE+}$ (input signal-to-noise ratio $SNR_i = P_s/P_{noise}$)
NF	noise figure $= 10\log(SNR_i/SNR_o)$
L_{max}	position along amplifier where $P_s(z)$ is maximum (see Fig.3)

Table 4.1, concluded.

miscible glass alloy of SiO_2 and Si_3N_4 whose composition control creates the possibility for an adjustable waveguide core refractive index, varying from $n_{core}=1.46 \leftrightarrow 2.2$. The current state of strip waveguide sidewall smoothing[44] has produced $\Delta n=0.755$ single mode waveguides with less than 4.5 dB/cm transmission loss[9] and less than 1 dB insertion loss[45]. Room temperature lifetime measurements for Er ion-implanted SiO_2 and Si_3N_4 [11] and our investigation of sputtered $SiON:Er$ (chapter 4) shows that the Er atom preserves millisecond scale lifetimes in such hosts. Pending a predicted $10\times$ reduction to ultra-low transmission loss (one of the research goals of our group in the next year), and given a sputter-deposited ms-scale Er lifetime in the presence of

amorphous SiON, we establish in this chapter's study a continuous device operation analysis ranging from $\Delta n \sim 0.06$ commercial EDFAs to $\Delta n \sim 0.75$ microphotonic WOAs.

Apart from Er, there are five other rare-earth alternative light-emitting atoms, dubbed in this work as optical dopants, whose inhomogeneously broadened gain spectra introduces the possibility of designing amplifier gain within the entire near-IR spectrum[46] (see Table 2.2). The deep inner-shell transition [47] of these rare-earth optical dopants results in a linewidth emission insensitivity (the PL wavelength stays approximately constant, as shown in chapter 4) to host material.

IR ODs	Yb	Nd	Ho	Pr	Er	Tm
λ_s (μm)	1.04	1.06	1.20	1.32	1.53	1.80

Table 2.2. Collection of rare-earth IR-emitting optical dopants (ODs), listing their PL peak's (~gain peak) wavelength.

Therefore, an SiON:Er device can be adjustably tuned with respect to power or areal footprint requirements or physical space by choice of refractive index difference, or adjustably tuned with respect to gain spectrum requirement (the required wavelength window for amplification) by choice of optical dopant, matching arbitrary PLC requirement. SiON:Er is therefore an ideal device platform for microphotonic WOAs requiring micron-scale physical and near-IR spectral design flexibility.

2.2.3 Areal Gain and the HIC-WOA

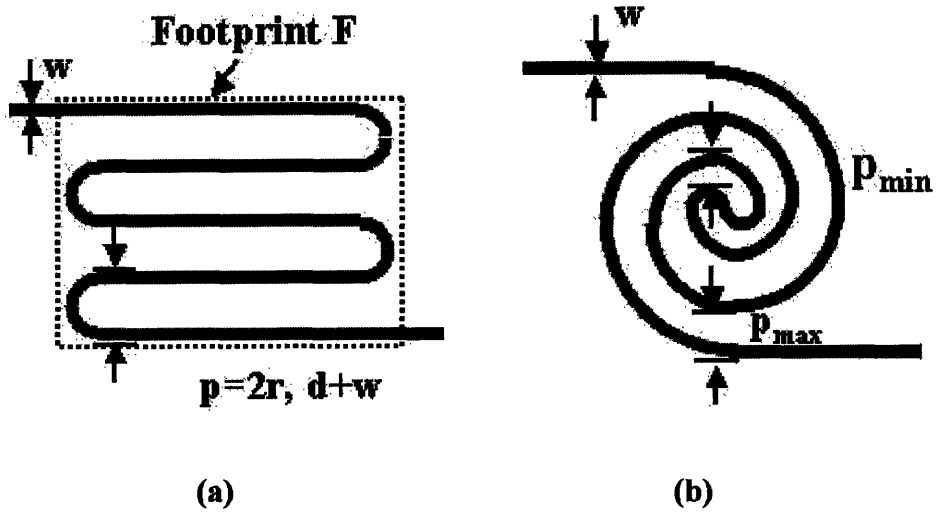


Fig. 2.1. Dimensional scaling for high gain planar HIC-WOAs (dB/cm²). (a) Serpentine structure, minimizing areal extent with straight-line waveguide segments. (b) Coil structure, optimally packing a planar area with curved waveguides. Nearest neighbor waveguide distance p is the larger of (i) radius r for 0.042 dB/cm turning loss[44] or (ii) decay length d corresponding to a 40 dB drop in evanescent cladding field intensity. In limit (i), magnitude of p is turning loss limited; in limit (ii) p is evanescent wave leakage limited. w is the waveguide width. Table 2.6 lists the equations relating WOA footprint size F to WOA length L_g .

For the PLC, we envision the High Index Contrast-Waveguide Optical Amplifier (HIC-WOA) as a compact low turning-loss strip waveguide amplifier, designed in Serpentine and Coil structures (see Fig. 2.1) that optimize device gain per unit area. The move from EDFA to WOA shifts device performance metric from gain per-unit-length (dB/cm) to gain per-unit-area (dB/cm²); we call this new metric “areal gain” (see definition in Table 2.1).

To date, Er has been the primary optical dopant used in fiber optic amplification[1], and has been studied in doped planar waveguides

	Optical Shrink Case Study	SiON Case Study
$\Delta n, A_{\text{core}}$	0.5, $0.3 \times 0.8 \mu\text{m}^2$	0.155, $0.8 \times 2.0 \mu\text{m}^2$
L_{gain}	1 m	2 cm
Optical dopant, N	Er atom, 10^{20}cm^{-3}	Er atom, $2 \times 10^{20} \text{cm}^{-3}$
λ_s, λ_p	1.55 μm , 0.98 μm	1.55 μm , 0.98 μm
P_n, P_s, P_p	1 μW , 10 μW , 10 mW	1 μW , 10 μW , NA
Γ_s, Γ_p	0.4, 0.64	0.4, 0.64
τ_r	12 ms	12 ms
τ_{nr}	60 ms	60 ms
τ, η	10 ms, 0.833	10 ms, 0.833
C_{24}	$4 \times 10^{-18} \text{cm}^3/\text{s}$ [48]	$4 \times 10^{-18} \text{cm}^3/\text{s}$
α_s, α_p	0 dB/cm, 0 dB/cm (0.2 dB/cm, 0.1 dB/cm)	0.2 dB/cm, 0.1 dB/cm

Table 2.3. Case study device parameter and control variable values used to generate Figs. 4.4-4.11. (NA means Not Applicable; the SiON case study was presented as a function of pump power P_p , and not at one particular P_p .)

[49,50,51,52,53,54,55,56,57]. Erbium-Doped Waveguide Amplifiers have recently been deployed for metropolitan fiber systems[58]. As a reference case study for this chapter's design analysis, we use the Er atom as our optical dopant, at a concentration of $1 \times 10^{20} \text{cm}^{-3}$ (see Table 2.3 for details). The contribution of upconversion is included as an optional, additional analysis. Waveguide transmission or propagation loss, our engineering design limit, has been omitted in order to draw general conclusions as to the physics of optical confinement. Propagation loss has been included for the particular case of $\Delta n=0.5$, in order to demonstrate the deviation of experimental design from theoretical

prediction. While the Optical Shrink case study was done for a device length intermediate to fiber optics and Microphotonics ($L_g=1\text{m}$), an SiON case study has been included to explicitly show the impact of Δn for a 3 dB microphotonic WOA (with $L_g=2\text{cm}$).

2.2.4 This Work: A Computer Simulation Study of Optical Shrink

We evaluate the device feasibility of the SiON:Er WOA system by computer simulations of the propagating power distribution within index-guided (total internal reflection confined) waveguides, in the presence of optical noise, by optical pumping.

Our results synthesize the performance and size scaling advantages of Optical Shrink into a Figure of Merit for device feasibility, quantitatively mapping the impact of Δn scaling on WOA performance, in contrast to a low index contrast EDFA. The performance and size scaling advantages are expanded into a set of guidelines for designing an optimum WOA length L_g , given a set of fixed device parameters and control variables (see definitions in Table 2.1). We discuss the underlying physical principles behind Optical Shrink as a transverse optical confinement effect; this motivates our exploration of alternative confinement effects in chapters 5 and 6, as forms of optical device engineering to improve the Figure of Merit for SiON:Er WOAs.

2.3 Amplifier Physics

2.3.1 Amplification Background

We review the equations of optical amplification[1] and discuss the impact of a co-propagating laser pump power (for the excitation of a population inversion) and spontaneous emission on power distribution along the amplifier ($0 < z < L_g$). An

additional term is included to account for Er-Er upconversion. Table 2.1 lists definitions for the notation used in this paper, classified as follows:

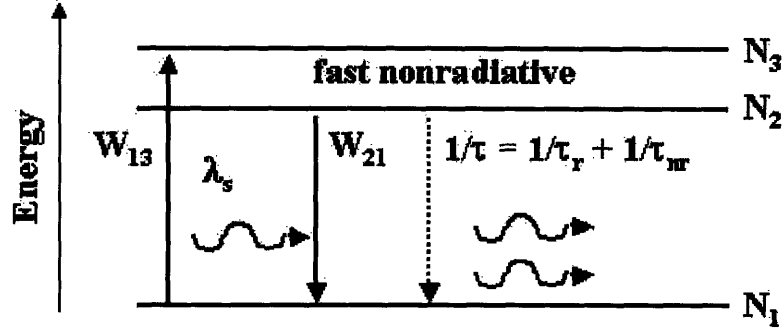


Fig. 2.2. Optical amplification in a three-level system. Signal photons (wave-like arrows) at wavelength λ_s undergo multiplication by stimulated emission W_{21} . Phonons mediate the rapid “fast nonradiative” de-excitation rate $N_3 \rightarrow N_2$.

- *device parameters* are design variables physically defining the dimensions and materials constitution of the amplifier,
- *control variables* are the input variables set to fixed value, defining amplifier operation,
- *performance functions* are the output response variables that evaluate amplifier performance.

The equations of optical amplification for an atomic three-level energy system (see Fig. 2.2), characteristic of optical dopants such as Er, are described by a coupled set of atomic density and power differential equations[1]:

$$\begin{aligned} \frac{dN_1}{dt} &= -W_{13}N_1 - W_{12}N_1 + W_{21}N_2 + \frac{1}{\tau} N_2 \\ \frac{dN_2}{dt} &= W_{12}N_1 - W_{21}N_2 - \frac{1}{\tau} N_2 + W_{13}N_1 - (C_{24}N_2^2) \\ N_3 &= N - N_1 - N_2 \approx 0 \end{aligned}$$

(2.1)

and

$$\begin{aligned}
\frac{dP_p}{dz} &= (N_2\sigma_{31} - N_1\sigma_{13})\Gamma_p P_p - \alpha_p P_p \\
\frac{dP_s}{dz} &= (N_2\sigma_{21} - N_1\sigma_{12})\Gamma_s P_s - \alpha_s P_s \\
\frac{dP_{ASE+}}{dz} &= (N_2\sigma_{ASE,21} - N_1\sigma_{ASE,12})\Gamma_s P_{ASE+} + \eta N_2\sigma_{ASE,21}\Gamma_s h\nu_{ASE}\Delta\nu_{ASE} - \alpha_s P_{ASE+} \\
\frac{dP_{ASE-}}{dz} &= -(N_2\sigma_{ASE,21} - N_1\sigma_{ASE,12})\Gamma_s P_{ASE-} - \eta N_2\sigma_{ASE,21}\Gamma_s h\nu_{ASE}\Delta\nu_{ASE} + \alpha_s P_{ASE-}
\end{aligned}$$

(2.2)

where we assume the nonradiative de-excitation rate between levels $i=3 \rightarrow j=2$ is orders of magnitude faster than W_{13} , W_{21} or $1/\tau$ (Fig. 2.2). Eqns. (2.1) describe the population of these energy levels as a function of time; the $C_{24}N_2^2$ term in parentheses for the dN_2/dt equation represents the influence of upconversion. Steady-state solutions ($dN_i/dt=0$) determine the level of population inversion N_2-N_1 ; with $N_3 \approx 0$, we solve N_2 for WOAs:

$$N_2 = N \frac{W_{13} + W_{12}}{W_{13} + W_{31} + \frac{1}{\tau} + W_{12} + W_{21}}$$

(2.3)

and for upconversion-dependant Er-doped WOAs:

$$N_2 = \frac{-(W_{13} + W_{12} + W_{21} + \frac{1}{\tau}) + \sqrt{(W_{13} + W_{21} + W_{12} + \frac{1}{\tau})^2 + 4NC_{24}(W_{13} + W_{12})}}{2C_{24}}$$

Eqns. (2.2) represent the steady-state pump, signal and spontaneously emitted photon population along the propagation length of the amplifier. Amplified Spontaneous Emission (ASE) describes the spontaneously emitted photon population, at signal wavelength λ_s , coupling into waveguide propagating modes and de-exciting optical

dopants upstream (ASE-) or downstream (ASE+) by stimulated emission[1]. The form and implication of the P_{ASE} equations in (2.2) is discussed in section 4.5. ASE results in a reduction of steady-state device gain γ_d , while increasing the output noise at λ_s (this is quantified by the Noise Figure performance function in Table 2.1).

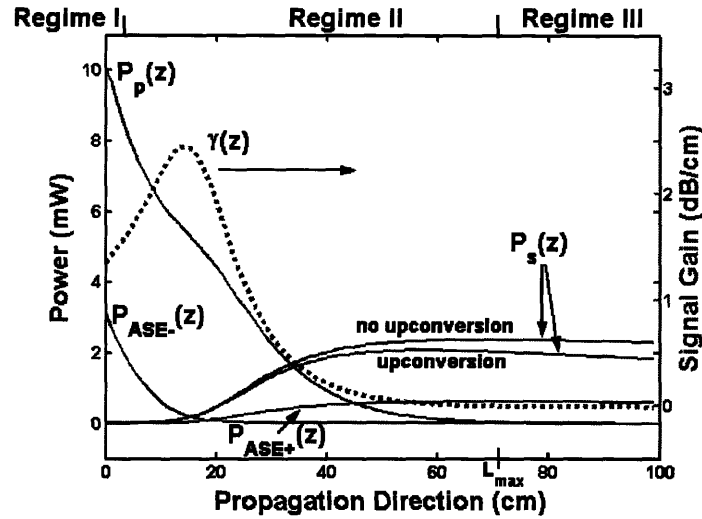


Fig. 2.3. Effect of co-propagating pump and spontaneous emission on power distribution along a WOA. L_{max} is defined in Table 1. (Data plotted for upconversion-free case study; power profile $P_s(z)$ for case study with upconversion is additionally plotted.)

A rigorous solution of power and gain profiles was calculated by substitution of Eqns. (2.1) into Eqns. (2.2) and solving (by Runge Kutta method computer simulation[59]) the resulting coupled differential equations, subject to the following boundary conditions: $P_p(z=0)=P_p$, $P_s(z=0)=P_s$, $P_{ASE+}(z=0)=0$, $P_{ASE-}(z=L_g)=0$. Fig. 2.3 plots such profiles for our case study system, illustrating a fundamental principal of optically pumped WOAs: the propagating signal P_s transits through three intrinsic Regimes of operation along the amplifier length. This trajectory is schematically represented for the upconversion-free case in Performance Map 1 (Fig. 2.4). Generally, there are four such light-optical dopant interacting Regimes.

(I) small signal gain: at low $P_s(z)$, when there is no dynamic competition between $P_s(z)$ and $P_p(z)$ to establish population inversion ($W_{21} < 1/\tau$, $W_{13} > 1/\tau$, $\gamma(z) > 0$).

(II) gain saturation: at high $P_s(z)$, when there is dynamic competition between $P_s(z)$ and $P_p(z)$ to establish population inversion ($W_{21} > 1/\tau$, $W_{13} > 1/\tau$, $\gamma(z) > 0$).

(III) absorption bleaching: at high $P_s(z)$ and low $P_p(z)$, a reduction in materials absorption due to the long lifetime decay of an absorbing optical dopant back to ground state ($W_{12} > 1/\tau$, $W_{13} < 1/\tau$, $\gamma(z) < 0$).

(IV) small signal absorption: at low $P_s(z)$ and low $P_p(z)$, the maximum materials absorption value, defined as $N\sigma_{21}$. ($W_{12} < 1/\tau$, $W_{13} < 1/\tau$, $\gamma(z) < 0$).

2.3.2 Optical Shrink as a Power Trajectory Path

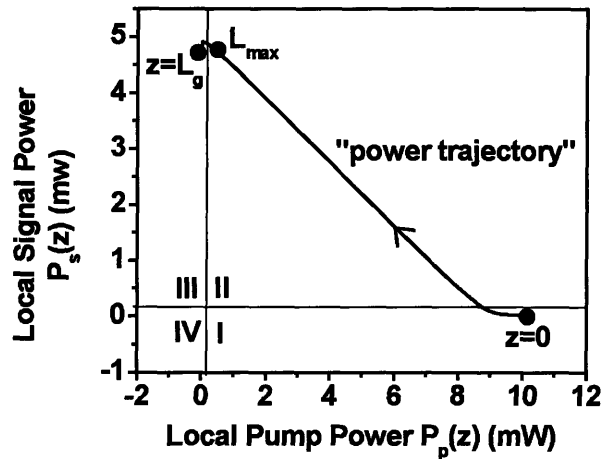


Fig. 2.4. Performance Map 1: $\lambda=1.55 \mu\text{m}$ Optical Amplification Regimes for Fig. 3 (upconversion-free) case study. The four operating regimes are quantitatively partitioned as a function of pump and signal power (mW). The inter-related effect of Δn and L_g determines the spatial extent of Regimes I-IV in Fig. 2.3, and the path of a “power trajectory” in this figure. The power trajectory represents $P_p(z)$ and $P_s(z)$ at local z positions along the Propagation Direction axis of Fig. 2.3.

The evolution of gain $\gamma(z)$ and $P_p(z)$, $P_s(z)$ profile along the propagation direction z , in Fig. 2.3, is represented as a “power trajectory” in Performance Map 1. The path of this power trajectory represents Optical Shrink’s inter-related effect of Δn and L_g on $P_s(z)$ profile and thus device gain. The power trajectory is influenced by L_g through (i) Backwards ASE $P_{ASE}(z)$, whose competition against pump power $P_p(z)$ reduces signal gain profile near $z=0$; and by Δn through (ii) Co-propagating pump power, where the sub-exponential decay of $P_p(z)$ along z sets a critical length L_g^* beyond which Regime II ends. (The pump power profile $P_p(z)$ is sub-exponential because of the high pump photon flux-rate resulting in bleaching of the $N_1 \rightarrow N_3$ absorption transition.) Counter-propagation pump schemes[18] permit an increase in L_g^* , but at the cost of a higher output noise figure (see 4.3.3 for more discussion). With the intent of low output noise, we adopt the co-propagating pump scheme for our WOA design and investigate optimization of Regime II, as controlled by Δn , for a given spontaneous emission lifetime τ_r and fixed input P_p and P_s . The scaling effect of Δn is depicted as Performance Maps in section 4.4. The influence of Δn on L_g determines the optimal value of L_g^* , for given Δn , in section 4.5. With the Performance Maps of section 4.4 and optimal L_g^* , we establish design rules to optimize device parameter values for a given Δn HIC-WOA.

2.3.3 Discussion: The Meaning of a Noise Figure

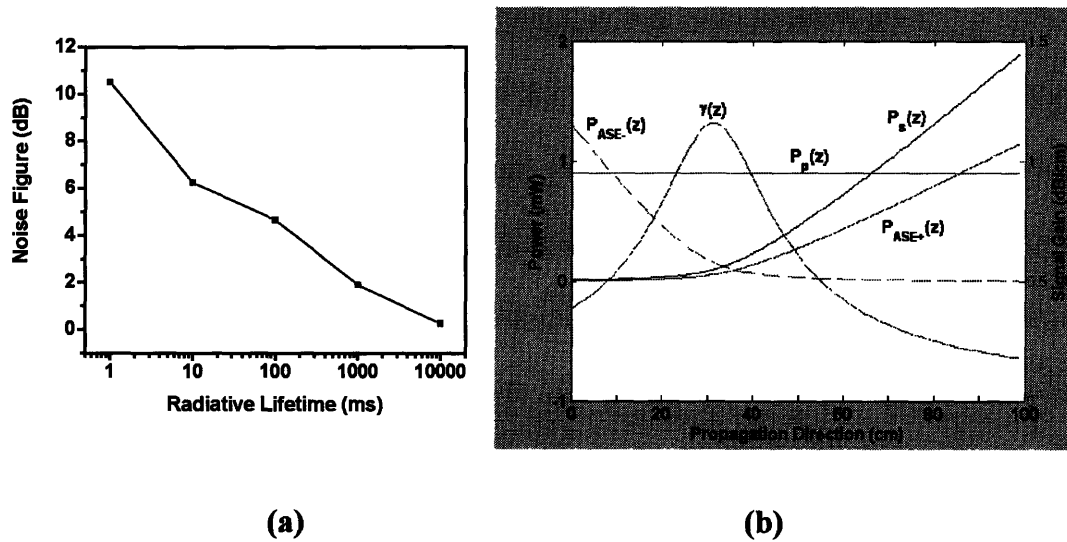


Fig. 2.5. (a) Noise Figure versus radiative lifetime, using the Optical Shrink case study with variable τ_r . (b) Case study simulation of power and gain profiles, with modification to a constant pump profile.

Equations (2.2) show that spontaneous emission generated within a WOA, which couples into propagating modes, undergoes stimulated emission from the population inverted E_r , and robbing the incoming signal λ_s of potential gain. Amplified Spontaneous Emission, or ASE, is an inevitable process that incurs a gain efficiency penalty for the WOA: less pump power is transferred to the signal as a result.

While the temporal intensity modulated signal acquires gain by stimulated emission of the optical dopant, the forward-traveling component of ASE (which of course has no temporal intensity modulation, and whose spectral profile is the PL linewidth of the optical dopant) contributes both spontaneous emission power and stimulated emission power to the input optical noise. As a result, the noise gain G_{noise} , defined in dB units as

10× the logarithmic ratio of the output optical noise $P_{n,o}$ (where $P_{ASE+(z=L_g)}=P_{n,o}$) to the input optical noise $P_{n,i}$, is greater than the signal gain G_{signal} .

We see this explicitly by expanding the Noise Figure definition (from Table 2.1):

$$\begin{aligned} NF &\equiv 10 \log\left(\frac{SNR_i}{SNR_o}\right) = 10 \log\left(\frac{P_{s,i}}{P_{n,i}} \div \frac{P_{s,o}}{P_{n,o}}\right) = -10 \log\left(\frac{P_{s,o}}{P_{s,i}}\right) + 10 \log\left(\frac{P_{n,o}}{P_{n,i}}\right) \\ &= -\text{Gain}_{\text{signal}} + \text{Gain}_{\text{noise}} \end{aligned}$$

(2.4)

therefore,

$$\text{Gain}_{\text{noise}} = NF + \text{Gain}_{\text{signal}}$$

(2.5)

and note,

$$\text{Gain}_{\text{noise}} = 10 \log\left(\frac{P_{n,o}}{P_{n,i}}\right) = 10 \log\left(\frac{P_{ASE+(z=L_g)}}{P_{n,i}}\right).$$

(2.6)

We see the Noise Figure is the amount of *excess* gain acquired by optical noise (thanks to ASE), in comparison to the signal gain. Since the spontaneous emission rate can not be turned off, we will always have $G_{\text{noise}} > G_{\text{signal}}$, or equivalently,

$$NF > 0.$$

(2.7)

The Noise Figure can not equal zero, for that's equivalent to setting the rate of spontaneous emission to zero; and by Fermi's golden rule, that implies no oscillator transition couples the excited state to the ground state, forcing the rate of stimulated

emission and $\sigma_{21}=0$. Noise can intrinsically not be minimized without reduction of σ_{21} and thus reduction of G_{signal} .

There are two reasons the Noise Figure will increase. (1) Reducing radiative lifetime τ_r will increase $P_{\text{ASE+}}$ in equation (2.2) at a faster rate than P_s (P_s increases because the τ_r decrease corresponds to an increase in interaction cross-section σ_{21}). In Fig. 2.5.a, our increasing lifetime in the case study shows Noise Figure slowly increase with τ_r . (2) Noise Figure will also increase is due to a less sub-exponential and more uniform optical pump profile. We simulate a uniform pump profile (see Fig. 2.5.b) for the case study, with pump power adjusted to yield the same device gain. The (sub-exponential pump profile) case study yields a Noise Figure of NF= 6.25 dB at 23 dB gain. With the uniform pump profile, we observe a Noise Figure of NF=7.85 dB at 23 dB gain.

In a co-propagating WOA or EDFA, the sub-exponential decay of (optical) pump power (see Fig. 2.3) as a function of z results in less spontaneous emission (dependent only on N_2 , not N_2-N_1) near the end of the amplifier, than near the beginning. More spontaneous emission is generated within such a uniform pump design.

2.4 Results and Discussion 1: Amplifier Scaling Principles

As mentioned in the Introduction, increasing index difference Δn has two scaling effects for WOAs, resulting in significant improvements of (i) device performance and (ii) operating efficiency per planar device unit area. We present our study of these high index contrast (HIC) scaling principles.

2.4.1 HIC Scaling Principle 1: Gain Efficiency

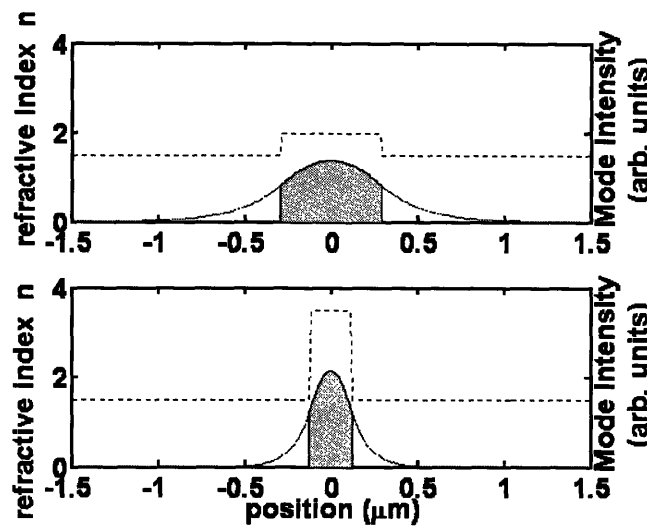


Fig. 2.6. $\lambda_s=1.55 \mu\text{m}$ wavelength mode profile in single mode cut-off WOA cross-section area, for $\Delta n=0.5, 2.0$. The shaded areas show that the same modal fraction is confined within the core of a single mode cut-off waveguide, regardless of Δn . For higher Δn , decreasing A_{core} thus implies an increase in flux density ϕ_s, ϕ_p within the WOA core.

Fig. 2.6 shows the cross-section area TE mode profile of two waveguides (simulated by the Finite Difference Method[60]) with dimensions below pump wavelength λ_p single mode cut-off (below single mode cut-off means there is only one waveguide propagating state at wavelength λ_p [5]). We observe that the same modal fraction is contained within both waveguide cores in Fig. 2.6.

Therefore, the waveguide with refractive index difference $\Delta n=2.0$, contains the same amount of propagating modal power as the waveguide with $\Delta n=0.5$. This same amount of modal power exists at a higher photon density within the smaller cross-section area $\Delta n=2.0$ waveguide core, and therefore at higher flux rate. ϕ_p (and ϕ_s) is higher within

the higher Δn waveguide core. This increases the optical pump rate W_{13} (and W_{12} , W_{21}) and the level of population inversion $\Delta N = N_2 - N_1$ in Regime I.

For a single mode cut-off waveguide, core cross-section area A_{core} scales as $\sim \Delta n^{-1.14}$ (see Appendix 1). We thus conclude for fixed P_p , higher Δn increases ΔN and thus the gain profile magnitude in Regime I.

However, Fig. 2.3 and Fig. 2.4 show us that the majority length of an optically pumped amplifier tends to be in Regime II. We therefore examine the influence of optical confinement in both regimes. We expand the gain expression, approximating $\sigma_{12} \approx \sigma_{21}$ and assuming that $N_3 \approx 0$ ($N_1 + N_2 \approx N$):

$$\gamma = N_2 \sigma_{21} - N_1 \sigma_{12} \cong (N_2 - N_1) \sigma_{21} \approx (N_2 - (N - N_2)) \sigma_{21} = 2N_2 \sigma_{21} - N \sigma_{21}$$

and using the expression in equation (2.3) (where our fast non-radiative decay from level 3 \rightarrow 2 implies $W_{31} \approx 0$), we conclude for Regime I

$$\begin{aligned} \gamma_I &\approx 2N \sigma_{21} \frac{W_{13} + W_{12}}{W_{13} + W_{12} + W_{21} + \frac{1}{\tau}} - N \sigma_{21} \\ &= 2N \sigma_{21} \frac{(\Gamma_p P_p / h \nu_p A) \sigma_{13} + (\Gamma_s P_s / h \nu_s A) \sigma_{12}}{(\Gamma_p P_p / h \nu_p A) \sigma_{13} + (\Gamma_s P_s / h \nu_s A) (\sigma_{12} + \sigma_{21}) + \frac{1}{\tau}} - N \sigma_{21} \\ &= 2N \sigma_{21} \frac{(\Gamma_p P_p / h \nu_p) \sigma_{13} + (\Gamma_s P_s / h \nu_s) \sigma_{12}}{(\Gamma_p P_p / h \nu_p) \sigma_{13} + (\Gamma_s P_s / h \nu_s) (\sigma_{12} + \sigma_{21}) + A \frac{1}{\tau}} - N \sigma_{21} \end{aligned}$$

(2.8)

We see here explicitly the influence of optical confinement: increasing Δn and decreasing single mode waveguide cross-section area A , while confining the same modal fraction within cross-section area A , applies to both pump and signal fluxes. The increase in small signal only occurs because of the spontaneous emission rate $1/\tau$ not having a dependence

on A and Δn . Thus, we interpret the confinement effect on increasing gain (in Regime I) as being the result of energy transferring more efficiently from pump directly to stimulated emission (i.e. W_{13} , W_{21} and W_{12} have increased, but $1/\tau$ hasn't). (Note that ASE will increase with the Δn confinement effect; we haven't explicitly listed $P_{\text{ASE}+}$ and $P_{\text{ASE}-}$ in equation (2.8)—for completeness one can approximately substitute P_s with $P_s + P_{\text{ASE}+} + P_{\text{ASE}-}$ in (2.8)).

But as the simulation in Fig. 2.3 reveals, the majority of an amplifier length is in Regime II, where W_{12} and $W_{21} \gg 1/\tau$, and the $1/\tau$ term becomes negligible in the denominator,

$$\begin{aligned}
\gamma_{II} &\approx 2N\sigma_{21} \frac{W_{13} + W_{12}}{W_{13} + W_{12} + W_{21}} - N\sigma_{21} \\
&= 2N\sigma_{21} \frac{(\Gamma_p P_p / h\nu_p A)\sigma_{13} + (\Gamma_s P_s / h\nu_s A)\sigma_{12}}{(\Gamma_p P_p / h\nu_p A)\sigma_{13} + (\Gamma_s P_s / h\nu_s A)(\sigma_{12} + \sigma_{21})} - N\sigma_{21} \\
&= 2N\sigma_{21} \frac{(\Gamma_p P_p / h\nu_p)\sigma_{13} + (\Gamma_s P_s / h\nu_s)\sigma_{12}}{(\Gamma_p P_p / h\nu_p)\sigma_{13} + (\Gamma_s P_s / h\nu_s)(\sigma_{12} + \sigma_{21})} - N\sigma_{21}
\end{aligned}$$

(2.9)

therefore, in Regime II, which dominates WOA amplification, the effect of transverse optical confinement—increasing Δn —does not appear to increase signal gain.

Yet increase in device gain as a function of higher Δn is experimentally observed and designed for in EDFAs. It is the reason why EDFA devices tend to have higher numerical aperture[63] (i.e. index difference) than conventional fiber. And we have reproduced such observations theoretically, in computer simulations of the coupled equations (2.1), (2.2) for different index difference Δn waveguides (see Fig. 2.8.a).

Closer examination of our computer simulation of the signal power profile $P_s(z)$ made us realize that the effect of increase in amplifier device gain with higher Δn is *not a purely optical confinement* (i.e. waveguide cross-section area A dependent) *effect*. The device increases with increasing Δn , only if the amplifier length L_g is kept *fixed*.

Thus we stop referring to the dependence of device gain on Δn as a transverse optical confinement effect, and re-dub it as an Optical Shrink effect: it is the influence of Δn (by optical confinement) on the signal power *profile*, along a WOA of fixed length L_g , which results in an increase of the WOA's gain. In increasing Δn does not improve the gain-per-unit-length (dB/cm) of a device, it rather Δn improves the gain (dB) of a fixed length device. This distinction qualifies Optical Shrink as a *distributed* effect (i.e. its effect occurs over a *finite* length of amplifier L_g), and not, like optical confinement, an intrinsic effect (i.e. per unit length).

We show this distributed effect with our case study (upconversion-free) in Fig. 2.7. In Fig. 2.7.a we observe the signal power profile for an incoming $P_{s,i}=1 \mu\text{W}$ signal in a $\Delta n=0.06$ single mode cut-off WOA (amplifier length $L_g=1 \text{ m}$). Fig. 2.7.b now overlaps the gain and signal power profiles of this example, versus the Optical Shrink case study. The case study has a higher optical confinement ($\Delta n=0.5$) for the same device length (i.e. 1m). We observe that the $\Delta n=0.5$ signal power profile $P_s(z)$ rises more quickly with propagation z , and saturates to a higher value. Once both signal power profiles have entered Regime II, we observe that the higher saturating P_s for the $\Delta n=0.5$ case results in less E_r absorption throughout Regime III. This is because the higher signal power flux for

this case results in higher steady-state bleaching of the Er atoms, and thus lower steady state absorption from Er atoms in Regime III.

Re-examining the second line of equation (2.9) reveals that while the gain profile is quantitatively independent of waveguide cross-section area in Regime II, the optical confinement effect of a smaller cross-section area for the $\Delta n=0.5$ case implies a higher rate of stimulated emission and hence faster signal power build-up $P_s(z)$, with z , as compared to the $\Delta n=0.06$ case. This is why the signal power profile rises faster in the $\Delta n=0.5$ case WOA, and why it dynamically reaches steady state saturation with a higher P_s value, than the $\Delta n=0.06$ case. The $P_s(z)$ value of both cases as the signal power enters Regime III then determines the final output value $P_s(z=L_g)$.

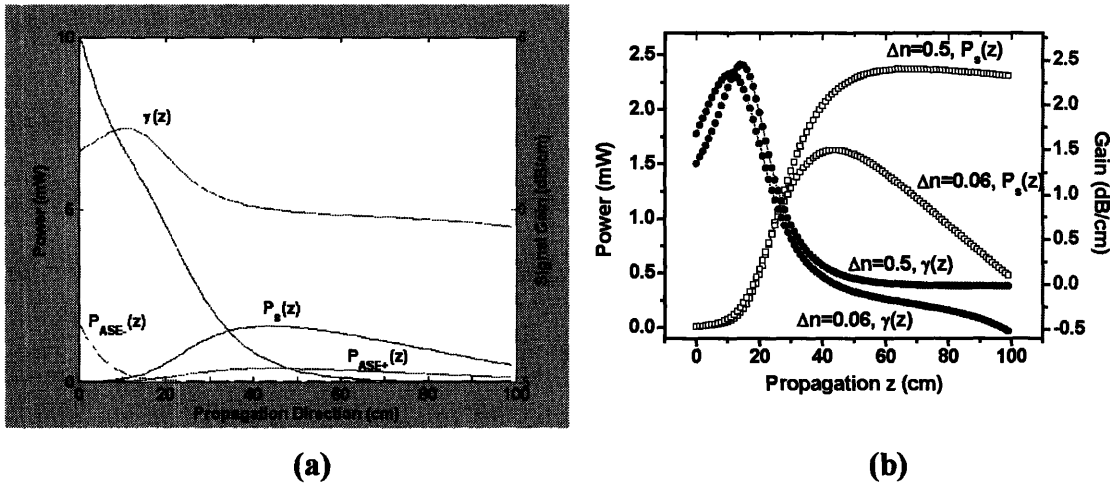


Fig. 2.7. (a) Plot of power and gain profiles using case study parameter with modification of index difference to value $\Delta n=0.06$. (b) Comparison of signal power $P_s(z)$ and gain $\gamma(z)$ profiles for $\Delta n=0.06$ case versus $\Delta n=0.5$ case study.

Thus, it is the simultaneous interaction of a Δn optical confinement effect (a faster $P_s(z)$ build-up in Regime II) with the fixed finite length of the WOA (involving the

bleaching of a *shorter* Regime III from the built-up $P_s(z)$ in Regime II) which results in an observed increase of the WOA device gain γ_d versus Δn (at fixed pump power).

We map this distributed Optical Shrink effect by simulating, for a given Δn , device gain γ_d versus input pump power P_p . The results for three Δn cases are shown in Fig. 2.8.a. We observe that the effect of $P_s(z)$ building up faster in a higher Δn WOA, is equivalent, to reducing the pump power in a higher Δn waveguide in order to achieve the same device gain γ_d , as a lower Δn WOA. In other words, the γ_d versus P_p slope of a WOA—defined as device Gain Efficiency γ_{eff} (see Table 2.1)—increases with Δn . Describing the Optical Shrink effect in terms of Gain Efficiency makes the impact of increasing Δn explicit: lower pump power sources can be used to achieve the same device gain γ_d .

This performance scaling effect of Δn on device gain efficiency was studied by us and published[61] for an $L_g=1$ m long WOA (Optical Shrink case study in Table 2.3). We chose the 1-meter length as an intermediate length scale between EDFA devices (typically 20-30 m long) and the microphotonic length scale of 1 cm or less. Demonstrating fixed amplifier length results at $L_g=1$ m thus gives a sense of the impact of Optical Shrink in comparison to current commercial EDFAs. At the conclusion of this section we repeat our simulations for an $L_g=2$ cm case study (all other parameters the same as in Table 2.3) in order to make explicit our final microphotonic amplifier design.

Performance Map 2 (see Fig. 2.8.b), shows for the $L_g=1$ m case study, the dependence of gain efficiency γ_{eff} versus Δn . We observe a gain efficiency increase of $\sim 25\times$ for a microphotonic scale $\Delta n=1.0$ system, compared to an EDFA scale $\Delta n=0.06$

system. This means $\sim 25\times$ less pump power is required to achieve the same small signal gain coefficient in a HIC-WOA, compared to an EDFA. For an Er-doped upconversion-dependent WOA, the increase in gain efficiency is $\sim 12\times$. This Scaling Principle enables creation of ultra-low pump power microphotonic waveguide amplifiers.

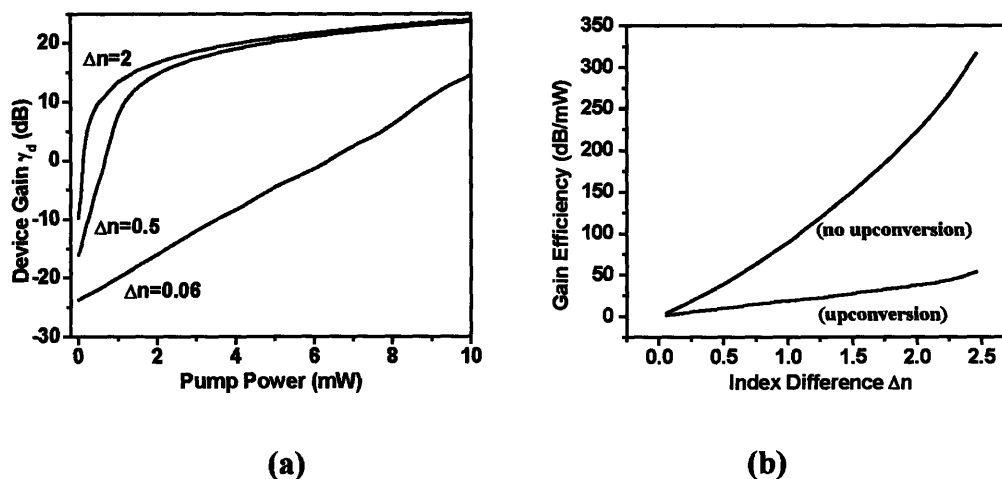


Fig. 2.8. (a) Device Gain for case study versus Pump Power (upconversion-free data) shows an increase in slope (i.e. gain efficiency) with increasing Δn . (b) Performance Map 2: plot of gain efficiency versus Δn . This data does not include the simulation of scattering transmission loss.

The data for Performance Map 2 is acquired by fitting the slope of device gain versus pump power simulations (such as those in Fig. 2.8.a) at device gain values below zero, where we observe a linear response from amplifiers simulated with $\Delta n = 0.06 \leftrightarrow 2.5$. Note in Fig. 2.8.a that the device gain vertical axis intercept (at $P_p = 0$ mW) is less negative with increasing Δn curves. This is a result of the confinement effect: a $10 \mu\text{W}$ signal is always entering the WOAs of these simulations, and the higher the Δn , the smaller the cross-section area and thus the more absorption bleaching due to higher signal flux. In the limit of lower Δn values, this loss number comes closer to the Er absorption

value ($\sim 2.4 \text{ dB/cm} \times 1 \text{ m} = 240 \text{ dB}$) for a 1 m long slab of material doped with 10^{20} Er/cm^3 .

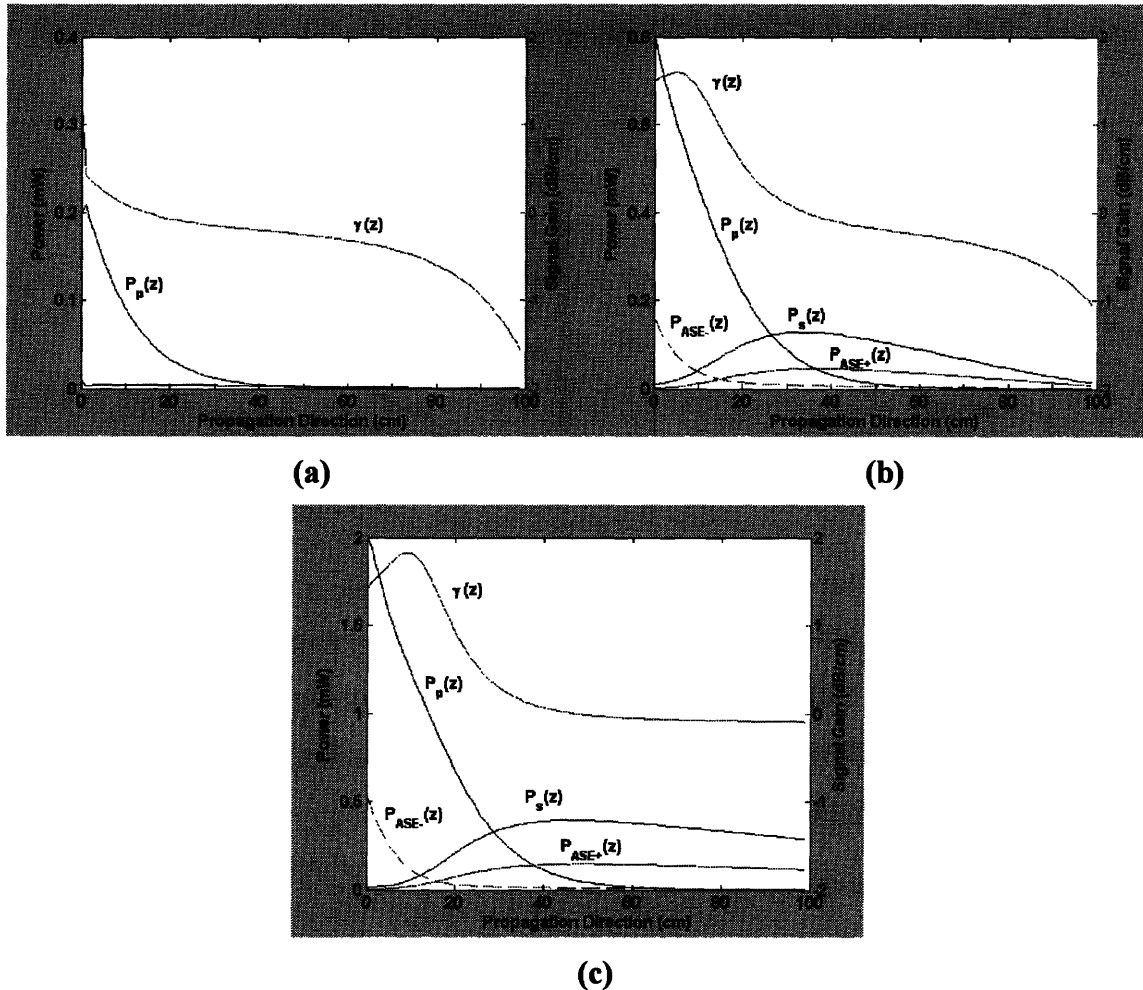


Fig. 2.9. Plot of power and gain profiles (upconversion-free case study) for a series of pump powers (a) $P_p=0.2 \text{ mW}$ (below population inversion), (b) $P_p=0.8 \text{ mW}$ (linear regime of gain from Fig. 2.8.a) and (c) $P_p=2 \text{ mW}$ (approaching gain saturation of the device).

Fig. 2.9 gives a series of plots showing the signal power and gain profile along the 1 m device length of the case study, as a function of different pump powers. We observe in Figs.a-b that positive gain (i.e. population inversion) begins near $z=0$, as expected with co-propagation. And we observe in Figs.b-c that the onset of gain saturation (i.e. the

range of pump power values which begin to give significant diminishing returns in increasing the device gain) is necessary to eliminate a $\gamma(z)<0$ gain profile near $z=L_g$ (and hence optimize device gain). Also, the onset of gain saturation (Figs.b-c) results in the build-up of sufficient backwards ASE so that the gain profile acquires a dip near $z=0$.

To model the effect of waveguide transmission loss (due to scattering from waveguide sidewall roughness[4]) on gain efficiency, we simulated solutions to Eqns (2.1) and (2.2) with the α_s , α_p values listed in Table 2.3 for $\Delta n=0.5$. For our case study, $L_g=1$ m creates an excessively lossy amplifier when including this transmission loss, resulting in a very low gain efficiency of 5 dB/mW (compared to the scattering loss-free value of 23

	$L_g=100$ cm	$L_g=35$ cm	Length Factor
$\alpha_s=\alpha_p=0$ dB/cm	23 dB/mW	75 dB/mW	3.26×
$\alpha_s=0.2, \alpha_p=0.1$ dB/cm	5 dB/mW	42 dB/mW	8.4×
Loss Factor	4.6×	1.8×	

Table 2.4. Gain Efficiency (upconversion-free case study) in the presence of loss, and optimization by reduction of amplifier length L_g .

dB/mW in Fig. 2.8). The optimum device length for operation (see L_g^* discussion in section 4.6) for the case study, when including the α_s , α_p values listed in Table 2.3, is found to be $L_g^* \sim 35$ cm for pump powers close to 10 mW. Setting $L_g=35$ cm, while retaining all other parameter values from Table 2.3 (i.e. $\Delta n=0.5$), we find the scattering loss-free gain efficiency to be 75 dB/mW, and the scattering loss-inclusive gain efficiency to be 42 dB/mW. These values are summarized in Table 2.4. The Loss and Length Factors in this table both summarize that (i) in the presence of scattering

transmission losses, there is a decrease in gain efficiency; and emphasize that (ii) the choice of optimal amplifier length L_g is even more crucial in order to still take advantage of HIC Scaling Principle 1. These two conclusions apply to the optimization of gain efficiency in the presence of upconversion as well.

While the dramatic increase of gain efficiency with Δn promises amplifier device design with low pump power sources, conservation of energy implies that the impact of this device design is more relevant for microphotronics than for fiber optic links. Fiber optic links require amplification of $\sim 10 \mu\text{W}$ signals by $100\times$ (+20 dB), to values of 1 mW, before transmitting the signal ~ 100 km (-0.2 dB/km fiber loss $\times 100$ km = -20 dB) to another optical amplifier. Fiber optic links thus require high output saturation devices; in other words, a high enough pump power that ensures enough energy transfer to the signal to give a 1 mW amplified output. Fiber optic link amplifiers, by virtue of being spaced ~ 100 km apart, are constrained to operate at pump powers > 10 mW (typically 50-100 mW for WDM EDFAs).

As we can see from our case study, the impact of Δn is to create gain saturation in amplifiers with pump powers as low as 1 mW. As a WDM amplifier, where $n\times$ more pump power is needed to amplify $n\times$ more channels, we quickly conclude that 1 mW pump power sources are relevant only for designs where the output amplified signal is on the order $\geq 100 \mu\text{W}$ (≥ 10 dB gain). Such signal power output might work with metropolitan scale fiber optic links, with amplifiers possibly spaced 10-30 km apart. For the case of microphotronics, as we have said, even a 3 dB doubling of signal power (i.e. from $10\mu\text{W}$ to $20 \mu\text{W}$) is enough for the < 1 cm lengths scales of a PLC.

We therefore conclude that the Performance Scaling effect of Δn on gain efficiency, while general in its physical principles, is most relevant (from a power budget perspective) in applications for microphotonics (optical interconnects), and not large-scale photonics (fiber optic links).

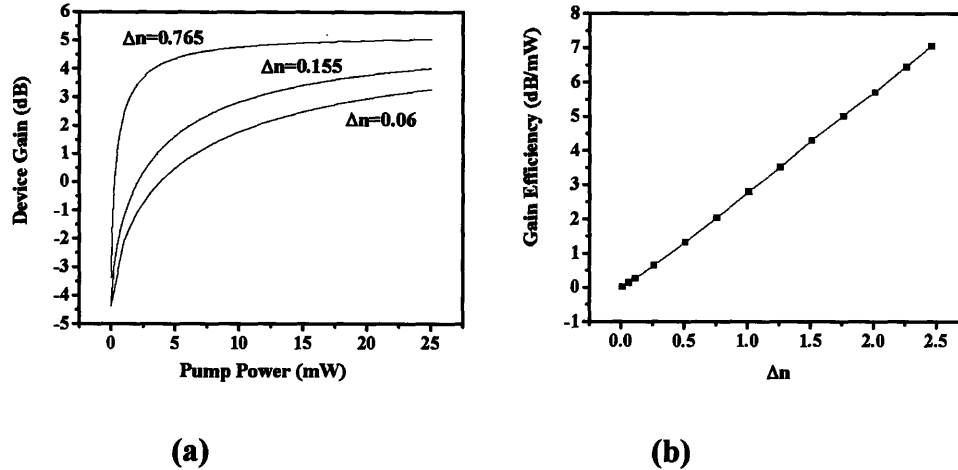


Fig. 2.10. HIC Scaling Principle 1 for Microphotonics. Simulation is for SiON:Er single mode cut-off waveguide ($\Delta n=0.155$) with $L_g=2$ cm. All other parameters same as case study; simulation performed with upconversion and no propagation loss. (a) Device Gain versus Pump Power shows an increase in slope (i.e. gain efficiency) with increasing Δn . (b) Plot of gain efficiency versus Δn .

We chose $L_g=2$ cm as an appropriate length scale for a SiON:Er microphotonic amplifier designed according to the principles of Optical Shrink. Fig. 2.10 plots the Performance Scaling effect of Δn for our SiON case study, with upconversion and propagation loss (see parameters in Table 2.3). Fig. 2.10.b plots the “3-dB Gain Efficiency,” which we define as 3 dB device gain γ_d , divided the pump power required to reach $\gamma_d=3$ dB. The information in this plot differs slightly from Fig. 2.8.b, which plotted the slope of a γ_d versus P_p plot. For the purpose of our Microphotonics 3 dB gain element

discussion, we deemed plotting 3-dB Gain Efficiency in Fig. 2.10.b was a more relevant quantitative measure of device performance within a PLC.

2.4.2 HIC Scaling Principle 2: Device Footprint

The higher Δn for planar WOAs reduces strip waveguide turning loss and cladding evanescent fields[62]. This stronger confinement permits a scaling down of the r and d parameters in Fig. 2.1, enabling design of planar WOAs that pack a gain medium into a smaller footprint area F . Performance Map 3 (Fig. 2.11) shows the scaling influence of Δn on F . Constant length ($L_g=1$ m, 1 cm) curves show the impact Δn has on *geometric* scaling: the WOA footprint decreases by 500 \times for a microphotonic scale $\Delta n=1.0$ system, compared to an EDFA scale $\Delta n=0.06$ system. Constant device gain ($\gamma_d=27$ dB, 3 dB) curves show the impact Δn has on *device* scaling: the microphotonic system can deliver the same amount of device gain from an area that is 500 \times smaller than the EDFA system; areal gain has thus increased by 500 \times . The 3 dB gain curve shows that this Scaling Principle permits design of such a gain element within a microphotonic-compatible $425 \times 425 \mu\text{m}^2$ area, for $\Delta n=0.155$ (SiON case study) and $P_p=10$ mW.

We qualify this effect of HIC Scaling Principle 2 on device footprint or areal gain, as the Size Scaling effect for the WOA, as function of Δn .

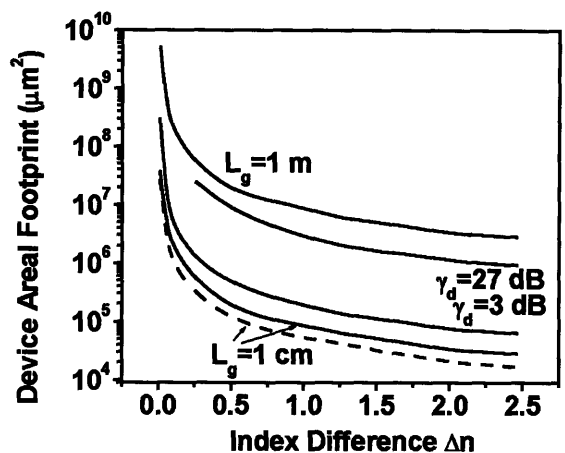


Fig. 2.11. Performance Map 3: Plot of Serpentine (solid) and Coil (dotted) footprints versus Δn . Shown are footprints for constant device lengths ($L_{\text{gain}}=1 \text{ cm}, 1\text{m}$) and constant device gain ($\gamma_d=3 \text{ dB}, 27 \text{ dB}$). Comparison of Serpentine and Coil structures for $L_{\text{gain}}=1 \text{ cm}$ shows that while comparable for small Δn , the Coil structure packs with a smaller footprint area at higher Δn , and thus is the structure providing higher Areal Gain. Formulas to compute F are given in Table 2.6.

4.4.3 HIC Scaling Principle 3: the Independence of Amplified Spontaneous Emission

The ASE equations in (2.2) are comprised of two terms: stimulated emission due to ASE light propagating through the waveguide, and a term representing the spontaneous emission which generates this light initially. This second term represents the fraction of luminescence from the optical dopant that couples into propagating modes. It can be accurately modeled by equating the rate of spontaneous emission into a

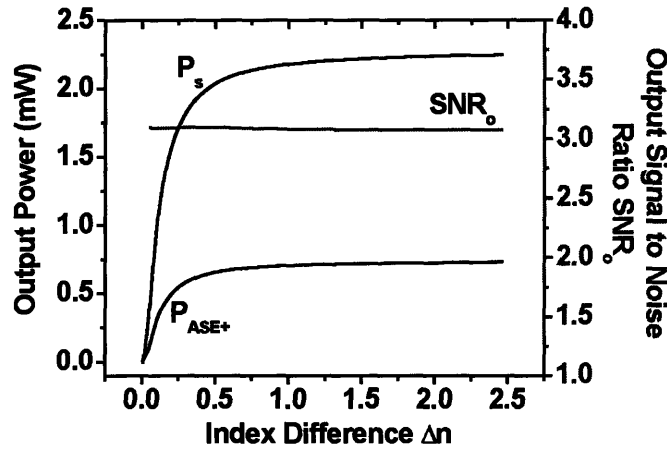


Fig. 2.12. Performance Map 4: (right axis) output signal-to-noise ratio versus Δn ; (left axis) P_s , P_{ASE+} versus Δn . (Data calculated for upconversion-free case study.)

waveguide mode, with the rate of stimulated emission into that mode with one photon already present[1]. This equivalence automatically accounts only for the number of spontaneously emitted photons coupling into propagating waveguide modes, within the frequency bandwidth $\Delta\nu$, where $\Delta\nu$ is the frequency bandwidth equivalent to the wavelength linewidth of the optical dopant. The functional dependence of the ASE equations on waveguide core A_{core} is now seen to be the same as the rest of the equations in (2.2); the output noise $P_{ASE+}(z=L_g)$ should therefore scale with output signal power $P_s(z=L_g)$, and this is seen to be the case (see Fig. 2.12). We thus observe a constant output signal-to-noise ratio $SNR_o = P_s/P_{ASE+}$ (at $z=L_g$), independent of Δn .

2.5 Results and Discussion 2: The Effect of L_g in Optical Shrink and Amplifier Design Rules

The design of efficient optically pumped EDFAs fundamentally relied on an understanding of the coupled optical pump, signal and noise modal profiles, as demonstrated in Fig. 2.3. The accurate simulation of these coupled fields led to the

recognition that amplifier length L_g is the most critical device parameter determining performance functions[63]. Optimal choice of L_g maximizes P_o , and hence device gain γ_d .

Fig. 2.3 indicates an optimal amplifier design should maximize the extent of Regime II, where Scaling Principles 1 dominates. And we observe from Fig. 2.9 that for fixed device length L_g , increasing Δn has the effect of extending Regime II: L_g^* increases with Δn . Thus increasing Δn increases the size of Regime II and decreases the size Regime III; this is what we refer to as Optical Shrink.

The goal of these Design Rules then is to determine the optimal length L_g^* , for a given Δn , thereby optimizing the effect of Optical Shrink on device gain γ_d .

Fig. 2.13 isolates the role of ASE on determining L_g^* . As indicated by Scaling Principle 3, ASE power depends on the absolute amount of optical dopant present in the WOA. If the length L_g of a WOA is decreased ($L_g:50\text{cm}\rightarrow 25\text{cm}$) there will be less

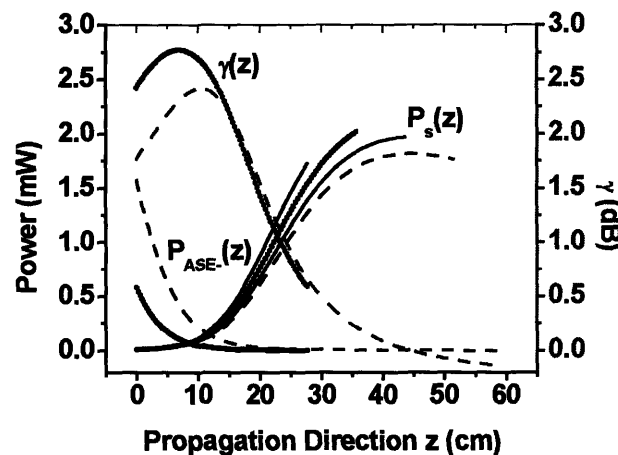


Fig. 2.13. Plot of signal profile using upconversion-free case study with different L_g . For different L_g , ASE causes a divergence in P_s profile; L_{max} is not a constant.

optical dopant present, hence less ASE. A decrease in P_{ASE} then implies a larger gain profile, and thus an increase in $P_s(z)$. This “divergence” effect is shown in Fig. 2.13, and can be artificially shut off by eliminating ASE in our computer simulation. In the absence of spontaneous emission, all the $P_s(z)$ curves in Fig. 2.13 overlap exactly. We thus conclude that while Δn dominantly controls Optical Shrink (i.e. increase in γ_d), ASE determines L_g^* .

L_g^* does not have a trivial dependence on Δn , and is critically influenced by the spontaneous emission lifetime τ of the optical dopant. For our case study (upconversion-free), Fig. 2.14 plots L_g^* versus Δn for $P_p=1, 10, 100$ mW. Fig. 2.14 comprises the final Performance Map to help establish our design rules, providing an *upper limit* on the length of the WOA. Device gain γ_d is maximum for $L_g=L_g^*$; therefore, for $L_g>L_g^*$, device gain per unit length (γ_d/L_g) drops dramatically.

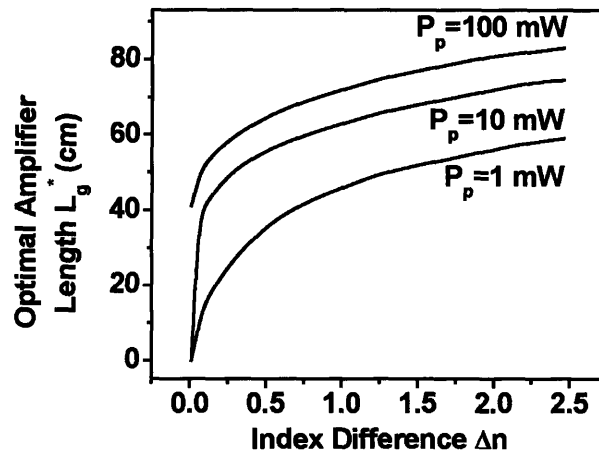


Fig. 2.14. Performance Map 5: Plot of Optimal Device Lengths versus Δn , for three different P_p , determined from numerical simulation, in the presence of no scattering transmission loss (upconversion-free case).

As mentioned in Section 4.5, the inclusion of scattering loss for waveguides reduces the optimal amplifier length. Optimizing device design therefore implies restricting to lengths below L_g^* ; the optimal device length, for a given experimentally measured α_s and α_p , can be exactly determined by simulating plots similar to Fig. 2.13, with the inclusion of α_s and α_p into Eqns (2.1) and (2.2).

2.6 Synthesis of Scaling Principles

2.6.1 Methodology

We suggest here a methodology for designing a HIC-WOA to demonstrate how these Performance Maps may be used to systematically develop amplifier design.

(1) Initial criteria: the WOA designer requires γ_d dB of gain to boost a signal P_s , within a fixed footprint F (need to solve for: Δn , τ_r , τ_{nr} , N , P_p); or designer requires γ_d dB using a fixed pump power source P_p (solve for: Δn , τ_r , τ_{nr} , N , F).

Table 2.5 gives a suggested rule of thumb pairing between P_p values and the lower limit on a range of Δn values (Δn_{min}):

P_p (mW)	Δn_{min}
1	1.0
10	0.1
100	0.01

Table 2.5. Order of magnitude pump powers sufficient to achieve population inversion in WOAs for index differences $\geq \Delta n_{min}$.

(2) Optical dopant: construct an analogous Performance Map 1, where boundaries between regimes are determined by the condition $W_{21}=1/\tau$, $W_{13}=1/\tau$. For the choice of P_p ,

observe if Regime II is the largest portion of flux trajectory space. If not, the choice of optical dopant (τ_r) may not be optimal.

(3) Optimal Amplifier Length: use Performance Map 5. In the case of $\tau_r \neq 12$ ms, rescale using equations in Table 2.6.

(4) Footprint: for a priori fixed choice of F, use Performance Map 3 to determine if $L_g \leq L_g^*$ can fit into this value of F. Use F versus L_g equations in Table 2.6 to rescale plot accordingly.

(5) Consistency check: Performance Maps 2-3 can be used as consistency checks to ensure the required values for the performance functions are finally met. Use the equations in Table 2.6 to rescale plots accordingly.

(6) Waveguide dimension: Fig. A1(Appendix 1) is part of a property map composed by Lee et al.[44] summarizing strip waveguide cross-section area and turning loss data, for a single mode cut-off waveguides. Use to finalize device lithography.

2.6.2 Figure of Merit

We define an amplifier Figure-of-Merit (FOM) as follows:

$$FOM = \frac{\gamma_{eff}}{F} NF$$

(2.10)

where Areal Gain per device pump power P_p , is approximated by the quantity γ_{eff}/F .

Fig. 2.15 plots the FOM versus Δn (upconversion-free case study), showing a dramatic power law scaling of $(\Delta n)^{2.6}$. Comparison of a commercial EDFA ($\Delta n=0.06$) versus Si microphotonic ($\Delta n=2.0$) system shows an increase in FOM by $\sim 10^4 \times$. This enormous

improvement in amplifier operation establishes Δn as a significant scaling law for affecting the design and performance of planar amplifiers.

Table 2.6 summarizes the set of design rules inferred from our analysis. Use of these equations allows prediction of performance functions for arbitrary N , τ_r , P_p , and F designed devices. The equations also summarize the influence of optimized design parameters on each other, giving insight into the rules of design constraining these parameter's values: L_g^* is not independent of Δn and P_p , and these equations help



Fig. 2.15. Figure of Merit versus Δn , for (upconversion-free) case study.

interpret that dependence as a series of power laws. The exponents in these power laws have been determined by empirical fit to the (Runge Kutta simulated) Performance Map trends.

2.7 Conclusion: Transverse Optical Confinement for the WOA

The materials gain per unit length reported in chapters 3, 4 sets an upper limit for our device gain. In order to optimize the integration of our SiON:Er amplifiers into a PLC design, we studied the influence of index difference Δn and amplifier length Δz . The

Performance Map	SCALING EQUATION
Threshold Flux (Fig. 2.4)	$\phi_{p,I \rightarrow II} = \frac{1}{\sigma_{13}\tau}; \phi_{s,III \rightarrow IV} = \frac{1}{\sigma_{21}\tau}$
Gain Efficiency (Fig. 2.10)	$\frac{d\gamma}{dP_p} \approx \frac{2N\sigma_{21}\Gamma_p}{A_{core}h\nu_p} \left[\frac{W_{21} + \frac{1}{\tau}}{(W_{13} + \frac{1}{\tau} + W_{21} + W_{12})^2} \right]$
Footprint (Fig. 2.11)	$F_{Serpentine} = L_g p - \frac{\pi}{2} p^2 + p^2; F_{Coil} = \left(\frac{p_{min} + p_{max}}{2} \right) L_g$
Optimal Length (Fig. 2.14)	$L_g^* \propto \frac{P_p^6 \Delta n^{5.5} \tau}{N}$
FOM (Fig. 2.15.)	$FOM = \frac{\gamma_{eff}}{F} \frac{SNR_o}{\eta_{heat}}$
Waveguide Width (Fig. A.1)	$w \propto \Delta n^{-0.57}$

Table 2.6. Design Rules: summary of scaling equations for interpolating arbitrary device parameters and performance functions from Performance Maps 1-6 (using upconversion-free case study, $\alpha_s = \alpha_p = 0$ dB/cm).

results of this Optical Shrink study helped us to quantify two High Index Contrast Scaling Principles:

(1) Performance Scaling: gain efficiency increases without upconversion as $\sim \Delta n^{1.2}$, and with upconversion as $\sim \Delta n^{0.93}$. The 1.2 power law emerges from solution of the transcendental equation describing single mode cut-off waveguide dimensions[5]. HIC-WOAs are more power efficient in theory than fiber amplifiers. The modal gain performance of the device increases by means of extending Regime II with Δn . Thus the

gain efficiency of a fixed length device increases with Δn , provided propagation losses are considerably low (see values in Table 2.3).

(2) Size Scaling: device footprint decreases as $\sim \Delta n^{1.4}$. The 1.4 power law emerges from dependence of device footprint size on a strip waveguide turning radius that gives fixed turning loss per unit length (Appendix 1). HIC-WOAs can be packed compactly in two dimensions. With a smaller footprint we can integrate numerous WOAs into a two-dimensional PLC layout without being limited by the areal details of the layout.

(3) The output signal-to-noise ratio remains independent of Δn ; HIC-WOAs should have in theory the same noise figure (see definition in Table 2.1) as fiber amplifiers.

We evaluated the cumulative impact of these two Scaling Principles in a Figure of Merit computation, which showed a $\Delta n^{2.6}$ improvement in a single-mode amplifier's integrated performance (within a PLC). We designed a lithography mask to test our simulation by experimental measure of device gain γ_d versus pump power P_p , for amplifier lengths $L_g=1 \text{ cm} \leftrightarrow 10 \text{ cm}$. Loss measurements of these waveguides, done by the Fabry Perot method [64], will be incorporated into our model to see if we can experimentally measure an improvement in the γ_d versus P_p slope (i.e. gain efficiency), for $\Delta n=0.155$ in comparison to $\Delta n=0.75$ (i.e. SiON:Er and Si₃N₄:Er waveguide cores of refractive index 1.6 and 2.2, respectively, surrounded by an SiO₂ cladding—see chapter 4). We also have a $\Delta n=0.06$ comparison for this work: a 30 m long coil of optical fiber donated to us by 3M, with an Er optically active concentration of $\sim 10^{20} \text{ cm}^{-3}$. However, these observations in increasing gain efficiency cannot be experimentally resolved until

we make further advances in waveguide sidewall smoothing that ensure propagation losses of ~ 0.2 dB/cm. Hence, the experimental verification of our Optical Shrink study has merged into a collaboration with my fellow group researcher's work in propagation loss minimization[65].

At the conclusion of this study, we have realized the effect of Optical Shrink should be more broadly understood as the engineering of a waveguide's electromagnetic boundary value conditions. As detailed by Fig. 2.3, increasing Δn results in an increase in the transverse optical confinement of the mode of light; for a fixed Δz , this increase in Δn extends Regime II and improves device gain per unit pump power.

Understanding Optical Shrink more generally as a modification in the propagating waveguide mode's transverse confinement motivated us to develop further techniques to engineer optimization of modal gain performance (increasing gain efficiency), and if simultaneously possible, PLC integrability (decreasing device footprint). Chapters 5 and 6 present our theoretical simulation and analysis of two more optical engineering approaches: resonant confinement and photonic band gap confinement.

Lastly, while the conclusions of this chapter derive from general physical principles and have applicability across all photonic length scales, we conclude from a power-budget analysis that the practical relevance for designing ultra-high gain efficiency devices operating on ultra-low pump power sources, will be for < 1 cm length scale microphotonic PLCs (e.g. $P_p=1$ mW sources powering 3-5 dB gain elements).

Chapter 3:

High Er Concentration Materials Systems for Si Microphotonic Amplifiers



Reactive sputtering of erbium oxide within RF magnetron system in Kimerling labs, MIT. Visible above the plasma-illuminated target are the Argon/Oxygen gas ring and the rotating sample holder. Image taken through glass view port, courtesy K. Chen.

“We have some very nice X-ray result.” -Dr. Xiaoman Duan (Research Associate, EMAT), the week before MRS Fall 2001.

“We’re not getting any plasma. I think we have to vent the chamber...” -Jessica G. Sandland (graduate student, EMAT), something that happened a lot.

3.1 Chapter Abstract

Following demonstration of room temperature IR luminescence[66], Er_2O_3 was explored as a potential high gain medium for ultra-compact waveguide amplifiers. With sputtered and annealed films, we observed three distinct optical centers (and measured lifetimes 7, 0.8 and 0.5 ms) and computed cooperative upconversion coefficients from 4.2 K lifetime data. We correlated these measurements with three crystalline phases: the thermodynamically stable BCC phase and metastable FCC and HCP phases. The 7 ms lifetime is correlated with the FCC phase, implying the metastable crystal state has a profound influence on inhibiting cooperative upconversion interaction between nearest-neighbor Er atoms. We combine these results to calculate the power requirements to achieve 3.0 dB/cm small signal gain and make concluding remarks concerning the feasibility of Er_2O_3 for ultra-high microphotonic gain.

3.2 Introduction

3.2.1 The Small Interaction Cross-Section of the Er Atom

The millisecond radiative lifetime for Er in dielectric host materials[1] makes Er an effective optical center for WDM gain, and contributes low output noise, as mentioned in chapter 1. But this long lifetime (as compared to ns-scale III-V emitters) atomic transition equivalently implies a weak rate of stimulated emission for optical gain. The physical principle of optical gain is described in detail in chapter 2; we briefly summarize here its relevant points. For a light signal λ_s confined and traveling along propagation direction z within an Er-doped waveguide, the build-up of the signal's optical power P_s , per unit length in the z -direction, is described by the differential equation (reproduced from chapter 2):

$$\frac{dP_s}{dz} = (N_2\sigma_{21} - N_1\sigma_{12})\Gamma_s P_s - \alpha_s P_s$$

(3.1)

where Γ_s is the fraction of P_s confined within the waveguide core (Fig. 4.6 gives a graphical depiction of this). N_1 is the concentration of Er (per unit volume) in the atomic ground state, N_2 is the concentration of Er in the atomic first excited state, and σ_{12} (or σ_{21}) are defined as the interaction cross-section[1] for absorption (or stimulated emission).

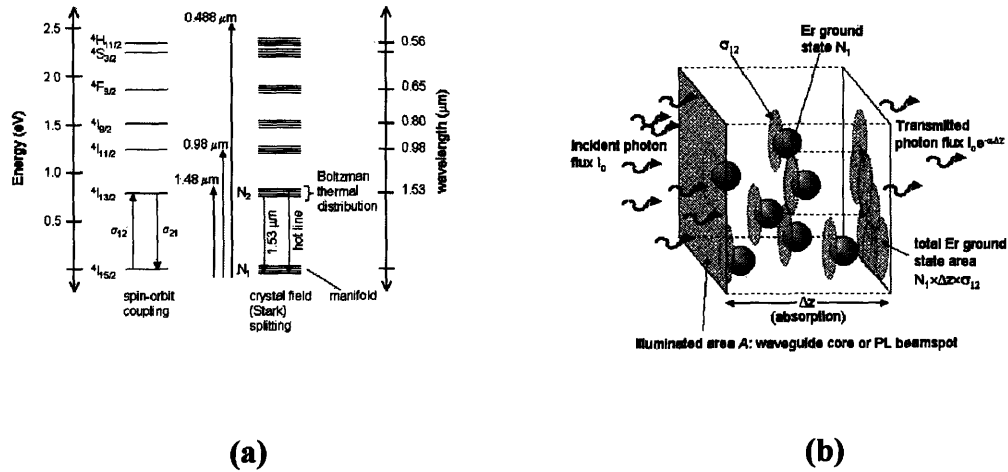


Fig. 3.1. (a) The atomic transition energy levels for Er[15], with labeling describing N_1 , N_2 , σ_{12} and σ_{21} . Spin-orbit coupling within the Er 4f-electron shell lifts a total angular momentum degeneracy of the shell, resulting in 4f-shell excited state $^4I_{13/2}$, $^4I_{11/2}$, $^4I_{9/2}$, etc. Local crystal field symmetry causes further Stark level splitting of spin-orbit states into meV-broadened manifolds. At room temperature, thermalizing phonons increase N_2 population energy higher into the $^4I_{13/2}$ manifold, resulting in hot line spontaneous emission, blue-shifted with respect to the dominant $^4I_{13/2} \rightarrow ^4I_{15/2}$ transition. (b) Schematic illustration of the intuitive interpretation of an absorption cross-section area σ_{12} .

Fig. 3.1.a shows a schematic picture the atomic transitions levels within the Er atom that result in infrared light emission around 1.55 μm , as determined from spectroscopic studies[15] of Er in ionic and dielectric hosts. The populations referred to by N_1 and N_2 are labeled in the figure. Spectroscopic notation[67] $^{2S+1}L_J$ is listed alongside the excited state energy levels in the figure. The interaction cross-section σ_{12} represents the strength of interaction to couple a photon (of energy $E=E_2-E_1$) into an atomic energy increase from ground state $^4I_{15/2}$ (we will refer to this atomic energy state as level 1) to the first excited state $^4I_{13/2}$ (we will refer to this atomic energy state as level 2). The interaction cross-section σ_{21} represents the strength of interaction to couple an atomic energy decrease, from level 2 to level 1, into a photon of energy $E=E_2-E_1$ (i.e. Er de-excitation from the first excited state to the ground state) by means of stimulated emission. Originally developed in the context of atomic particle scattering theory, σ_{12} and σ_{21} , in units of cm^2 , are intuitively interpreted as an effective cross-sectional area (for absorption or stimulated emission) presented by the Er atom to propagating photons of light—while the photons are mathematically described as a flux of point particles per unit area[1].

This intuitive description implies that the product $N_1\sigma_{12}$ represents the rate of photon coupling to Er $^4I_{15/2} \rightarrow ^4I_{13/2}$ excitation, i.e. the rate of photon absorption. Similarly $N_2\sigma_{21}$ represents the rate of photon generation from Er atoms, due to stimulated emission by the flux of photons, resulting in a coherent build-up of photon flux. Fig. 3.1.b shows an intuitive explanation for the interpretation of $N_1\sigma_{12}$ as an absorption rate: in propagation distance Δz , $N_{\Delta z} \equiv N_1(\Delta z A)$ Er atoms present an effective area σ_{12} for photon absorption (A is the cross-section area of an Er-doped waveguide core). The probability of

photon absorption p_{abs} within this waveguide core, for photons (defined by a given flux density) traveling a distance Δz , is the sum of $N_{\Delta z}$ absorption cross-sections σ_{12} , divided by the waveguide core cross-section A . The probability of photon absorption p_{abs} per unit length in the propagation direction is

$$\frac{p_{abs}}{\Delta z} = \frac{(N_{\Delta z} \sigma_{12}) / A}{\Delta z} = \frac{1}{\Delta z} \frac{\sigma_{12}}{A} N_1(\Delta z A) = N_1 \sigma_{12} \equiv \alpha$$

(3.2)

which is defined as the absorption coefficient (quantified in units of cm^{-1} or decibels per unit centimeter dB/cm). Similarly, the small signal gain coefficient is defined as $\gamma = N_2 \sigma_{21}$ [68].

The atomic energy levels in Fig. 3.1.a do not represent single electron promotion within Er atomic levels, but rather promotion of the entire 4f electron shell from a ground state configuration to excited states [15]. The excited states are the result of a degeneracy-lifting effect on the total atomic angular momentum J (referring to spectroscopic notation $^{2S+1}L_J$), due to spin-orbit coupling. When doped within a host material with given crystal symmetry or short range order due to the polar ligands (i.e. bonding molecular orbitals) of nearest neighbor host atoms, the spin-orbit levels within the Er atom 4f-shell undergo a further Stark effect splitting into multiple energy levels termed manifolds (see Fig. 3.1.a). It is the presence of these manifolds that results in Er infrared emission having a characteristic two-peak profile (see Fig. 3.6.b). Room temperature thermal populating of the higher energy manifold levels (whose population distribution is governed by a Boltzman factor) results in spontaneous emission of photons with a higher energy (i.e. blue-shifted) with respect to the dominant emission (the dominant emission occurs from

the bottom of the ${}^4I_{13/2}$ manifold). These blue-shifted Boltzman distribution controlled emission lines are called hot lines, and we examine them in section 2.4.

A subtle consequence of ground state ${}^4I_{15/2}$ and excited state ${}^4I_{13/2}$ being different spin-orbit levels is that for an atomic energy transition from ${}^4I_{15/2}$ to ${}^4I_{13/2}$, the initial and final density of states is not the same as for a transition from ${}^4I_{13/2}$ to ${}^4I_{15/2}$. Fermi's Golden rule[60] dictates that the oscillator transition strength between these levels is therefore not the same, for absorption versus emission, i.e. $\sigma_{12} \neq \sigma_{21}$. However, it is a reasonable assumption to assume $\sigma_{12} \approx \sigma_{21}$. The exact difference between σ_{12} and σ_{21} is phenomenologically described for Er in SiO₂-based glass systems by the McCumber relation[1]:

$$\sigma_{21}(\nu) = \sigma_{12}(\nu) e^{(\varepsilon - h\nu)/kT}$$

(3.3)

where ε is the average energy difference between the ground state ${}^4I_{15/2}$ and first excited state ${}^4I_{13/2}$ manifolds (0.71 eV, corresponding to 1.55 μm), h is Planck's constant and ν is the frequency of light.

Since the interaction cross-section is proportional to Fermi's Golden rule for spontaneous emission, a relation can be derived between σ_{21} and the radiative lifetime τ_r (the radiative lifetime represents the rate of spontaneous de-excitation from ${}^4I_{13/2}$ to ${}^4I_{15/2}$ that results in photon emission)[68]:

$$\sigma(\nu) = \frac{\lambda^2}{8\pi\tau_r} g(\nu)$$

(3.4)

where λ is the wavelength of light and $g(\nu)$ is called a lineshape function, $\propto 1/\Delta\nu$.

This result has important implications for Er-based optical gain. A ~ 10 ms[1] scale lifetime for Er, doped in the numerous glass systems used for fiber optic EDFAs, implies a considerably small interaction cross-section, typically on the order $\sim 6 \times 10^{-21}$ cm². In comparison, the interaction cross-section for a de-localized conduction electron in III-V semiconductors is $\sim 10^{-17}$ cm²[69]. The highly confined and atomically screened 4f electron shell of the Er atom is $10^4 \times$ weaker at interacting with light, than a free-moving conduction electron. For a material doped with Er atoms to a concentration of 1.2×10^{20} cm⁻³, this results in a gain coefficient of

$$\gamma = N_2 \sigma_{21} \cong 0.72 \text{ cm}^{-1} = 3 \text{ dB/cm} .$$

(3.5)

This means that for an Er-based 3 dB gain microphotonic device, we have to design a waveguide amplifier that is ~ 1 cm = 10^4 μ m long. This is a prohibitively large device length that cannot be integrated into the PLC design of Si Microphotronics (chapter 1). If the Er doping concentration can be increased by a factor of 100, the device length will correspondingly decrease to ~ 100 μ m, which is a reasonably compatible microphotonic length scale[70]. With this motivation in mind, we explored erbium oxide (Er₂O₃) as an ultra-high Er concentration materials system that represents the limiting reach of increasing Er count per unit volume, in an oxygen-rich oxide environment.

However, the literature on EDFA devices had long since discovered a critical gain-limiting effect in Er-doped glasses, known as cooperative upconversion. And it is an effect that is concentration dependent.

3.2.2 Cooperative upconversion and Its Influence on Er₂O₃

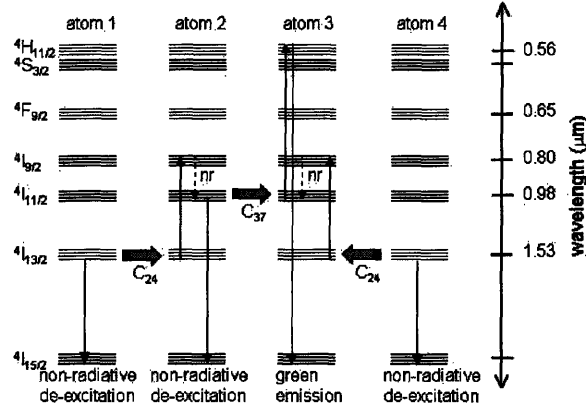


Fig. 3.2. The cooperative upconversion effect is a two-step non-radiative resonant energy transfer (phenomenologically represented by coefficients C_{24} , C_{37}) between nearest neighbor Er atoms, resulting in the non-radiative de-excitation of 3 Er atoms from the first excited state for every 1 Er atom emitting green radiation at $\lambda \sim 560$ nm.

Cooperative upconversion is a gain-limiting effect in Er optical transitions due to a dipole-dipole non-radiative interaction[4] between nearest neighbor excited state Er atoms. The energy difference between levels 2 ($^4I_{13/2}$) and 4 ($^4I_{9/2}$) (see Fig. 3.2) is an approximate resonant match to the energy difference between levels 1 ($^4I_{15/2}$) and 2 ($^4I_{13/2}$). The dipole-dipole interaction de-excites Er atoms 1 and 4 by transferring their atomic energy to Er atoms 2 and 3, promoting them to state $^4I_{9/2}$. The interaction process is phenomenologically quantified by a cooperative upconversion coefficient C_{24} (with units cm^3/s) and appears in the differential equation describing the rate of Er excitation as

$$\frac{dN_2}{dt} = W_p N_1 - \frac{1}{\tau} N_2 - (C_{24} N_2^2) \quad (3.6)$$

where τ is the net lifetime of excited state Er (i.e. the sum of spontaneous emission radiative rate and non-radiative de-excitation rates), W_p is the optical pump rate (defined as $W_p = \phi_p \sigma_p$, where ϕ_p is the pump wavelength photon flux which excites the Er atom and σ_p is its absorption cross-section; for a $\lambda_p = 980$ nm pump wavelength, $\sigma_p = \sigma_{13}$; for a $\lambda_p = 488$ nm pump (see Fig. 3.1.a) wavelength, $\sigma_p = \sigma_{17}$; chapter 2 explains equation (2.6) in full detail). If the Er is pumped at a high enough optical power P_p (where $\phi_p = \Gamma_p P_p / (h\nu_p A)$; Γ_p is the fraction of pump power within waveguide core and ν_p is pump frequency), a second resonant dipole-dipole interaction (described by an cooperative upconversion coefficient C_{37}) between levels 3 (${}^4I_{11/2}$) and 7 (${}^4H_{11/2}$) (see Fig. 3.2) results in the promotion of Er atom 3 to level 7, and the non-radiative de-excitation of Er atoms 1, 2 and 4. This Er atom in level 7 tends to de-excite by a faster radiative rate, giving off a ~green photon around 560 nm.

Cooperative upconversion thus renders excited Er optical centers useless for 1.55 μm infrared (IR) signal amplification. This dipole-dipole effect has been modeled as some form of power-law interaction, and in EDFAs has been observed to become significant, versus typical 10-100 mW optical pump rates[1], for Er nearest neighbor distances that correspond to Er dopant concentrations in excess of 10^{20}cm^{-3} [4].

For this reason, Er_2O_3 has long been considered an ineffective materials candidate for IR optical gain. Few reports existed on the optical properties of Er_2O_3 thin films, and there were no published papers regarding its light emission, until the Kasuya et al.[71] study of green luminescence and our group's (Chen et al.[66]) demonstration of room temperature IR emission near 1.54 μm .

3.2.3 This Work

We have continued[72] from Chen's initial work, completing luminescence studies on Er_2O_3 to understand the optical character of the Er atom in an Er_2O_3 thin film crystalline state, and to experimentally determine what is the effect of cooperative upconversion in comparison to Er-doped EDFAs materials. The goal of this evaluation is to quantitatively determine the potential of Er_2O_3 for ultra-high concentration Er-based IR gain. If all the Er in Er_2O_3 can truly be harnessed for IR gain, a gain coefficient as high as 300 dB/cm may be realized—comparable to the gain per unit length performance of commercial III-V Semiconductor Optical Amplifiers.

3.3 Experimental Details

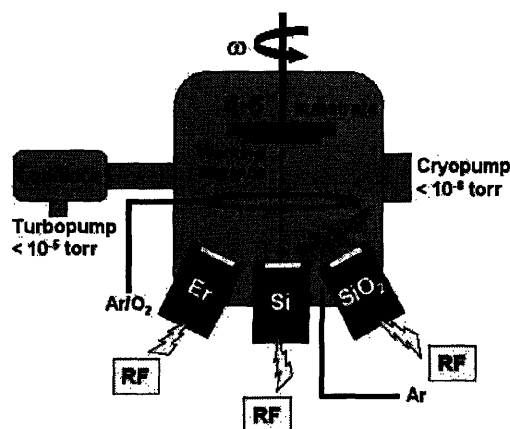


Fig. 3.3. Schematic of RF magnetron sputter machine, purchased from Kurt J. Lesker Company. The sputter machine can simultaneously sputter from three targets. RF sputter guns enable sputtering of metals (such as Er), semiconductors (such as Si) or dielectric insulators (such as SiO_2 and Si_3N_4). Three gas lines deliver Ar gas directly below each gun for Ar-sputtering; one gas ring disperses Ar/ O_2 (10% O_2) gas above the guns for oxygen reactive sputtering.

Thin films of Er_2O_3 were grown by reactive magnetron sputtering in a system custom designed by the Kurt J. Lesker Company (see Fig. 3.3 for schematic). For deposition, an Er metal target was reactively sputtered, using an Ar- O_2 plasma (90% Ar, 10% O_2), onto a Si substrate, after the Ar-sputtering of 90 nm of SiO_2 . The substrate was not heated nor temperature controlled during deposition; estimated thermocouple measurements suggest substrate temperatures to range between 200-250°C by the end of a 1-2 hour deposition.

The base chamber pressure was evacuated down to ultra-high vacuum (1×10^{-8} torr) prior to deposition, to minimize film contamination. As-sputtered Er_2O_3 films were 100 nm in thickness and partially crystallized. Film samples were annealed into complete crystallization using either a conventional tube furnace under an oxygen gas overpressure, or samples were annealed in a rapid thermal annealing (RTA) system under a nitrogen gas ambient. Conventional tube furnace anneals were systematically varied between 2-20 hours and 600-1050 °C[66]. RTA anneals were systematically varied between 5 seconds-



Fig. 3.4. Cross-section TEM of annealed Er_2O_3 thin film shows large grained complete crystallization.

2 minutes and 700-1100 °C.

A JEOL-2010F was used to perform transmission electron microscopy (TEM) on film cross-sections (see Fig. 3.4 for a cross-section TEM example of crystallinity). Crystallinity characterization was done using a Rigaku X-ray diffraction set-up. Photoluminescence and lifetime measurements were done using an Ar-ion pump laser (pump wavelength $\lambda_p=488$ nm), SPEX spectrometer, Hamamatsu liquid-nitrogen cooled photomultiplier tube detector, lock-in amplifier and oscilloscope, and an Oxford Instruments liquid-He cooled cryostat.

Fig. 3.5.a is a plot of the Hamamatsu photomultiplier tube's spectral responsivity (the amount of mA photocurrent generated per unit W photon power, as a function

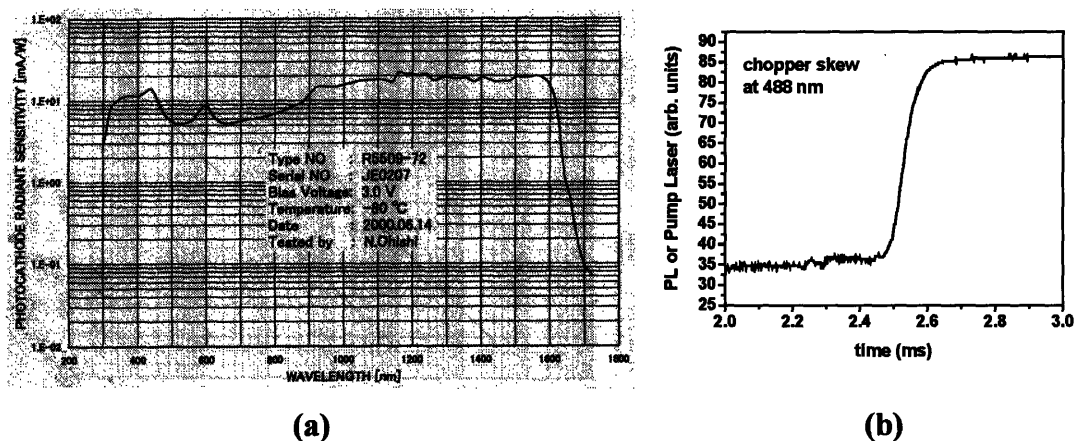


Fig. 3.5. (a) The spectral responsivity of the Hamamatsu photomultiplier tube, as measured prior to installation in May, 2001. (b) Lifetime plots overlaying mechanical chopper temporal skew and 980 nm luminescence from Er-doped commercial glass. Lifetimes less than 100 μ s cannot be temporally resolved.

of wavelength λ). The responsivity drops at a power law rate for $\lambda>1600$ nm. Our IR emission studies yield spectral profiles within the $\lambda=1400-1600$ nm range, which has approximately constant responsivity. We have also done studies of visible emission in the $\lambda=500-700$ nm range, and here we observe the photomultiplier tube's spectral

responsivity to have a profile about 600 nm, varying over a value of 5-9 mA/W. Care should thus be taken in reporting any photoluminescence profile centered about $\lambda=600$ nm. While we have not done any quantitative comparison between visible and IR PL emission intensities, Fig. 3.5.a shows a difference in responsivity between these two spectral ranges on the order of $\sim 20/5 = 4\times$. In addition, the SPEX spectrometer has a non-uniform transmission spectral profile over the visible-IR wavelength scale; since we have no need to explicitly compare visible versus IR emissions, we have not characterized this transmission profile variation.

Fig. 3.5.b shows a plot determining our lower limit experimental resolution for PL lifetime measurements. The Ar-ion pump laser was mechanically chopped using a Stanford Research systems chopper, whose rate was fed to the lock-in amplifier as a reference signal. The finite-size beam diameter of the Ar-ion laser corresponds to a characteristic time, within which the blade of a 50/50 duty-cycle chopper passes through the beam diameter, and completely extinguishes transmission of the laser light to the Hamamatsu detector. This time to extinguish light transmission can be temporally resolved on an oscilloscope, as a linear change in laser light intensity at $\lambda=488$ nm. By confining the chopper within two convex lenses (spaced focal distances apart from one another), we position the chopper's blade to lie within the focal place of both the lenses. At this position the laser beam diameter is minimized as a function of the convex lens' curvatures. Working with the equipment at our disposal, we were able to minimize this chopper time delay to an experimentally observed value of about 100 μs (Fig. 3.5.b). This means that PL lifetimes less than 100 μs will lie below this temporal skew and cannot be resolved by our system; an example of the 980 nm emission (${}^4I_{11/2} \rightarrow {}^4I_{15/2}$) from an Er-

doped glass reference sample from Corning Inc. is overlaid for comparison. In our Er_2O_3 work, the smallest measured lifetimes were on the order of 500 μs , safely above this chopper skew limitation.

3.4 Reference Sample Studies

As a reference comparison to our sputtered Er_2O_3 study, we used two reference samples: an Er-doped commercial glass (material used for EDFAs) donated by Corning Inc., and commercially sold Er_2O_3 powder (typically used in Scanning Electron Microscopy work as an IR luminescence reference). The use of these reference samples helped to increase our understanding of the optical properties of sputtered Er_2O_3 . We summarize our optical characterization of these references in the next two sub-sections.

2.4.1 Characterization of Er-Doped Corning Glass

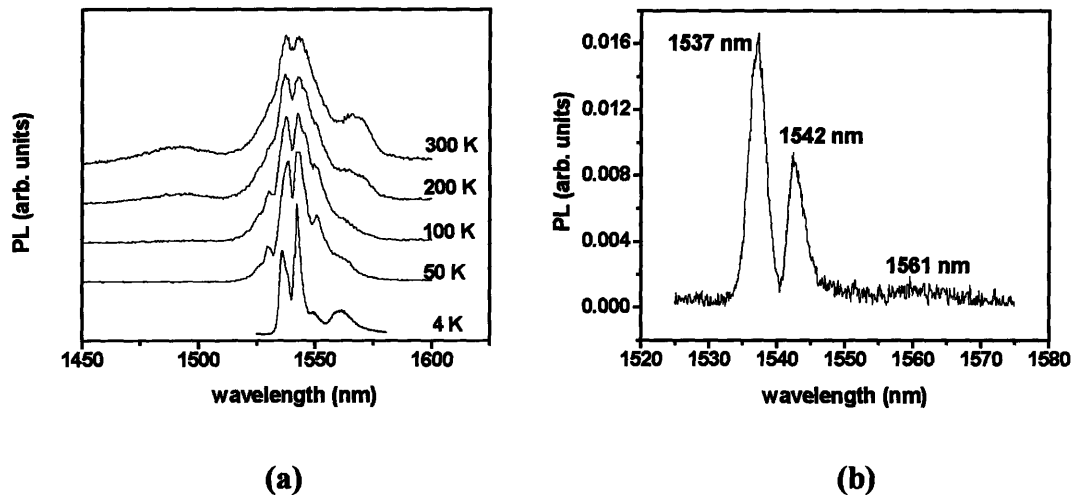


Fig. 3.6. (a) PL profile of Sample 7 at different temperatures, normalized to peak intensity. (b) 1 Å high resolution scan of Sample 7 PL at 4 K. High resolution scan reveals 1537 nm peak to be dominant intensity and therefore dominant ${}^4\text{I}_{13/2} \rightarrow {}^4\text{I}_{15/2}$ transition.

Sample 1	Sample 2	Sample 3	Sample 4	Sample 5	Sample 6	Sample 7
1.07×10^{17} cm^{-3}	3.23×10^{17} cm^{-3}	1.07×10^{18} cm^{-3}	3.23×10^{18} cm^{-3}	1.07×10^{19} cm^{-3}	3.23×10^{19} cm^{-3}	1.07×10^{20} cm^{-3}

Table 3.1. Summary of Er-doped glass samples donated by Corning Inc. to the Kimerling Research Group, MIT University. Listed are the doped Er concentrations N_{doped} . Corning certifies $N_{\text{doped}}/N_{\text{active}} \cong 1$ for all samples.

Glass samples doped with Er, were donated by Corning Inc. (see Table 3.1) to our research group for application as reference standards, against which to compare the 4 Kelvin (K) integrated photo-luminescence (PL) intensity of Er-doped sputtered films. The luminescence data reported in this section is for a glass Sample 7 (doped with 1.07×10^{20} Er atoms/ cm^3) where the optical yield, defined as the concentration of doped Er (N_{doped}) divided by the concentration of light-emitting Er (N_{active}), is certified by Corning glass chemists to be $N_{\text{doped}}/N_{\text{active}} \cong 1$. We used Sample 7 as the reference against which to compare Er_2O_3 thin film PL intensity.

Fig. 3.6.a plots the normalized PL intensity of Sample 7 from 4 K up to room temperature. All plots are taken at 4 angstrom (\AA) spectrometer slit resolution, and this resolution is observed to be below peak linewidths for all temperature except 4 K. A 4 K, a 1 \AA resolution scan shows (see Fig. 3.6.b) the 4 K spectra to have a ~ 2 nm linewidth, indicating an inhomogeneously broadened spectra, characteristic of a glass host matrix.

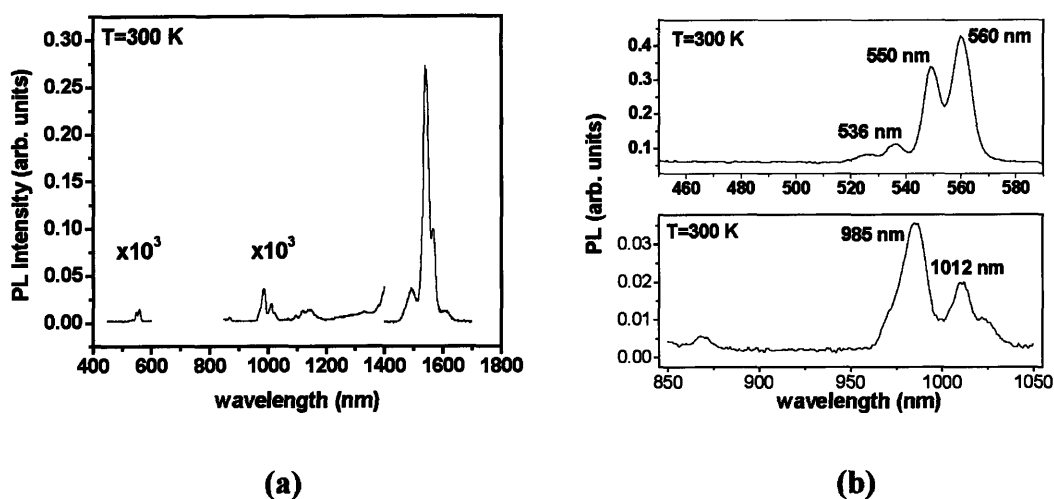


Fig. 3.7. (a) Room temperature wide-range (visible to IR) PL profile of Sample 7. (b) Magnification of room temperature PL profiles in visible and 980 nm ranges.

We attribute the dominant 1537 nm peak to be a transition from the bottom of the first excited-state ${}^4I_{13/2}$ manifold to the bottom of the ground state ${}^4I_{15/2}$ manifold; transition peaks at 1542 nm and 1561 nm likely correspond to energy transitions from the bottom of the first excited-state manifold to higher energy levels in the ground state manifold. Increasing temperature shows a decrease in PL intensity, due to a rising non-radiative decay rate (see lifetime measurements in Table 3.2) which we attribute to an increasing thermal equilibrium concentration of phonons: Fig. 3.6.a shows the presence of hot lines (at $\lambda < 1537$ nm) with increasing temperature. The hot lines form due to thermal phonon populating of the higher energy levels within the ${}^4I_{13/2}$ first excited-state manifold.

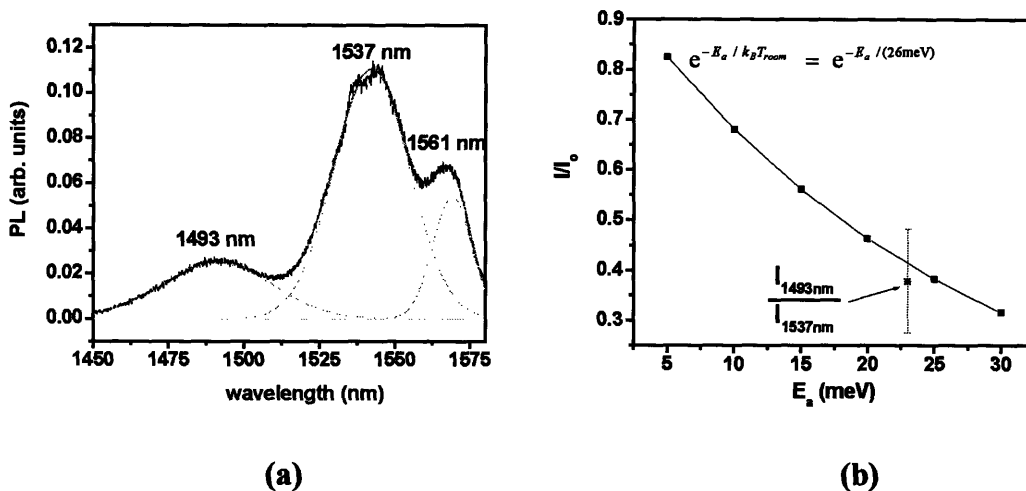


Fig. 3.8. (a) Gaussian function fits to room temperature PL profile of Corning Sample 7. (b) Room temperature Boltzmann factor versus activation energy E_a , quantifying thermal population of hot line emission ($\lambda=1493$ nm) state. The experimental data in red overlaps the ratio of fitted $I(\lambda=1537$ nm)/ $I(\lambda=1493$ nm) from the measurement in (a), at $E(\lambda=1493$ nm)- $E(\lambda=1493$ nm)=23 meV.

Fig. 3.7.a is a wide range room temperature PL scan across the visible to IR spectral range, showing light emission around 560 nm (${}^4H_{11/2} \rightarrow {}^4I_{15/2}$), 980 nm (${}^4I_{11/2} \rightarrow {}^4I_{15/2}$) and 1530 nm (${}^4I_{13/2} \rightarrow {}^4I_{15/2}$). Despite the $\sim 4\times$ detector correction for comparing visible to IR emission, the $10^4\times$ greater IR emission intensity makes it clear that de-excitation from ${}^4H_{11/2}$ and ${}^4I_{11/2}$ atomic levels is more likely to occur by non-radiative (i.e. phonon-mediated) mechanisms. The closer energetic spacing of these higher excited state levels (see Fig. 3.1.a) is consistent with this interpretation: fewer phonons are needed to nonradiatively relax ${}^4H_{11/2}$ and ${}^4I_{11/2}$ atomic levels down to the next excited state. Fig. 3.7.b is a magnification of the spectral profiles in the 560 nm and 980 nm regions.

Fig. 3.8.a shows three Gaussian fits to the room temperature IR emission profile. If the peak at 1493 nm is truly a hot line of the principal 1537 nm PL peak, then the

energy difference between 1493 nm and 1537 nm, corresponding to 23 meV, locates the hot line transition level as being 23 meV above the lowest ${}^4I_{13/2}$ manifold energy level. And the population probability of this hot line transition level will be governed by a Boltzmann factor of form $e^{-(23\text{meV})/k_B T}$. Fig. 3.8.b plots $e^{-E_a/k_B T_{\text{room}}} = e^{-E_a/(26\text{meV})}$ versus E_a , and overlays the ratio of PL peak intensities $I(\lambda=1537\text{nm})/I(\lambda=1493\text{nm})$ (where the peak intensities are acquired from the Gaussian fits of Fig. 3.8.a) at $E_a=23$ meV. We observe that the PL peak intensity ratio has agreement with the Boltzmann plot, within the experimental error bars of the Fig. 3.8.a fit; this supports the interpretation of the 1493 nm PL peak as a hot line of the 1537 nm peak, whose thermal population is governed by the activation energy that locates this hot line energy level within the ${}^4I_{13/2}$ excited state manifold (i.e. 23 meV above the lowest ${}^4I_{13/2}$ manifold level).

Fig. 3.9.a is an experimental plot of PL time decay at 4 K, as measured on an oscilloscope. The fitted single exponential time constant gives a record lifetime measurement of 27.8 ms. Typical Er lifetimes in glass hosts are ~ 10 ms; the Corning glass is a proprietary glass composition of undisclosed additives, whose phonon density of states enables such lengthy ms-scale lifetimes. The Fig. 3.9.b inset plots fitted 4 K lifetimes versus pump power: the decrease in lifetime with higher pump power is a

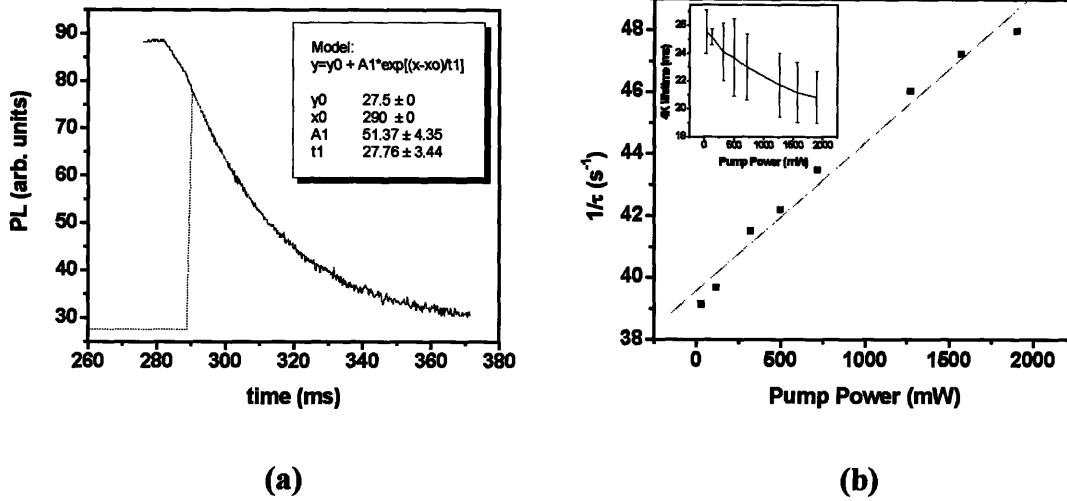


Fig. 3.9. (a) Single exponential fit of 4 K PL intensity decay (at $\lambda=1537$ nm) at 30 mW pump excitation power. (b) Inset: plot of fitted 4 K lifetime versus pump power (at $\lambda=1537$ nm). Outset: plot of 1/lifetime versus pump power; slope determines cooperative upconversion coefficient.

fingerprint of the cooperative upconversion power-parasitic process. Pumping at higher pump powers results in more N_2 population Er atoms, which in turn increases the upconversion rate $C_{24}N_2 >$ the spontaneous emission rate $1/\tau$, de-excite Er even faster. Thus, pumping Er with higher energy, in the hopes of increasing PL intensity (due to radiative spontaneous emission), only results in increasing the cooperative upconversion rate $C_{24}N_2^2$. The Fig. 3.9.b outset plots the inverse of this measured 4 K lifetime, versus pump power. From equation (2.6), we approximate a pump power relation for the experimentally measured net lifetime:

$$\frac{1}{\tau_{net}} = \frac{1}{\tau} + CNW_p \tau \quad (3.7)$$

where τ_{net} is the experimentally fitted lifetime, τ is the actual 4 K lifetime, N is the concentration of optically active Er atoms, W_p is the optical pump rate, and C is the cooperative upconversion coefficient. We can thus determine the actual lifetime τ and cooperative upconversion coefficient C from a straight line fit of $1/\tau_{\text{net}}$ versus pump power P_p . The accuracy and applicability of approximation (2.7) is quantitatively determined in section 2.5 for both Er_2O_3 thin films and Corning Sample 7.

A straight line fit of Fig. 3.9.b determined the 4 K cooperative upconversion coefficient to be $1 \times 10^{-17} \text{ cm}^3/\text{s}$ and the actual 4 K radiative lifetime to be $27 \pm 2 \text{ ms}$. Room temperature lifetime was fitted to be $19 \pm 1.5 \text{ ms}$.

The 4 K measurement of cooperative upconversion is a factor of ten better than commercially reported values of cooperative upconversion in $\sim 10^{20} \text{ Er}/\text{cm}^{-3}$ EDFAs. We believe this coefficient is not grossly temperature sensitive, since cooperative upconversion is a resonant process of energy transfer. Table 3.2 summarizes our lifetime measurements at room temperature (300 K) and 4 K.

Room T	4 K
$27 \pm 2 \text{ ms}$	$19 \pm 1.5 \text{ ms}$

Table 3.2. Lifetime measurement summary of Corning Sample 7.

2.4.2 Characterization of Er_2O_3 Commercial Powder

For reference purposes in comparison against the sputtered Er_2O_3 thin films, we examined the PL spectra and lifetime of Er_2O_3 powder, a commercially available IR luminescent polycrystal, made up of the Er_2O_3 thermodynamically stable Body Centered Cubic (BCC) phase. Fig. 3.10.a shows a 4 K PL scan of Er_2O_3 powder, with peak

emission at 1549.5 nm. This is a significantly different profile from the Corning reference sample; comparison with sputtered Er-doped SiO₂ (see chapter 4) shows a similar PL peak at 1550 nm.

We conclude here that for an Er microenvironment of oxygen nearest neighbors, Fig. 3.10.a indicates a $\sim 1550\text{nm} = 0.8\text{ eV}$ energy transition to be the strongest oscillator strength coupling a ${}^4I_{13/2} \rightarrow {}^4I_{15/2}$ relaxation. Fig. 3.10.b is a lifetime measurement of the 1549.5 nm PL peak, showing a 4 K lifetime of 552 μs . Given the high ms-scale lifetime for Er in glass hosts, we hypothesize the low lifetime in Er₂O₃ powder to be due to a high cooperative upconversion rate for Er particles spaced on the order of an atomic distance (i.e. an Er density of $\sim 10^{22}\text{ cm}^{-3}$) from each other.

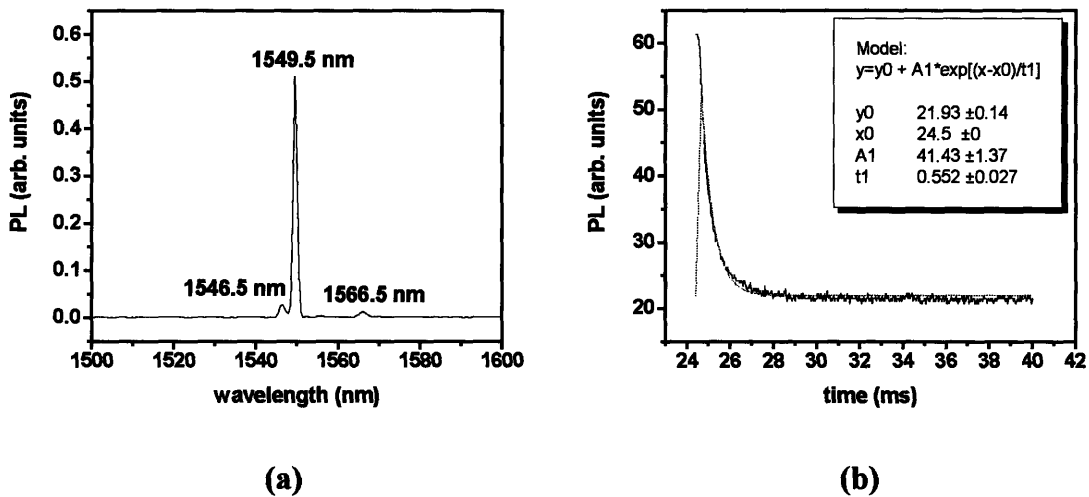


Fig. 3.10. (a) 4 K PL profile of Er₂O₃ powder. (b) 4 K lifetime decay of $\lambda = 1549.5\text{ nm}$ PL peak.

Figure 3.11 shows the 4K PL profile of Er₂O₃ powder in the visible spectrum. We observe emission lines at 540 nm and 560 nm, and a lower intensity $\sim 685\text{ nm}$ peak, characteristic of the ${}^4H_{11/2} \rightarrow {}^4I_{15/2}$ (540nm, 560 nm) and ${}^4S_{3/2} \rightarrow {}^4I_{15/2}$ ($\sim 685\text{ nm}$) transitions.

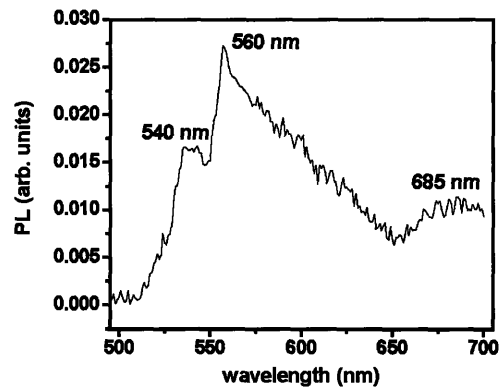


Figure 3.11. 4 K PL profile of Er_2O_3 powder in the visible spectrum.

3.5 Sputtered Er_2O_3 Thin Films: Results and Discussion

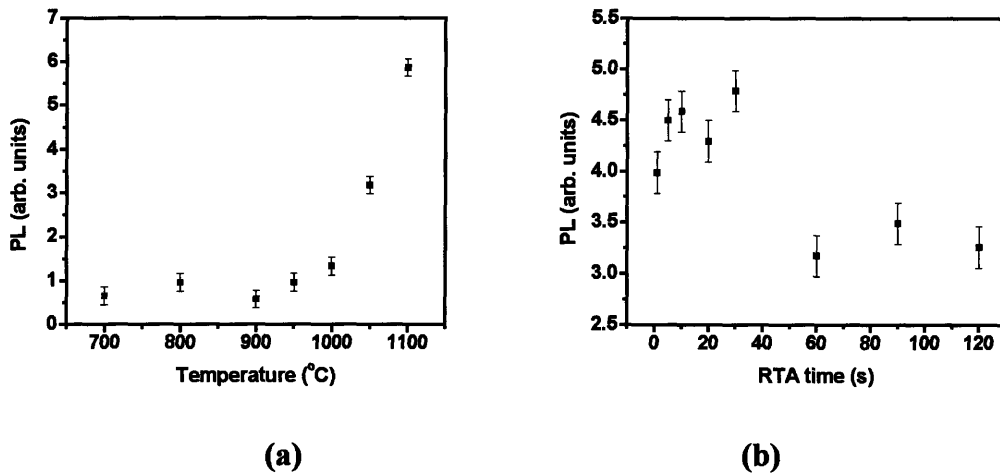


Fig. 3.12. (a) Plot of spectrally integrated PL versus temperature for $t=1$ hour anneals. (b) Plot of spectrally integrated PL versus time for $T=1050^\circ\text{C}$ anneals. Samples were annealed in a Rapid Thermal Anneal furnace under forming gas ambient.

Previous results[66] show high temperature Er_2O_3 thin film anneals of $1050\text{--}1100^\circ\text{C}$ produce higher room temperature photoluminescence (PL) than low temperature anneals of 650°C . RTA annealed (see Fig. 3.12.a) samples showed a monotonic rise in room temperature PL, with our highest RTA anneal at $T=1100^\circ\text{C}$. At 1050°C , anneals for different times showed a decrease in luminescence for samples

annealed longer than $t=60$ s. This possibly suggests a diffusion-limited process that possibly results in Er-Er clustering and subsequent optical deactivation. Such observations have been made for annealing temperatures $> 1000^\circ\text{C}$ for Er-implanted SiO_2 and Si_3N_4 glasses[35]. Comparison of RTA samples versus furnace annealed samples revealed RTA annealed samples to be 1.5-2 \times brighter. TEM results (see below) suggest this to be due to the RTA process resulting in a rapid cooling of the annealed sample, resulting in the quenching of metastable phases and subsequent increase in PL. We study one such RTA ($T=1050^\circ\text{C}$ for $t=30$ s) anneal-enhanced light-emitting sample.

3.5.1 Low Temperature Study Reveals Three Optical Centers

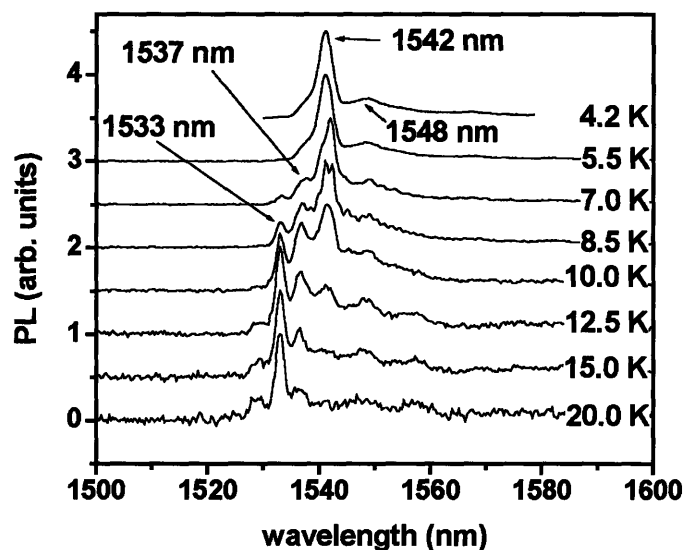


Fig. 3.13. Photoluminescence of Er_2O_3 films at different temperatures. All spectral profiles are normalized with respect to their peak intensities (in order to plot all the profiles within one graph).

PL emission from the RTA annealed thin film was measured at low temperature in order to remove phonon mediated non-radiative processes and resolve the nature of radiative transitions taking place in this system. A complex spectral behavior was

observed between 4.2 and 20 K (see Fig. 3.13). At 4.2 K, PL intensity is dominated by a peak located at 1542 nm; as the temperature is raised above 7.0 K, this peak intensity rapidly decays, and two new peaks at 1537 nm and 1533 nm resolve above the 1542 nm peak background. 4.2 K lifetime measurements at the three wavelengths are summarized in Table 3.3. The lower intensity of the 1537 and 1533 nm peaks, compared to the 1542 nm peak, may suggest these peaks represent hot lines[4,73] from the same Er atomic site.

In the case of the spectral scans in Fig. 3.13, the 1542 nm peak may correspond to a transition from the bottom of the of the first excited state $I^{13/2}$ manifold to the bottom of the ground state $I^{15/2}$ manifold; and the 1533, 1537 nm peaks may correspond to hot line transitions from thermally populated higher manifold levels in the first excited $I^{13/2}$ state, to the bottom of the ground state $I^{15/2}$ manifold. However, if the 1533 and 1537 nm transitions occurred from the same Er optical center (i.e. atomic site), their lifetimes would be comparable to the 1542 nm transition. We observe (see Table 3.3) that the 1542 nm peak has a 7 ms lifetime, whereas the 1533 and 1537 nm peaks have sub-ms lifetimes.

λ (nm)	4K Lifetime (ms)	Cooperative upconversion (cm^3/s)	Apparent Density of Er (cm^{-3})	Phase
1537	0.5	1.5×10^{-17}	5×10^{22}	BCC
1542	7.0	7.7×10^{-18}	1.6×10^{21}	FCC
1533	0.8	-	-	HCP

Table 3.3. Assignment of 4 K lifetime, 4 K cooperative upconversion coefficient, apparent density and crystal phases of Er_2O_3 thin films. Cooperative upconversion coefficient and density could not be computed for the 1533 nm phase.

We conclude that the 1533 and 1537 nm peaks are luminescence transitions from a different Er optical center than the 1542 nm peak.

The observation of a 7 ms lifetime in Er_2O_3 is a surprising discovery, contrary to popular expectations[1] of cooperative upconversion being a lifetime-killing process. This is the first critical piece of evidence suggesting the possibility of acquiring gain from Er_2O_3 . The sub-ms lifetimes associated with the 1533 and 1537 nm peaks are more consistent with a severely cooperative upconversion-reduced lifetime assumption (as observed with the Er_2O_3 powder). Pump powers used to acquire these lifetime measurements at 4 K were on the order of 50-100 mW.

If the 1533 and 1537 nm peaks are not hot lines for the 1542 nm emission, the question remains as to why they have lower PL intensity. At this point we make two interpretations: (i) these two optical transitions have a lower volume fraction than the number of Er optical centers emitting at 1542 nm; and/or (ii) the measured sub-ms

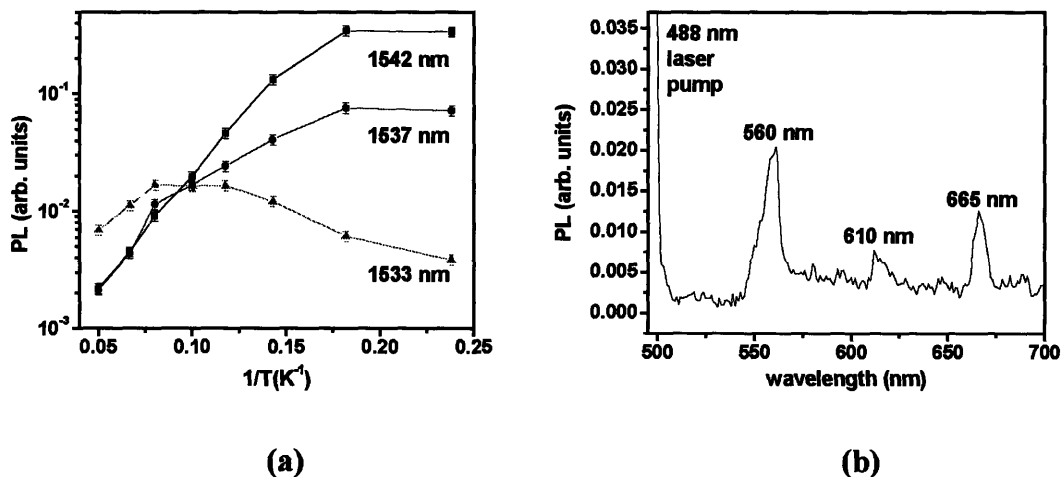


Fig. 3.14. (a) Peak intensity versus temperature at $\lambda=1533, 1537, 1542$ nm. (b) Visible PL emission from Er_2O_3 at 4K, consistent with the results of Kasuya et al.[71].

lifetime is not purely radiative, confirming the presence of a competing non-radiative temperature-independent de-excitation process, such as cooperative upconversion. We resolve this question shortly.

Fig. 3.14.a compares the peak intensities of all three centers versus temperature on an Arrhenius plot. Peak intensities were determined by Gaussian fits to the PL spectra (at each temperature) of Fig. 3.13, Gaussian fits were done in order to remove peak overlap and resolve individual peak intensities. Fig. 3.14.a summarizes the fitted peak intensities; we observe a monotonic decrease in peak intensity of the 1542 nm and 1537 nm optical centers, but the intensity of the 1533 nm optical center increases, which might suggest it to be a hot line of the 1537 nm optical center.

However, the 20 K spectral profile (Fig. 3.13) shows the 1537 nm luminescence to be *lower* than the 1533 nm luminescence: this is not behavior characteristic of hot lines (see section 2.4.1 for hot line spectral characteristics). The rapid relaxation of an Er atom within the first excited $I^{13/2}$ state manifold implies the population of higher energy levels within this manifold, is controlled by an Arrhenius type Boltzman factor. The population of hot line transitions is thus always lower than the principal transition (i.e. the transition from the bottom of the first excited $I^{13/2}$ state manifold to the bottom of the ground $I^{15/2}$ state manifold). The dominance of the 1533 nm PL peak for temperatures greater than 20 K clearly implies this emission comes from an optical center that is distinctly different from the 1537 nm center.

We thus conclude that our Er_2O_3 films have at the very least three distinct optical centers. We suggest the observed increase in the 1533 nm PL peak intensity with

temperature (Fig. 3.14.a) may be due to an unforeseen temperature dependent energy migration mechanism[4] from the 1537 nm optical center.

3.5.2 Energy Migration and the Rapid Quench of the 7 ms Optical Center

The increase in the 1533 nm optical center's PL intensity with increasing temperature may be a very important explanation for the sudden quenching of the 1542 nm long lifetime by $T \sim 20$ K. $T = 20$ K corresponds to a thermal energy of 1.53 meV; even if phonons with this energy are available, they nonetheless provide inefficient multi-phonon de-excitation of the 1542 nm optical center, which corresponds to an energy gap of 804 meV between the first excited state ${}^4I_{13/2}$ and the ground state ${}^4I_{15/2}$. We observe a far lower rate of PL intensity decay with increasing T for Er in the Corning reference Sample 7 (data from Fig. 3.6.a), it is therefore unlikely that within an insulator environment (such as Er_2O_3), direct phonon de-excitation can account for this sudden quenching of light from the 1542 nm optical center. What Fig. 3.14.a may imply, however, is that the ~ 1.53 meV phonons provide enough energy matching to help transfer the 1542 nm optical center's energy, by non-radiative energy transfer, to the 1533 nm optical center. The 1533 nm optical center corresponds to an energy gap of 808.9 meV between ${}^4I_{13/2}$ and ${}^4I_{15/2}$; this is an energy mismatch of $808.9 \text{ meV} - 804 \text{ meV} = 4.9 \text{ meV}$. It is therefore more likely the ~ 1.53 meV phonons can bridge this energy mismatch. Lastly, the sub-ms lifetime of the 1533 nm PL peak then suggests this energy, once transferred from the 1542 nm optical center to the 1533 nm optical center, is rapidly quenched by a temperature-independent non-radiative process—and the most likely candidate for this would be cooperative upconversion.

If we could therefore remove the 1533 nm optical center, we might preserve the 1542 nm optical center's 7 ms lifetime to a reasonable >ms value at room temperature.

3.5.3 Absorption Versus Luminescence

Fig. 3.14.b shows the visible range PL profile of sputtered Er_2O_3 . Consistent with the first Er_2O_3 luminescence results reported by Kasuya et al.[71], we observe emission peaks at 560 nm and 655 nm. We also observe a lower intensity peak at 610 nm; we are unsure what this transition represents.

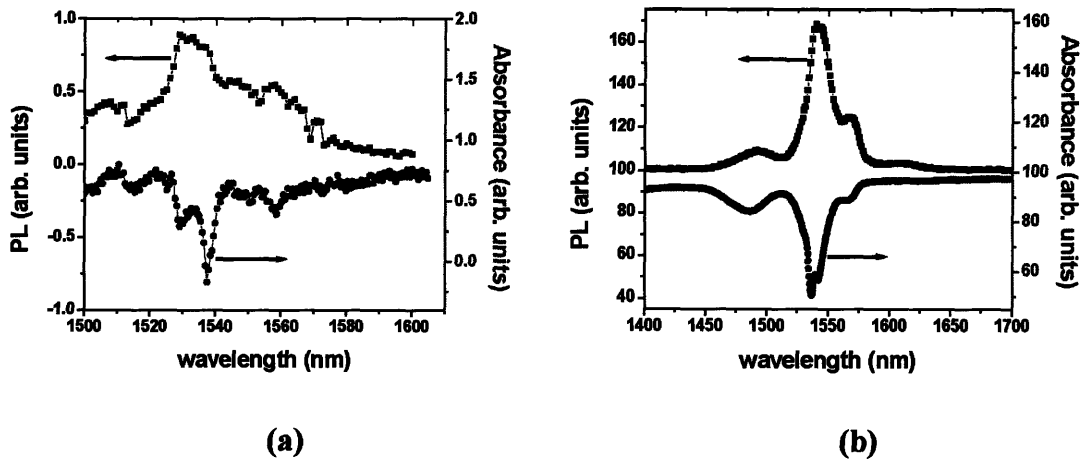


Fig. 3.15. Room temperature absorption versus luminescence for (a) an Er_2O_3 thin film and (b) the Er-doped Corning reference (Sample 7).

Fig. 3.15 compares room temperature PL and absorption profiles for Er_2O_3 (Fig. 3.15.a), versus the Er-doped Corning reference Sample 7 (Fig. 3.15.b)). Unlike the Er-doped glass system (used in fiber amplifiers), the Er_2O_3 thin film absorption profile lineshape does *not* closely match its PL spectral lineshape. Absorption peaks are located at 1530 and 1537 nm, whereas luminescence peaks are located at 1530, 1533 and 1537 nm(Fig. 3.15.a). This discrepancy can be explained by assuming presence of a majority

phase corresponding to the 1537 nm optical center, and it is this phase whose majority by volume dominates the room temperature absorption profile.

The room temperature luminescence profile, dependent on the concentration of optical centers having a high radiative efficiency rate, will have a different lineshape if: (a) the 1537 nm optical center majority phase has a poor radiative efficiency, and (b) there exists a minority phase corresponding to the 1533 nm optical center, which has a higher radiative efficiency.

3.5.4 Er₂O₃ Powder: Confirming the BCC Phase

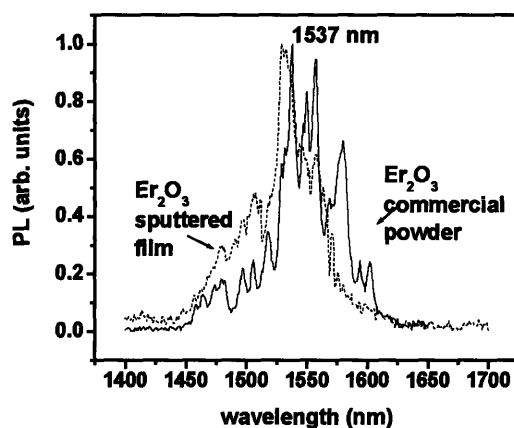


Fig. 3.16. Overlap of room temperature PL profile for Er₂O₃ powder and sputtered thin film. The overlap indicates the 1537 nm optical center in sputtered Er₂O₃ corresponds to the BCC crystal phase commonly seen in the powder sample.

The decrease in room temperature PL for Er₂O₃ powder (see Fig. 3.16) at wavelengths just below 1537 nm, in comparison to the Er₂O₃ thin film, shows that the 1533 nm peak is not present in the room temperature PL for Er₂O₃ powder, while the 1537 nm and a new 1530 nm peak are present in the room temperature PL for both powder and thin film. We conclude that the room temperature 1530 nm PL/absorption

peak is a hot line from the 1537 nm optical center, and that the 1537 nm room temperature optical center corresponds to the BCC phase making up Er_2O_3 powder (giving a first confirmation towards hypothesis (a) & (b) from 2.5.3). The apparent higher room temperature PL intensity of the 1533 nm peak in the thin film (see Fig. 3.15.a), versus the 1537 nm PL peak, is due to spectral overlap with the 1530 nm peak.

Further, the close match in 4 K lifetime of the Er_2O_3 powder (0.5 ms), and the sputtered film's 1537 nm optical center, gives a second confirmation that the 1537 nm peak corresponds to the BCC phase commonly observed in Er_2O_3 powder.

With Fig. 3.15, Fig. 3.16 and lifetime measurements establishing the 1537 nm optical center as belonging to a majority volume phase, we conclude that the explanation for the lower PL intensity of the 1533, 1537 nm peaks, is best explained not by section 2.5.1's interpretation (i) (lower volume fraction of the 1533 and 1537 nm optical centers), but rather interpretation (ii): a competing non-radiative temperature-independent de-excitation process is reducing the radiative efficiency of these optical centers at 4 K. And this process is most likely the cooperative upconversion energy promotion process.

3.5.5 Optical Center Volume Fractions and Crystal Phases

Comparison of 4 K luminescence (Fig. 3.13) versus room temperature absorption intensities (Fig. 3.15) of the Er_2O_3 thin film and the Corning Sample 7 reference—where the reference is doped with an accurately known optically active concentration of Er—allows us to determine quantitatively the number of 1537 and 1542 nm optical centers per unit volume (see apparent density in Table 3.3).

Because the Er_2O_3 thin film's 1542 nm optical center dominates PL spectra at 4 K, comparison of this 4 K integrated PL spectrum versus the 4 K integrated PL spectrum of the Corning reference, determines the concentration of emitting 1542 nm optical centers.

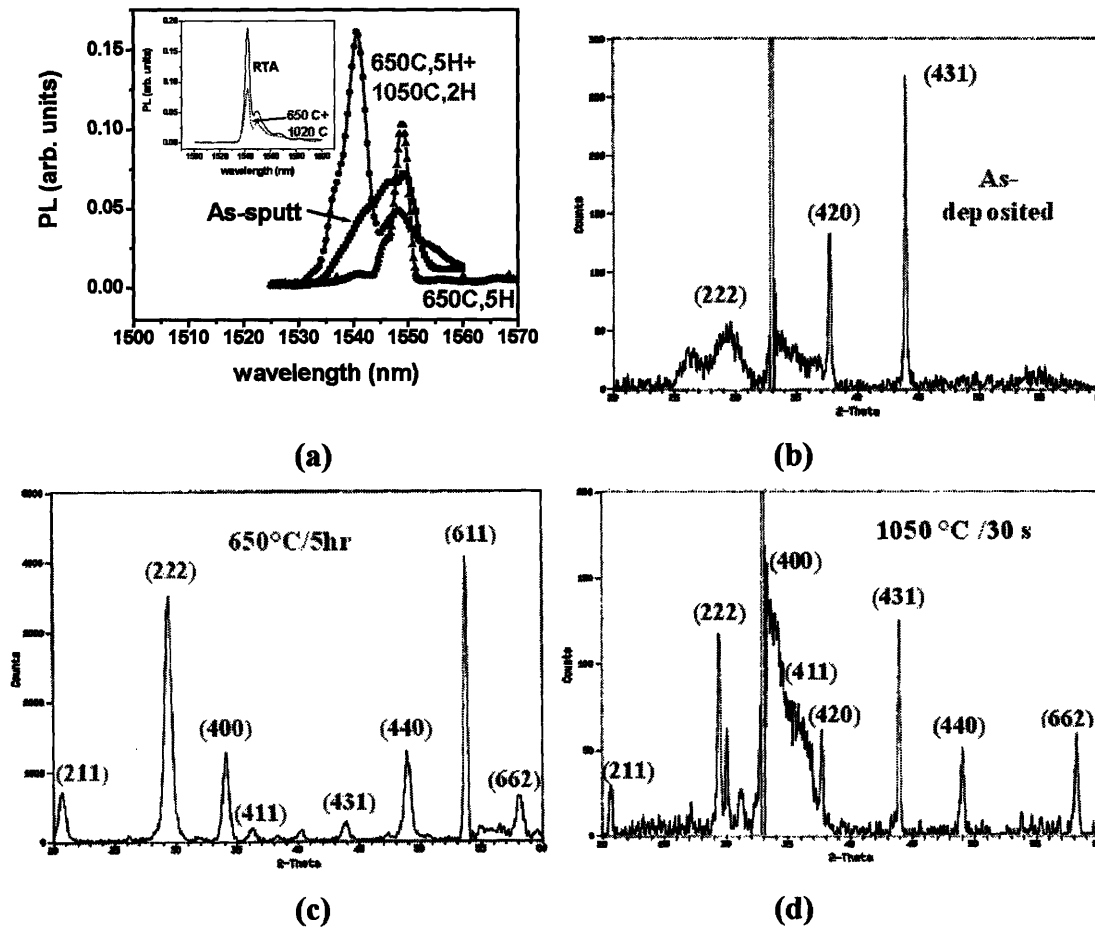


Fig. 3.17. (a) 4 K Photoluminescence of Er_2O_3 thin film as-sputtered, after a low temperature anneal and after a hybrid low + high temperature anneal. Inset: comparison of PL intensity of 30 s RTA annealed sample versus hybrid low + high temperature anneal sample. Corresponding X-ray diffraction scans: (b) as-sputtered Er_2O_3 thin film, (c) low temperature 650 °C anneal, and (d) high temperature 1050 °C anneal.

Because the 1537 nm optical center dominates room temperature absorption in the Er_2O_3 thin film, comparison of this integrated absorption spectrum versus the integrated

absorption spectrum of the Corning reference, determines the concentration of absorbing 1537 nm optical centers. Table 3.3 lists these concentration calculations as apparent densities for the 1537 and 1542 nm optical center phases: the lower computed density of the 1542 nm optical centers is due to this phase being a minority volume within the thin film; the actual 1542 nm optical center phase's atomic density should be on the order of 10^{22} cm^{-3} , as reported for all known phases of Er_2O_3 in the literature[74,75]. Therefore the more accurate quantitative analysis is to examine the ratio of these apparent densities, which is equivalent to the ratio of the volume fraction of the 1542 nm phase versus the 1537 nm phase.

From this ratio we conclude that roughly 3% of the Er optical centers in this Er_2O_3 thin film correspond to the 1542 nm emission peak. X-ray diffraction (see Fig. 3.17) indicates the majority phase in these films to be the thermodynamically stable body-centered cubic (BCC) phase found in the commercial Er_2O_3 powder sample. Metastable FCC and HCP phases are observed to crystallize as a result of the high temperature anneal; the FCC phase has been well documented in thin film literature[74]. We make a tentative assignment of the 3 crystal phases alongside the observed 4 K lifetimes in Table 3.3.

3.5.6 The Effect of Annealing on Recrystallization

Comparison of 4 K PL spectra versus X-ray diffraction (see Fig. 3.17.a) conclusively shows as-sputtered films have an inhomogeneously broad PL emission peak centered at 1550 nm and a low BCC phase crystallinity(Fig. 3.17.b). This is consistent with the observation of 1549.5 nm PL peak emission (at 4 K) from the Er_2O_3 powder (Fig. 3.10.a). The PL peak linewidth narrows after a low temperature 650°C anneal and forms

more crystalline BCC phase (Fig. 3.17.c). A high temperature 1050°C anneal introduces minority HCP and FCC crystal phases (Fig. 3.17.d) and gives rise to the high intensity PL peak at 1542 nm.

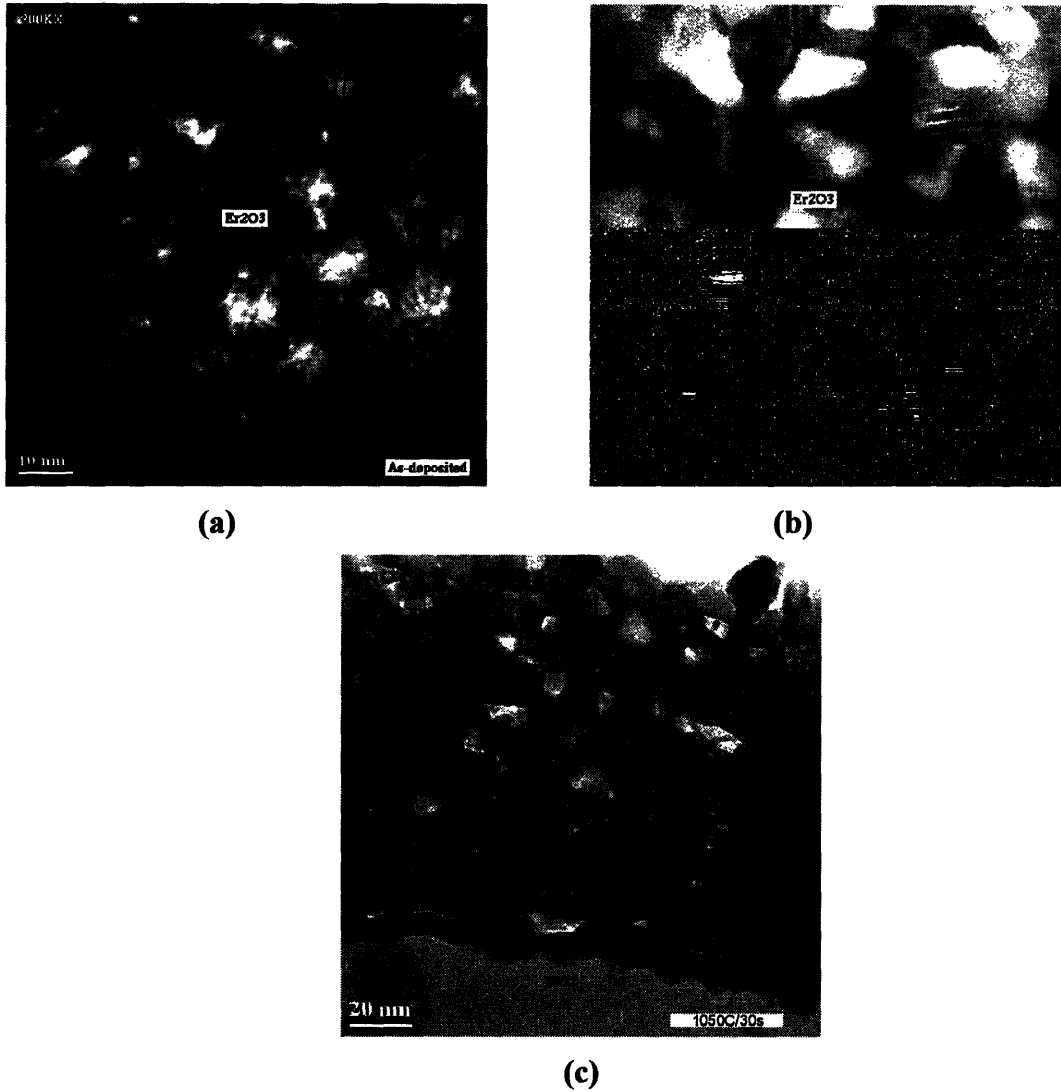


Fig. 3.18. Transmission electron microscopy of (a) as-sputtered Er_2O_3 thin film, (b) low temperature 650 °C anneal, and (c) rapid thermal anneal at 1050 °C.

We also observe that after high temperature annealing of the sputtered Er_2O_3 thin films, PL emission from the 1550 nm peak diminishes (see Fig. 3.17.a) while the majority volume crystal phase with the most intense X-ray diffraction peaks is the BCC phase. At

the same time, our room temperature absorption measurements on these Er_2O_3 thin films correlate the 1537 nm site with the majority phase. Room temperature PL of the Er_2O_3 powder (Fig. 3.16) shows us both the 1537 and 1550 nm emission peaks belong to the majority BCC phase. The BCC phase has been observed under Zeeman effect spectroscopy[75] to have two distinct Er^{+3} sites. High temperature 1050°C annealing possibly results in structurally relaxing BCC phase Er from the as-sputtered 1550 nm emitting Er^{+3} site to a thermodynamically more stable 1537 nm emitting Er^{+3} site.

TEM analysis shows as-sputtered Er_2O_3 thin films to be a mix of amorphous and crystal grains(see Fig. 3.18.a). Low temperature (650°C) annealing results in a growth of grain size(Fig. 3.18.b); X-ray diffraction confirmed these larger grains to be the BCC phase (Fig. 3.17.c).

High temperature (1050°C) two hour (not shown) and 30 s RTA annealing (Fig. 3.18.c) produce a fully crystalline volume comprised of smaller sized crystal grains; grain size appears to be the same for these two high temperature anneals, suggesting a high nucleation rate inhibits the later stage grain growth characteristic of the low temperature anneal. The observation of no grain coarsening with the two hour anneal sample (versus the 30 s anneal sample) further suggests the diffusion coefficient for the Er_2O_3 molecule is very low.

We observe (see Fig. 3.17.a, inset) higher luminescence from the RTA 30 s anneal sample than a sample with a hybrid anneal (a low temperature 650°C pre-anneal for 6 hours, followed by a high temperature 1050°C anneal for 2 hours) history. We conclude that the larger grain size (i.e. larger bulk crystal yield), resulting from a low temperature anneal, does not improve luminescence. Luminescence rather increases after

a high temperature anneal, which correlates with the formation of metastable FCC and HCP phases (see Fig. 3.17.d). The observation that an RTA anneal further improves luminescence, suggests the rapid thermal anneal results in a more effective metastable phase quench during post-anneal cooling down, thus yielding a larger volume fraction of FCC and HCP phases. We tentatively suggest the FCC phase to be connected with the 7 ms 1542 nm optical center, given the FCC phase's higher oxygen coordination number about Er; this is discussed in the next section.

3.5.7 Cooperative upconversion in Sputtered Er_2O_3

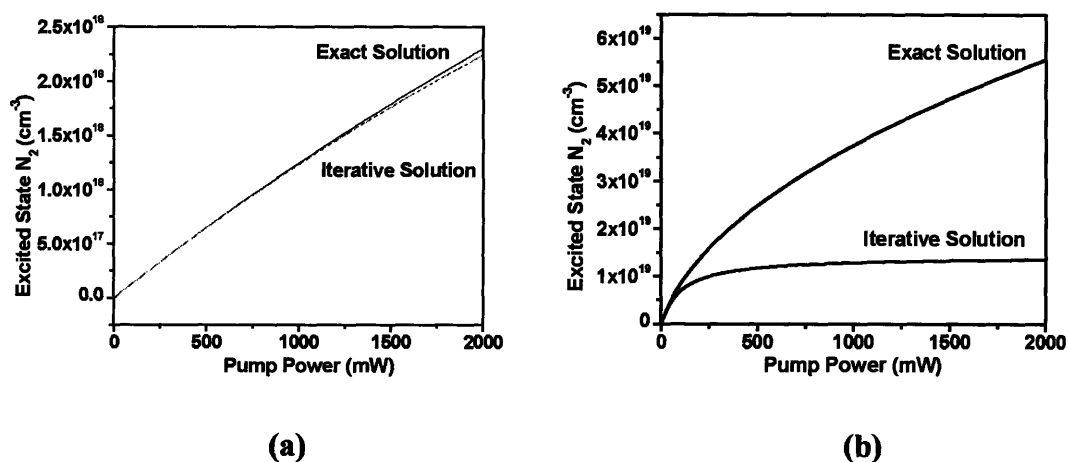


Fig. 3.19. Deviation in calculation of excited state population N_2 in the presence of cooperative upconversion, using an exact solution versus an iterative solution, (a) for Corning reference Sample 7, and (b) for sputtered Er_2O_3 . (Using an assumed cooperative upconversion coefficient of $10^{17} \text{ cm}^3/\text{s}$ for both case (a) and (b).)

In order to evaluate Er_2O_3 (RTA annealed sample) as a material candidate for an ultra-high gain amplifier, we compute the cooperative upconversion coefficient for its majority 1537 nm phase and minority 1542 nm phase, (see Table 3.3). In the limit of low pump power, the cooperative upconversion rate of Er-Er de-excitation can be first-order approximated by Eqn. (2.7). This expression for lifetime is approximated by the

observation in Eqn. (2.6) that the cooperative upconversion rate may be defined as $C_{24}N_2$; it is this quantity that competes dynamically in Eqn. (2.6) against the spontaneous emission rate $1/\tau$, for de-excitation of the excited state population N_2 . Setting $C=0$ in Eqn. (2.6) and solving for the steady state solution of N_2 , we find:

$$N_2 = N \frac{W_p}{W_p + \frac{1}{\tau}}.$$

(3.8)

In the limit of low pump power fluxes ($W_p \ll 1/\tau$) we approximate $N_2 \approx NW_p\tau$ and substitute this cooperative upconversion-free low-power flux expression for N_2 into the dynamic expression (2.7) for de-excitation from the excited state:

$$\frac{1}{\tau_{net}} = \frac{1}{\tau} + CN_2 \approx \frac{1}{\tau} + CNW_p\tau.$$

(3.9)

This is an iterative approximation using the linear pumping regime expression for N_2 . We evaluate its accuracy by comparing the exact steady state N_2 solution of Eqn. (2.6) (see chapter 2 for details about this expression)),

$$N_2 = \frac{-(W_p + \frac{1}{\tau}) + \sqrt{(W_p + \frac{1}{\tau})^2 + 4NC_{24}(W_{13})}}{2C_{24}}$$

(3.10)

with the solution N_2 determined when we substitute expression (2.9) into the spontaneous emission term $1/\tau$ in the denominator of Eqn. (2.8), i.e.

$$N_2 = N \frac{W_p}{W_p + \frac{1}{\tau} + CNW_p\tau}.$$

(3.11)

We study the divergence in expression (3.10) versus (3.11) for Er optically active concentrations of $N=1\times 10^{20} \text{ cm}^{-3}$ (for the Corning Sample 7 reference, see Fig. 3.19.a) and $N=1\times 10^{22} \text{ cm}^{-3}$ (for the sputtered Er_2O_3 film, see Fig. 3.19.b). The two plots in Fig. 3.19 show that for an assumed cooperative upconversion coefficient value of $\sim 10^{17} \text{ cm}^3/\text{s}$, in the case of the Corning reference, Eqn. (3.11) is very close to Eqn. (3.10) over pump powers ranging from 0 to 2 W. For this assumed cooperative upconversion coefficient, in the case of the sputtered Er_2O_3 sample, a divergence between Eqns (3.11) and (3.10) occurs for pump powers exceeding $\sim 100 \text{ mW}$. Hence the applicability of expression (3.11) should be limited to pump powers $< 100 \text{ mW}$. However, for this low range of pump powers, insufficient data points were initially collected (see inset of Fig. 3.20). We note that for the highest pump power of 2 W, the worst-case divergence in Fig. 3.19.b (i.e. at

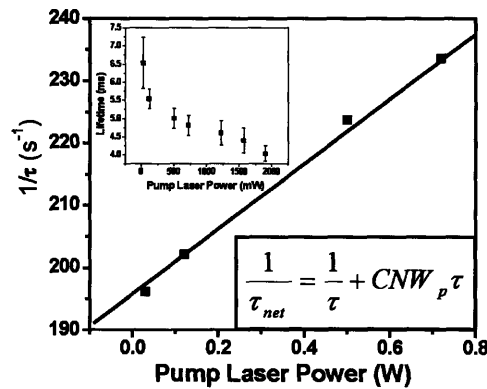


Fig. 3.20. 4 K cooperative upconversion coefficient calculation for Er_2O_3 FCC phase (1542 nm PL peak). Plot of $1/(\text{lifetime})$ versus pump power. Fitted linear slope derives an approximate value for the cooperative upconversion coefficient. Inset: plot of lifetime at 4 K as a function of Ar-ion pump power.

2 W pump power) is a factor of $\sim 6\times$. Therefore, we went ahead and applied expression (3.11) to experimentally measured 4 K lifetime versus pump power data, bearing in mind that our fitted cooperative upconversion coefficient may be as much as a factor of $6\times$ smaller than the actual value.

We fit expression (3.5) to the data of $1/\tau_{\text{net}}$ versus pump power, at 4 K (see Fig. 3.20). Since the atomic density of the FCC and BCC phases must be comparable, a value of 5×10^{22} Er/cm³ (the apparent BCC phase density listed in Table 3.3) was used for calculating the cooperative upconversion coefficient C for both phases; the results are listed in Table 3.3.

Cooperative upconversion for the 1537 nm BCC phase is found to be comparable to the SiO₂:Er system with [Er]= 10^{20} cm⁻³. The potential $\sim 6\times$ correction may account for this result, given that difference in Er-Er distances will be on the order $(10^{22}/10^{20})^{1/3} \cong 4.6\times$. In addition, at doping concentrations $>10^{20}$ cm⁻³, Er atoms tend to cluster together in SiO₂ glass hosts[1]. The resulting increase in Er atom-atom proximity gives SiO₂:Er upconversion coefficient values larger than what would be observed with a homogeneous distribution. Calculated values of clustering proximity[76] are within a factor of ten compared to Er-Er nearest neighbor distance in Er₂O₃[77].

As a relative comparison, we can more accurately conclude that the FCC phase has a lower cooperative upconversion coefficient than the BCC phase. We attribute this lower cooperative upconversion value to correlate with a more effective screening of nearest neighbor Er atoms in the FCC phase, due to a higher oxygen coordination number about the Er atom. The coordination number of a BCC and FCC phase are 8 and 12,

respectively; experimental studies of the large lattice parameter BCC phase have further established the presence of two oxygen vacancies, lowering the oxygen coordination number to 6[75,77]. The smaller lattice parameter and higher atomic packing factor of the FCC phase[74] implies less accommodation of such non-stoichiometry, supporting our hypothesis of a larger FCC oxygen coordination number. We conclude that the optimum Er_2O_3 material for an amplifier application would be a 100 % volume fraction yield of the 7 ms lifetime metastable FCC phase.

3.5.8 Population Inversion Calculation

We performed a population inversion calculation with these computed cooperative upconversion coefficients, using the steady-state derivation for population inversion of a three level system with upconversion (see chapter 2). In a single mode waveguide structure (dimensions $1.5 \times 1.5 \mu\text{m}^2$) comprised of an Er_2O_3 core, we determined that a $\lambda=980$ nm pump power of 3.5 W will maintain a population inversion of $\Delta N=1.25 \times 10^{20} \text{ Er/cm}^3$ in the BCC majority phase Er_2O_3 ; and a pump power of 450 mW will maintain this same population inversion in a waveguide core comprised purely of the metastable FCC phase. A population inversion of $\Delta N=1.25 \times 10^{20} \text{ Er/cm}^3$ corresponds to a gain coefficient of 3.0 dB/cm, which is approximately the upper gain coefficient limit realizable in commercial EDFAs. If a total pump power of 900 mW can be efficiently coupled into a pure FCC phase waveguide core, we can even achieve a gain coefficient as high as 30 dB/cm. The pump power for the highest gain 3.0 dB/cm EDFAs is ~ 100 mW, which is almost a factor of ten lower than 900 mW. Thus, while the FCC phase is an optimal candidate for ultra-high Er-based gain, promising a factor of ten

higher small signal gain than state of the art EDFAs, it will have comparable gain efficiency per unit length.

	Pump Power	Small Signal Gain	Gain Efficiency in 1 cm device
BCC phase	3.5 W	3.0 dB/cm	8.6×10^{-4} dB/mW
FCC phase	450 mW	3.0 dB/cm	0.0067 dB/mW
FCC phase	900 mW	30 dB/cm	0.033 dB/mW
EDFA	100 mW	3.0 dB/cm	0.03 dB/mW

Table 3.4. Summary of small signal gain and gain efficiency calculations.

3.6 Chapter Conclusion

We examined a new material system with $\sim 10^{22}$ Er/cm³ in order to evaluate its performance as an ultra-high gain Er-amplification based medium. We conclude that cooperative upconversion remains a critical impediment against achieving more than 1% population inversion, with the thermodynamically stable BCC crystal phase. Cooperative upconversion calculations show this gain-limiting effect to perhaps be comparable to commercial EDFAs doped $\geq 10^{20}$ cm⁻³. Alternatively, a 7 ms lifetime at 4K indicates cooperative upconversion is not as serious a problem as originally imagined for the FCC metastable phase. We attribute the quenching of this lifetime for temperatures above 20 K to be attributed to phonon-mediated energy transfer mechanisms in the co-existing HCP phase, as suggested by the Arrhenius profile of the 1533 nm optical center in Fig. 3.14.a.

We conclude that for a ($\lambda=980$ nm) pump power of 900 mW, a single waveguide core, comprised solely of the long lifetime FCC metastable phase, will yield a 30 dB/cm gain coefficient. This gain coefficient is a factor of ten higher than the best commercial

EDFAs, indicating the FCC phase may be the most suitable Er_2O_3 candidate for ultra-high gain, while retaining the same gain efficiency as state of the art EDFAs.

With Er and Er_2O_3 being CMOS-compatible materials, the 7 ms lifetime of FCC Er_2O_3 promises to be a powerful candidate for ultra-high microphotonic gain (i.e. for a pump power of 900 mW, 30 dB/cm gain: a 3.0 dB gain within a 1000 μm length scale). However we were unable to optimize FCC phase volumetric yield beyond 3%, by any obvious modulation of sputtering parameters. Considerable work must be further pursued in order to determine if it is at all possible to isolate this non-equilibrium crystal phase.

Chapter 4:

Adjustable Refractive Index Materials for Er-doped Si Microphotonic Amplifiers



**13-4124. The PL lab I was in charge of,
10/1999–05/2004.**

“You have to invert the data from the oscilloscope. So the risetime is actually the decay time.” –a forgotten warning from Dr. Michal Lipson (Post-Doctoral Associate, EMAT), 3.5 years ago...

“We should put dry pumps on all the high vacuum systems.” –Dr. Anat Eshed (Post-Doctoral Associate, EMAT)

4.1 Chapter Abstract

Si_3N_4 and SiON materials have been investigated as host systems for Er doping, however past work has limited itself to spectra and lifetime studies of Er in these materials. Further, most of the studies samples involved Er ion implantation into CVD-grown hosts.

We extend this investigation into Er co-sputtered films, and in addition to lifetime and spectral studies, we perform PL measurements to determine clustering properties in the host material, measure of Er-Er cooperative upconversion, optical pump absorption cross-section, and optical gain.

Our results show the nitride environment is better at inhibiting clustering and upconversion, and provides a dramatically $10^5\times$ higher pump absorption cross-section (in the form of an unidentified host material sensitizer, which we hypothesize to be some form of Si-based nanocrystals) than the oxide environment. Unfortunately, the nitride environment also has an unexplainably high materials loss at the signal wavelength, as a result of which net gain is not possible with our grown $\text{Si}_3\text{N}_4\text{:Er}$ film.

Our SiON:Er co-sputtered film appears to partake of the best of both worlds, having the low signal propagation losses characteristic of an oxide environment while at the same time have the high absorption cross-section, low upconversion characteristic of the nitride environment.

We report experimentally fitted gain versus pump power data, from which we extrapolate small signal gain coefficient values for co-sputtered SiON:Er and $\text{Si}_3\text{N}_4\text{:Er}$.

We fit a 14 dB/cm gain against a background host material loss of 37 dB/cm in SiON:Er and 23 dB/cm gain against a background host material loss of 122 dB/cm in Si₃N₄:Er.

Cumulative measurements suggest the 37 dB/cm host material loss in SiON:Er is likely due to clustered Er from an excessively highly doped sample. We suggest repeating these measurement with a lower concentration Er co-sputtered sample, once the VSL gain apparatus used for measurements has been re-fitted with a higher pump power source, in order to collect a high density of gain coefficient measurement in the gain saturation region of a gain versus pump power plot.

We make some suggestions concerning further experiments to perform on the Si₃N₄:Er samples in order to identify the large source of loss at signal wavelength. Lastly, we conclude Er co-sputtered Si₃N₄ has produced the shortest Er radiative lifetime reported in this material to date; however, temperature dependent non-radiative mechanisms reduce this lifetime by $1/0.2=5\times$ at room temperature.

4.2 Introduction

Silicon oxide (SiO₂) and silicon nitride (Si₃N₄) are two ubiquitous material systems used in Si processing, and when combined to process a waveguide core and cladding, allow us to engineer high index difference waveguides over the range $\Delta n=0.1-0.765$. We investigate the feasibility of Er light emission in these materials, using the SiO₂:Er systems as our reference investigation against which to compare SiON:Er and Si₃N₄:Er photoluminescence data and optical gain measurements. We do this materials study using the sputtering Physical Vapor Deposition process.

To date, there is very little published work on Er light emission from Si_3N_4 or SiON materials, by either CVD or PVD deposition processes. Polman, Eaglesham, Poate et al.[11] made the first report of Er PL emission from ion-implanted CVD Si_3N_4 at Bell labs in 1991. They concluded higher anneal temperatures were required to optically activate implanted Er in Si_3N_4 versus SiO_2 , and that while Er ion-implanted SiO_2 annealed above 900°C showed a degradation in the concentration of light-emitting Er, no degradation was observed in Er ion-implanted Si_3N_4 ; lastly, a room temperature Er lifetime of 7 ms was observed. While Polman et al acknowledged the final application of this study towards evaluating $\text{Si}_3\text{N}_4:\text{Er}$ as a material candidate for optical amplification, no follow-up work was pursued. Chaumont, Chelnokov, Plowman et al[78][79][80] reproduced these results once again by Er ion-implantation in CVD-grown materials and demonstrated loss modulation, but not net gain, in SiON:Er waveguides in 1995.

Since then Bell, Nunes and Zanatta[81] have explored the light emission of Er in sputtered Si_3N_4 . They reported non-resonant pump excitation of Er in sputtered Si_3N_4 [81], and postulated this to be due to an unknown energy transfer mechanism in the host material[82]. However, no lifetime measurements for the Er infra-red (IR) emission were reported in this sputtered film work. After this initial work only Zanatta has pursued further research, but with a shifted interest in these materials towards studying green light emission at Er concentrations (grown by co-sputtering with Si_3N_4) close to 10 atomic %[83][84][85].

There have been no experimentally reported results on Er co-sputtered SiON materials.

Prior to the report of Si nanocrystals as efficient light emitters in the 700-900nm wavelength range[86] and their possible application as sensitizers (a sensitizer is an intermediate absorption center which transfers optical pump power to the Er atoms with greater efficiency; the historically most common sensitizer for Er in EDFAs has been the Yb atom) for Er excitation, sputtered materials work in SiO₂:Er was minimally explored, with one published report by Solomon et al[87] on 2 ms room temperature Er lifetime in Er co-sputtered SiO₂ films. Since the discovery of nanocrystals, sputtering has become one of several deposition methods being actively explored to grow Si-rich SiO₂:Er[88][89][90][91][92].

But no further work has resumed on studying Er IR emission and optical gain measurements in Si₃N₄:Er, sputtered or otherwise.

In this work we return to Polman's original 1991 study, and continue from there, investigating the reproducibility of his Er-implanted studies in SiO₂ and Si₃N₄, but this time looking at Er co-sputtered thin films of SiO₂ and Si₃N₄. In addition, we also examine the light emission properties of Er co-sputtered in SiON thin films, seeking to match and extend the optical characterization work of Chaumont et al on Er in such materials.

We studied the applicability of sputtering for growing these samples because as PVD process, sputtering requires no substrate heating, thus removing overhead complexity in potential integration of a PLC with a microelectronic chip. But more importantly, as a physical vapor deposition non-equilibrium process, sputtering may help to minimize the Er steric clustering effect observed[93] in CVD-based glasses.

We investigate Er-doped waveguide core material host with a refractive index on the order of $\Delta n \sim 0.1-0.75$ higher than an SiO₂ waveguide cladding, i.e. SiON:Er with

index $n_2 \sim 1.6$ (at $\lambda = 1533$ nm) and $\text{Si}_3\text{N}_4:\text{Er}$ with index $n_2 \sim 2.2$ (at $\lambda = 1533$ nm). These films are sputtered by both Ar/O₂ reactive and conventional Ar magnetron sputtering.

The principal advantage of high deposition rate Ar/O₂ reactive or conventional Ar sputtered SiON and SiO₂/Si₃N₄ films, respectively, is the absence of hydrogen (H) incorporation in the thin films. Plasma Enhanced Chemical Vapor Deposition, a widespread high deposition rate tool, produces H-incorporated SiON films, with an N-H bond absorption band in the 1.55 μm wavelength range [94,95].

Secondly, we have shown reliable reproducibility of refractive index control in reactively sputtered SiON films (see Fig.1)[96], as a function of the Ar/O₂ (10% O₂) gas flow rate.

Thirdly, the choice of sputtering allows for doping of Er by co-sputtering, thus avoiding the costly process of ion implantation while optimizing the amount of overlap between a homogeneous Er profile and the guided light mode.

Efficient operation of a waveguide optical amplifier relies on two critical constraints: (i) low optical loss both in the waveguide core bulk and at the core-cladding interface, in order to ensure net gain is greater than zero; and (ii) a long spontaneous emission lifetime from the Er atom at room temperature, to allow population inversion for low pump powers. Given the upconversion gain limitation of the Er atom[93] at concentrations in excess of 10^{20} Er/cm³, we have until now approximated a potential upper limit on Er based gain (using literature values for Er absorption and emission cross-sections in SiO₂[6]) of ~ 3 dB/cm. Thus, we require losses due to criterion (i) must have a

cumulative value significantly less than 3 dB/cm, in order to realize a waveguide amplifier with net gain.

4.3 Experimental Procedure

RF magnetron sputtering was used to deposit 0.3-0.5 μm thick films of Er-doped SiO_2 , SiON and Si_3N_4 . The SiO_2 and Si_3N_4 films were sputtered using Ar gas with SiO_2 and Si_3N_4 targets, respectively. The SiON films were grown both by reactive sputtering of a Si_3N_4 target using an Ar/ O_2 (10%) gas, and by co-sputtering of the SiO_2 and Si_3N_4 targets using Ar gas. In all cases, Er doping was done by co-sputtering a metal Er target at low target powers in order to ensure doping concentrations on the order of 1% atomic fraction. Sputtering was done in a Kurt-Lesker UHV sputter system (see chapter 3 Experimental section for details), with a base pressure of $1\text{-}5 \times 10^{-8}$ torr.

Film thickness was measured by profilometry and refractive index was measured by both ellipsometry and prism coupler measurements. Optical loss in the films was measured by a modified prism coupler measurement detecting scattered light decay as a function of distance. Er dopant concentrations were determined by Rutherford Back-Scattering.

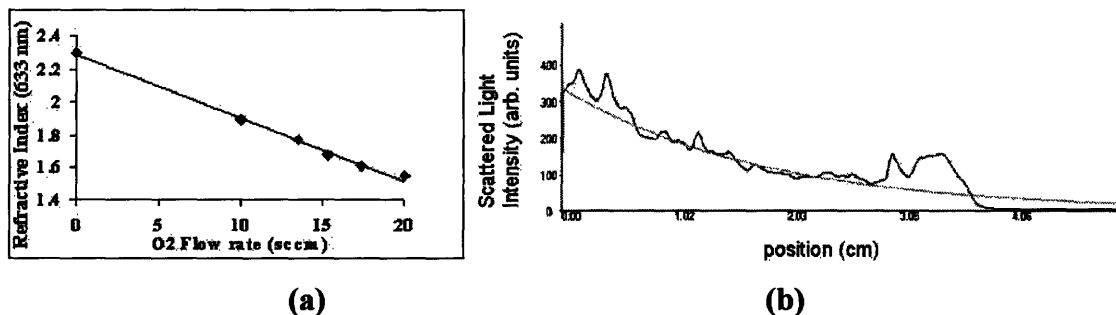


Fig. 4.1 (a) Adjustable control of refractive index for reactively sputtered SiON films, as a function of Ar/ O_2 (10% O_2) gas flow rate[99].

Fig. 4.1.a demonstrates the robust reproducibility of sputtered film refractive index[99] achieved in with our sputter system. Error bars are within the size of the data points. Fig. 4.1.b is a characteristic raw data scan of the light intensity decay of a propagating 1-D slab mode of light within the SiON and Si₃N₄ thin films. By measuring the decay as a function of position within a modified prism coupler, we are able to decay a propagation loss exponential decay coefficient to this data and thus estimate the material loss per unit length in our films.

Room temperature, 4 Kelvin (K) photoluminescence (PL) intensity and lifetime measurements were done in an Oxford Instruments liquid helium cooled cryostat, using a mechanically chopped Ar ion 488 nm laser as the excitation source. PL intensity was collected using a Spex spectrometer and liquid nitrogen cooled Hamamatsu photo-multiplier tube. In order to quantitatively compare our acquired PL emission from SiO₂:Er, SiON:Er and Si₃N₄:Er—three samples with different indices of refraction—we re-normalized collected PL emission data with respect to a refractive index based extraction efficiency for the fraction of PL emission which can escape from these high refractive index film into free space air,

$$\eta_{film} = \eta_{Re\ flection} \eta_{Total\ Internal\ Re\ flection} = \left(1 - \left(\frac{n_{film} - n_{air}}{n_{film} + n_{air}} \right)^2 \right) \times \left(1 - \sqrt{1 - \frac{n_{air}}{n_{film}}} \right).$$

4.4 Results & Discussion

4.4.1 Photoluminescence: Room Temperature Data

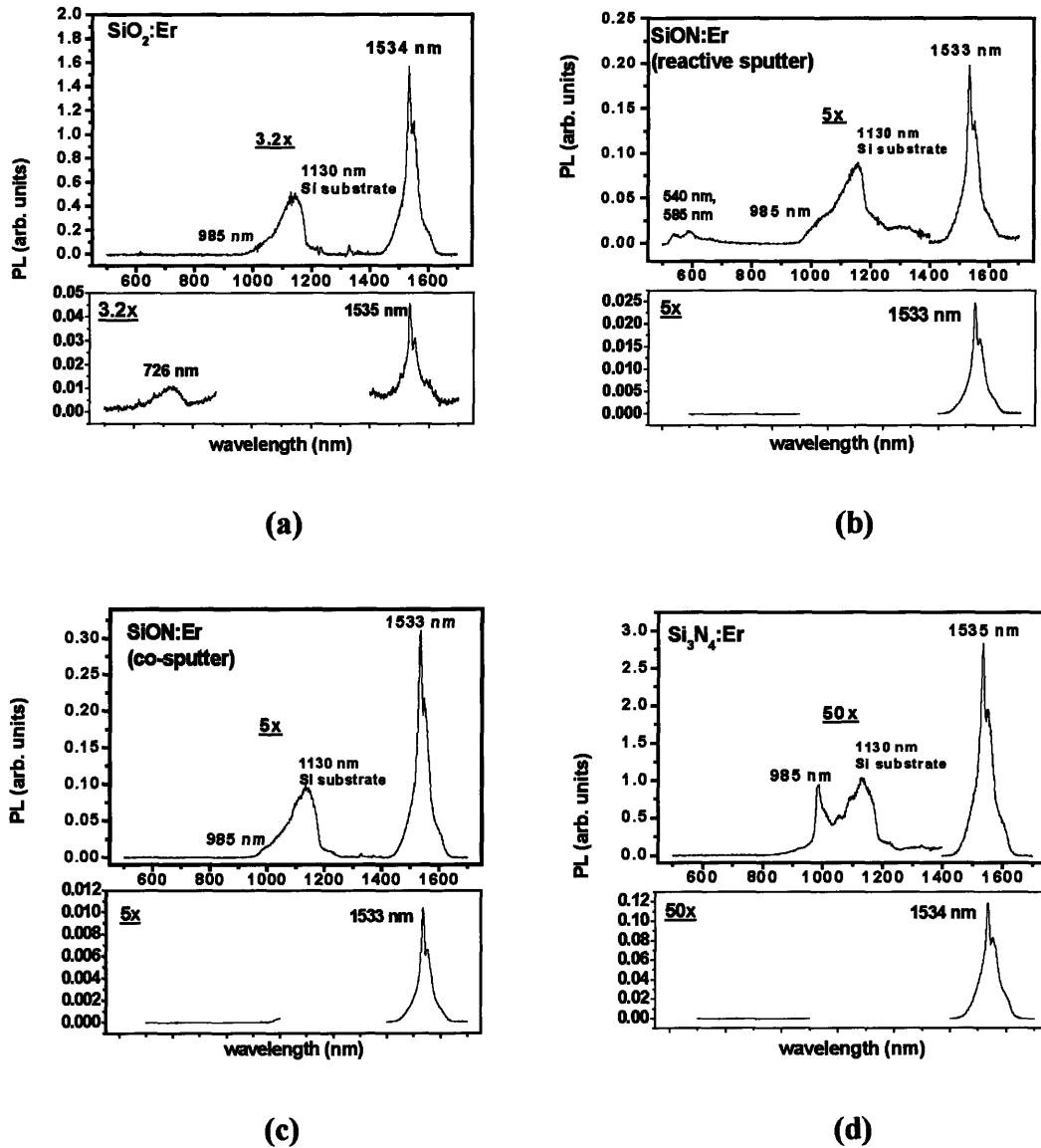


Fig. 4.2. Room temperature PL scans from visible to IR (500-1700 nm) of as-sputtered (lower plot) and $T=1000^{\circ}\text{C}$ (for $t=1$ hour) annealed (upper plot) thin films of (a) $\text{SiO}_2:\text{Er}$ (b) $\text{SiON}:\text{Er}$, reactively sputtered, (c) $\text{SiON}:\text{Er}$, co-sputtered, and (d) $\text{Si}_3\text{N}_4:\text{Er}$. Data in the visible spectral range has been magnified by factors listed. All data has been renormalized with respect to Er concentration, film thickness, and luminescence extraction efficiency.

We studied the optical properties of Er doped (by co-sputtering) in four different thin films: (i) SiO₂:Er deposited by Ar sputtering, (ii) SiON:Er (with refractive index 1.6) deposited by reactive Ar/O₂ sputtering, (iii) SiON:Er (with refractive index 1.64) deposited by Ar co-sputtering, and (iv) Si₃N₄:Er deposited by Ar sputtering. Table 4.1 summarizes the deposition parameters for all four samples.

Sample	SiO ₂ :Er	SiON:Er (reactive)	SiON:Er (co-sputter)	Si ₃ N ₄ :Er
Ar gas flow (sccm)	7.1	--	7.1	7.1
Ar/O ₂ gas flow (sccm)	--	13.1	--	--
SiO ₂ target power (W)	400	--	400	--
Si ₃ N ₄ target power (W)	--	400	200	400
Er target power (W)		30	14	11
Refractive index (633nm)	1.457	1.62	1.61	2.05
Refractive index (1555nm)	--	1.65	1.64	2.2
[Er] _{RBS} (cm ⁻³)	0.92×10 ²⁰	5.83×10 ²⁰	6.1×10 ²⁰	4.95×10 ²⁰

Table 4.1. Deposition parameters for the four sputtered samples. Also listed are measured refractive indices by thin film ellipsometry ($\lambda=633$ nm), refractive index measurement (for samples with an index higher than thermal oxide) by a prism coupler ($\lambda=1555$ nm), and measured Rutherford Back Scattering (RBS) Er concentrations.

Fig. 4.2 shows room temperature photo-luminescence (PL) data, collected across a visible (500 nm) to the infra-red (1700 nm), or IR, spectral range. All the data in Fig. 4.2 has been renormalized with respect to Er concentration (as-measured by RBS), film thickness (as measured by profilometry) and luminescence extraction efficiency, allowing

us to make direct comparison of measured PL intensity between the different samples. All the samples are optically pumped at $P_p=1.8$ mW ($\lambda_p=488$ nm) pump power.

There is one caveat to note: it is not possible for us to renormalize the experimentally collected data in Fig. 4.2, with respect to transmitted pump power. The refractive index mismatch between the thin film samples and air result in different power transmission coefficients T for the $P_p=1.8$ mW pump, from free space into the samples (see Table 4.2 for summary of different normal incidence transmission coefficients). The differing values of T imply less power transmits into the higher index SiON and Si₃N₄ films than the SiO₂ film. Whether the excitation model for Er in these films is a (i) trivial three-level system, (ii) such a system with cooperative upconversion, or (iii) additional unknown energy quenching mechanisms (such as excited state absorption[4], for example), results in more and more complex models relating emitted PL intensity to pump power (see for example the expression for $N_2=N_2(P_p)$ describing models (i) and (ii) in Eqns. (2.3).

Therefore, we note that the film and concentration renormalized data in Fig. 4.2, underestimates the emission of SiON and Si₃N₄ films, relative to SiO₂, for our $P_p=1.8$ mW excitation.

Despite this underestimation, we make an important observation: the PL intensity from the annealed Si₃N₄:Er film is the greatest of all the samples. We therefore conclude the annealed Si₃N₄:Er sample has a higher radiative emission rate (is a better light-emitter) than annealed SiO₂:Er and SiON:Er.

While as-sputtered thin films showed an experimentally resolvable PL intensity with good signal-to-noise ratio, annealing the samples resulted in significant PL

Sample	SiO ₂ :Er	SiON:Er (reactive)	SiON:Er (co-sputter)	Si ₃ N ₄ :Er
Deposition time (minutes)	1.457	1.62	1.61	2.05
Film thickness (nm)	--	1.65	1.64	2.2
$\lambda=488\text{nm}$ P _p transmission coefficient approximation (using $\lambda=633\text{nm}$ index values)	0.81	0.76	0.77	0.49
η_{ext} ($\lambda=1533\text{nm}$)	0.26	0.2	0.2	0.08

Table 4.2. Deposition time and deposited film thickness (measured by profilometry), estimate of normal incidence pump power transmission coefficient (at $\lambda=488$ nm) into films (using $\lambda=633$ nm measured index values from Table 4.1), luminescence extraction efficiency ($\lambda=1533$ nm), and PL peak intensity enhancement or T=1000°C annealed (t=1hour) versus as-sputtered sample.

enhancement, ranging from a $\sim 5\times$ increase for SiO₂:Er, to a $\sim 30\times$ increase for Si₃N₄:Er (see Table 4.3 for lifetime increase with anneal). The measured lifetimes for as-sputtered and annealed samples at room temperature are listed in Table 4.3. Comparing these lifetimes and the PL enhancement listed in Table 4.3, we conclude that as-sputtered SiO₂:Er is very close to being an optimized Er-light emitting system (a 10 ms lifetime is on the order of the best reported Er lifetimes in EDFA-quality SiO₂, from the literature), while as-sputtered SiON:Er and Si₃N₄:Er require relatively more thermal activation to optimize light emission.

For all the samples, except for SiON:Er (reactive) we observe an increase in lifetime and PL emission intensity with annealing. We conclude the annealing reduces host material non-radiative de-excitation mechanisms.

We note there is some green PL emission observed from the SiON:Er (reactive) reactive sample. It appears reactive sputtering preferentially increases Er-Er clustering, and is not the optimal method for growing SiON:Er; rather, co-sputtered SiON:Er is the better alternative, with a 4 K lifetime that compares with SiO₂:Er.

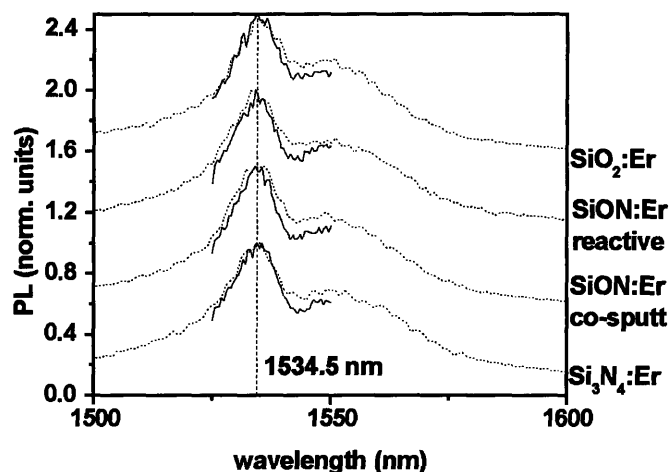


Fig. 4.3. Normalized plots of Er IR emission in the four samples. The plots are staggered and overlaid with 2 nm resolution PL scans. The negligible change in peak linewidth indicates inhomogeneous broadening.

Fig. 4.3 shows the IR emission profile from the annealed samples, normalized to peak intensity. Fig. 4.3.a overlays the four profiles and shows the Er IR emission to be effectively identical in all four hosts. The 4 K lifetime measurement of the annealed samples show similar Er lifetimes for SiO₂ and SiON, but a drastically smaller lifetime for Si₃N₄. Assuming 4 K lifetimes are an approximate measure of the radiative lifetime, we conclude the nitrogen host environment does have an effect on Er emission. However, the spectral profiles in Fig. 4.3.a, collected at a spectrometer resolution of 6 nm, are identical. The PL profile is a measure of the emission cross-section (σ_{21}) profile of Er in these host environments, and if radiative lifetimes are different for Er in Si₃N₄ versus

SiO₂, we would observe different natural linewidths for Er in these hosts. The identical linewidths suggest the Er atom is in an amorphous (glass) environment in all four samples, resulting in inhomogeneous broadening of the PL emission.

In order to confirm this, we remove spectrometer-limited resolution by reducing spectrometer slit width. The data is presented in Fig. 4.3.b, where we vertically offset the normalized 6 nm resolutions PL scans and overlay on them 2 nm resolution normalized PL scans. Spectrometer resolution below 2 nm does not show further decrease in normalized PL emission linewidth. We conclude all four samples remain in a glass state even the 1000°C anneals.

Fig. 4.4 confirms this conclusion for the Si₃N₄:Er annealed sample, showing its X-ray diffraction scan. We observe no Bragg peaks, the sample remains amorphous.

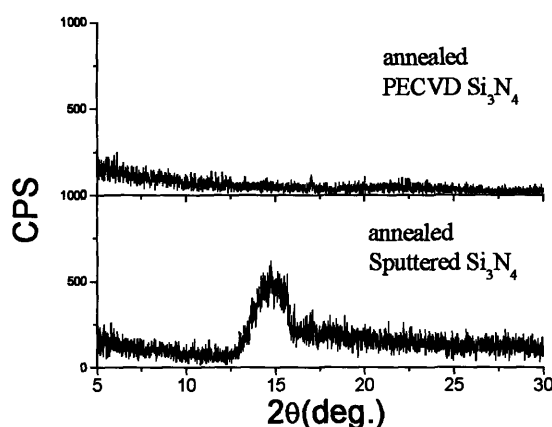


Fig. 4.4. X-ray diffraction scan of T=1000°C (t=1hour) annealed Si₃N₄:Er sample, grown by PECVD and sputtering. The emergence of a short-range order around 2θ=15° may correspond with the formation nanocrystals of some other form of an Er-sensitizer. (Data courtesy Jifeng Liu.)

	τ_{4K} (ms)		τ_{roomT} (ms)		$\eta = \tau_{roomT} / \tau_{4K}$	
	as-sputt	anneal	as-sputt	anneal	as-sputt	anneal
CVD SiO ₂ :Er	--	27	--	19	--	0.7
SiO ₂ :Er	3.79	16.6	3.3	14	0.87	0.84
SiON:Er reactive	5.08	5.24	0.8	0.48	0.15	0.09
SiON:Er co-sputtered	6.46	10.62	0.55	3.8	0.08	0.36
Si ₃ N ₄ :Er	1.02	2.4	0.54	0.487	0.53	0.2

Table 4.3. List of lifetimes (at 4K and room temperature) for SiO₂:Er, SiON:Er (reactive), SiON:Er (co-sputter) and Si₃N₄:Er samples, as-sputtered and after a T=1000°C anneal (for t=1 hour).

We conclude the optical activation required to anneal the samples still preserves a full-width-half-maximum linewidth of ~ 30 nm, and is therefore a good material for WDM gain.

The peak maxima location appears to be approximately the same for all four samples, it might be slightly red-shifted for the Si₃N₄:Er sample, with respect to the SiO₂:Er sample.

4.4.2 Photoluminescence: Thermal Activation

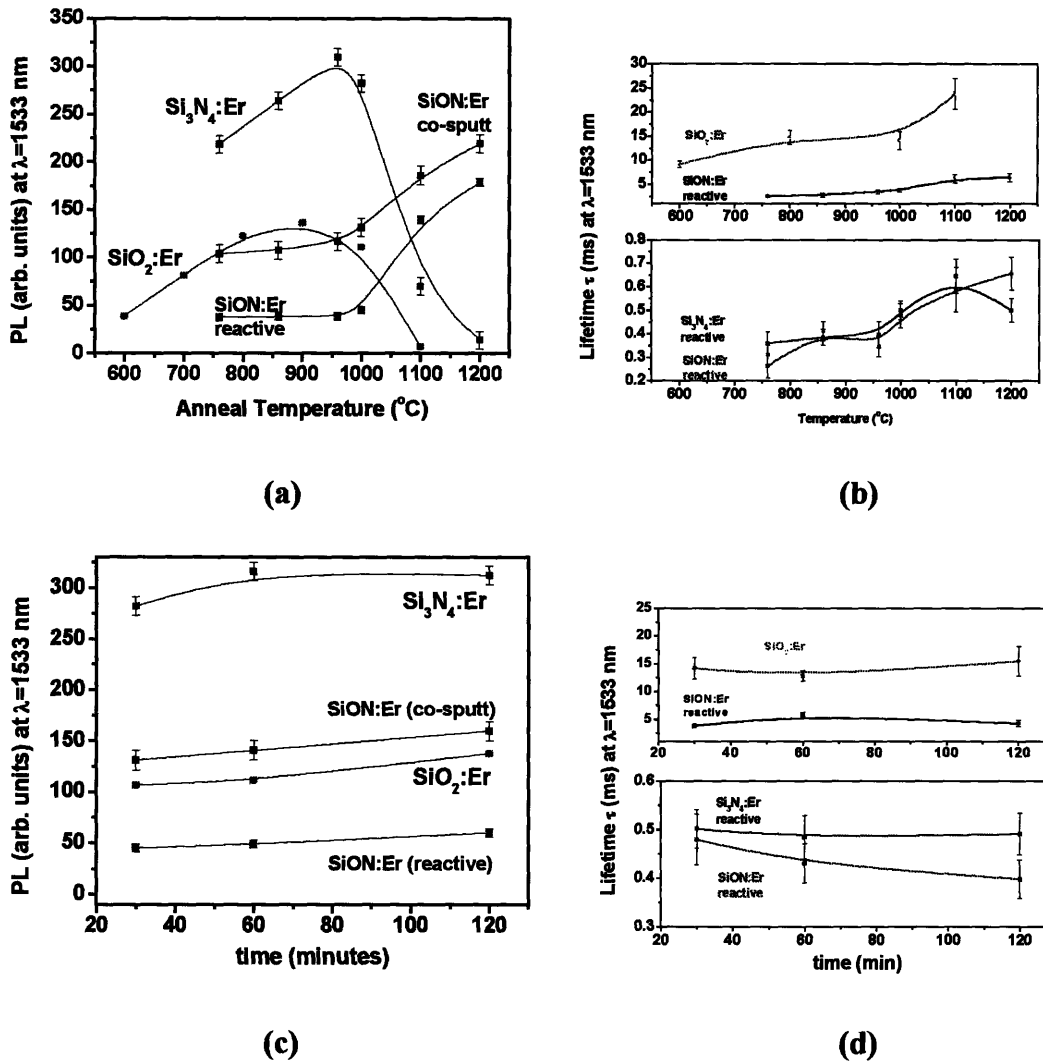


Fig. 4.5. Photoluminescence (PL), normalized to peak intensity, from sputtered $\text{SiO}_2:\text{Er}$, SiON:Er and $\text{Si}_3\text{N}_4:\text{Er}$. Peak position is at 1533 nm. (b) Plot of PL peak intensity versus annealing temperature for $\text{SiO}_2:\text{Er}$ and $\text{Si}_3\text{N}_4:\text{Er}$ samples. The lines are B-spline curves meant to guide the eye.

We observed that thermal activation by annealing was required to increase Er emission from the as-sputtered films. We studied this thermal activation by annealing (for $t=0.5$ hour) the four samples, from $T=600^{\circ}\text{C}$ to $T=1200^{\circ}\text{C}$, at temperatures spaced 100°C apart. Fig. 4.5.a plots the measured PL peak intensity, at $\lambda=1533$ nm, versus temperature.

Fig. 4.5.b plots the measured lifetime at $\lambda=1533$ nm, versus temperature. Increasing anneal temperature results in a monotonic increase of lifetime, however the PL intensity for SiO₂:Er and Si₃N₄:Er rise to a maximum value, located at a temperature T_{anneal}, listed in Table 4.4, and then decrease rapidly with increasing T. Such behavior has been similarly catalogued for Er ion-implanted samples of SiO₂, Si₃N₄, P₂O₅[11], and Er co-sputtered films of SiO₂[87] and Al₂O₃[8]. The conclusions of these studies are that the Er atoms cluster together at high anneal temperatures and optically de-activate.

The increase in lifetime despite PL intensity reduction at higher anneal temperatures is the fingerprint for this atomic process: the high temperature is not damaging the host material and its effect on Er lifetime, but rather reducing the concentration of optically active Er by de-activating the Er⁺³ light-emitting state[15] in clustering Er atoms. We have reproduced longer lifetime results than the reported Er co-sputtered SiO₂:Er from [87] and observed an even shorter radiative lifetime behavior in Er co-sputtered Si₃N₄:Er than reported for Er ion-implanted Si₃N₄:Er[11].

The higher T_{anneal} for Si₃N₄:Er versus SiO₂:Er is consistent with the higher melting temperature T_m of Si₃N₄ versus SiO₂ (Table 4.4). We expected to interpolate a similar anneal profile in Fig. 4.5.a for the two SiON:Er samples, but instead we observe drastically different behavior: PL intensity rises with annealing temperature only above a particular threshold value (which we label T_{thres} in Table 4.4), and for T>T_{thres} the PL intensity rise monotonically up to the highest furnace anneal capability we have, T=1200°C. T_{thres} for both reactive and co-sputtered SiON:Er samples is approximately the same, and T_{thres} appears to be between the T_{anneal} values for SiO₂:Er and Si₃N₄:Er.

Sample	SiO ₂ :Er	SiON:Er (reactive)	SiON:Er (co-sputter)	Si ₃ N ₄ :Er
T _{anneal}	875°C	--	--	960°C
T _{thres}	--	960°C	945°C	--
T _{melt}	1600°C	--	--	1900°C

Table 4.4. Listing T_{anneal}, T_{thres}, T_{melt} for the four study samples.

The lifetimes of reactive SiON:Er and co-sputtered SiON:Er don't have such a threshold profile (Fig. 4.5.b), thus the threshold profile for PL intensity in Fig. 4.5.b is attributed to the concentration of light-emitting Er, and not the host material's phonon density or other intrinsic materials properties. We observe that reactively sputtered Er has a lower room temperature lifetime and lower room temperature PL intensity, than co-sputtered Er. Therefore the reactively sputtered material has a larger number of non-radiative quenching mechanisms intrinsically in the host material. This conclusion may correlate with the observation of higher host material optical loss as shown in section 3.4.5.

But both SiON:Er samples have the threshold profile behavior, distinctly different from the maxima profile behavior of SiO₂:Er and Si₃N₄:Er. This suggests that both reactive and co-sputtered SiON:Er create similar nearest neighbor environments around the Er atom, and the structural re-organization (i.e. relaxation) required to activate Er into the Er⁺³ light emitting state, will have a similar T-dependent characteristic.

Why this temperature-dependent activation characteristic has a threshold type profile and not a maxima type profile, can not be fully understood from PL data alone. There are two possible interpretations. (i) A sputtered mixture of SiO₂ and Si₃N₄ results

in a structural environment that is less electropositive than SiO_2 or Si_3N_4 alone, thus Er is not optimally in its Er^{+3} charge state in as-sputtered films (the results of [28] confirm optimal Er emission occurs in the Er^{+3} charge state). The value of T_{thres} lying between $T_{\text{anneal}(\text{SiO}_2)}$ and $T_{\text{anneal}(\text{Si}_3\text{N}_4)}$ suggests that when a temperature weighted between the melting points of SiO_2 and Si_3N_4 is reached, the as-sputtered SiON experiences a structural relaxation of its SiO_2 and Si_3N_4 units, which continues to improve with increasing anneal temperature. Our anneal furnace is limited to an upper temperature limit of 1200°C . At higher temperature the SiON mixture should eventually relax to an optimum electropositive environment around Er, resulting in a maximum PL intensity.

(ii) The threshold behavior correlates with the precipitation of a sensitizer for temperatures $> T_{\text{thres}}$. As we will see below, interaction cross-section and PL studies have confirmed the presence of sensitizers in both SiON and Si_3N_4 . We do not know if the sensitization is occurring from the same physical structure in both, hence the threshold behavior of annealed SiON:Er versus the saturation behavior of annealed Si_3N_4 :Er may indicate distinctly different sensitization mechanisms.

Fig. 4.5.c and Fig. 4.5.d plot room temperature PL intensity and lifetime, respectively, for times ranging from 30 minutes to 2 hours, at an anneal temperature of 1000°C . We observe no notable increase in either PL intensity or lifetime, within error bars, for these times. We conclude the optical de-activation of Er is a temperature-dependent process that cannot increase with time at a fixed temperature anneal. Secondly, we conclude that there is a diffusion-controlled process involved in optically activating the Er atom to the Er^{+3} charge state, it occurs for time scales less than 30 minutes, at $T=1000^\circ\text{C}$.

4.4.3 Photoluminescence: Temperature=4 K Data

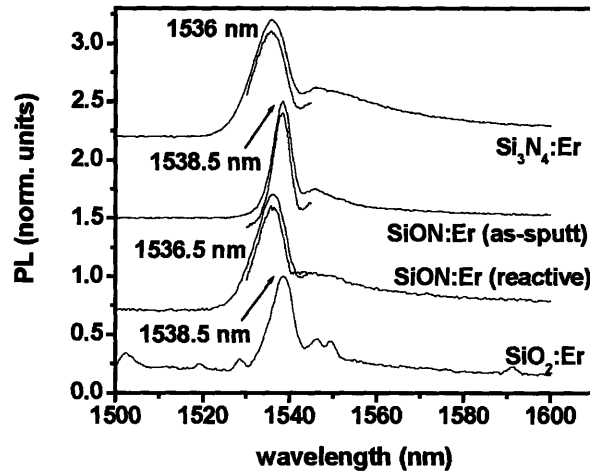


Fig. 4.6. 4K PL spectral of samples, overlaid with 2 nm resolution scans. The negligible change in linewidth confirms inhomogeneous broadening.

For completeness, we examine 4 Kelvin luminescence of the $T=1000^{\circ}\text{C}$ annealed samples, in order to remove thermal broadening. Fig. 4.6.a and Fig. 4.6.b are plots similar to Fig. 4.3, where the broad spectral scan in Fig. 4.6.b is at 6 nm resolution and the shorter range spectral scan is at 2 nm resolution. This confirms that the reported linewidth in from Fig. 4.3 is indeed due to inhomogeneous broadening (and not thermal broadening). Fig. 4.6.b shows that once thermal broadening is removed, the emission lineshapes are indeed almost identical for Er in all the four different glass environments.

The measured 4 K lifetimes for the four samples, as-sputtered and annealed, are reported in Table 4.3. We observe a short 2.6 ms lifetime for Er in Si_3N_4 at 4 K. Given the brightest PL emission from this sample, we conclude this short lifetime to represent a fast radiative emission rate.

Sputtered SiO₂:Er is our control sample for investigating the influence of a sputtered host material on the Er lifetime, by comparing PL lifetime with a chemical vapor deposition (CVD) grown host. Our CVD grown SiO₂:Er reference is an SiO₂ majority constituent glass, optimized for EDFA application by Corning. We observe that sputtered SiO₂:Er has remarkably similar performance to CVD SiO₂:Er. The CVD sample contains proprietary chemical additives to minimize Er-Er clustering at a nominally claimed concentration of 1.1×10^{20} Er/cm³. For a similar concentration of Er, sputtered SiO₂:Er, without any de-clustering additives, produces comparable lifetimes at $\lambda=1533$ nm. 10-13 ms lifetimes are the typical range achieved in the literature for Er ion implanted samples. The quantum internal efficiency, defined as the ratio of room temperature to 4 K lifetimes (we are assuming a lifetime measured at 4 K is representative of the Er atom's radiative lifetime), is similar for sputtered SiO₂:Er and the CVD sample. We conclude the sputtering process has the inherent capability to produce the optical quality requisite for an Er atom-transition based optical amplifier.

We observe both SiON:Er samples have long lifetimes at 4 K, which quench by over a factor of two at room temperature. We conclude the host matrix for reactive and co-sputtered SiON has a considerable amount of temperature dependant non-radiative de-excitation sites. Our conclusion of 2.6 ms radiative lifetime in sputtered Si₃N₄:Er contradicts the results of Polman[11], however we feel confident to attribute this 4 K measure to radiative lifetime, on account of the highest room temperature PL emission brightness of this sample, and unpublished lifetime measurements we have done on MBE-grown GaN:Er (grown by the Steckl group[97] at University of Cincinnati), where we similarly observed the effect of a nitrogen environment to result in 4 ms radiative

lifetimes and high PL brightness samples. We suggest the co-sputter process for Er-doping results in a more optimal structural location of the Er atom in Si_3N_4 , than by ion implantation. The more optimized ligand field in sputtered films results in a stronger oscillator transition strength for the Er de-excitation and hence a shorter radiative lifetime.

4.4.4 Photoluminescence: Process Map

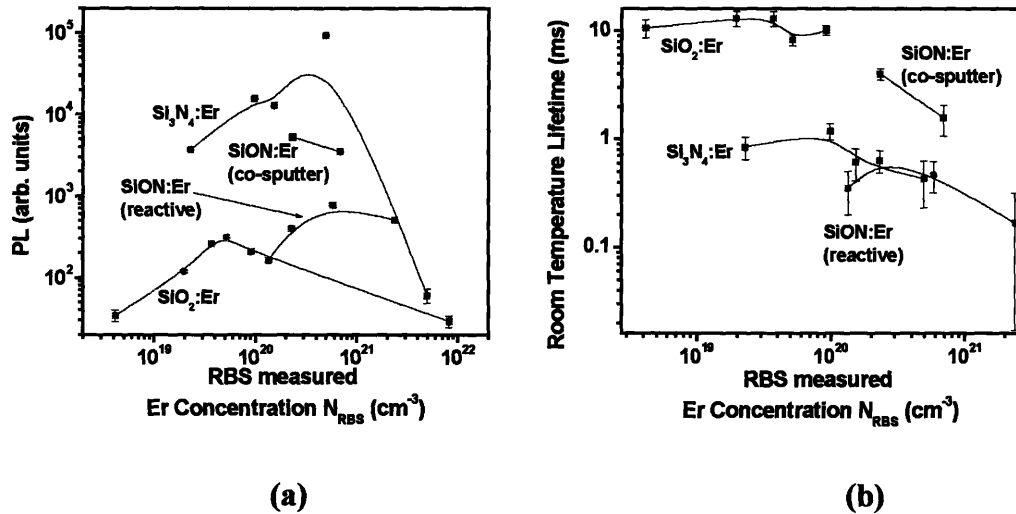


Fig. 4.7. Process Map for $T=1000^\circ\text{C}$ ($t=1$ hour) annealed sputter samples. (a) Measure of Er clustering process in different hosts. (b) Measure of Er cooperative upconversion process in different hosts. The lines are spline curves meant to guide the eye.

We conclude our PL studies with a Process Map summarizing PL emission intensity and room temperature lifetime measurements for a series of samples we grew during calibration runs, comprised of different concentrations of Er, as measured by RBS (horizontal axis). All of these samples were annealed at $T=1000^\circ\text{C}$ for $t=1$ hour. From Fig. 4.7.b we see that for this anneal temperature, room temperature lifetimes begin to show a decrease with doping concentrations greater than 10^{20} cm^{-3} . We interpret this observation as proof of the Er cooperative upconversion effect: increasing Er

concentration results in a faster non-radiative de-excitation mechanism. However, the drop in PL emission intensity in Fig. 4.7.a for these same samples happens roughly over a 10× larger range, and onsets at different Er concentrations than the process in Fig. 4.7.a. We interpret Fig. 4.7.a as a measure of the Er-Er clustering process, which results in optical de-activation and the precipitous drop in PL intensity, observed in Fig. 4.3.a.

We interpret that clustering onsets at a higher Er concentration in nitride environments than in oxide environments. Similarly, upconversion onsets at a higher Er concentration in nitride environments than in oxide environments; this conclusion is consistently supported by upconversion measurements, reported below. We thus conclude the nitride environment is better suited to hosting high doping concentrations of $\text{Er} > 10^{20} \text{ cm}^{-3}$.

4.4.5 Materials Loss Measurements

As stated in the Introduction, materials and waveguide transmission losses need to be less than the Er-based optical gain in order to achieve net gain in a WOA. We evaluate sputtered materials loss in this section, and sputtered film roughness in the next. Materials loss was measured using a prism coupler set-up that was re-fitted with a traveling fiber to measure the decay in scattered loss from a propagating slab mode of light.

	SiO_2	SiON (reactive)	SiON (co-sputter)	Si_3N_4
loss α_{material}	--	2 dB/cm	0.8 dB/cm	≥ 20 dB/cm
RMS roughness	--	1.922 nm (as-sputt)	0.256 nm (as-sputt) 0.276 nm (anneal)	0.218 nm (as-sputt)

Table 4.5. Loss measurements of propagating slab modes in Er-free films

The loss measurements for all four samples are summarized Table 4.5. We observe the lowest materials loss in co-sputtered SiON.

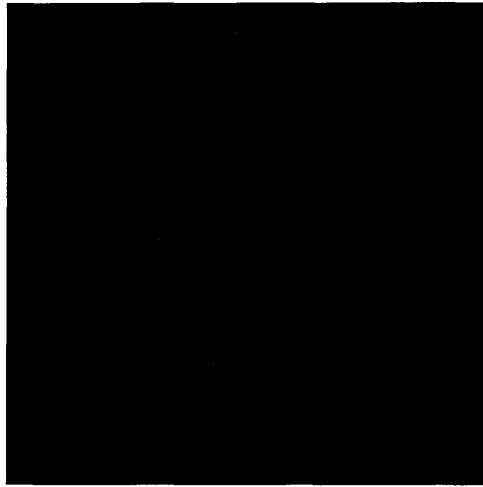
The Si_3N_4 film is observed to have prohibitively high loss values of 15-20 dB/cm. The low bulk materials loss of co-sputtered SiON:Er thus makes it a feasible sputtering candidate for a waveguide amplifier.

The higher propagation loss of SiON:Er (reactive) may correlate with its lower measured lifetimes and surface roughness, in the next section.

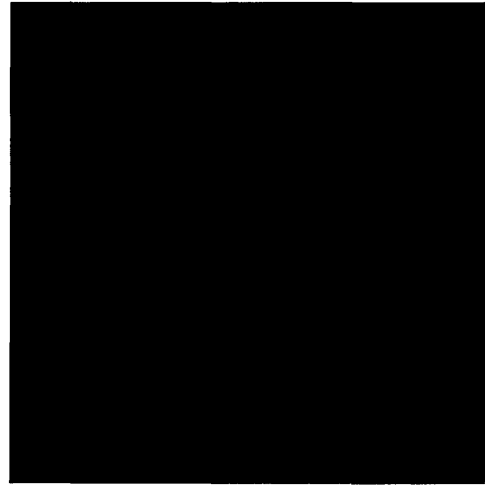
4.4.6 AFM Results

Atomic force microscopy results show a root-mean-square surface roughness values summarized in Table 4.5. We observe that reactively sputtered SiON:Er is very rough, and we hypothesize this roughness may correlate the sputter-deposition morphology of this film. The Ar-sputtered Si_3N_4 :Er and SiON:Er (co-sputter) films have sub-nm (experimental AFM detection limit) roughness. After a $T=1000^\circ\text{C}$ ($t=1$ hour), the co-sputtered SiON retains its roughness value.

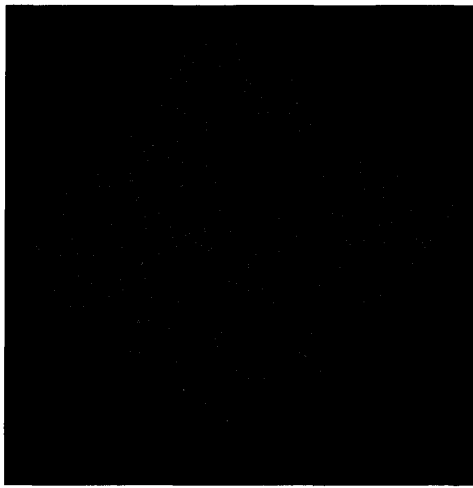
A possible explanation for the higher roughness morphology of reactive deposition may be due to the formation of clustered SiON constituents during the chemical reaction of O_2 with Si_3N_4 at the Si_3N_4 target; or, higher energy imparted to the SiON species may initiate Volmer-Weber islanding[98] during deposition on the SiO_2 substrate and thus a rough film morphology. In contrast, Ar-sputtered deposition is a more non-equilibrium process, resulting in better wetting of the SiON mixture to the SiO_2 substrate.



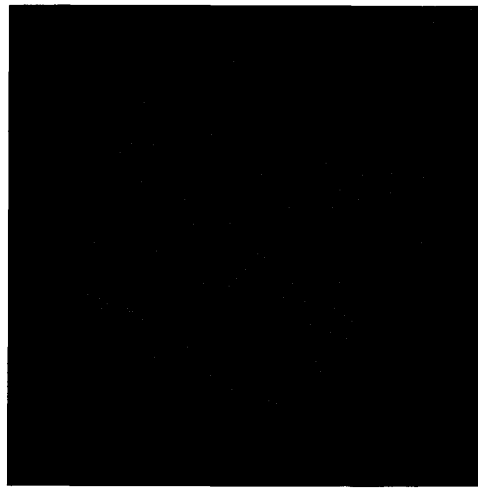
(a)



(b)



(c)



(d)



(e)



(f)

Fig. 4.8. AFM. (a) Si₃N₄:Er, as-sputtered (b) SiON:Er reactive, as-sputtered (c) and (e) SiON:Er co-sputter, as-sputtered (d) and (f) SiON:Er co-sputter, annealed.

We conclude the Ar-sputtered samples can be used to process waveguide cores with smooth core/cladding interfaces and thus potentially low waveguide scattering loss.

4.4.7 Optical Pump Absorption Cross-Section Measurement

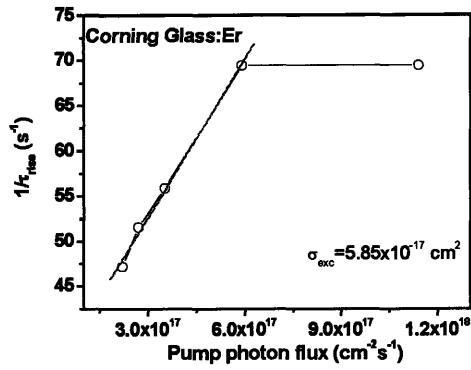
In order to model material gain from an Er-doped system, we need to acquire experimental measurements of room temperature lifetime τ , doped Er concentration N ,

(1) the pump absorption cross-section σ_p (referred to as σ_{13} in chapter 2), which tells us for a given pump power P_p , what is the optical excitation rate W_p of the Er atoms;

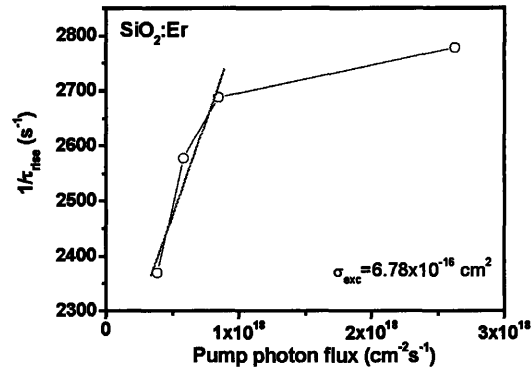
(2) the upconversion coefficient C_{24} , which tells us (alongside lifetime τ) for a given pump power P_p , how much of the excited state population N_2 is available for optical gain; and

the stimulated emission cross-section for the signal gain, σ_{21} . The lifetimes τ we have already measured above. We now devised a series of experiments to determine σ_p and C_{24} , where our choice of pump wavelength would be an Ar ion laser, $\lambda_p=488$ nm. We did not have the experimental facilities to determine σ_{21} , however the well documented literature values for σ_{21} in SiO₂-based hosts[32] and the exhaustive study of Er atomic transitions[28] allow us to make a theoretical prediction of σ_{21} in SiON:Er and Si₃N₄:Er with reasonable confidence.

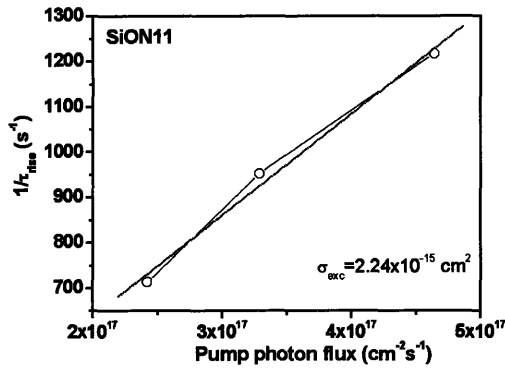
We proceed with the experimental analysis to determine σ_p at $\lambda_p=488$ nm, as acquired from Er IR emission lifetime measurements.



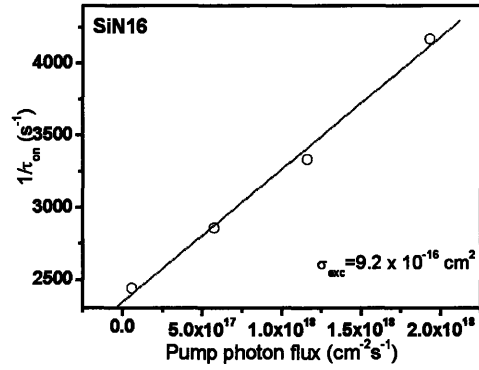
(a)



(b)



(c)



(d)

Fig. 4.9. Optical pump cross-section σ_p measurements determined from plotting PL risetime versus pump photon flux, for (a) the Corning reference sample, (b) $\text{SiO}_2\text{:Er}$, (c) SiON:Er , (d) $\text{Si}_3\text{N}_4\text{:Er}$. (Data acquired courtesy of Jae Hyung Yi and Dr. Luca Dal Negro, MIT.)

Fig. 4.9.a-d plots experimental measurements of PL risetime and decay time, as collected by an oscilloscope. At low pump power (low pump photon flux) the solution of the Er excited-state (N_2) differential equation,

$$\begin{aligned} \frac{dN_1}{dt} &= -W_{13}N_1 - W_{12}N_1 + W_{21}N_2 + \frac{1}{\tau} N_2 \\ \frac{dN_2}{dt} &= W_{12}N_1 - W_{21}N_2 - \frac{1}{\tau} N_2 + W_{13}N_1 - (C_{24}N_2^2) \\ N_3 &= N - N_1 - N_2 \approx 0 \end{aligned}$$

(see chapter 2 for definitions of the variables) can be solved with the omission of upconversion ($C_{24} \approx 0$), in which case the transient solution, subject to an initial condition of turning the optical pump P_p on at $t=0$ (i.e. $W_{13} \neq 0$) and the steady-state solution

$$N_2(t \rightarrow \infty) = N \frac{W_{13} + W_{12}}{W_{13} + W_{31} + \frac{1}{\tau} + W_{12} + W_{21}}$$

(see Eqn (2.3) for details) results in a solution of the form

$(N_2(t \rightarrow \infty))(1 - \exp(-t / \tau_{rise}))$, where $\frac{1}{\tau_{rise}} = \phi_p \sigma_p + \frac{1}{\tau}$. ϕ_p is the pump photon flux

(photons/cm²/s) and σ_p is the pump absorption cross-section. Solving the excited-state differential equation for the initial condition of $P_p=0$ (turning the optical pump off), and steady state condition $N_2(t \rightarrow \infty)=0$, results in decay solution $(N_2(t=0) \exp(-t / \tau_{decay}))$,

where $\frac{1}{\tau_{decay}} = \frac{1}{\tau}$. Thus, we have the relation

$$\frac{1}{\tau_{rise}} = \phi_p \sigma_p + \frac{1}{\tau_{decay}}.$$

(4.1)

Fitting the rise time τ_{rise} and decay time τ_{decay} from the experimental data, we plot Fig. 4.9 for the four samples, and acquire the absorption cross-section σ_p (at pump wavelength $\lambda_p=488$ nm) from the plotted slopes. The cross-section results are listed in Table 4.6.

The cross-section for absorption of 488nm light by the Er atom in an SiO₂ host has been reported to be 3×10^{-21} cm²[5]. We observe that the Corning donated SiO₂:Er sample has a significantly higher cross-section, due to *sensitizing* proprietary additives (the most common reported sensitizer is Yb co-doping in SiO₂:Er-based EDFAs[1])

which act as intermediate absorption centers for the λ_p , absorbing pump photons at a significantly higher cross-section and transferring the excited energy to the Er atom by non-radiative mechanisms[4]. The $\sim 10^{-17}$ cm² value for this sample's cross-section is consistent with reported values for commercially used sensitizers[93]. More importantly, the vertical-axis intercept to this data fit yields a decay lifetime of 22 ms, in close consistency with our measured room temperature lifetime, as reported above.

Absorption cross-section measurements on the SiO₂:Er sputtered sample, however, showed significant noise; it was hard to accurately resolve risetime modification with pump power, outside an error bar. In fitting a straight line to the acquired data (Fig. 4.9.b), we measured a vertical axis intercept for decay time of 0.4 ms, a significant error in comparison to the experimentally measured decay time of 14 ms. We attribute this error due to the combination of (i) significant mechanical chopper wobble at the low 4 Hz chopper rate required for resolving ~ 10 ms lifetimes, with (ii) very weak changes in risetime (due to the very low value of σ_{21} in SiO₂:Er), thus resulting in a risetime decrease versus pump power which can not be resolved above the chopper wobble noise. We thus conclude cross-section measurements from this data are not accurate, and list the aforementioned literature reported value[5] in Table 4.6.

The sputtered SiO₂:Er sample was only a PL reference study for determining the optical quality of Er-doped sputtered material; the sample we were interested in for evaluating gain measurements by the VSL technique are the SiON:Er (co-sputtered) and Si₃N₄:Er samples. For these two samples, straight line fits of the risetime data resulted in vertical-axis intercepts giving decay times with high accuracy match to the experimentally measures values reported in the previous section. This match certifies the

accuracy of the cross-section fit, and we see from the results reported in Table 4.6 that the pump absorption cross-section at $\lambda_p=488$ nm is orders of magnitude larger than the literature reported of $\sigma_p=3\times 10^{-21}$ for SiO₂:Er.

	[Er] (cm ⁻³)	τ_{roomT} (ms)	$\sigma_{488\text{nm}}$ (cm ²)	σ_{21}	C ₂₄ (cm ³ /s)	Gain (dB/cm)
CVD SiO ₂	1.01×10^{20}	19	5.85×10^{-17}	--	--	--
SiO ₂ :Er	0.92×10^{20}	14	3×10^{-21} [5]	6×10^{-21} [5]	--	--
SiON:Er reactive	5.83×10^{20}	0.48	--	--	--	--
SiON:Er co-sputtered	6.1×10^{20}	3.8	2.24×10^{-15}	4.66×10^{-21}	4×10^{-18}	13.98
Si ₃ N ₄ :Er	4.95×10^{20}	0.487	9.2×10^{-16}	10.78×10^{-21}	1.5×10^{-18}	23.2

Table 4.6. Refractive index, 4 K and room temperature lifetime data, and Rutherford Back-Scattering(RBS) Er concentration measurements, for SiO₂:Er, SiON:Er and Si₃N₄:Er. ‘CVD SiO₂’ refers to a CVD grown SiO₂:Er sample donated by Corning, Inc. The Er concentration for the CVD sample is a nominally prepared composition as determined by Corning manufacturers.

This result is a new discovery whose physical origin may be in common with the recent actively developing field of oxide materials research: SiO₂ doped with Si nanocrystals.

The large $\sim 10^{-15}$ cm² magnitude for pump absorption at $\lambda_p=488$ nm is comparable with published absorption cross-section results for Si nanocrystals, precipitated from Si-rich SiO₂ films[86]. Measured Si₃N₄ refractive index values of ~ 2.2 at $\lambda=1550$ nm grown by sputtering have been correlated with a stoichiometric excess of Si[99]. To search for

evidence of nanocrystal-like sensitizers in our sputtered SiON and Si₃N₄ films, we followed the research route studying nanocrystals in Si-rich SiO₂: search for photoluminescence from annealed (at T=1100°C for t=1 hour) SiON and Si₃N₄ films, where these films have no Er doping.

Our results are summarized in Fig. 4.10, where we observed PL emission in the 950-1000 nm range, which is similar to the range of light emission observed from Si nanocrystals in SiO₂. Our not being able to resolve these emission peaks in the Er-doped samples of SiON and Si₃N₄ (Fig. 4.2) suggests that Er quenches this light emitting mechanism, i.e. the energy emitted from this structure within the host material will preferentially transfer to the Er atom rather than result in a photon. Whether this light-emitting structure is truly a Si nanocrystal, or some other form of inhomogeneity in the SiON and Si₃N₄ films, is currently a matter of active investigation in our research group.

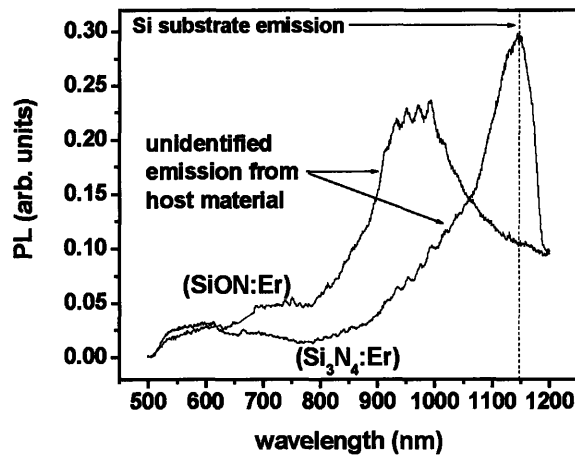


Fig. 4.10. Possible formation of nanocrystals in annealed SiON and Si₃N₄.

What we can say conclusively, is that given the Er radiative lifetime at $\lambda=1533$ nm changes by a factor of $14/2.4 \approx 5.8$ for Er in an SiO₂ versus Si₃N₄ environment, σ_{21} and

σ_{12} should change by a similar factor (see below for discussion on relation between σ_{21} and τ). We argue that σ_p , representing absorption by the 4f-shell electron from the ground state $^4I_{15/2}$ to $^4H_{11/2}$, should modify by a similar factor as well. Our observation of a $10^{16}/10^{-21} \cong 10^5$ order of magnitude change in σ_p for Er, from SiO_2 to Si_3N_4 , clearly shows the presence of some sort of intermediate sensitizer. And PL results on Er-free samples show the presence of a light-emitting structure that ceases to emit when in the presence of Er. Current research in our group is examining these phenomena further to prove or disprove the nanocrystal hypothesis.

We end this section by detailing how we theoretically estimated the stimulated emission cross-section, σ_{21} . The relation between the rate of stimulated emission ($\phi_s \sigma_{21}$) and the rate of (radiative) spontaneous emission ($1/\tau_r$) for an oscillator transition between two energy levels has been derived as[15]:

$$\sigma_{21} = \frac{\lambda_o^2}{8\pi n^2 \tau_r} g(\nu)$$

(4.2)

where n is the refractive index of the host medium, λ_o is the free space signal wavelength corresponding the oscillator energy transition, and $g(\nu)$ is called the lineshape function, $g(\nu) \propto 1/\Delta\nu$ ($\Delta\nu$ is the frequency bandwidth of the transition, i.e. it corresponds to the (homogeneous broadened) PL natural linewidth).

We will assume the Er PL emission natural linewidth $\Delta\nu$ is approximately the same in the $\text{SiO}_2:\text{Er}$, $\text{SiON}:\text{Er}$ and $\text{Si}_3\text{N}_4:\text{Er}$ samples (recall their PL spectra have identical

overlap). For similar linewidths, we can we theoretically estimate σ_{21} for SiON:Er by modifying the literature reported SiO₂:Er value of $\sigma_{21}(=6 \times 10^{-21} \text{cm}^2)$, :

$$\sigma_{21}(\text{SiON} : \text{Er}) = \sigma_{21}(\text{SiO}_2 : \text{Er}) \times \frac{\tau_r(\text{SiO}_2)}{\tau_r(\text{SiON})} \times \left(\frac{n(\text{SiO}_2)}{n(\text{SiON})} \right)^2$$

and similarly for estimating σ_{21} for Si₃N₄:Er.

4.4.8 Cooperative Upconversion Measurement

We evaluate the cooperative upconversion coefficient C_{24} , for the SiON:Er co-sputtered and Si₃N₄:Er samples. In order to verify that the cooperative upconversion process is the principal de-excitation mechanism, other than spontaneous emission and stimulated emission, we observed emission PL intensity as a function of pump power at wavelengths $\lambda=1533$ nm and $\lambda=985$ nm (Fig. 4.11.a, c). PL emission at $\lambda=1533$ nm corresponds to a quantitative measure of the concentration of excited state (N_2) Er atoms, while PL emission at $\lambda=985$ nm represents a second excited state population (N_3) of Er atoms, coming from both to the pump wavelength (488 nm) exciting Er from the ground state, and coming from the first (see chapter 2 for details) cooperative upconversion process C_{24} , corresponding to a de-excitation of N_2 state atoms not by spontaneous emission, but by resonant energy transfer to excite a neighbor N_2 state atom to the N_4 state; from there the N_4 population rapidly relaxes to N_3 .

Re-plotting the PL emission intensities from level 2→1 de-excitation ($\lambda=1533$ nm) versus PL emission intensities from level 3→1 de-excitation ($\lambda=985$ nm), where pump power is a common parameter to these two variables, results in a correlation plot[7] whose slope quantifies the power law process governing transitions from population N_2

to N_3 . A slope of 2 in such correlation plots is the characteristic fingerprint of the cooperative upconversion process.

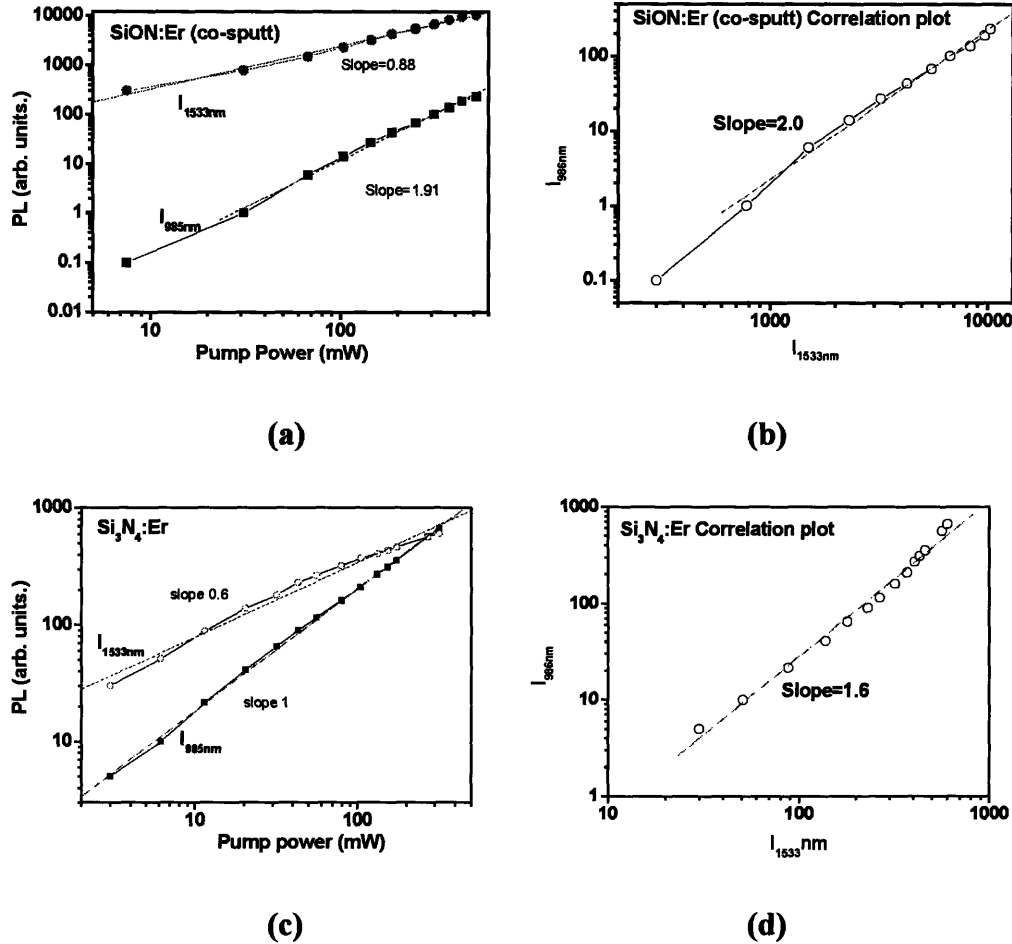


Fig. 4.11. PL peak intensity at $\lambda=1533$ nm versus $\lambda=985$ nm for (a) SiON:Er and (c) Si₃N₄:Er. Correlation plots identifying the upconversion process for (b) SiON:Er and (d) Si₃N₄:Er. (Data collected courtesy Jae Hyung Li.)

We observe a slope of 2.0 for the SiON:Er (co-sputter) correlation plot (Fig. 4.11.b) and a slope of 1.6 for the Si₃N₄:Er correlation plot (Fig. 4.11.d). From this we conclude that the Er energy model (as presented with cooperative upconversion in chapter 2) is appropriately described for SiON:Er, but not entirely for Si₃N₄:Er. There are potential additional energy transfers mechanisms involved in Si₃N₄:Er. New research

activities to identify the nature of these additional mechanisms are currently under consideration by our research group.

Nonetheless, we perform an upconversion fit to PL emission decay data (Fig. 4.12) for both SiON:Er and Si₃N₄:Er. If the additional energy transfer mechanisms involve pump excited state absorption, a fit to the PL decay in time (where P_p=0) of excited Si₃N₄:Er should still provide cooperative upconversion information.

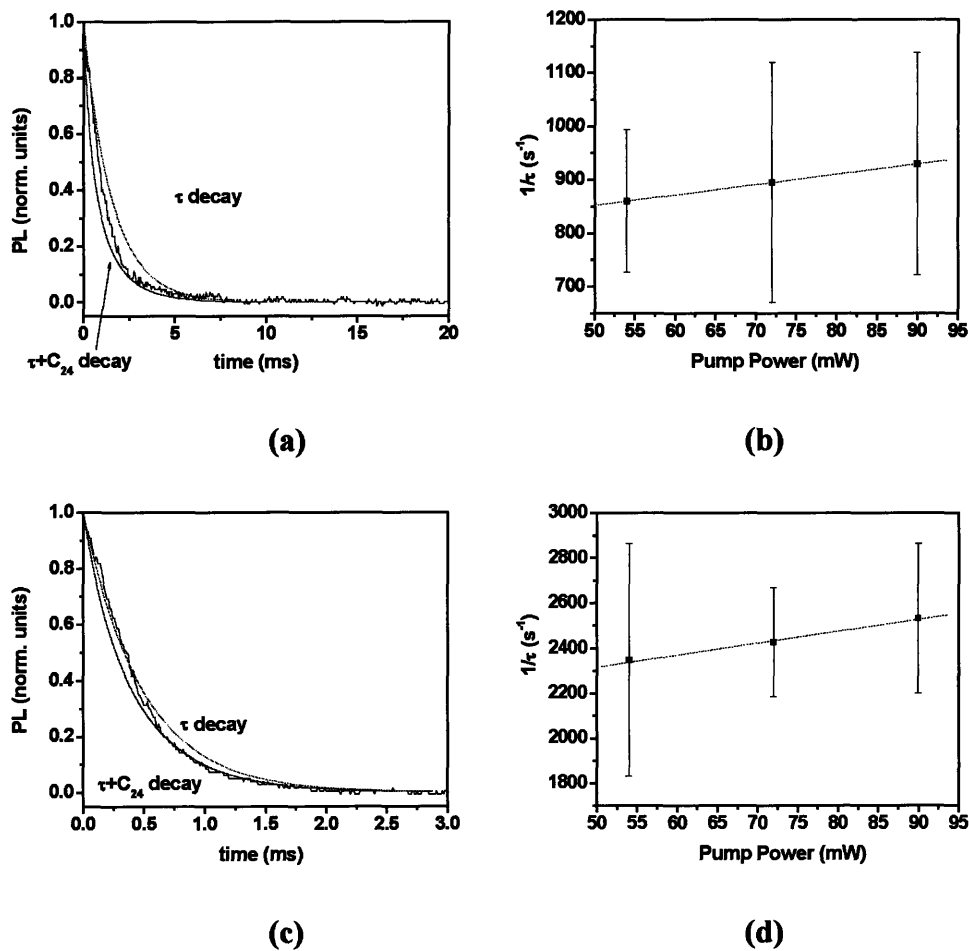


Fig. 4.12. Upconversion coefficient C_{24} simulation fits to PL emission decay data for (P_p :90 mW→0 mW at $t=0$) (a) SiON:Er and (c) Si₃N₄:Er. As comparison, the approximation technique for measuring C_{24} in chapter 3 is also plotted for (b) SiON:Er and (d) Si₃N₄:Er.

We also compare in Fig. 4.12.b,d the approximate measurement technique we employed for estimating C_{24} from chapter 3. In that technique, we renormalized the upconversion effect into a fitted single exponential decay, with an associated error bar. The error is a critical element to this approximation technique: it acknowledges that exponential fit is being forced onto raw PL emission decay data (which is composed spontaneous emission based exponential decay and a fast upconversion decay component). However, if the error bar is smaller than the range of exponential fit lifetimes made at different pump powers, then Eqn. (3.11) may yield a reasonable approximation to C_{24} (this method of renormalizing upconversion decay into a forced exponential fit with error bar was demonstrated in [1]).

From Fig. 3.20 inset, we see that for the Er_2O_3 case, the ultra-high concentration of Er reduced lifetime with pump power over a range of values larger than the error bar associated with each forced lifetime fit. Thus, equation (3.11) could be used as an approximation. But in Fig. 4.12.b,d, we see that the $\sim 100\times$ lower Er concentration results in a lifetime reduction with pump power which lies within the error bar associated with each forced lifetime fit. As a result, we can not trust the cooperative upconversion coefficient derived from this technique (linear fits to Fig. 4.12.b,d result in $C_{24} \sim 10^{-22}$ cm^3/s values), and must rely on a direct simulation of upconversion decay of experimentally acquired PL emission decay data (Fig. 4.12.a,c).

In Fig. 4.12.a,c we plot experimentally acquired data, a pure exponential decay (based on the experimentally measured room temperatures lifetimes in reported in the previous section) and a decay that includes cooperative upconversion. We observe a systematic artifact in measured PL emission decay at short times: a wobble in our

mechanical chopper (which decreases with increasing chopper frequency) results in a beat modulation of our optical pump, creating a ripple pattern in oscilloscope measurements. For thick samples, such as our Corning SiO₂:Er (thickness=1.92 mm), this ripple pattern is less noticeable against the high PL emission signal. But for our thin films (thickness~500 nm), the ripple can not be avoided. Time averaging on the oscilloscope helps eliminate this ripple effect, but at the cost of creating an artifact in the PL emission profile: for short times, PL emission decay appears to drop linearly, and then finally merge into a greater-than-exponential decay. We selected C₂₄ values that fitted our data at these longer times, where we observe greater-than-exponential decay. Our fitted results are listed in Table 4.6. Literature reported[93] values for C₂₄ in SiO₂:Er (for ~10²⁰ cm⁻³ concentrations) are higher than our fitted values for SiON:Er and Si₃N₄:Er. Making note of the observation that the short-time linear artifact in PL decay implies our fits are at the least an upper limit estimate for C₂₄ values, we conclude that upconversion in SiON:Er and Si₃N₄:Er samples is lower than SiO₂:Er. The nitrogen environment appears to help reduce the influence of cooperative upconversion between neighbor Er atoms.

We now combine the results of Table 4.6 to analyze experimental gain measurement data on SiON:Er, acquired by the Variable Stripe Length method.

4.4.9 VSL Gain Measurements

The Variable Stripe Length (VSL) method[100]² was used to measure gain per unit length from the SiON:Er (co-sputter) and Si₃N₄:Er samples. The samples were

² VSL measurements were performed at the Charles Stark Draper Laboratory within an IR-D Collaboration project. We thank Dr. L. Dal Negro from MIT and the staff at Draper for their valuable experimental assistance. We acknowledge Dr. J. Haavisto, J. LeBlanc and M. Stolfi.

grown on a 10 μm thick wet thermal oxide on Si substrate. The thermal oxide layer isolated a propagating slab mode within the thin films, index-guided from above due to refractive index difference between the film versus lower index air, and from below due to refractive index between the film versus lower index thermal oxide.

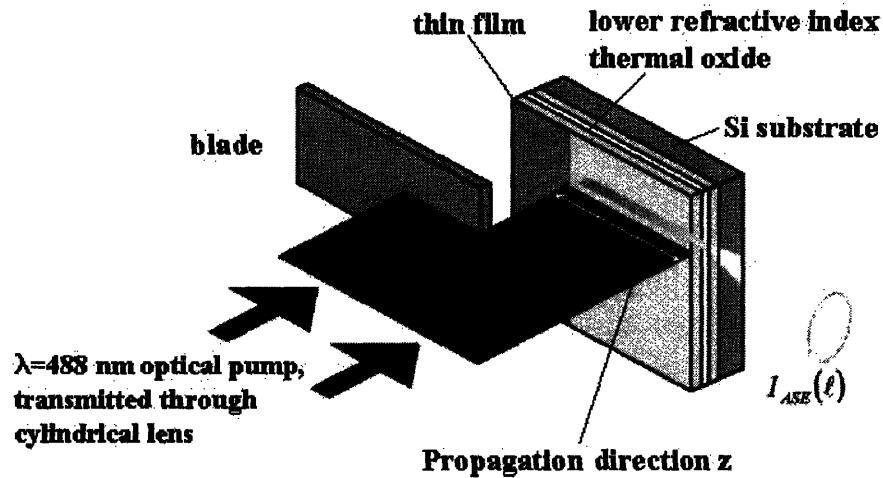


Fig. 4.13. Schematic diagram of VSL set-up, depicted in a sideways (as opposed to overhead optical pump) profile. (Image courtesy Dr. Luca Dal Negro, MIT.)

The VSL method is a one-dimension confinement method by which the 488 nm optical pump illuminates from overhead, through a cylindrical lens into a stripe pattern on the thin film (see schematic diagram in Fig. 4.13). The dimensions of this stripe pattern are 200 μm width and 1.5 mm length in the direction arbitrarily defined as the propagation direction, z. The pump power, which transmits into this stripe pattern, excites the Er atoms into population inversion. Resulting spontaneous emission propagates (as 1-D slab modes) in all directions within the two-dimension film plane. But for spontaneous emission propagating in the z-direction, under the stripe-pumped region of the film, stimulated emission occurs. Hence light intensity propagating along the z-direction I_{ASE} can be collected by a collimating lens into a photo-detector. And the amount of ASE

occurring within this collected light will have exponential dependence on the stripe pattern's length dimension.

Along the propagation direction, a blade is advanced by micrometer stage to reduce the 1.5 mm length dimension of illumination. If an exponential dependence is observed in collected output intensity I_{ASE} , of the form[100]

$$I_{ASE}(z) = A + \frac{I_o}{\gamma} (e^{\gamma z} - 1)$$

(4.3)

(A and I_o are constants) we can fit the $I_{ASE}(z)$ data and determine a gain coefficient γ per unit length at $\lambda=1533$ nm.

Fig. 4.14.c,d and Fig. 4.15.c,d show two such gain coefficient γ fits at different pump powers P_p . The different fits are summarized in a plot of fitted gain versus pump power on linear power axis (Fig. 4.14.a and Fig. 4.15.a) and on a logarithmic power axis (Fig. 4.14.b and Fig. 4.15.b). We have overlaid in these γ versus P_p plots a theoretical gain curve, computed for uniform optical pumping by an overhead 488 nm laser, using the experimentally measured lifetime, pump absorption cross-section, fitted upconversion coefficient and theoretical estimate for stimulated emission cross-section at $\lambda=1533$ nm (the data summarized in Table 4.6). The free parameters we used in overlaying the calculated gain curves were the optically active Er concentration and the background materials loss in the films, which should correspond to materials loss for the Er-free films listed in Table 4.5.

Our first comment is that a very limited range of experimental data is available from these plots. The VSL set-up used for these experiments used an Ar ion laser with a maximum pump power of 130 mW. With this much optical power, our VSL collaborators have demonstrated experimental measure of gain saturation in a γ versus P_p plot, when exciting Si-rich $\text{SiO}_2\text{:Er}$ samples. We conclude from the available data that the much shorter room temperature lifetimes of the SiON:Er (co-sputter) and $\text{Si}_3\text{N}_4\text{:Er}$ samples are unable to show decisively a gain saturation. More pump power is required, and our VSL collaborators are making future plans to set-up a VSL facility at MIT which uses an Ar ion laser with up to 2 Watts pump power.

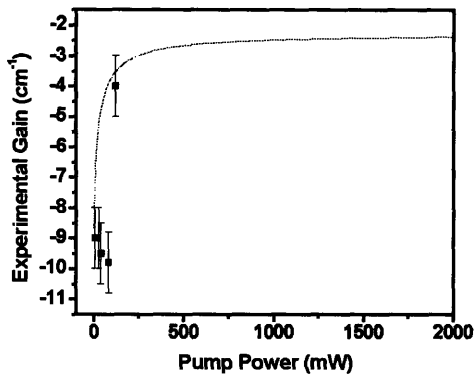
Our second comment is that a very limited amount of data is currently available, but from this data we conclude that the experimentally measured increase in gain, about the inflection point on the semi-log plots, rises more steeply with pump power than predicted by any simulation we tried, using the Table 4.6 parameters and even by modulating them. The steeper rise in experimental data indicates there are additional excitation/de-excitation dynamics for the Er atom than simply spontaneous emission and cooperative upconversion. This is consistent with our <2 correlation slope for the $\text{Si}_3\text{N}_4\text{:Er}$ sample in Fig. 4.11.

Our third comment is that for the SiON:Er , a slab mode loss measurement technique called Shift Excitation Spot (SES)[100] establishes that the total materials loss in the SiON:Er film, including Er absorption, is 8.5 cm^{-1} (Fig. 4.14.e). Thus, with this confirmed value for the gain curve at $P_p \rightarrow 0$, the best fit we can achieve to the SiON:Er experimental data requires our reducing the Er concentration to half its value as measured by RBS.

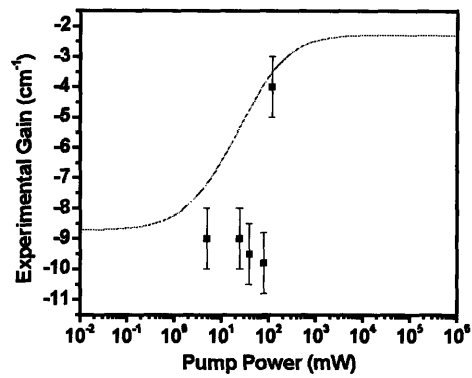
Our fourth comment is that for the $\text{Si}_3\text{N}_4:\text{Er}$ gain curve calculation (Fig. 4.15.a,b) the Er concentration as measured by RBS (and listed in Table 4.6).

We now compare the background materials loss value used to offset these calculated gain curves, versus the experimentally measured materials loss values by slab mode loss measurements in a modified prism coupler device (the data reported in Table 4.5). The modified prism coupler was unable to quantify propagation loss accurately for the Si_3N_4 sample, showing loss values that varied by 20-30 dB/cm. The background materials loss in Fig. 4.15.b, read as the gain measure at which the calculated curve goes through an inflection point in the semi log plot, to be on the order $-28 \text{ cm}^{-1} = -122 \text{ dB/cm}$. These enormous slab mode propagation losses may be due to the higher scattering loss for propagating modes with no lateral confinement, in a thin film with scattering loss centers. In any case, there is a $\sim 4\times$ discrepancy between background materials loss estimates from these two measurement techniques.

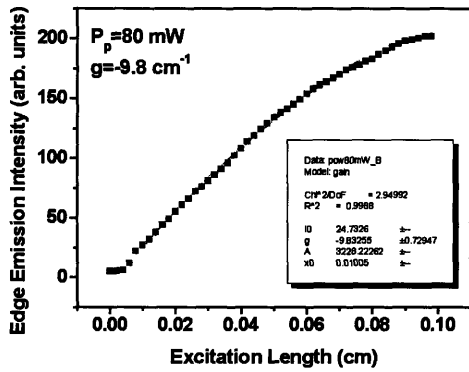
The discrepancy between experimentally measured slab mode propagation loss and calculated γ versus P_p profile, is far more severe for the $\text{SiON}:\text{Er}$ sample. According to prism coupler based propagation loss measurements, the background materials loss for a propagating slab mode should be $0.8 \text{ dB/cm} \approx 0.184 \text{ cm}^{-1}$ (see Table 4.5); but the theoretical gain curve calculation in Fig. 4.14.a,b which seems to best represent a trend amongst the data points while at the same time matching an SES measurement requirement of 8.5 cm^{-1} for $P_p \rightarrow 0$, results in a background materials loss around $\sim -5.5 \text{ cm}^{-1}$. This significantly larger background materials loss can be accounted for if we



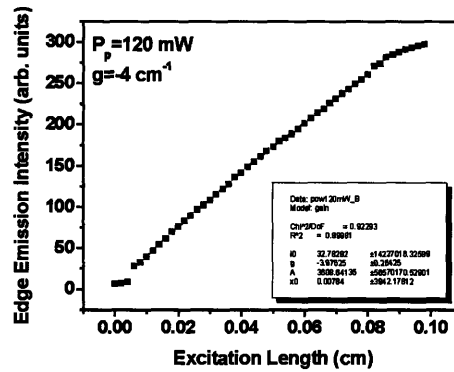
(a)



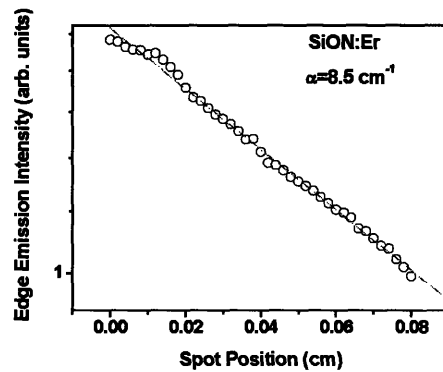
(b)



(c)



(d)



(e)

Fig. 4.14. Variable Stripe Length method for measuring Amplified Spontaneous Emission[100] from SiON:Er (co-sputtered). Results show a decrease in modal loss as a function of pump power. (Data acquired courtesy Dr. L. Dal Negro.)

assume only ~50% of the Er concentration is optically active, and the remaining are in a deactivated, perhaps clustered state, in which they can not contribute gain at $\lambda=1533$ nm, but can still contribute absorption. This reduction in the magnitude for fitting the concentration of optically active Er also results in a gain curve that appears closer to the limited spread of gain versus pump experimental data points available for this sample. More importantly, we have already learned from our materials processing study that not all the Er in SiON:Er (co-sputter) is optically active (see Fig. 4.2.a). The reported gain measurements in this section have been done on a $T=1000^{\circ}\text{C}$ ($t=1$ hour) annealed samples of Si₃N₄:Er and SiON:Er, and for the SiON:Er case in particular, we see from Fig. 4.2.a that not all the Er is optically activated yet, and that annealing temperatures higher than the 1200°C upper limit of our furnace are required.

We conclude further annealing studies are required in order to ensure that all the Er atoms are optically activated by high temperature $>1200^{\circ}\text{C}$ annealing in the SiON:Er sample. A higher temperature furnace than what is at our disposal must be found for this work. Once the Er concentration has been optimally activated, we should observe a net positive gain in a VSL measurement of this sample, with a background materials loss value matching the host materials loss measurement reported in Table 4.5.

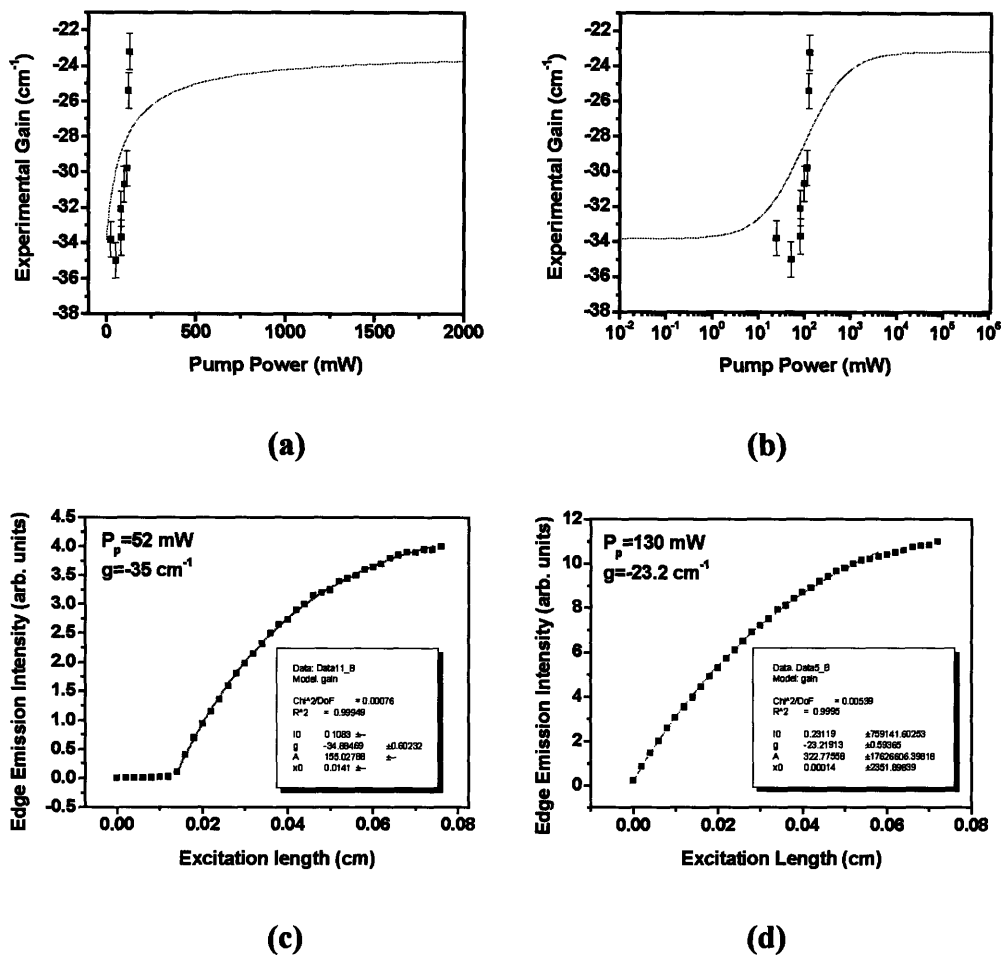


Fig. 4.15. Variable Stripe Length method for measuring Amplified Spontaneous Emission[100] from $\text{Si}_3\text{N}_4:\text{Er}$. Results show a decrease in modal loss as a function of pump power. (Data acquired courtesy Dr. L. Dal Negro.)

The enormous background materials loss observed by the VSL technique in our $\text{Si}_3\text{N}_4:\text{Er}$ sample, while being closer in consistency with the results of Table 4.5, is a far more serious materials science indication of the limitation in using this material for net optical gain. AFM studies have established these films to have sub-nm root-mean-square roughness (Table 4.5), in which case this large background loss can not be attributed to a high Δn slab mode scattering loss between the thin film and air above ($\Delta n=2.2-1=1.2$), or the thin film and thermal oxide below ($\Delta n=2.2-1.445=0.755$). Therefore, this large

background loss for the slab mode is either due to absorptive or scattering effects in the host sputtered Si_3N_4 material itself. The observed sensitizers in this material, which we hypothesized to be Si nanocrystals or some as-yet unidentified structural inhomogeneity in the host material, may also be the contributor to absorption or scattering loss at $\lambda=1533$ nm. Considerable more research has to be done on Er-free sputtered Si_3N_4 films in order to identify this large background loss, first reported by our group in[99]. Once the mechanisms of $\lambda=1533$ nm loss in sputtered Si_3N_4 have been understood and reduced—if possible—only then shall it be feasible to resume the optical gain study of $\text{Si}_3\text{N}_4:\text{Er}$.

Putting aside the background materials loss present in these two samples, we now inspect the gain modulation suggested by the theoretical fit gain curves in Fig. 4.14 and Fig. 4.15. The advantage of plotting these gain curves on semi log (P_p) plots is help visually identify absorption ($P_p \rightarrow 0$) and gain saturation (see definition of these Regimes in chapter 2). The modulation in gain between these two regimes, for the uniform optical pump profile of the VSL method, corresponds to $2\gamma_s=2\sigma_{21}\Delta N$, where γ_s is the definition of small-signal gain and ΔN is a number close to the optically active Er concentration N . Our measure of γ_s from the calculated gain curves for $\text{SiON}:\text{Er}$ and $\text{Si}_3\text{N}_4:\text{Er}$ are listed in Table 4.6. The small signal gain results are considerably larger than our a priori assumption of $\sim 3\text{-}5.5$ dB/cm for $N=1\text{-}2 \times 10^{20}$ cm^{-3} Er-doping concentrations. The reason is due to (i) the lower cooperative upconversion effect due to the addition of a nitride environment in $\text{SiON}:\text{Er}$ and $\text{Si}_3\text{N}_4:\text{Er}$ resulting in population inversion even for Er concentrations of $4.5\text{-}6 \times 10^{20}$ cm^{-3} , and (ii) the resulting decrease in radiative lifetime, or equivalently the enhancement in stimulated emission cross-section σ_{21} , due to the nitride environment in $\text{Si}_3\text{N}_4:\text{Er}$.

From the results of this gain study we conclude our best materials candidate for net gain at $\lambda=1533$ nm is the co-sputtered SiON:Er film. Sputtered Si₃N₄:Er may potentially deliver small signal gain values as high as 25 dB/cm, but this is of no value if background materials loss can not be reduced to values $\ll 25$ dB/cm.

One final important question to pose is whether the modulation in negative gain which we have experimentally reported in Fig. 4.14 and Fig. 4.15 is due to gain modulation from Er, or due to loss modulation from the host material. The good match in threshold pump power, about which the experimental data points and the calculated gain curve begin to climb, indicates the energy transition center involved in this negative gain modulation has lifetimes and dynamics closely matching our Er lifetime and upconversion measurements. We therefore conclude this modulation in negative experimentally measured gain is indeed to population inverting Er atoms. For the sake of completeness, we make a future recommendation to repeat these VSL gain measurements, once the new higher pump power facility is set-up, on both Er-doped and Er-free sputtered samples of SiON and Si₃N₄, in order to confirm the absence of negative gain modulation with P_p , in the Er-free samples.

4.5 Conclusions

Our study of Er as an optical dopant for gain near 1.55 μm light concludes that the nitride material environment helps to increase Er gain, by

(i) increasing Er clustering onset: higher concentrations of Er can be doped into SiON and Si₃N₄ than SiO₂ before reaching optical deactivation;

(ii) lower cooperative upconversion: Er-Er cooperative upconversion appears to have a smaller interaction strength in the nitride environment;

(iii) shorter radiative lifetime/enhanced stimulated emission cross-section: the nitride environment increases the cross-section for stimulated emission σ_{21} (and hence gain per unit length), as evidenced by a shorter radiative lifetime; and

(iv) a dramatic increase in pump absorption cross-section, by means of an unknown host material based sensitizer. Current PL results are tentatively suggesting the sensitizer to be some form of Si nanocrystal, this continues to be an open activity of research.

The sputter process was evaluated as a deposition technique for suitable low materials loss by comparing Er 4 K and room temperature lifetimes in co-sputtered SiO₂ versus commercial EDFA glass. The room temperature quench factors were comparable. We conclude the sputter process can create low defect material.

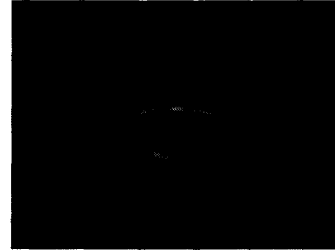
Further experiments are required to identify the high loss mechanism in Si₃N₄ host material. We recommend a pump probe experiment in Er-free samples to determine if the pump wavelength λ_p sensitizer is also a source for signal λ_s absorption.

SiON:Er (co-sputter) is our most promising current material candidate for the WOA. We recommend another sample be grown, with lower Er concentration (to avoid clustering), in order to confirm that the VSL and modified prism coupler based background materials loss coefficients match, and be approximately 0.8 dB/cm. The VSL system has to be re-fitted with a higher pump Ar ion laser in order to complete these measurements with accuracy.

The materials dynamics of $\text{Si}_3\text{N}_4:\text{Er}$ must be further studies in order to explain the physical dynamics represented by the 1.6 correlation plot slope value. In light of acquiring a more complete understanding of the dynamical model, cooperative upconversion must be once again fitted from the data to determine what magnitude correction may occur.

If the background host materials loss in $\text{Si}_3\text{N}_4:\text{Er}$ can be identified and minimized, $\text{Si}_3\text{N}_4:\text{Er}$ will produce a > 10 dB/cm high material gain system for WDM-compatible low noise WOAs.

Chapter 5: the Effect of Longitudinal Confinement in Ring Resonator Waveguide Amplifiers



Green light emission (due to upconversion) from an Er-doped silica microsphere, fabricated with experimentally measured quality factor of $\sim 10^{10}$, makes possible the lasing of Er under high $\Delta n = 1.445 - 1.0 = 0.445$ confinement. (Reference: reproduced from Vahala Research Group website, CalTech, <http://www.its.caltech.edu/~vahalagr/>).

“If you are designing photomasks for i-line stepper in ICL, please consider the following. The i-stepper has lateral misalignment as much as 0.2 μ m-0.3 μ m which, as I believe, is coming from the insufficient system optimization. But good news is that there is no vertical misalignment at all as far as I know. So if you are planning to make multi-layer device, I would recommend to put your waveguide like - not like |”-the email that saved the vertical coupling design of lithography mask *MASK Amplifier H-tree*—from to Shoji Akiyama (graduate student, EMAT), 03/05/2004.

“That’s like putting gas in someone else’s car. *Why* would you do that?” –Dan Sparacin(graduate student, EMAT), on life at the MIT.

5.1 Chapter Abstract

Chapter 2's study of index difference Δn influence on Waveguide Optical Amplifier (WOA) size and gain performance developed into an understanding of the effect of engineering WOA boundary conditions in order to extend the regime of gain saturation within the amplifier medium. We extend this idea of device engineering further in this chapter by investigating the effect of resonant confinement along the longitudinal direction of mode propagation, of a WOA.

We study this effect in an Er-doped ring Resonator Waveguide Optical Amplifier (R-WOA) by modifying the photon number differential equation for a two-level system with the addition of a Modified Purcell Factor term to model coupling of the signal and optical noise into the resonant cavity. As a reference study, comparison is made with theoretical studies and experimental published results in resonantly confined Semiconductor Optical Amplifiers; we find good agreement for our model.

We apply our differential equation model to the R-WOA design and simulate its performance. We conclude that for a fixed Δn and given waveguide transmission loss, an optimal ring resonator, described by external quality factor Q_e , can be chosen to (i) increase gain efficiency, and (iii) decrease areal footprint. Using the SiON as our best Er-host candidate from chapter 4 and the SiON case study (includes upconversion) simulated at the end of chapter 2, we make quantitative comparison of amplifier enhancement by Longitudinal Resonant Confinement ($Q_e > 0$), versus transverse confinement ($Q_e=0$, $\Delta n =0.155$). For a $Q_e=10^4$ structure, we observe a maximum 3-dB gain efficiency

of 37 dB/mW, within a $100 \times 100 \mu\text{m}^2$ footprint. This is a $120 \times$ increase in gain efficiency and $18 \times$ decrease in footprint, as compared to the non-resonant SiON coil structure WOA.

Resonant confinement of $Q_e \sim 10^4$ reduces amplifier bandwidth to ~ 20 GHz, however the large ring resonator dimension (chosen in order to limit radiative turning loss to 0.1 dB/cm) results in a multi-modes structure, thus the R-WOA retains considerable WDM applicability, however transmission rates per channel are limited by the 20 GHz bandwidth to approximately 2.5 Gbit/s. We conclude both coil structure WOAs and R-WOAs have application-specific value for in-line and pre-amplifier roles in a PLC.

Similar to the results of chapter 2, the impressive device performance of a ring amplifier is completely dependent on the realization of ultra-low waveguide transmission losses of 0.3 dB/cm and negligible host material losses, a loss benchmark currently met by only SiON planar processed waveguides. We have developed a lithography mask to test SiON:Er ring lasers and R-WOAs.

Additional studies into modeling an Er-doped ring laser and a photo-detector integrated ring de-multiplexer are presented. We conclude the similar scattering loss requirements for the ring laser. The ring de-multiplexer, however, is robustly feasible against 2-4 dB/cm scattering losses, typical of current planar processed Si_3N_4 waveguides.

5.2 Introduction

5.2.1 The Ring Resonator

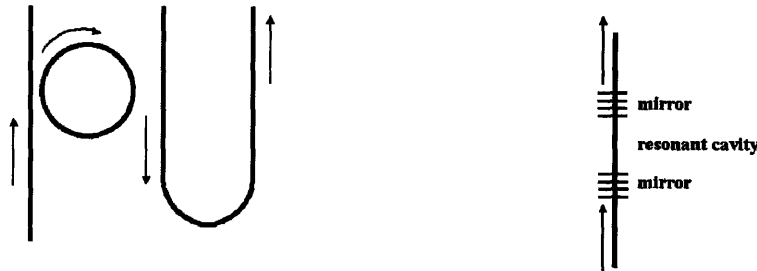


Fig. 5.1. (a) Schematic diagram showing the fundamental elements of a (traveling wave) ring resonator WDM de-multiplexer. (b) Comparison with a Fabry-Perot standing wave resonator.

The most well known resonant photonic device is the laser, a structure relying on the principles of (i) a weak coupling between photons emitted within a light emitting cavity, and (ii) wavelength selectivity of the lasing photon, based on choice of the cavity length.

The interference principle of (ii) has today defined a new class of wavelength-selective photonic devices[101][102][103], some of them commercially sold and used in telecommunications for isolating (“dropping”) single carrier frequencies ν_i (or wavelength λ_i) from Wavelength Division Multiplexed (WDM) fiber optic signals.

Ring resonators[104] are a state-of-the-art example of such WDM de-multiplexers, using traveling wave resonator geometry to selectively drop one WDM channel from an input waveguide *bus* (named bus for its role to transmit multiple carrier wavelengths) to a waveguide *drop port* (see Fig. 5.1.a). Coupled-Mode-in-Time analysis of resonators their potential in the form of waveguide rings were introduced and studied by Dr.

H.A. Haus at MIT in the 1990s, the result of one of his historical memos. Since then ring resonators have been experimentally demonstrated and their performance optimized today to the point of commercial application[105]³.

The long-standing form of resonant structures in III-V laser devices have been standing wave resonators[106], comprised of a light-emitting cavity confined along the signal propagation direction by high reflectivity mirrors (see Fig. 5.1.b). There are no fundamental WDM advantages to the traveling wave versus standing wave geometry. In the traveling wave geometry, coupling between bus and ring resonator is by evanescent coupling of waveguide propagating modes. In the standing wave geometry, coupling between waveguide and resonant cavity is normal incident transmission through a reflector (typically a Bragg reflector stack made up of periodic pairs of varying propagation constant β , i.e. varying effective index n_{eff} —see chapter 2 for definitions).

From the perspective of process engineering, the evanescent coupling mechanism of ring resonators, microdisks[107] and spherical resonators[108] make such structures naturally amenable for designing ultra-weak coupling[109] between bus and ring: increase the gap distance (Fig. 5.1) between bus and ring. This coupling between incident waveguide (the bus) and resonator (the ring) is called the external coupling of the ring resonator, quantified by an external quality factor Q_e , defined as

$$Q_e \equiv \frac{\omega_o \tau}{2} = \frac{\lambda_o}{\Delta\lambda}$$

³ As Dr. B.E. Little said at an MIT RLE ring resonators review colloquium in spring 2004, “I’m reporting back to you on the progress of (Dr. Haus’ memo).”

[110] where ω_0 is the natural harmonic frequency—i.e. the frequency (or wavelength λ_0) that is selectively trapped within the cavity, $\Delta\lambda$ is the spectral linewidth of this selective confinement around λ_0 , and τ is the characteristic time a λ_0 photon remains trapped within the resonator.

Ring resonators have been designed for either in-plane (i.e. parallel to a deposition Si substrate) coupling or out-of-plane coupling[111]; they have been processed in both optically passive dielectric materials and in optically active III-V emitting materials[112]. While typical ring resonator coupling geometry is in-plane, with lithography defining the gap distance between bus and ring, the design choice for our work was out-of-plane coupling (see Fig. 5.2), in order to grow by sputtering a ring resonator doped with Er, which couples to an Er-free waveguide bus.

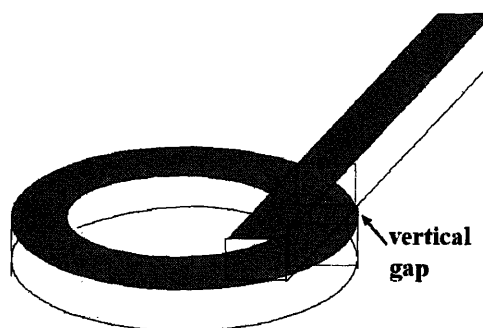


Fig. 5.2. Schematic of out-of-plane coupling between waveguide bus and ring resonator.

5.2.2 Er-Doped Ring Resonators

While ring resonators have been modeled and processed for increasingly complex filter applications[113] and as electrically-pumped lasers[114] or optical

switches[115], there has been no work published on studying the light emission properties of an optically pumped Er-doped resonant structure, until this year[116].

The Vahala research group at CalTech University experimentally demonstrated ultra-high micro-toroid resonant cavities with measured $Q \sim 10^7 - 10^8$ [109]. They achieved this by taking advantage of the lower thermal conductivity of SiO_2 (versus Si) and the surface tension properties of SiO_2 in order to process SiO_2 toroids with unprecedented surface smoothness. This resulted in ultra-low transmission losses (see definition of Q_{loss} in section 5.3) within this ultra-low material absorbing structure, enabling $Q_e \rightarrow 10^7$ and higher values. They recently followed this work with the processing and optically pumping of $\text{SiO}_2:\text{Er}$ micro-toroids[116], resulting in the first demonstration of a microphotonic Er-based laser light source.

During this time, our group has been studying the advantage of using a ring resonator for an Er-based (1) laser light source, and (2) an optical amplifier which takes advantage of the traveling wave resonator geometry to *re-circulate* both pump and signal power within a micro-ring.

The two advantages for using a micro-ring structure for optical amplification are:

(i) Footprint: by re-circulating the carrier signal within a ring, an effective optical path length can be created which is larger than the actual ring diameter. A ring amplifier will thus have a much smaller areal footprint than a WOA coil structure (chapter 2).

(ii) Gain Efficiency: the re-circulation, or equivalently, resonant confinement of *both* pump and signal power within the ring should produce a higher device gain efficiency in comparison to a WOA coil structure with length matched to the effective

path length: a ring amplifier should deliver more dB gain at λ_s for the same pump power P_p than was calculated chapter 2.

The work in this chapter presents our study of the effect of resonant confinement, quantified by the Q_e parameter, on the gain efficiency of (ring) Resonant Waveguide Optical Amplifiers (R-WOAs). Using the SiON example that concluded our Optical Shrink (quantified by the Δn parameter) chapter 2 study, we examine the possibility of further enhancement in device gain efficiency for an R-WOA versus a WOA (at fixed Δn), as a function of Q_e .

In the last few years, resonant confinement of an optical amplifier has been studied in III-V Semiconductor Optical Amplifier (SOA) devices, reporting enhancement in gain of 1 μ W by signals by 100-300 \times [117]. These results have been experimentally demonstrated[118] and further studies are continuing[119]. These resonantly confined SOAs, dubbed Vertical-Cavity SOAs (VS-SOAs), are essentially Vertical Cavity Surface Emitting Lasers (VCSELs) operated below lasing threshold. For such SOAs, the direction of signal gain occurs along the direction of film deposition, and not in-plane. Conventional SOAs, with gain propagation within the plane of the deposited film, can be processed to have gain medium lengths of 100-300 μ m, making possible commercial devices with 10-30 dB gain (for λ_s). Deposited films are MBE or CVD growth rate limited to thickness of 1-2 μ m. Hence, the length of the gain medium is $\sim 100\times$ smaller in VCISOAs, as compared to SOAs. The goal pursued and achieved in the reported VCISOA papers was to use resonant confinement in order to overcome this gain medium length limitation, yielding optical gain from a VCISOA that is comparable to the SOA. 17 dB

fiber-to-fiber gain using a VC SOA was reported in [117], which the authors extrapolate to a VC SOA internal gain (i.e. before coupling loss from VC SOA to fiber) of ~24 dB.

The theoretical modeling of an Er-doped ring laser performance, is a natural precursor to the resonant amplifier study. We have implemented both laser and amplifier designs into a two-level lithography mask set, designed for device dimensions allowing us to work with our most promising Er-doped hosts from chapter 4, SiON (and potentially Si₃N₄, provided background materials loss can be significantly reduced). The goal of working with a two-level mask was to employ vertical coupling between waveguide bus and ring resonator, affording us two advantages:

(i) the ability to adjust bus to ring gap distance independent of mask design. Using the same lithography mask, we can process and experimentally study the power performance of difference Q_e ring lasers, amplifiers and switches; and

(ii) a PVD (or CVD)-compatible process for Er-doping. Our work in chapter 4 is based on Er co-sputtering during SiON (or Si₃N₄) deposition. In order to selectively dope the ring resonator while maintaining undoped waveguide bus and drop ports, two layers of dielectric films, separated by an SiO₂ layer corresponding to the gap distance, will be deposited. The first layer comprises SiON (or Si₃N₄) doped with Er to concentration $2 \times 10^{20} \text{ cm}^{-3}$ (lithographically patterned into rings); the second layer comprises undoped SiON (or Si₃N₄).

In the course of this theoretical study we also came up with the idea for a very promising size and performance efficient photo-detector-integrated WDM de-multiplexer

for Si Microphotonics. We conclude our Results and Discussion section with these theoretical findings.

5.3 Theoretical Background

5.3.1 Relating Power within the Ring Resonator to the Waveguide Bus (the Modified Purcell Factor)

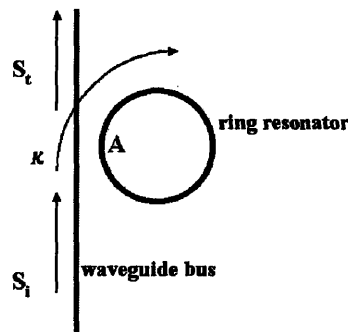


Fig. 5.3. Schematic illustration of transfer of incident power $|s_i|^2$ from waveguide bus to ring resonator power $|A|^2$, through field coupling coefficient κ . $|s_t|^2$ is the transmitted power continuing in the waveguide bus after coupling.

Fig. 5.3 schematically shows the coupling of an incident waveguide bus' signal power $|s_i|^2$, (we define s_i to be the electric field amplitude of the propagating mode of light) to the ring resonator power $|A|^2$ by a unit less coupling constant κ . κ is the fraction of the waveguide bus' modal field that couples to the ring resonator in a *single pass*, or vice versa:

$$|s_{leak}|^2 = \kappa^2 |A(t)|^2.$$

(5.1)

Resonance for a ring resonator is satisfied by the condition

$$2\pi r = m\lambda_{\text{eff}} = m\lambda_o / n_{\text{eff}}$$

(5.2)

where r is the ring radius (see Fig. 5.3), $m=1,2,\dots$, λ_o and λ_{eff} are the free-space ($k_o=2\pi/\lambda_o$) and effective wavelengths ($\beta=2\pi/\lambda_{\text{eff}}$, where β is the propagation constant of the mode of light within a Δn confined waveguide core) and n_{eff} is the effective index of the propagating light mode ($\beta=n_{\text{eff}}k_o$). The resonant condition determines once a waveguiding mode's incident energy enters from the bus into the ring and circuits around, whether its electric field adds constructively with more incoming energy from the bus. This incident energy continues to circuit the ring a characteristic number of times n , which we call the Circuit Number:

$$n = \frac{L_{\text{eff}}}{2\pi r} = \frac{v_g \tau}{2\pi r} = \frac{v_g}{2\pi r} \frac{2Q}{\omega} = \frac{Qv_g}{\pi\omega r}$$

(5.3)

L_{eff} is the effective path length traveled by the waveguide mode within the ring resonator, which is the product of the mode's group velocity v_g and resonator lifetime τ (the characteristic time light remains trapped within the resonator). τ is related to the resonant structure's total quality factor Q ($Q \equiv \omega\tau/2$)[110]. If the incident mode energy circuits the ring a characteristic n number of times, before leaking back out, this means that in steady state, the relation between the incident electric field amplitude within the bus, s_i , and the field amplitude within the ring, A , is:

$$A = n(\kappa s_i).$$

(5.4)

Substituting in the expression for n and taking the amplitude squared of equation (5.4) allows us to express in terms of power (where $P_{ring} \propto |S_r|^2$):

$$P_{ring} = \left(\frac{Q\kappa v_g}{\pi\omega r} \right)^2 P_{bus}.$$

(5.5)

We express the unit less coupling constant κ in terms of the resonator lifetime[104]:

$$\kappa^2 = \mu^2 \frac{2\pi r}{v_g} = \frac{2}{\tau_e} \frac{2\pi r}{v_g} = \frac{\omega}{Q_e} \frac{2\pi r}{v_g}.$$

(5.6)

Where τ_e is the characteristic lifetime for light to couple out of the ring resonator and back into the bus, and Q_e is defined as the external quality factor (where $Q_e = \omega \tau_e / 2$).

The relation between the total quality factor Q and the external quality factor Q_e comes from relating the rates of all loss mechanisms for light trapped within a resonator. They are,

$$\left[\begin{array}{c} \text{Total Rate of Escape} \\ \text{from Resonator} \end{array} \right] = \left[\begin{array}{c} \text{Rate of External} \\ \text{Coupling Loss} \end{array} \right] + \left[\begin{array}{c} \text{Rate of} \\ \text{Scattering Loss} \end{array} \right] + \left[\begin{array}{c} \text{Rate of Radiative} \\ \text{Turning Loss} \end{array} \right]$$

which we express mathematically,

$$\frac{1}{\tau} = \frac{1}{\tau_e} + \frac{1}{\tau_s} + \frac{1}{\tau_r}$$

(5.7)

multiplying through by $2/\omega$, we have

$$\frac{1}{Q} = \frac{1}{Q_e} + \frac{1}{Q_s} + \frac{1}{Q_r}.$$

(5.8)

Substituting equation (5.6) into equation (5.5), we conclude

$$P_{ring} = \frac{Q}{Q_e} \frac{Q}{r} \frac{2v_g}{\pi\omega} P_{bus}.$$

(5.9)

The Q/Q_e ratio physically accounts for the asymmetry of energy flow through available coupling mechanisms to the ring resonator: energy can couple in from the waveguide bus only through the external coupling mechanism, whereas energy within the ring resonator can couple out by external coupling, transmission loss and radiative turning loss. The Q/r ratio measures the aforementioned Circuit Number; it Q/r is proportional to the photon lifetime τ within the resonator, divided by the transit time required to circuit the ring once ($\text{transit}=2\pi r/v_g$). This factor measures the energy density within the cavity, and it is similar to the Purcell Factor[120], it does not represent the Purcell Effect.

As reference [120] makes clear, the Purcell Factor (arising from the Purcell Effect) is defined as a constant measuring the enhancement of spontaneous emission from a light-emitter, in the presence of a perturbation from an optical cavity or dielectric medium. The Purcell Factor is proportional to Q/V , and is thus similar to the factor $Q^2/Q_e r$ we derived in (5.9). We refer to the proportionality constant relating P_{ring} to P_{bus} hereon as a Modified Purcell Factor, bearing in mind that this factor is not measuring spontaneous emission enhancement, but rather the interferometric build-up of optical energy within the ring resonator.

We now examine the influence of the Modified Purcell Factor on the coupling strength between the waveguide bus and ring resonator (at either λ_s or λ_p).

5.3.2 Regimes of Coupling: Under-, Over- and Critical

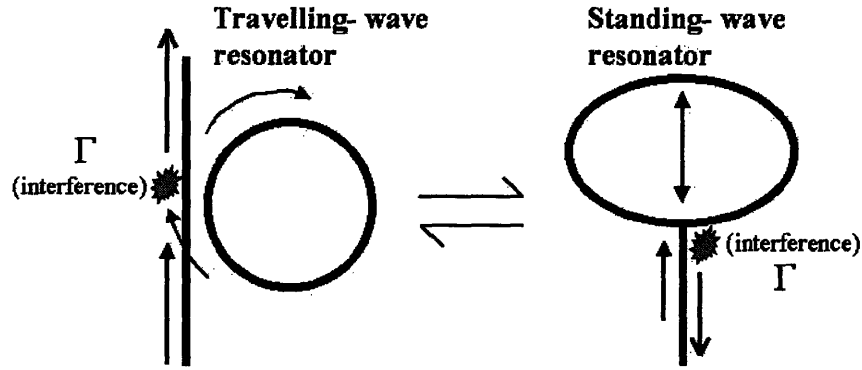


Fig. 5.4. Equivalence between a traveling-wave ring resonator and standing wave resonator cavity. Transmitted power downstream from the ring (open arrow-head in (a)) is equivalent to the reflected power from a resonator cavity (open arrow-head in (b)).

The traveling wave geometry (see Fig. 5.4.a) of a ring resonator implies that the power transmitted past the ring resonator (the open arrow in Fig. 5.4.a, also referred to as the power downstream from the ring resonator), represents the multi-interferometric effect (represented by the Modified Purcell Factor) of modes of light coupling out from the resonator and back into the waveguide. In a standing wave resonator, as schematically shows in Fig. 5.4.b, this same interferometric effect is quantified by Coupled Mode Theory by a steady-state reflection coefficient Γ ,

$$\Gamma = \frac{\frac{1}{\tau_r} - \frac{1}{\tau_o} - j(\omega - \omega_o)}{\frac{1}{\tau_r} + \frac{1}{\tau_o} + j(\omega - \omega_o)}$$

(5.10)

where $\omega=2\pi\nu=2\pi c/\lambda$ is the angular frequency of propagating light (in the waveguide bus, external to the resonator) and ω_o is the natural harmonic frequency (i.e. frequency of resonant confinement) for the resonator; in the case of the ring, the wavelength λ_o corresponding to ω_o must satisfy equation (5.2). For the ring resonator, the traveling-wave geometry interprets equation (5.10) not as a reflection coefficient, but rather as the transmission coefficient of optical power in the waveguide bus, downstream from the ring. (See the location of Γ in Fig. 5.4.a versus Fig. 5.4.b.).

$1/\tau_o$ is referred to as the damping rate of the resonator, and is the sum of all loss rates within the resonator, in this case

$$\frac{1}{\tau} = \frac{1}{\tau_e} + \frac{1}{\tau_s} + \frac{1}{\tau_r} + \frac{1}{\tau_{Er}} \equiv \frac{1}{\tau_e} + \frac{1}{\tau_o}$$

(5.11)

where τ_{Er} is the characteristic time for photon absorption inside a cavity doped with N Er atoms per cm^3 ; τ_{Er} is related to the Er absorption coefficient α_{Er} ($\alpha_{Er}=N_1\sigma_{13}$ for λ_p) by multiplying (5.11) through by $1/v_g$:

$$\alpha = \alpha_e + \alpha_s + \alpha_r + \alpha_{Er}$$

(5.12)

α_e represents the coupling rate from resonant cavity out to the waveguide bus, re-expressed as coupling loss per unit length. In Fabry Perot cavity lasers, α_e is typically referred to as the “mirror loss”[3].

Equation (5.10) represents the confinement physics of the Modified Purcell Factor, while making mathematically obvious that optimal resonant coupling between bus and ring must satisfy two Impedance Matching Conditions:

- (1) Resonance: the incident signal wavelength must resonantly match its *external frequency* ω to the natural harmonic frequency of the resonator ω_0 (i.e. per equation (5.2), the effective signal wavelength λ/n_{eff} must integrally fit into the ring circumference $2\pi r$)
- (2) Coupling Strength: The *external coupling* strength or rate $1/\tau_e$ must match the damping strength or dissipation rate $1/\tau_0$ of the resonator (i.e. the evanescent coupling distance between bus and ring must be optimally chosen).

Electrical circuit[121] theory refers to conditions (1) and (2) (and consequently having $\Gamma=0$) as the impedance matching of a resonator to a transmission line (Figure 5.5 shows the Reflection Diagram plotted from (5.10)).

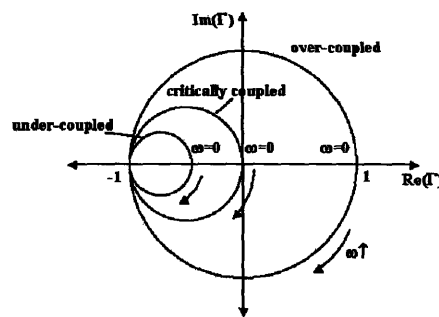


Figure 5.5. Reflection diagram reproduced from [110], plotting $\text{Im}(\Gamma)$ versus $\text{Re}(\Gamma)$.

At resonance, we examine the three coupling strength conditions of (a) undercoupling, (b) critical coupling, and (c) overcoupling from a transient $t=0$ onset to

$t \rightarrow \infty$ steady state, and establish conclusions for the performance of Er-doped ring resonators.

In approaching steady state, the traveling wave field amplitude builds up within the ring from initial value $A_{\text{incoupled}}$ to a steady state value A_{steady} . We define the steady state power leaking from the ring back out into the waveguide bus as $|s_{\text{leak}}|^2$, where

$$s_{\text{leak}} = \kappa A_{\text{steady}}$$

(5.13)

A signal that enters the ring through evanescent coupling (from the waveguide bus) experiences a $\sim \pi/2$ phase shift due to transmission from a lower refractive index cladding n_1 into the higher refractive index of the ring's waveguide core n_2 (this is the phase transmission principle of wave optics for light entering a higher refractive index medium, see Fig. 5.3.b). Upon circuiting the ring and leaking back out into the bus, after the characteristic time τ_e , a second phase shift $\sim \pi/2$ is imparted to the field, this time due to transmission from the cladding n_1 into the waveguide bus higher refractive index n_2 . Thus, s_{leak} is $\sim \pi/2 + \pi/2 = \pi$ out of phase with s_i .

In steady state, if $|s_{\text{leak}}| = |s_i|$, complete destructive interference occurs in the waveguide bus and no incident power transmits past the ring resonator, i.e. $s_t = s_{\text{leak}} + s_i = 0$.

We derive an expression for the transmitted power $|s_t|^2$, using our Modified Purcell Factor expression:

$$A_{\text{steady}} = \left[\frac{Q}{Q_e} \frac{2Qv_g}{\pi\omega r} \right]^{1/2} s_i e^{i\pi/2} = \left[\left(1 + \frac{1/\tau_o}{1/\tau_e} \right)^{-1} \frac{2Qv_g}{\pi\omega r} \right]^{1/2} s_i e^{i\pi/2}.$$

(5.14)

The field that leaks back out to the waveguide in steady state s_{leak} , is then

$$s_{leak} = \kappa A_{steady} e^{i\pi/2} = - \left[4 \left(1 + \frac{1/\tau_o}{1/\tau_e} \right)^{-1} \frac{Q}{Q_e} \right]^{1/2} s_i = -2 \left(1 + \frac{1/\tau_o}{1/\tau_e} \right)^{-1} s_i.$$

(5.15)

We observe in the special case of $\frac{1}{\tau_e} = \frac{1}{\tau_o}$, $s_{leak} = -s_i$. We define the field in the ring for

this case as A_{steady}^{crit} .

$$A_{steady}^{crit} = \left[\frac{Qv_g}{\pi\omega r} \right]^{1/2} s_i e^{i\pi/2}.$$

(5.16)

We now examine the three cases of coupling strength.

(a) undercoupling: $\frac{1}{\tau_e} < \frac{1}{\tau_o}$

When the external coupling rate $1/\tau_e$ is less than the dissipation rate $1/\tau_o$, the ring resonator acts as a weakly coupled absorptive device to the waveguide bus. The large amount of damping with the resonator results in a steady state (electric) field which can not build up to a large value ($A_{steady} < A_{steady}^{crit}$), and therefore an sufficient amount of interference occurs between the leaked power and the incident power in the bus, i.e.

$$|s_{leak}| < |s_i|.$$

(5.17)

The incident power $|s_i|^2$ continues downstream past the ring, with a diminished value

$$|s_t|^2 = |s_{leak} + s_i|^2 < |s_i|^2.$$

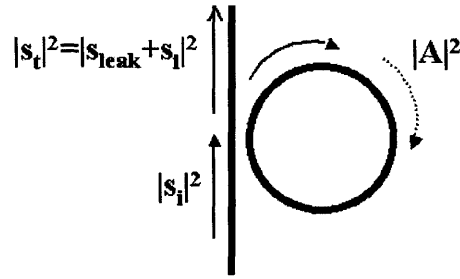


Figure 5.6. Undercoupling.

The undercoupled case results in an Er-doped ring resonator leaching a fraction $((|s_i|^2 - |s_t|^2) / |s_i|^2)$ of the incident power from the waveguide bus. The higher the Q of the ring, the smaller this fraction of power leached. We conclude that in the absence of the resonator,

$$\frac{s_t}{s_i} = 1$$

(5.18)

and with the resonator, in this weakly undercoupling regime,

$$0 < \frac{s_t}{s_i} < 1.$$

(5.19)

(b) critical coupling: $\frac{1}{\tau_e} = \frac{1}{\tau_o}$

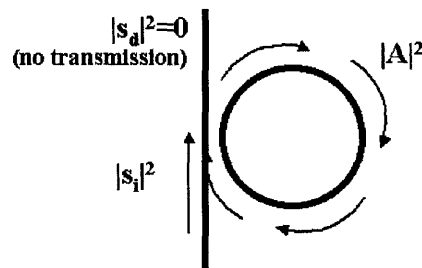


Figure 5.7. Critical coupling.

When the external coupling rate $1/\tau_e$ is equal to the dissipation rate $1/\tau_o$, the ring acts as a perfect power drop to the waveguide bus. $A_{\text{steady}}=A_{\text{steady}}^{\text{crit}}$, and we observe from equation (5.15),

$$|s_{\text{leak}}| = |s_i|$$

(5.20)

(specifically $s_{\text{leak}}=-s_i$) and $s_t=0$. The net flow of power downstream from the ring is zero.

We conclude in this critical coupling regime,

$$\frac{s_t}{s_i} = 0.$$

(5.21)

(c) overcoupling: $\frac{1}{\tau_e} > \frac{1}{\tau_o}$

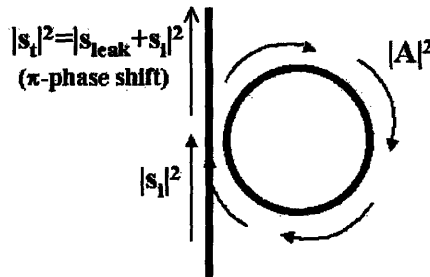


Fig. 5.8. Overcoupling.

When the external coupling rate $1/\tau_e$ is larger than the dissipation rate $1/\tau_o$, the ring acts as a weakly absorbing phase delaying device, to the waveguide bus. As power builds within the ring by coherently adding up while making n circuits around the ring, the low dissipation rate $1/\tau_o$ implies steady state power build-up in the device will now exceed $A_{\text{steady}}^{\text{crit}}$ (i.e. $A_{\text{steady}} > A_{\text{steady}}^{\text{crit}}$). This results in

$$|s_{leak}| > |s_i|$$

(5.22)

and the signal travels in the bus downstream from the micro-ring, with a π -shift. Thus, the micro-ring here acts as a weakly absorptive π -phase shift element. Note that in the limit of $1/\tau_e \rightarrow \infty$ or $1/\tau_o \rightarrow 0$, $s_{leak} \rightarrow -2s_i$, and where the resonator is now a purely π -phase shift element to the waveguide bus. $1/\tau_e \rightarrow \infty$ is equivalent to saying we no longer have a resonant (ring) cavity that couples light away from the waveguide bus; $1/\tau_o \rightarrow 0$ is possible with the presence of population inverted Er providing gain that counteracts the resonator loss mechanisms. If it was possible to have $1/\tau_o < 0$, we further observe that up until $1/\tau_o \leq -1/\tau_e$, equation (5.15) tells us gain (i.e. $|s_t| > |s_i|$) is possible. At $1/\tau_o \leq -1/\tau_e$, (5.15) blows up, representing the onset of lasing.

We thus conclude in this overcoupling regime,

$$-1 < \frac{s_t}{s_i} < 0$$

(5.23)

and in reducing damping through population inversion of the Er in the ring, we can achieve

$$-\infty < \frac{s_t}{s_i} < -1$$

(5.24)

i.e. gain with a π -phase shift can be delivered to the waveguide bus, up until the lasing threshold of the ring begin to contribute a laser emission to s_t .

The results of conditions (a)-(c) on signal propagation downstream from the micro-ring ($|s_t|^2$) have been summarized in the plot below.

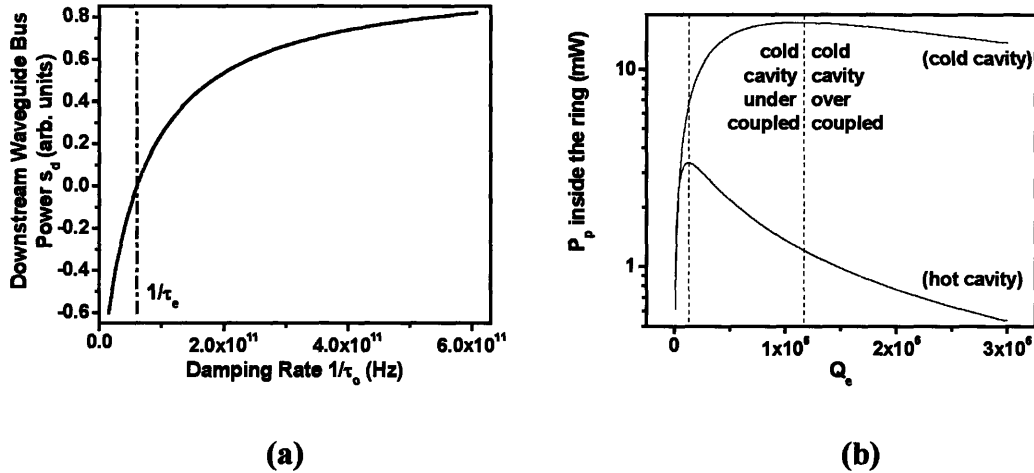


Figure 5.9. (a) Plot of s_t versus $1/\tau_o$, for a fixed $1/\tau_e$. Using SiON case study parameters. (b) P_{ring} versus Q_e shows optimal power transfer at critical coupling $Q_e = Q_o$.

Figure 5.9.a shows the transmitted field s_t downstream from the ring resonator, as a function of damping rate. For damping rates less than $1/\tau_e$, the system is overcoupled and s_t propagates with a π -phase shift with respect to incident field s_i (the negative values for s_t in the plot). For damping rates greater than $1/\tau_e$, less power couples into the resonant cavity, and $s_t \rightarrow +1$. Figure 5.9.b returns to the Modified Purcell Factor expression (5.9) and plots power within the ring resonator, as a function of Q_e , for a cavity free of Er (dubbed “cold cavity”) and a cavity doped with 2×10^{20} Er/cm³ (dubbed “hot cavity”). Device parameters for this simulation are listed in Table 5.1. We see that power within the resonant cavity is maximized at critical coupling, and that the presence of Er, a loss mechanism within the ring resonator which can be bleached by high power (i.e. the Er is a saturable absorber for λ_p), (i) changes the profile of the P_p versus Q_e plot,

and (ii) shift critical coupling to a lower Q_e value. This observation must be kept in mind when designing power efficient ring resonator amplifiers; we'll return to it in section 5.4.2.

5.4 Applications

To study the feasibility of resonant structures for creating even higher gain efficiency WOAs than high Δn waveguides, we (i) quantified the performance and size advantage of ring resonators as a function of external device quality factor Q_e , and (ii) developed two alternative device applications based on absorptive/light emitting rings: a WDM broadband laser light source and an integrated WDM de-multiplexer for Ge or SiGe photo-detectors.

From a theoretical framework, it is simpler to discuss the laser light source design and its processing requirements before generalizing to the performance and size study for ring resonator WOAs (R-WOAs). We present our study in the following order of device analysis: (i) laser light source, (ii) R-WOA (ring Resonator Waveguide Optical Amplifier) and (iii) integrated de-multiplexer.

All device simulation and analysis have been done using the SiON case study presented at the end of chapter 2, in order to make direct comparison of optical amplification. Table 5.1 re-lists the device parameters.

5.4.1 Rings for a WDM Laser Light Source

The ms-scale radiative lifetime of the Er atom makes it a very difficult light emitter with which to build a lasing cavity. A laser cavity is a resonant structure trapping a light emitter's photons and releasing them to the outside world, at an escape rate lower

N	$2 \times 10^{20} \text{ cm}^{-3}$
$Q_e(\lambda_s), Q_e(\lambda_p)$	$10^5, 1.43 \times 10^8$
α_s, α_p (scatt+rad)	$0.2+0.1 (\lambda_s), 0.1+0.1 (\lambda_p) \text{ dB/cm}$
$\alpha_{\text{host}} (\lambda_s)$	0.8 dB/cm
τ_{Er} (total lifetime)	10 ms
C_{24}	$4 \times 10^{-18} \text{ cm}^3/\text{s}$
$\Delta n, \text{Area}$	$0.155, 2.0 \times 0.5 \text{ } \mu\text{m}^2$

Table 5.1. Summary of device parameters used for ring laser and amplifier.

than the rate of photon generation within the cavity. This lower escape versus generation rate guarantees in steady state, an accumulation of photons within the resonant cavity. (The role of resonance here is to determine the spectral distribution, i.e. which λ_o , of photons will be selectively accumulated within the cavity.) The steady state accumulation, or density, of photons is clamped by the feedback effect of stimulated emission, which acts to reduce the total rate of light generation and match it to the escape rate.

As seen from the theory section of this chapter, the escape rates through which photons couple out of a ring resonator are external coupling to the waveguide bus, and two loss mechanisms—scattering loss and radiative turning loss. It is the low photon generation rate (whose maximum value is $\sim v_g \sigma_{21} N$) of the ms-scale (long lifetime τ implies small cross-section σ_{21}) light-emitting Er atom that makes it impossible (even at $N=2 \times 10^{20} \text{ cm}^{-3}$) to overcome the rates of loss mechanisms occurring from $\sim 5 \text{ dB/cm}$ transmission loss.

Current reactive ion etched processes by our group[9] have produced strip SiON waveguides with measured transmission losses as low as 0.2-1 dB/cm. This is the state of

the art, as current strip waveguide propagation losses in $\Delta n=0.1-0.7$ waveguides range from 1-10 dB/cm in the literature[122]. Er-based lasers have thus far been developed in low Δn optical fibers[32] and only recently in ultra-smooth silica microspheres[116]. Our study set out to develop an Er-doped laser similar to [116], but in a planar SiON ring resonator, and not a (effectively) free-standing SiO₂ microsphere. Our study seeks to answer two questions:

(i) Minimum Loss Threshold: what is the minimum reduction in scattering + radiative loss required for Er-doped Si₃N₄↔SiON ring resonators, in order to achieve lasing; and

(ii) Power Performance: for a selected scattering + radiative loss per unit cm, what magnitude output signal power at λ_s can we expect for a given input pump power at λ_p .

(i) Minimum Loss Threshold

The feedback effect of clamping a lasing cavity's light generation rate to equal the total escape rate is defined as the gain clamping condition[60], identifying a threshold value for small signal gain at the onset of lasing:

$$\gamma_{th} = N_2\sigma_{21} - N_1\sigma_{12}|_{th} \cong \sigma_{21}(\Delta N_{th}) = \alpha_{cold}$$

(5.25)

where ΔN_{th} is the threshold level of population inversion $N_2(P_{p,th})-N_1(P_{p,th})$. We define α_{cold} is the total sum of mechanisms by which photons escape the cavity (i.e. $\alpha_{cold} = \alpha_e + \alpha_t + \alpha_r$). The 'cold' subscript refers to these being escape mechanisms for photons out of a cold cavity, i.e. a cavity with no Er. With Er present, an additional loss mechanism of

Er absorption is present, which the ΔN term in (5.25) explicitly accounts for by giving us the net photon generation by the Er atom.

Expressing α_{cold} in terms of a cold cavity quality factor Q_{cold} allows us to re-write (5.25),

$$Q_{\text{cold}} = \frac{\omega_0}{2\sigma\Delta N_{\text{th}}\nu_g}.$$

(5.26)

Using the expression (2.3) for excited state population N_2 from chapter 2 (with and without upconversion) and the relation $\Delta N \approx 2N_2 - N_1$, we solve for a required threshold pump power $P_{\text{p,th}}$ (or more generally, a required pump photon flux threshold $\phi_{\text{p,th}}$) in order to reach the threshold population inversion level ΔN_{th} . Expression (2.3) requires

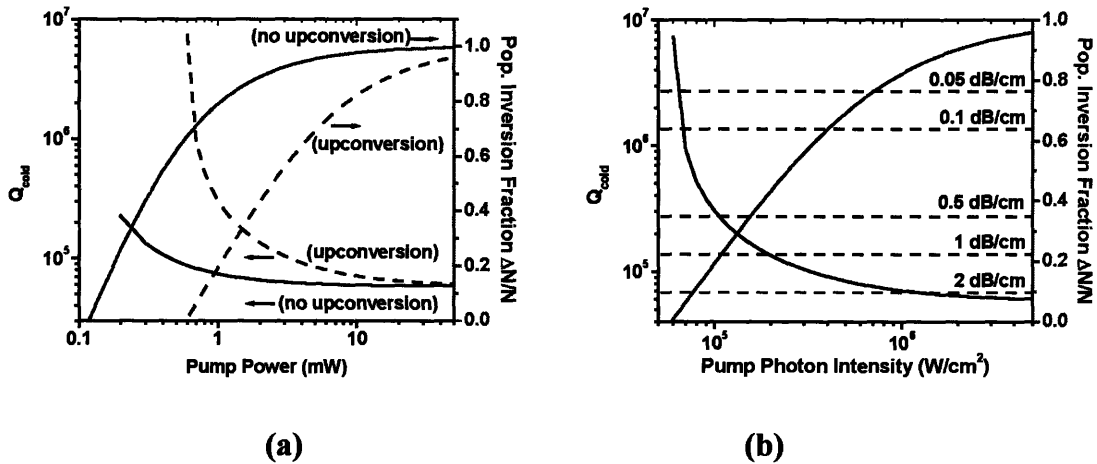


Figure 5.10. (a) Lasing threshold calculation for the SiON case study, in units of threshold pump power $P_{\text{p,th}}$. (b) Magnification of upconversion case from (a), in units of threshold pump power flux $\phi_{\text{p,th}}$. Right axis in both plots show the fraction threshold population inversion $\Delta N_{\text{th}}/N$ corresponding to $P_{\text{p,th}}$, $\phi_{\text{p,th}}$.

calculation of stimulated emission and absorption rates W_{12} , W_{21} , due to the presence of λ_s photons within the cavity. Until the onset of lasing, the population density of λ_s photons is negligible, in comparison to the density of pump λ_p photons; it is convention for lasing threshold calculations to assume $W_{21} \cong W_{21} \approx 0$ in order to approximately solve for $P_{p,th}$.

The results of our calculation are shown in Figure 5.10.a as a plot of Q_{cold} and $\Delta N_{th}/N$ versus pump power $P_{p,th}$ (SiON case study), with and without upconversion. In order to approximate $Q_{cold} \approx Q_e$, we suggest materials and processing constraints should limit scattering + radiative turning loss ($\alpha_s + \alpha_r$) in these devices to be $\sim 10\times$ lower than the cavity external coupling loss α_e (thus resulting in $Q_{loss} \approx 10Q_e$ and therefore $Q_{cold} = (Q_e^{-1} + Q_{loss}^{-1})^{-1} \approx Q_e$).

We observe that with even 10 mW of pump power within the resonator, the upconversion-free case is close to complete population inversion; with upconversion, there is only 80% inversion at 10 mW pump power. We examine the requirements for lasing more carefully using the upconversion case in Figure 5.10.b: horizontal lines representing cold cavity loss α_{cold} values, in terms of Q_{cold} , are overlaid. For a given Q_{cold} , pump power must exceed the value marked by the threshold curve in order to initiate lasing.

Prior research[123] in our group suggests that the $\sim 10\%$ insertion loss involved in coupling a III-V pump laser's optical mode into a high Δn waveguide implies we should plan for a pump power budget of $P_p = 1-10$ mW into a waveguide core. For this range of pump powers, we observe that $Q_{cold} \sim 7 \times 10^4$ is a lower limit value for lasing in ring

resonators. This corresponds to a cold cavity loss on the order of $\alpha_{\text{cold}} \sim 2$ dB/cm. Recalling our suggestion that transmission + radiative loss rate be $\leq 10\%$ of the external coupling rate, implies that $\alpha_s + \alpha_r \cong 0.1 \times \alpha_{\text{cold}} = 0.2$ dB/cm and $Q_e \cong Q_{\text{cold}} \times (10/9) \sim 8 \times 10^4$.

A required waveguide transmission loss of $\alpha_s + \alpha_r = 0.2$ dB/cm is similar to our loss requirements of chapter 2. Our best reported materials loss ($\equiv \alpha_{\text{host}}$) figures from chapter 4 were 0.8 dB/cm for SiON:Er (refractive index $n=1.65$), contributing a third loss mechanism to waveguide transmission loss. α_{host} may be further reduced by current research activities in our group, specifically plans to grow Er co-doped CVD films of Si₃N₄ or SiON at MIT within the next two years. We design our ring laser study with a total transmission loss value of $\alpha_t + \alpha_r = (0.2 + 0.1)$ dB/cm = 0.3 dB/cm. For a total cold cavity loss of $\alpha_{\text{cold}} = 1.75$ dB/cm, this implies $\alpha_e = 1.45$ dB/cm, corresponding to an external coupling of $Q_e = 10^5$.

Since our pump is optical as well, selecting $Q_e = 10^5$ at λ_s implies a weaker external coupling rate at λ_p : the smaller pump wavelength has a weaker evanescent coupling between bus and ring, than the longer signal wavelength. Fig. 5.11 plots a one-dimension calculation of quality factors Q_e at λ_s and λ_p , as a function of the gap distance separating waveguide bus and ring resonator (SiON case study). We see that a $Q_e = 10^5$ at λ_s is achieved with a gap spacing of 1.3 μm . For this gap spacing, $Q_e = 1.43 \times 10^8$ at λ_p .

This value of $Q_e(\lambda_p)$ implies the optical pump is undercoupled to the ring resonator, thus influencing the *external* power efficiency of our ring resonator laser, as we'll see in section (ii). While the effect is not prohibitive in its magnitude, it has

relevance for the R-WOA study in section 5.4.2, from the perspective of optimizing device gain efficiency.

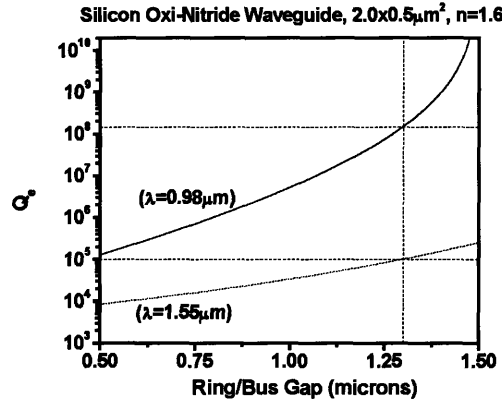


Fig. 5.11. Coupling strength of waveguide bus to resonator. Plot of Q_e and coupling efficiency η versus gap δ . Extrapolate δ required for given Q_e . The derivation of these plots is shown in Appendix 2. (Calculation performed by Daniel Sparacin, MIT.)

(ii) Power Performance

To quantitatively simulate the photon build-up within a resonant structure, we require coupling the rate equation for Er excitation, equation (2.3), with the rate equation for photon *number* generation within a resonant cavity[60],

$$\frac{dn}{dt} = v_g \sigma_{21} \frac{l}{L} (N_2 - N_1)(n + 1) - \frac{l}{L} v_g \alpha_{cold} n$$

(5.27)

where l is the length of the cavity and L is the effective length of the resonantly trapped mode of light (when confining light within non-metallic materials, an evanescent tail of light leaks out of the confining cavity, thus $L > l$). The first term represents stimulated emission and spontaneous emission within the cavity, occurring at a gain rate of

$v_g \gamma = v_g (N_2 \sigma_{21} - N_1 \sigma_{12}) \approx v_g \sigma_{21} (\Delta N)$. Writing a rate equation for photon number allows us to re-express spontaneous emission as the equivalent of stimulated emission occurring from 1 photon within the cavity optical mode. This equivalence will help to solve analytically for n with ease. The second term in (5.27) represents the rate of escape of cavity photons through the cold cavity loss mechanism (external coupling and transmission + radiative loss). The gain clamping condition allows us to re-write $\alpha_{\text{cold}} = \gamma_{\text{th}} \approx \sigma_{21} \Delta N_{\text{th}}$. Steady state solution of (5.27) yields

$$\bar{n}_s = \frac{\sigma_{21} \Delta N}{g_{\text{th}} - \sigma_{21} \Delta N} = \frac{\sigma_{21} \Delta N}{\sigma_{21} \Delta N_{\text{th}} - \sigma_{21} \Delta N}.$$

(5.28)

Recalling from chapter 2, the expression for $\Delta N = 2N_2 - N_1$, without upconversion ($W_{12} \approx W_{21}$), is

$$\Delta N = \frac{N(W_{13} - \frac{1}{\tau})}{W_{13} + 2W_{21} + \frac{1}{\tau}}$$

(5.29)

which we expand using $W_{21} = \phi_s \sigma_{21}$ and the identity photon flux $\phi = n_s v_g / V$ (V is the cavity volume $2\pi r \times \text{Area}$); defining a variable n_{sat} as

$$n_{\text{sat}} = \frac{W_{13} + \frac{1}{\tau}}{2v_g \sigma_{21}} V$$

(5.30)

we re-express (5.29) as

$$\Delta N = \frac{N(W_{13} - \frac{1}{\tau})}{(W_{13} + \frac{1}{\tau}) \left(1 + \frac{\bar{n}_s}{n_{sat}}\right)}$$

(5.31)

Defining the new variables $x = \frac{\Delta N}{\Delta N_{th}}$ and $y = \frac{\Delta N_0}{\Delta N_{th}}$ (where $\Delta N_0 = \frac{N(W_{13} - \frac{1}{\tau})}{(W_{13} + \frac{1}{\tau})}$ is the

small signal population difference) we write equations (5.28) and (5.31) in the simpler form

$$\bar{n}_s = \frac{x}{1-x} \quad \& \quad x = \frac{y}{1 + \frac{\bar{n}_s}{n_{sat}}}$$

(5.32)

which can be substituted into one another to yield the quadratic equation

$$\bar{n}^2 + n_{sat}(1-y)\bar{n} - n_{sat}y = 0$$

(5.33)

whose solution gives us the generated signal power as $P_s = h\nu_s \frac{v_g}{V} \bar{n}_s \frac{A}{\Gamma_s}$.

The upconversion expression from (2.3) is re-expressed as

$$x = -y_1 \left[1 + \frac{n_s}{n_{sat}}\right] + \sqrt{y_1^2 \left[1 + \frac{n_s}{n_{sat}}\right]^2 + y_2 \left[1 + \frac{n_s}{n_{sat2}}\right]} - y_3$$

(5.34)

where $y_1 = \frac{W_{13} + \frac{1}{\tau}}{\Delta N_{th}^2 C_{24}}$, $y_2 = \frac{4NW_{13}}{\Delta N_{th}^2 C_{24}}$, $y_3 = \frac{N}{\Delta N_{th}}$ and $n_{sat2} = \frac{VW_{13}}{\sigma_{21}v_g}$. Solving the

first expression in (5.32) for x and equating it to (5.34), we proceed to numerically solve for n_s .

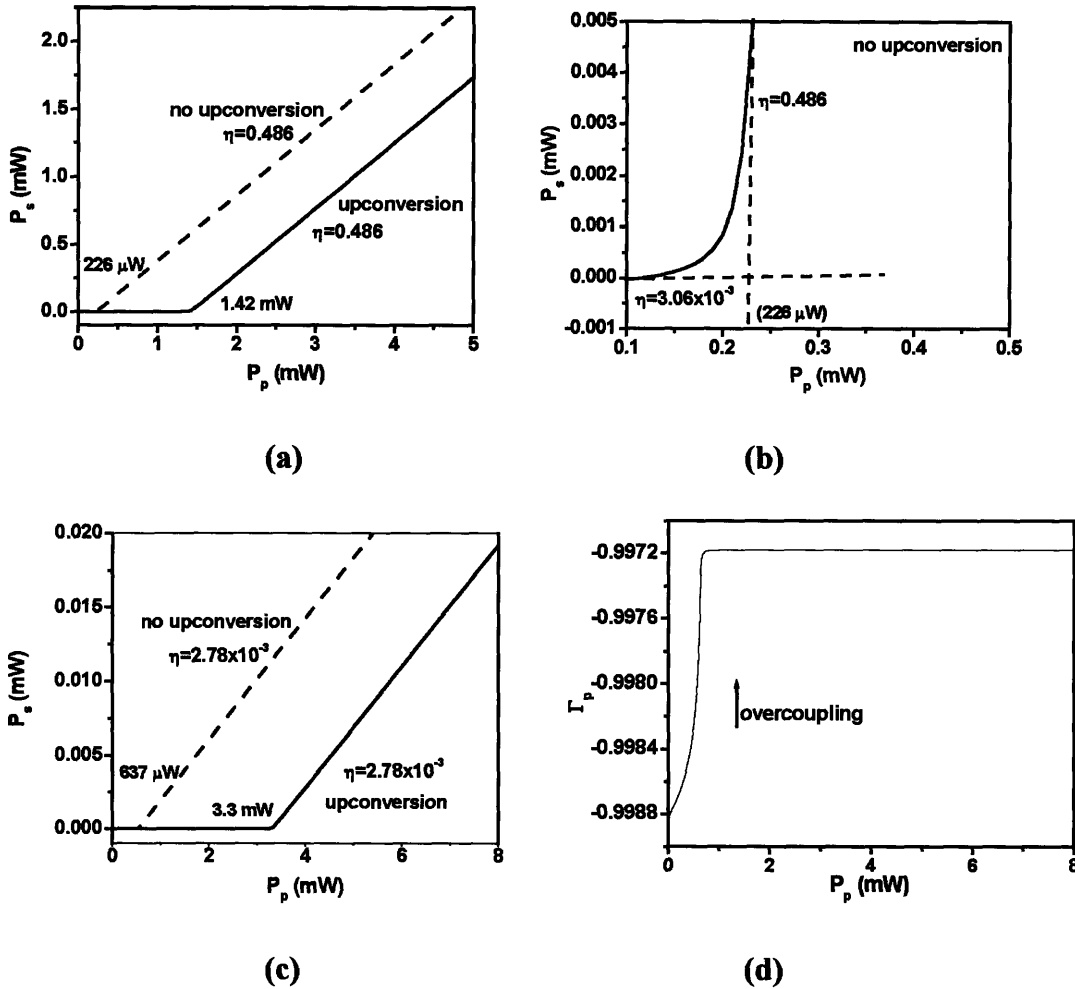


Fig. 5.12. (a) Signal power versus pump power inside the resonator, with and without upconversion. (b) Magnification of (a), showing abrupt change in quantum efficiency above and below lasing threshold. (c) Signal power versus pump power outside the resonator, with and without upconversion, shows a lower slope and a higher lasing threshold for the upconversion case. (d) Coupling of optical pump from the waveguide bus into the ring laser clamps to a constant value above lasing threshold.

Fig. 5.12.a versus Fig. 5.12.c show the effect of having an ultra-high Q_e on the lasing performance of the ring resonator, with respect to the waveguide bus. Fig. 5.12.a plots the lasing power (at λ_s) generated inside the ring resonator, versus the pump power inside the resonator. Lasing threshold (with and without upconversion) and internal differential slope efficiency η_{int} are listed in Table 5.2. Fig. 5.12.c plots the lasing power which leaks out to the waveguide bus, as a function of the incident pump power within the bus. Here we observe a $\sim 140\times$ decrease in external differential slope efficiency η_{ext} , relative to η_{int} . Despite this poor performance, we observe such a laser design is reasonable for Microphotonics: for an 8 mW pump power, an Er-doped ring laser with upconversion, gives an output lasing power of close to 20 μ W. Fig. 5.12.b is a magnification of Fig. 5.12.a to visually confirm the presence of a lasing threshold (signified by abrupt change in slope).

Fig. 5.12.d plots the pump transmittance Γ_p (Γ is defined by the Coupled Mode Theory in time, see section 5.3.2) for the upconversion-free simulation, in the waveguide bus. We observe the transmittance improves as its level of undercoupling dynamically decreases with Er excitation up to lasing threshold, at which point the Er population inversion is gain-clamped, and hence the damping rate $1/\tau_o$ (and Γ_p) become independent of P_p . Fig. 5.12.d shows us that the high Q_e requirements at λ_s , in order to ensure signal lasing, make it impossible to critically couple the pump λ_p to the ring resonator. However, as Fig. 5.12.c shows us, the pump power requirements are not prohibitive: $P_p=5-8$ mW in the waveguide bus is feasible, given a 10% insertion loss from a 100-mW III-V pump power source. Given that the pump will not be critically coupled to the ring laser, we note

this implies both a lasing signal non-zero pump power will emerge from the waveguide bus, downstream from the ring laser.

	P_{th}	$P_{th, upconversion}$	η	$\eta_{upconversion}$
Internal	226 μ W	1.42 mW	0.486	2.78×10^{-3}
external	637 μ W	3.3 mW	0.486	2.78×10^{-3}

Table 5.2. Summary of lasing threshold and quantum efficiencies (with and without upconversion), both inside and outside the ring laser.

We note that the derivation of equation (5.29) relied on our assumption of the Er atom as an effective two-level system, i.e. we assume $N_3 \approx 0$, or equivalently, the transition rate R_{32} from level 3 to level 2 (see chapter 2 for definitions) to be $\sim \infty$. This results in the W_{31} transition due to pump photons to be zero, and therefore laser light emission (at λ_s) can't saturate with pump power. In reality $R_{32} \sim 10^5 \text{ s}^{-1}$ [4] for Er in glass hosts. For optical pump rates $W_{13} > R_{32}$, we should observe saturation in real devices, and this corresponds to a pump power (inside the ring laser) upper limit of $\sim 400 \text{ mW}$ at $\lambda_p = 980 \text{ nm}$, for the SiON case study.

Our most significant processing challenge are (i) improving the processing of waveguides to create ultra-low scattering loss for waveguide cores closer in composition to Si_3N_4 , and (ii) further reduction of host material absorption (by perhaps eventually shifting from PVD to CVD deposition techniques) than our current SiON:Er material. Table 5.3 lists our ring laser design summary for three index difference waveguides. These three designs have been implemented into a lithography mask for patterning Er-doped ring lasers with vertical coupling to undoped waveguide buses. SiON:Er rings are being developed this summer as a preliminary experimental attempt to observe lasing,

	Si-rich Si ₃ N ₄	Si ₃ N ₄	SiON
n_{core}	2.2	2.0	1.6
$\Delta n = n_{\text{core}} - n_{\text{cladding}}$	0.75	0.54	0.14
Dimensions: $l \times w$ (μm^2)	0.8×0.3	0.8×0.5	2.0×0.5
$\lambda = 1.55 \mu\text{m}$: n_{eff}, n_g	1.675, 2.195 (TE)	1.654, 2.051 (TE)	1.481, 1.547 (TE)
$\lambda = 0.98 \mu\text{m}$: n_{eff}, n_g	1.896, 2.303 (TE) 1.793, 2.336 (TM)	1.813, 2.092 (TE) 1.789, 2.11 (TM)	1.516, 1.594 (TE) 1.509, 1.589 (TM)
α_{scatt} (1.55 μm) (0.98 μm)	0.15 dB/cm 0.1	0.15 dB/cm 0.1	0.15 dB/cm 0.1
Ring radius (μm)	10	15	50
α_{rad} (1.55 μm) (0.98 μm)	0.15 dB/cm 0.1	0.15 dB/cm 0.1	0.15 dB/cm 0.1
Free spectral range (TE modes) (1.55 μm) (0.98 μm)	(4 FP peaks within FWHM) • 7.92 nm • 2.88 nm	(5 FP peaks within FWHM) • 6.04 nm • 2.32 nm	(9 FP peaks within FWHM) • 3.20 • 1.20
Waveguide bus-resonator gap	0.41 μm	0.41 μm	1.3 μm
Q_e (1.55 μm) (0.98 μm)	1.0×10^5 2×10^8	1×10^5 2×10^8	1×10^5 1.43×10^8
Q_{Er} (0.98 μm) Er ground state absorption of pump	(t=0s) 1.07×10^5 (t=steady state) 8.65×10^5	(t=0s) 1.07×10^5 (t=steady state) 8.65×10^5	(t=0s) 1.07×10^5 (t=steady state) 8.65×10^5

Table 5.3. Summary of ring laser device dimension and specifications. Designs implanted in lithography mask *MASK Amplifier H-tree* (see chapter 2 introduction image).

with $\alpha_{\text{host}}=0.8$ dB/cm and $\alpha_s+\alpha_r\sim 0.3$ dB/cm. All three designs in Table 5.3 make use of an SiO_2 cladding.

Figure 5.13 shows the multiple Fabry-Perot modes that exist within the SiON:Er case study's $r=50$ μm ring radius design. The SiON:Er ring radius cannot be smaller than 50 μm , due to our $\alpha_r=0.1$ dB/cm constraint. We conclude that when overlapped with the Er emission profile in SiON, there are several lasing lines. The ring laser is radiative turning loss limited to be a multiple-wavelength emitting broadband laser. The number of lasing peaks in turn decreases the differential slope efficiency of our simulated design; hence more power efficient lasers will be possible in Si_3N_4 :Er (provided transmission loss and host material losses can be reduced), whose smaller ring radius implies a larger free spectral range and thus fewer lasing peaks.

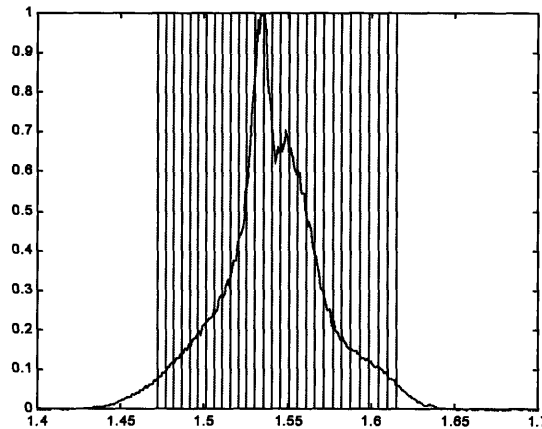


Figure 5.13. Ring resonator Fabry-Perot mode locations for SiON case study, overlapped with Er PL emission profile from SiON:Er.

5.4.2 Optical Amplifier

The resonant cavity of a ring resonator implies that trapped light circulates within an enclosed length multiple times: the effective path length of the photon is the

characteristic distance a photon travels while inside a resonator, $L_{\text{eff}}=v_g\tau$ (where $Q=\omega_c\tau/2$). For a ring resonator of diameter $2\pi r$, L_{eff} is independent of r and $L_{\text{eff}} \gg r$, in order for the interference effect of the resonator to apply. The ring resonator may therefore be an amplifying device which produces an effective path length for optical gain on the order of $L_{\text{eff}}=1$ cm, within a ring of diameter $50 \mu\text{m}$ (i.e. the SiON ring design from 5.4.1). Fig. 5.14 shows the areal footprint of a ring resonator whose radius is lower-limited to ensure a radial turning loss of ≤ 0.1 dB/cm (at $\Delta n=0.155$ this matches up to the $r=50 \mu\text{m}$ radius of our SiON case study). With increasing Δn , this lower limit on ring diameter decreases, and the footprint shrinks. Comparison is made with the 1 cm coil structure from chapter 2. We observe the ring resonator footprint is orders of magnitude of smaller. If an $L_{\text{eff}}\approx 1$ cm can be practically designed, this will be an ultra-compact gain element for the PLC.

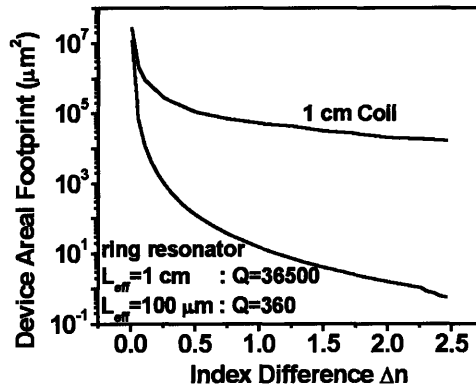


Fig. 5.14. Property Map 1. Areal footprint of a ring resonator, whose radius is radiative loss-limited ($\alpha_{\text{rad}}=0.1$ dB/cm), as a function of Δn . An effective path length $L_{\text{eff}}=1$ cm (or $100 \mu\text{m}$) corresponds to a total quality factor $Q=36\ 500$ (or 360).

The potential penalty for working with a resonant confinement design is intersymbol interference: the characteristic photon lifetime τ inside the resonator places

an upper limit for the speed of pulse-encoded transmission on the λ_s carrier wavelength. For example (see Table 5.4), a total quality factor of $Q \sim 10^5$ corresponds to a photon lifetime τ , which lengthens (in time) and causes interference (at photo-detection) between temporally encoded pulses spaced \sim less than 164 ps apart. As a safety margin, we suggest the temporal gap between pulses to be at least 10τ (Table 5.4)—corresponding (for a 50/50 duty cycle of pulse-encoding) to an information data rate of 0.3 Gbit/s. This intersymbol interference is equivalently described as a limitation in transmission bandwidth through a resonator: $Q=10^5$ implies a frequency bandwidth of $\Delta\nu=2$ GHz ($Q \approx \nu/\Delta\nu$), setting a constraint on the upper limit of transmission encoding to be (the bandwidth theorem $\Delta t \Delta\nu \sim \pi$), which for a 50/50 duty cycle corresponds to 0.3 Gbit/s.

Q	τ	Pulse Width	Data Rate	Bandwidth
10^5	164 ps	1.64 ns	0.3 Gbit/s	2 GHz

Table 5.4. Data transmission limit due to resonant confinement.

To evaluate the effect of resonant confinement on WOA device gain, we simulated the effect of varying external coupling Q_e , on the SiON case study used for our laser design. All other parameters were kept the same as in Table 5.1 (the input coupling powers of the signal and noise (at $\lambda_s=1.55$ μm) were 10 μW and 1 μW , respectively).

We modeled the input coupling of signal and optical noise into the ring resonator by expanding (5.27) into two equations, one for modeling signal photons n_s ,

$$\frac{dn_s}{dt} = v_g \sigma_{21} \frac{l}{L} (N_2 - N_1)(n_s) - \frac{l}{L} v_g \alpha_{cold} n_s + \frac{l}{L} v_g \left(\frac{\alpha_e}{\alpha_{cold}} \frac{1}{\pi r} \right) n_{s,bus}$$

(5.35)

and one for modelling noise photons n_n ,

$$\frac{dn_n}{dt} = v_g \sigma_{21} \frac{l}{L} (N_2 - N_1)(n_n + 1) - \frac{l}{L} v_g \alpha_{cold} n_n + \frac{l}{L} v_g \left(\frac{\alpha_e}{\alpha_{cold}} \frac{1}{\pi r} \right) n_{n,bus}$$

(5.36)

where $n_{s,bus}$ and $n_{n,bus}$ are the photon numbers (within the ring resonator volume V) corresponding to the 10 μ W incident signal and 1 μ W optical noise power in the waveguide bus. Since spontaneous emission only contributes to increasing the noise photon count, the first term in

(5.35) has an (n_s) factor (stimulated emission for signal photons), while the first term in

(5.36) only an (n_n+1) factor (stimulated + spontaneous emission for noise photons). We

solve these coupled equations with (5.29) in the same fashion as in the ring laser section,

with modifications $W_{21}=(\phi_s+\phi_n)\sigma_{21}=(n_s+n_n)\sigma_{21}v_g/V$ (similarly for W_{12}) and

$$\bar{n}_s = \frac{a}{1-x}, \quad \bar{n}_n = \frac{x+b}{1-x}$$

(5.37)

where $a = \frac{\alpha_e n_{s,bus}}{\sigma_{21} \Delta N_{th}}$ and $b = \frac{\alpha_e n_{n,bus}}{\sigma_{21} \Delta N_{th}}$.

The last term in Eqns (5.35) and (5.36) represent the coupling of signal and noise photons from the waveguide bus into the ring resonator, at a rate $\alpha_e v_g$. The interference effect leading to coherent build-up of power within the resonator, is represented by the $1/(\alpha_{cold} \pi r)$ factor in this term (recall α_{cold} is the loss per unit length in the cavity due to coupling to the waveguide, scattering loss, and radiative turning loss). $1/(\alpha_{cold} \pi r)$ is

proportional to ratio τ/t_{transit} , and represents the coherent build-up of resonantly confined light within the ring volume, forming the Q/r portion of the Modified Purcell factor from section 5.3.1. If we eliminate the E_r population from these equations by setting $N_1=N_2=0$, the steady state expression for (5.35) simplifies to

$$n_s = \frac{Q}{Q_e} \frac{Q2v_g}{\pi r \omega} n_{s,bus},$$

(5.38)

i.e. we recover the Modified Purcell factor relation between ring resonator photon number (or power) and waveguide bus photon number (power), first expressed in section 5.3.1.

We test the physical validity Eqn (5.35) by altering its parameters to approximate optical amplification in a III-V Vertical-Cavity SOA (VC SOA), as modeled and experimentally demonstrated in [119]. A VC SOA is a semiconductor optical amplifier whose direction of propagation is parallel to the direction of film deposition, hence the optical cavity length is the thickness of a deposited thin film (2.2 μm for the example studied in [119]). In order to enhance gain from such a small SOA cavity length (typical cavity lengths for in-plane SOAs are $\sim 300\text{-}500 \mu\text{m}$ for 20-40 dB gain in telecommunications), the cavity is clad above and below by GaAs/AlAs mirrors. Hence, the VC SOA is the standing-wave resonator equivalent of the R-WOA: both devices use resonant confinement to increase an optical amplifier's effective path length, while maintaining the device below lasing threshold.

Publication [119] lists the Fabry-Perot equation (at its peak gain value) for transmission coefficient G_r through an active filter in a reflection-mode geometry (i.e. the amplified signal is measured from the same direction as the incident signal),

$$G_r = \frac{(\sqrt{R_t} - \sqrt{R_b} g_s)^2}{(1 - \sqrt{R_t R_b} g_s)^2}$$

(5.39)

where R_t and R_b are top mirror and bottom mirror reflectivities, respectively, and g_s is single-pass gain ($g_s = e^{\gamma d}$, γ =gain per unit length, d =cavity length=2.2 μm). Fig. 5.15.a plots this equation (as a function R_t , with fixed $R_b=0.999$) for 5% single-pass gain ($g=1.05$) and 1% single-pass gain ($g=1.01$). We see from these plots that lasing onset occurs at $R_t \approx 0.905$ (for 5% single-pass gain) and $R_t \approx 0.98$ (for 1% single-pass gain).

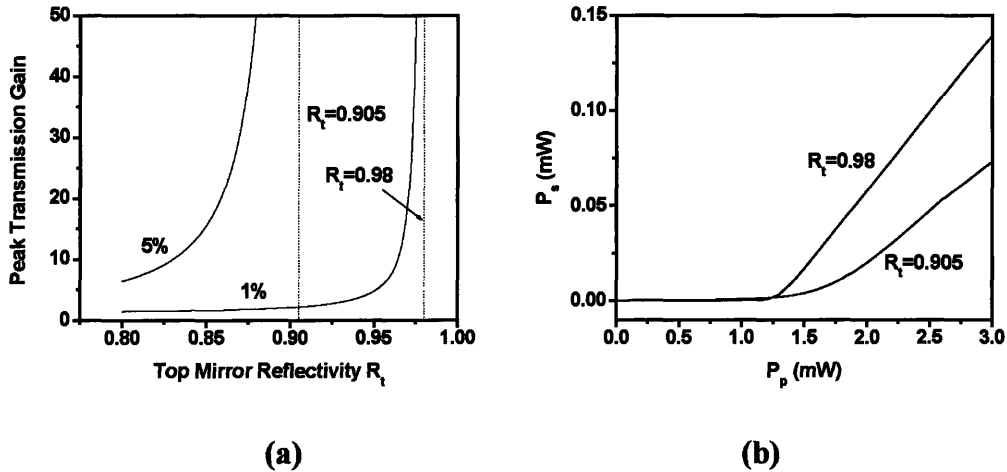


Fig. 5.15. (a) Analytic calculation of enhancement in small signal transmission versus reflectivity, in a VCSCOA. (b) Simulation of power inside the resonant cavity, using (5.35), of the VCSCOA reported in [119].

The gain medium in the VCSCOA from [119] is comprised of seven quantum wells that are optically pumped. Our goal is to test the resonant confinement physics of (5.35);

as such we modify parameters $\sigma_{\text{pump}}=\sigma_{13}$, σ_{21} and N in order to approximate the single pass gain of a quantum well-based VC SOA structure, as a three-level gain system with instantaneous relaxation from the pump-excited conduction band state, to the bottom of the conduction band. σ_{21} represents stimulated emission coupling from the bottom of the conduction band to the top of the valence band, N represents the number of excess electron-hole pairs generated by optical excitation σ_{pump} , and τ is the spontaneous emission lifetime. Referencing InGaAsP SOA data from [124], we assign nominal values to these parameters in Table 5.5.

σ_{pump}	σ_{21}	τ	N	R_b	Area
$3 \times 10^{-15} \text{ cm}^2$	$5.58 \times 10^{-15} \text{ cm}^2$	2.5 ns	$2 \times 10^{17} \text{ cm}^{-3}$	0.999	$2.0 \times 1.0 \text{ } \mu\text{m}^2$

Table 5.5. Nominally assigned values to device parameters for (5.35) in order to approximate gain performance of a III-V VC SOA.

For these parameter values, we find (i) a 5% single-pass gain corresponds to an optical pump power of $P_p=1.74 \text{ mW}$, and (ii) a 1% single-pass gain corresponds to $P_p=1.259 \text{ mW}$.

Fig. 5.15.b plots the photon number versus pump power for our VC SOA simulation (sing equation (5.35) with the Table 5.5 parameter values), at $R_t=0.905$ and at $R_t=0.98$. We observe that the lasing threshold for these two resonant structures are $P_p=1.75 \text{ mW}$ and $P_p=1.25 \text{ mW}$, respectively. These two threshold P_p values correspond to the required P_p power to maintain 5% and 1% single-pass gain, respectively. Fig. 5.15.b therefore tells us (i) at 5% single-pass gain, $R_t>0.905$ will result in lasing within the VC SOA resonant cavity, and (ii) at 1% single-pass gain, $R_t>0.98$ will result in lasing within the VC SOA resonant cavity. This is the same information predicted by the Fabry-

Perot active filter equation plots in Fig. 5.15.a. We conclude equation (5.35) accurately models the Fabry-Perot active filter equation and hence a resonantly confined optical amplifier.

We now apply (5.35) and (5.36) to the Er-doped R-WOA. Keeping in mind that the amplified signal and amplified noise that leak from the ring back into the waveguide have a π -phase shift with respect to incident signal and noise power, we do a complex summation of incident and amplified field amplitudes in order to acquire transmitted power ($|s_t|^2$ from the Background section) downstream from the ring amplifier. Our first step is to approximate waveguide bus transmission past the ring resonator by using the Fabry Perot transmission equation (at its peak value) for an active filter[119]:

$$G_t = \frac{(1 - R_t)(1 - R_b)g_s}{(1 - \sqrt{R_t R_b} g_s)^2}.$$

(5.40)

The resulting transmission profile for 1% and 5% single-pass gain is plotted in Fig. 5.16.a, showing us lasing thresholds in the $Q_e \sim 10^4$ range. For 2×10^{20} Er/cm³, a pump power of $P_p = 10$ mW within the ring resonator approximately corresponds to 5% single-pass gain, for one circuit around a 50 μm radius ring resonator(our SiON case study from Table 5.3).

We thus conclude $Q_e \sim 10^4$ forms an approximate upper limit for our R-WOA design, above which the amplifier will lase. In principal there is no problem with having a lasing R-WOA, provided the signal λ_s matches the lasing wavelength exactly. In order to retain the R-WOA as a practical device with a spectral range of amplification (and hence WDM applicability), we require its operation be below lasing threshold.

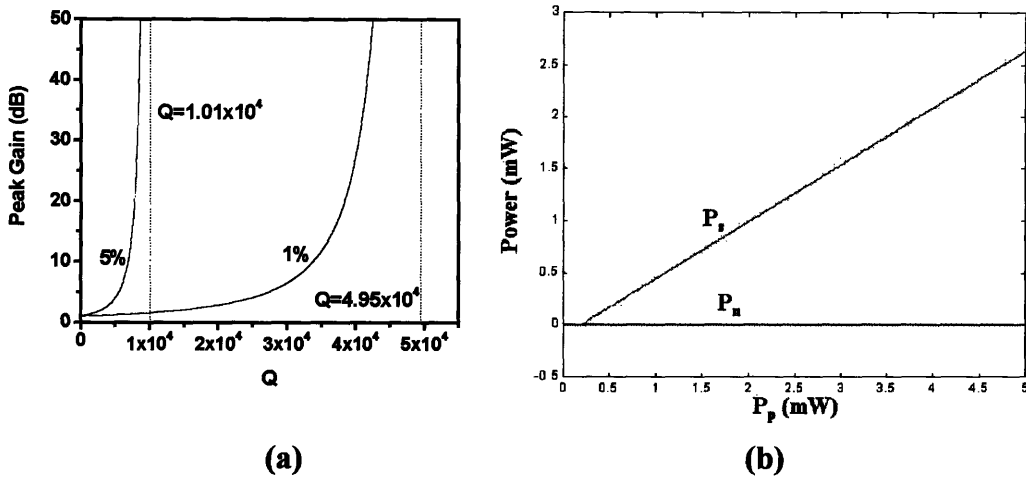


Fig. 5.16. (a) Analytic calculation of enhancement in small signal gain for transmission past the R-WOA. (b) Plot of Fig. 5.17.d for case when incident signal is shut off; we recover the ring laser L-I curve from section 5.4.1.

We proceed with our more accurate modeling, using Eqns (5.35) and (5.36) (coupled with Eqn (5.29)). Fig. 5.16.b tests the form of our simulation by turning off input signal and noise powers, with $Q_e=10^5$. We consistently recover the ring laser performance of 5.4.1. Our results simulating the R-WOA are now shown: Fig. 5.17.a and Fig. 5.17.c plot the device gain and amplified signal and noise power in the waveguide bus (as a function of P_p in the waveguide bus), downstream from the R-WOA, for $Q_e=7 \times 10^3$ and $Q_e=1 \times 10^4$, respectively; Fig. 5.17.b and Fig. 5.17.d plot the signal and noise power inside the R-WOA (as a function of P_p inside the R-WOA), for these same two Q_e values.

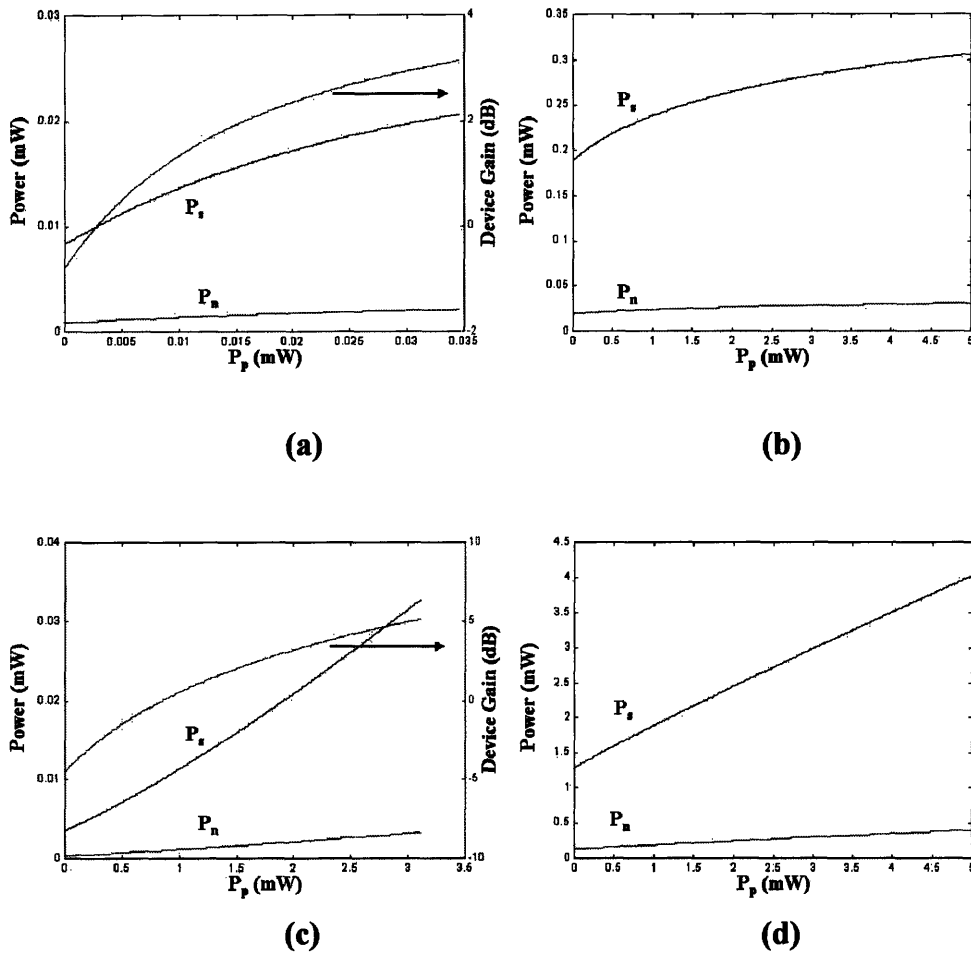


Fig. 5.17. (a) Device gain, signal and noise power in waveguide bus for $Q_e=7 \times 10^3$. (b) Signal and noise power inside R-WOA for $Q_e=7 \times 10^3$. (c) Device gain, signal and noise power in waveguide bus for $Q_e=1 \times 10^4$. (d) Signal and noise power inside R-WOA for $Q_e=1 \times 10^4$.

We observe, consistent with our simpler analytic plot from Fig. 5.16.a, that indeed the power profile inside the resonator shows a sub-threshold characteristic (Fig. 5.17.b) for $Q_e < 10^4$ and a lasing characteristic (Fig. 5.17.d) for $Q_e > 10^4$. In both cases, 3 dB amplification is easily achieved downstream from the R-WOA (Fig. 5.17.a, Fig. 5.17.c), but we note a considerably higher pump power in the waveguide bus (horizontal axis in Fig. 5.17.a, Fig. 5.17.c) is required, in order to reach $P_p \sim 10$ mW within the

R-WOA. This important observation contrasts the power performance of a R-WOA, in comparison to the VCISOA.

The VCISOA is a standing-wave resonator whose Bragg Reflector-based reflectivity stop-band is centered about λ_s . The pump wavelength $\lambda_p=980\text{nm}$ [119] is outside this stop-band, and as such is minimally subject to the confinement effect of the Bragg Reflectors. Hence within a VCISOA, the confinement effect of the Bragg Reflector mirrors is to increase the optical path length of the signal photons, λ_s . In contrast, the coupling mechanism between waveguide bus and R-WOA is not Bragg Reflector transmission, but rather evanescent coupling. And evanescent coupling results in a strong confinement effect for both λ_s and λ_p ; in fact because $\lambda_s < \lambda_p$, this longitudinal confinement effect will be stronger for the pump wavelength λ_p than for the signal wavelength λ_s (λ_s leaks out of the waveguide bus or R-WOA more than λ_p).

The R-WOA thus increases the optical path length for pump photons λ_p as well as signal photons λ_s . When increasing the gap between waveguide bus and R-WOA, Fig. 5.11 shows us that Q_e increases for λ_p much faster than for λ_s , as a result of which the pump wavelength rapidly transitions deeper into critical coupling (Eqn ()) relates the horizontal axis P_p values in Fig. 5.17.a versus Fig. 5.17.b, Fig. 5.17.c versus Fig. 5.17.d). And as a result, prohibitively high pump powers are required to maintain $P_p \sim 10$ mW within the R-WOA. Fig. 5.18.a plots the 3-dB device gain efficiency—defined as the ratio of 3 dB gain in the waveguide bus (downstream from the R-WOA) to the required pump power in the waveguide bus—versus Q_e (at $\lambda=\lambda_s$). As $Q_e(\lambda_s)$ increases, 3-dB gain

efficiency passes through a maxima and rapidly decays. These results are shown for the SiON:Er case study, with upconversion.

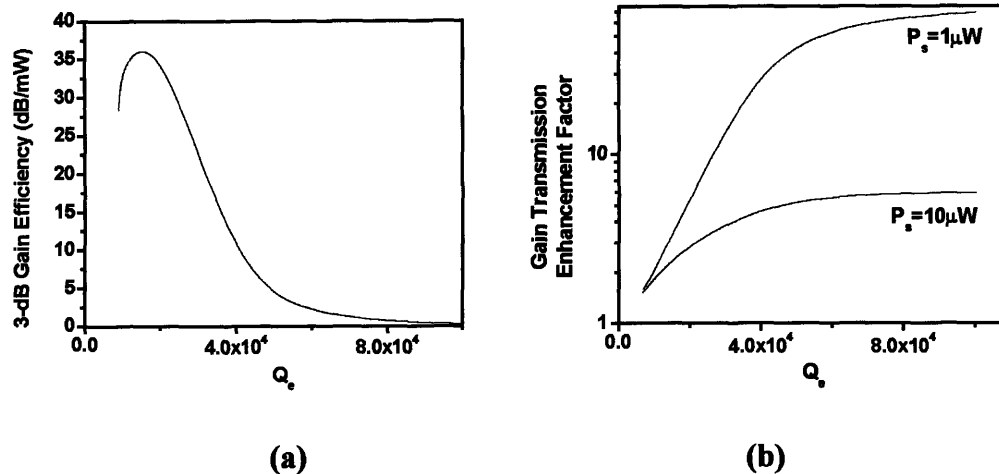


Fig. 5.18. Ring Amplifier Property Map 2 & 3: for ring amplifiers giving a 3 dB output gain, (a) Gain Efficiency (3 dB/ P_p) versus Q_e and (b) Transmission Enhancement for $P_s=1, 10 \mu\text{W}$, versus Q_e .

The enhancement of Gain Transmission is plotted in Fig. 5.18.b, for a $P_s=1 \mu\text{W}$ and $P_s=10 \mu\text{W}$ incident signal. Gain Transmission enhancement for $P_s=1 \mu\text{W}$ is a closer approximation to the measure of small signal gain enhancement, represented by the Fabry Perot active filter equation (5.40), we observe good agreement between Fig. 5.18.b and Fig. 5.16.a. In terms of device gain (i.e. enhancement in dB), the enhancement of the $P_s=1\mu\text{W}$ signal corresponds to $\sim 120\times$, consistent with the reported VCSOA results of [119].

Returning to Fig. 5.18.a, comparison with 3-dB gain efficiency for the SiON case study from chapter 2 (Fig. 2.10), which shows a gain efficiency of 0.35 dB/mW, shows a 3-dB gain efficiency enhancement of up to $(37 \text{ dB/mW})/(0.35 \text{ dB/mW})=106\times$. Thus, the R-WOA can provide significantly ultra-low powered optical amplifiers for the PLC,

provided care is taken to account for optimal pump power coupling. In addition, the areal footprint of this 50 μm -radius ring is $100 \times 100 \mu\text{m}^2$, $\sim 18\times$ smaller than the coil structured WOA of chapter 2.

We thus observe significant improvements in gain efficiency and footprint for the R-WOA versus the WOA. Resonant confinement comes at the cost of reducing gain transmission bandwidth to approximately $\Delta\nu=20$ GHz, where typical WDM pulse-encoded signals have a carrier spectral linewidth of ~ 40 GHz, corresponding to a transmission rate of 5 Gbit/s. Hence the transmission rate through a R-WOA has upper limit of approximately 2.5 Gbit/s—which is acceptable for microphotonic data rates, but not necessarily fiber optic communication.

While a 20 GHz bandwidth means the ring amplifier can only ever amplify one WDM channel, the large turning loss limited radius results in the overlap of multiple Fabry Perot modes (Fig. 5.14) across the ~ 30 nm inhomogeneously broadened high gain Er spectrum. The R-WOA remains a feasible device for WDM communications, if not dense-WDM communications.

We conclude with a modified Figure of Merit (FOM_ν), defined as:

$$\text{FOM}_\nu = \frac{\gamma_d}{P_p \times F} \times \Delta\nu.$$

(5.41)

Distilling these performance numbers into the Figure of Merit (FOM) defined in chapter 2, we conclude for the SiON case study as a coil structure, $\text{FOM}_{\text{coil}}=1.97 \times 10^{-6}$ dB²/mW/ μm^2 without the bandwidth factor and

$FOM_{v,coil}=0.0076 \text{ dB}^2 \cdot \text{GHz}/\text{mW}/\mu\text{m}^2$ with it. For the ring amplifier, $FOM_{ring}=3.7 \times 10^{-3} \text{ dB}^2/\text{mW}/\mu\text{m}^2$ without the bandwidth factor and $FOM_{v,ring}=0.074 \text{ dB}^2 \cdot \text{GHz}/\text{mW}/\mu\text{m}^2$ with it.

We conclude that while the R-WOA is overall a superior amplifier, both the coil structure WOA and the R-WOA contribute complementary amplification roles to the PLC. The coil structure WOA is more useful as an in-line amplifier at a global optical interconnect level, amplifying WDM channels on arbitrary carrier frequencies. At this global level there is also a greater footprint allowance, consistent with coil WOA requirements. At a lower optical interconnect level or just before the photo-detector, the ring amplifier will be a more suitable device (i.e. a pre-amplifier), conforming to a smaller footprint allowance and providing selective amplification to a given WDM demultiplexed carrier frequency.

5.4.3 WDM Ring Detector

Our study of impedance-matching a ring resonator to a waveguide bus (reviewed in 5.3) inspired a novel idea for creating a monolithically-integrated WDM demultiplexer which efficiently couples, with a minimal areal footprint, a WDM channel signal into a Ge or SiGe photodetector (on a PLC).

As discussed in chapter 1, the materials constraint of Si Microphotonics is to construct all passive device elements using dielectric materials whose amorphous structure promises smooth waveguiding interfaces (thus minimal scattering loss) when integrated with an SiO_2 cladding. Amongst the active device elements, the photo-detector, by its very nature of being an optical to electrical transducer, is most efficiently designed

out of semiconductor material as a pn-junction device. The optimal semiconductor materials choice for integration with Si Microphotonics is Germanium (Ge) and Silicon-Germanium (SiGe); the Kimerling research group has demonstrated the integration of Ge detectors on a Si-substrate[125] with a good responsivity of 0.48 A/W at $\lambda_s=1.55 \mu\text{m}$, for modulations rates of $\leq 2.5 \text{ GHz}$ [126].

The next materials challenge for the photo-detector is to develop a processing scheme which monolithically integrates such a semiconductor device into a dielectrics-majority PLC, with minimal areal footprint. A current project[25] is exploring this integration in a two level process comprised of (1) the growth and annealing optimization of the Ge (SiGe) photodetector, patterned in the form of square-shaped mesas on a Si substrate, followed by (2) the deposition and planarization of an SiO_2 layer which leaves exposed the Ge (SiGe) mesas. Subsequent deposition of an Si_3N_4 (or SiON) single-mode waveguide on top of the Ge mesas, designed such that the propagation constant of the SiON waveguide matches the wavevector of the λ_s signal within Ge, ensures an optimal transfer of the propagating mode to the detector. This evanescently coupled transfer is characterized by a waveguide absorption coefficient of $2900 \leftrightarrow 150 \text{ dB/cm}$ (equivalent to an absorption length of $15 \leftrightarrow 300 \mu\text{m}$) in Si_3N_4 and SiON waveguides. In comparison, the direct absorption of $\lambda_s \sim 1.55 \mu\text{m}$ into Ge is approximately 8695 dB/cm [127].

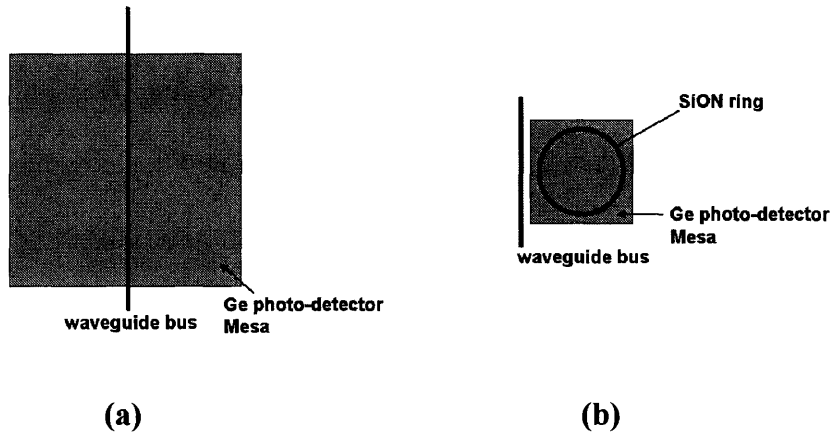


Fig. 5.19. (a) Current Si Microphotonic designs for efficient coupling of dielectric materials-based optical interconnects to a semiconductor-based photo-detector. (b) The WDM Ring Detector design.

The characteristic length of these evanescently decaying Si_3N_4 (or SiON) waveguides is typically on the order of $300\ \mu\text{m}$, which takes up a considerable amount of planar area (see Fig. 5.19.a). There are two options to consider for minimizing their footprint, or equivalently, the size of the Ge (SiGe) photodetector mesa: winding the waveguide into a coil structure, or replacing the waveguide with a ring resonator that sits on top of the photodetector mesa (Fig. 5.19.b).

A ring resonator coupling to the photodetector has two advantages:

(i) improved photo-detector responsivity: ultra-small areal footprint, allowing for ultra-small Ge mesas, whose small size has been demonstrated to help anneal out all threading dislocations[128] into purely misfit dislocations. This removal of threading dislocations from the photo-detector mesa surface is believed to improve the measured device responsivity (Amps of current detected per Watt of signal photons). Secondly, the resonant nature of the ring coherently builds up signal power by a factor of $\sim Q$, thus increasing the total number of photo-generated carriers and device responsivity.

(ii) WDM compatibility: integration of a resonant device that can de-multiplex, i.e. selectively chose one channel λ_i , from a WDM signal.

Table 5.6 summarizes the device parameters for our proposed device. In order to transfer 100% of the WDM channel from waveguide bus into ring resonator, we must critically couple, i.e. match the external coupling rate to the (photo-detector) loss rate within the ring. We considered the option of making the ring resonator directly out of Ge (SiGe) material, but this results in 3 disadvantages: (i) the high refractive index (Ge \rightarrow Si: 4.0 \rightarrow 3.5) requires the lithographic patterning of single mode waveguide dimensions below conventional I-line lithographic capabilities (such as those present at MIT's MTL laboratories); (ii) the highly increased surface to volume ratio of such a patterned Ge pn-junction drastically increases the amount of surface recombination of photo-generated electron-hole pairs, thereby decreasing the device responsivity; and most importantly, (iii) the \sim 8700 dB/cm absorption length of \sim 1.55 μ m wavelength signals in Ge corresponds to a loss rate of $Q_{\text{loss}}\sim 10$. Critical coupling ($Q_e=Q_{\text{loss}}$) to such a device results in a total quality factor of $Q\sim 5$, corresponding to a resonator bandwidth of $\Delta\lambda=310$ nm, or $\Delta\nu=4\times 10^5$ GHz. Typical Gbit/s transmitted WDM signal have a 40 GHz bandwidth and could be spaced 200-500 GHz apart. The broad spectral response of such a low Q device therefore makes it impossible to WDM de-multiplex.

We designed a resonant device with a $\Delta\nu=50$ GHz bandwidth, corresponding to an external coupling of $Q_e=4000$, or $\alpha_e=34$ dB/cm. With a \sim 2-4 dB/cm permitted loss (i.e. \sim 10% of the total ring resonator damping loss), this results in 90% of the resonantly trapped signal coupling by evanescently absorption into the Ge (SiGe) photo-detector, at

an absorption rate of 30-32 dB/cm. We suggest placing an appropriate thickness undercladding SiO₂ spacer layer between ring and photo-detector, in order to tailor evanescent loss this value for either Si₃N₄ or SiON based waveguides (we have not presented this calculation).

Table 5.6 introduces two WDM de-multiplexing performance figure of merits (FOMs) to evaluate whether and Si₃N₄ or SiON waveguide core present a better WDM ring detector design. The first FOM is defined as WDM Sensitivity,

$$\eta_{WDM} = \frac{\Delta\lambda_{WDM}}{\Delta\lambda_{ring}}$$

where $\Delta\lambda_{WDM}$ and $\Delta\lambda_{ring}$ are the wavelength spacing between WDM channels and resonator bandwidth, respectively. The second FOM is defined as WDM Selectivity,

$$\delta_{WDM} = \frac{FSR_{ring}}{\Delta\lambda_{WDM}}$$

where FSR is the ring resonator's Free Spectral Range. η_{WDM} quantifies the degree of cross talk between WDM channels imparted to the photo-detector from the de-multiplexing ring (we want $\eta_{WDM}>1$). δ_{WDM} quantifies the number of WDM channels dropped to the ring resonator (we want $\delta_{WDM}>1$). The product $\eta_{WDM} \times \delta_{WDM} = FSR_{ring} / \Delta\lambda_{ring} \equiv \text{Cavity Finesse}$. Keeping these two parameters in mind, for a $\Delta\lambda_{WDM}=3.87$ nm (500 GHz channel spacing), Table 5.6 indicates the Si₃N₄ design has a better δ_{WDM} de-multiplexing performance than the SiON design.

Index difference Δn	Si ₃ N ₄ : 2.2-1.445=0.755	SiON: 1.6-1.445=0.155
Abs. Coeff. (dB/cm)	66.1	58.5
Q _e	2000	2000
Linewidth $\Delta\lambda \sim \lambda/Q_e$ (nm)	1.55	1.55
n _{eff} (TE)	1.675	1.481
Ring radius (μm)	3	50
Areal Footprint ($\mu\text{m} \times \mu\text{m}$)	6 \times 6	100 \times 100
FSR (nm)	26.4	3.2
$\Delta\nu_{\text{WDM}}$ (GHz), $\Delta\lambda_{\text{WDM}}$ (nm)	500, 3.87	500, 3.87
η_{WDM}	2.5	2.5
δ_{WDM}	6.8	0.8

Table 5.6. Summary of detector design.

5.5 Conclusion

We investigated Er-doped ring resonators to quantify the effect of sub-threshold resonant confinement on device gain efficiency, within an ultra-compact areal footprint. For the $\Delta n=1.55$ SiON case study, our results show that 3-dB gain efficiency can be enhanced up to $\sim 120\times$ and areal footprint can be reduced by $\sim 18\times$. We conclude after Optical Shrink (effect of Δn on a fixed length WOA), Longitudinal Resonant Confinement (i.e. $Q_e > 0$) is a second effective method to increase WOA performance. Also, while Optical Shrink is a materials-dependent application, Longitudinal Resonant Confinement can be engineered within one host materials system for Er, by means of controlling the waveguide bus to ring resonator coupling strength.

Unlike the VC SOA, the resonant confinement properties of a R-WOA do not increase monotonically with Q_e , showing a trade-off between the competing processes of signal gain enhancement versus pump under-coupling. And while the onset of lasing with higher Q_e reduces WDM applicability of the R-WOA, this pump coupling limitation affects gain efficiency enhancement significantly.

We conclude that while the R-WOA has a higher Figure-of-Merit than the coil structure WOA (of chapter 2), but amplifier designs have application-specific value within a PLC.

We also present two device analysis for ring resonator applications as an Er-doped laser and a Ge (or SiGe) photo-detector coupled de-multiplexer. Current lithographically achieved scattering losses of ~ 0.2 dB/cm for SiON waveguides are sufficient to meet both ring laser and R-WOA requirements. Further work must be done in minimizing scattering loss in Si_3N_4 waveguides in order to achieve ring lasers with 4 Fabry Perot lasing modes or less within the Er high gain 30 nm bandwidth.

Ring lasers and R-WOAs are currently being processed in sputtered SiON waveguides. We have created a lithography mask containing numerous ring laser and R-WOA device designs, to be implemented in this processing run. Devices will be tested sometime in the fall by fellow research group members.

The WDM ring amplifier de-multiplexer is compact device most feasible at dropping a single channel (to a Ge detector) when made of a $\Delta n=1.55$ Si_3N_4 waveguide core (SiO_2 cladding). Current 2-5 dB/cm scattering loss limited Si_3N_4 waveguides are more than sufficient to meet design specifications.

Chapter 6: the Effect of Transverse Resonant Confinement in Photonic Band Gap Waveguide Amplifiers



Scanning Electron Micrograph of an $\text{Si}/\text{Si}_3\text{N}_4$ Photonic Crystal two-dimensionally cladding an SiO_2 waveguide core, fabricated on an oxidized Si wafer by Yasha Yi and Shoji Akiyama (Kimerling group), in the Microsystems Technology Laboratories, MIT.

“What if you could slow down the photon? That might be useful.” –Prof. Kazumi Wada (Visiting Scientist, EMAT), in the beginning...

“Yeah, if you look in chapter eleven of Pochi Yeh’s book, there you can find a derivation for asymmetric waveguide. We can use that to solve PBG defect state.” –Yasha Yi (graduate student, EMAT), months before a lot of Matlab code de-bugging.

“What you doing, man? I don’t understand.” –Victor Nguyen (graduate student, EMAT), a frequent comment.

6.1 Chapter Abstract

The study of ring resonator WOAs (R-WOAs) in chapter 5 concluded with our realizing that resonant confinement along the longitudinal direction of a WOA provides an advantage in increasing optical pump efficiency and signal gain, while simultaneously providing a disadvantage in coupling signal gain from this cavity to the PLC. This coupling disadvantage also results in a limitation for WDM-compatibility.

In seeking to further optimize the modal gain of a WOA, our last research study attempted to make use of the advantages of pump resonance while simultaneously decoupling the effect of resonance on the λ_s signal transmission. We do this by using a novel paradigm for waveguide propagation, Photonic Crystal (or Photonic Band Gap) confinement of light to a defect state. The defect state is an anomalous refractive index and/or anomalous sized region of material (the defect core) within which λ_s and λ_p remain confined and propagate, independent of the principle of total internal reflection.

We conclude that such a 3 dB gain Photonic-Crystal WOA (PC-WOA), is a moderate WDM rate-compatible device (500 GHz channel spacing) with dispersion limitations which make the device practical for only $L_g \sim 1\text{cm}$ Si Microphotonics, at data rates < 10 Gbit/s per channel.

We study by computer simulation the influence of a resonance-enabled uniform pump power distribution across L_g and conclude this power coupling scheme yields a 3 dB gain efficiency, $1.84\times$ lower than the SiON HIC-WOA case study (end of chapter 2). The < 3 dB/cm propagation loss requirements at λ_s imply severe resonant undercoupling of λ_p to the defect core, drastically reducing pump power coupling efficiency.

The increased confinement effect of a PBG based on the high Δn Si/SiO₂ system implies this PC-WOA can be fit within a PLC areal footprint that of 185×185 μm^2 , 5.2× smaller than the SiON case study footprint.

We suggest a modified hybrid PC-WOA design that attempts to optically confine λ_p by resonance while confining λ_s only by total internal reflection. This hybrid confinement design eliminates the dispersion limitation on λ_s transmission rate, however still yield a gain efficiency 1.13× less than the SiON case study.

To experimentally test the angular principles involving resonant coupling of λ_p into the PC-WOA with a uniform power profile across L_g , we have grown by sputter deposition a PC-WOA with an SiO₂:Er defect core (the best reported luminescing sputter-material from chapter 4). Optical measurements to test the angular coupling principle are waiting to be done.

6.2 Introduction

In chapter 2 we studied the effect on optical gain due to increasing an optical mode's confinement in the transverse direction (i.e. perpendicular to the direction of propagation z), where the physical principle of confinement was due to total internal reflection. In chapter 5 we studied the effect on optical gain due to the creation of confinement in the longitudinal direction (i.e. parallel to the direction of propagation z), where the physical principle of confinement was due to resonance. Both approaches provided relative value as measured by the metrics of gain efficiency, footprint and WDM applicability; this value was quantified in a Figure of Merit.

In our final work on optimizing the modal gain performance of optically pumped WOAs, we sought to hybridize these two confinement principles in an attempt to selectively take advantage of the best of both these approaches, for WOA device optimization. By designing a WOA based on the physical principles of Photonic Crystals[14] and Photonic Band Gap(PBG) confinement, we studied the effect of (a PBG-based) resonant confinement in the *transverse* direction (and not, like the work of chapter 5, resonant confinement in the longitudinal direction). In taking this approach we seek to break with the pump co-propagation scheme that has guided our understanding of WOAs thus far. By coupling a pump from overhead, into a PBG-confined *defect* layer (see Fig. 6.1), we hope to resonantly confine the pump wavelength with a uniform power distribution across the WOA device length L_g .

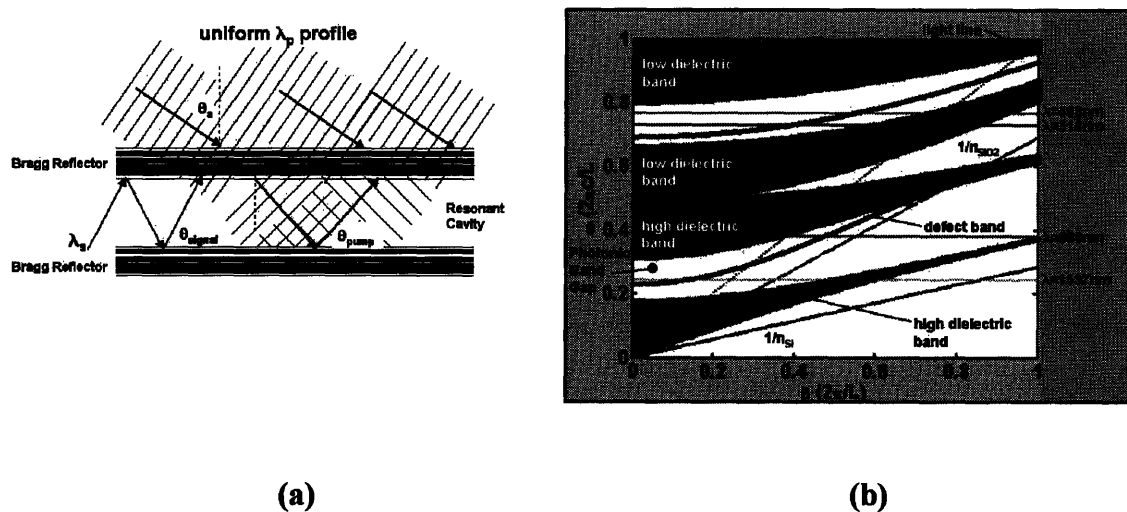


Fig. 6.1. (a) Transverse-resonant optical pump scheme will give uniform power profile along z-direction of propagation. (b) A Projection Band Diagram of the case study for this chapter. Pertinent PBG features are labeled.

The questions we will examine are (i) what are the effects of a uniform power profile on gain efficiency, and (ii) what are the effects of PBG-based waveguiding

(instead of total internal reflection-based waveguiding) on device footprint and WDM applicability. Our first experimental step to test the principles of resonant transverse confinement was to grow and model a one-dimensional PBG-based waveguide. The device was entirely grown by sputtering on a Si substrate that has 10 μm of wet thermal oxide (SiO_2). (See chapter 4 for specific sputter details for such $\text{SiO}_2\text{:Er}$ materials.)

The tremendous materials advantage for Microphotonics, due to PBG-based optical confinement, is the ability to propagate light with micron-scale device densities, inside an SiO_2 waveguide core. Our study of sputtered SiON:Er materials in chapter 4 showed the longest 10 ms Er lifetimes (at concentration $\sim 2 \times 10^{20} \text{ cm}^{-3}$) in sputtered $\text{SiO}_2\text{:Er}$, with negligible lifetime quenching between 4 K and room temperature: sputtered SiO_2 shows the least amount of non-radiative de-excitation mechanisms, versus sputtered SiON:Er or $\text{Si}_3\text{N}_4\text{:Er}$. We developed our PBG-confinement based WOA design with an $\text{SiO}_2\text{:Er}$ core, and grew the device by sputtering. SEM results are presented on the sputtered structure.

6.3 Theoretical Background

As mentioned in the Introduction, our first experimental testing of resonant transverse confinement using a Photonic Band Gap (PBG), is a one-dimensional (1-D) structure. The physics of 1-D PBG-based light confinement within a “defect layer” is most simply understood as a dielectric stack or Bragg reflector[129]—comprised of periodic pairs of two different refractive index materials n_1 and n_2 with corresponding thickness t_1 and t_2 —which contains one anomalous thickness film layer $t_g \neq t_1 \neq t_2$, which we call the “defect layer” (see Fig. 6.7).

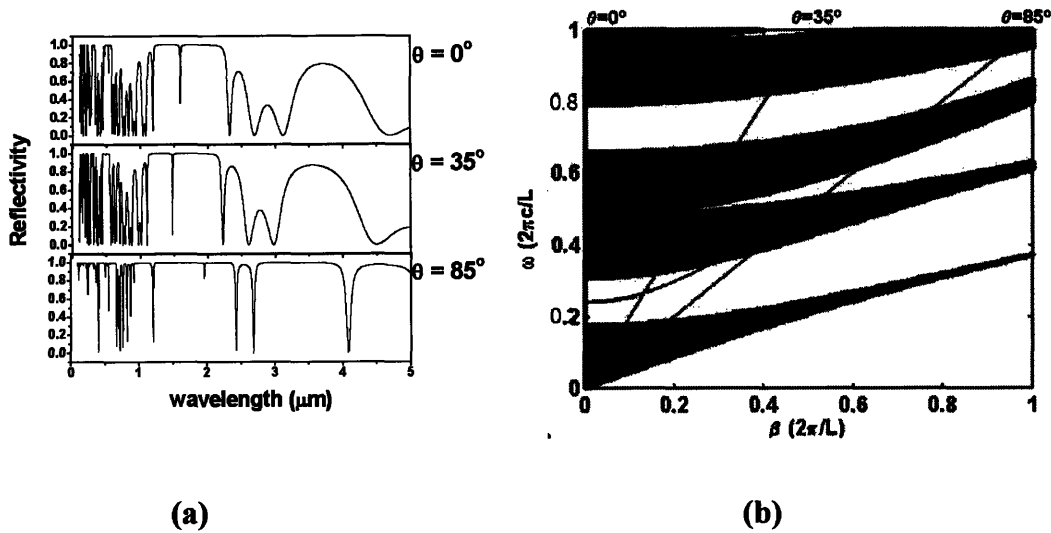


Fig. 6.2. (a) Reflectivity spectra for a Bragg reflector at three different angles of incidence (from ambient free space). (b) The spectra of (a) viewed as linear trajectories on a Photonic Crystal projection band diagram.

De-constructive interference in Bragg reflectors, designed with the condition $t_1 = \lambda_0/4n_1$ and $t_2 = \lambda_0/4n_2$, results in zero transmission at λ_0 . Light propagation in a media n_i is physically descriptive of an electromagnetic field with periodicity λ_0/n_i ; the quarter wavelength design of t_1 and t_2 , coupled with a π -phase shift imparted from reflection at every $n_1 < n_2$ interface, implies no traveling-wave solution exists within the Bragg reflector at λ_0 . Alongside thin film interference effects[16], this optical stopband—i.e. a broad spectral range of zero transmission, centered about λ_0 —of Bragg Reflectors has been a well-studied phenomenon[16].

The insight provided by the idea of Photonic Crystals has been to recognize that the influence of a periodic refractive index on a traveling light wave is equivalent to the influence of a periodic charge potential on a traveling electron wave. Specifically, the Helmholtz (light) wave equation is mathematically similar to the Schrodinger electron wave equation. As a result, the spectral reflectivity of a Bragg Reflector (see Fig. 6.2.a)

can be more broadly understood as the representation of a trajectory on a band diagram that summarizes the dispersion relation for all modes of light propagating through the Bragg Reflector (Fig. 6.2.b). We'll return to this shortly.

The derivation of Fig. 6.2.b from the Helmholtz equation has been very elegantly described in [129], we shall not repeat the derivation here. The solution in [129] to the Helmholtz equation

$$\frac{dE(x)}{dx} + k_x^2 E(x) = 0$$

(6.1)

is found to be of the form

$$E_n(x) = \left[a_o e^{ik_{1x}x(x-nL)} + b_o e^{-ik_{1x}x(x-nL)} \right] e^{-ik_g(x-nL)} e^{ik_g x}$$

(6.2)

where $k_g = \sqrt{(k_o n_g)^2 - \beta^2}$ is the Bloch wavenumber, $k_{1x} = \sqrt{(k_o n_1)^2 - \beta^2}$,

$k_{2x} = \sqrt{(k_o n_2)^2 - \beta^2}$; and

$$\begin{bmatrix} a_o \\ b_o \end{bmatrix} = \begin{bmatrix} B \\ e^{ik_g L} - A \end{bmatrix}, \quad \text{where } A = e^{ik_{1x}t_1} \left[\cos k_{2x}t_2 - \frac{i}{2} \left(\frac{k_{2x}}{k_{1x}} + \frac{k_{1x}}{k_{2x}} \right) \sin k_{2x}t_2 \right] \quad \text{and}$$

$$B = e^{ik_{1x}t_1} \left[-\frac{i}{2} \left(\frac{k_{2x}}{k_{1x}} + \frac{k_{1x}}{k_{2x}} \right) \sin k_{2x}t_2 \right].$$

The propagation constant β in this solution, has identical meaning as the β -solution of total internal reflection waveguiding solutions, i.e. β represents the projection of the propagating modes' wavevector k , along the propagation direction z-axis. For a one

dimensional confined structure, such as the schematic of Fig. 6.1, the mode of light is free to propagate in either the z-direction, y-direction, or a linear combination of the two. We chose as convention the z-direction for propagation, and equation (6.2) determines what values of β correspond to evanescent states— β is complex—or propagating states— β is purely real. Propagating states are colored blue in Fig. 6.1.b, evanescent states are not colored, corresponding to the presence of an optical band gap of prohibited photon states. The constraint $k = \sqrt{k_x^2 + k_y^2 + \beta^2}$, always holds true, and implies two things (i) for a given frequency ω or free space wavelength λ_o of light (corresponding to a given $k=n2\pi/\lambda_o$), β has a maximum possible value of $\beta=k$; and (ii) a plot of ω versus β —limited to values within the *confinement line* $\omega = (\frac{1}{n})\beta$ --contains for a given propagating real-valued β , all the possible combination of k_x and k_y values. Any given blue region in Fig. 6.1.b represents a projection of propagating states with all possible values of k_x and k_y that vectorially sum with β to the given k ; Fig. 6.1.b is thus referred to as a Projection Band Diagram.

An important consequence of (i) stems from the question, what is the meaning of n in the expression $k=n2\pi/\lambda_o$? The Bragg Reflector is composed of two materials with refractive indices n_1 and n_2 ; thus, the maximum possible value for n is n_2 , and the minimum possible value is n_1 . For photons traveling in a bulk dielectric medium of refractive index n_i , the linear dispersion relation is

$$\frac{\omega}{k} = \frac{2\pi c / \lambda_o}{2\pi n_i / \lambda_o} = \frac{c}{n_i}$$

where c is the free space speed of light. Fig. 6.1.b gives plots of ω versus β in units of $2\pi c/L$ and $2\pi/L$, respectively (where $L \equiv t_1 + t_2$). The linear dispersion plot of ω versus β for the bulk dielectric medium will be $\omega = \left(\frac{1}{n_i}\right)\beta$ ($i=1,2$) on this graph. We refer to these lines as confinement lines, and we see their intuitive value when overlaid on Fig. 6.1.b: as $\omega \rightarrow \infty$, the largest value of β (blue colored regions) asymptotically approaches either the confinement line with slope $1/n_1$ or the confinement line with slope $1/n_2$. $\omega \rightarrow \infty$ corresponds to decreasing λ_0 to an infinitesimal size; the dielectric material within which the majority of a given propagating mode's field intensity lies, asymptotically appears as the bulk dielectric to the decreasing λ_0 wavelength.

Thus, propagating states which asymptotically approach the $1/n_1$ confinement line as $\omega \rightarrow \infty$, are modes of light with field intensity maxima within the t_1 layers of the Bragg Reflector, i.e. most of the mode's optical power lies within the lower refractive index layers of the Bragg Reflector; we call these modes low dielectric bands (referred to in [14] as 'air bands').

Similarly, propagating states which asymptotically approach the $1/n_2$ confinement line as $\omega \rightarrow \infty$, are modes of light with field intensity maxima within the t_2 layers of the Bragg Reflector, i.e. most of the mode's optical power lies within the higher refractive index layers of the Bragg Reflector; we call these modes high dielectric bands (referred to in [14] as 'dielectric bands').

We can now explain the physical interpretation of straight lines on the Projection Band Diagram (Fig. 6.2.b). Setting $k_y=0$ by appropriate choice of propagation direction z , we see that β can be related to k ,

$$\beta = k \cos \theta_m = n_i k_o \cos \theta_m$$

(6.3)

where θ_m is the angle the k -vector makes with the z -axis of propagation (and $k_o \equiv 2\pi/\lambda_o$). We now see that Snell's Law, determining the angles a wavevector of light k makes with respect to the normal incident within dielectric media n_1 and n_2 , is equivalent to requiring the propagation constant be the same in both media:

$$\begin{aligned} n_1 \sin \theta_1 &= n_2 \sin \theta_2 \\ k_o n_1 \sin \theta_1 &= k_o n_2 \sin \theta_2 \\ k_o n_1 \cos \theta_{m1} &= k_o n_2 \cos \theta_{m2} \\ \beta_1 &= \beta_2 \end{aligned}$$

We now understand the Reflectivity plots of Fig. 6.2.a, showing reflectivity (or the converse of transmission, which is proportional to the optical density of states within the Bragg Reflector) as a function of λ_o at a constant angle θ in ambient air, to be represented on the Fig. 6.2.b plot as $\beta = n_{\text{air}} k_o \cos \theta_m = (2\pi/\lambda_o) \sin \theta$ ($n_{\text{air}}=1.0$), plotted for different frequency values $\omega = 2\pi/\lambda_o$. This produces a straight line with slope $\omega/\beta = 1/\sin \theta$. Thus, normal incidence corresponds to a vertical trajectory (slope $+\infty$) in Fig. 6.2.b, and $\theta \rightarrow \pi/2$ corresponds to the slope of this trajectory decreasing from $+\infty$ to $1/\sin(\pi/2)=1$. We thus see that the reflectivity stopband corresponds to the Photonic Band Gap of the Projection Band Diagram.

The line with slope $\omega/\beta=1$ is referred to as the light line, and confines, for a given frequency ω , all the possible values that β (i.e. the z -axis projection of k) can have in air (i.e. free space). For light coupling into a Bragg Reflector from free space, the light line represents the confinement value on all possible β values within the Bragg Reflector. For

a given ω , there are larger β values lying beneath the light line, but these are optical modes of propagation of light to which ambient free space cannot couple, since these larger values of β do not exist in free space.

Light may be incident on the Bragg Reflector with either a Transverse Electric (TE) polarization—with electric field vector parallel to the incident surface—or the light may be incident with a Transverse Magnetic(TM) polarization—with magnetic field vector parallel to the incident surface. TM polarization results in an interference effect[121] at an angle termed the Brewster angle, θ_B , which leads to zero reflectance for light transmission from dielectric media n_1 into dielectric media n_2 :

$$\theta_{B(1 \rightarrow 2)} = \tan^{-1} \left(\frac{n_2}{n_1} \right)$$

(6.4)

We can express $\beta_1 = n_1 k_o \sin \theta_{B(1 \rightarrow 2)} = n_1 k_o \frac{n_2}{\sqrt{n_1^2 + n_2^2}}$, from which we see that this

angle of transmission through the Bragg Reflector can be plotted as a straight-line trajectory with slope $\frac{\sqrt{n_1^2 + n_2^2}}{n_1 n_2}$. Fig. 6.4 shows this slope trajectory overlaid on the

TM mode Projection Band Diagram. We observe that along this line, the photonic band gap closes up and is a meeting point of the different dielectric bands. A light line with slope larger than this Brewster line corresponds to $n_{\text{air}} \sin \theta < n_1 \sin \theta_{B(1 \rightarrow 2)}$ for all $0 < \theta < \pi/2$; i.e. the Brewster angle for the Bragg Reflector lies outside the critical angle of media n_1 versus ambient air. This means light incident at any angle from the ambient air, cannot

couple into the Brewster angle for transmission into the Bragg Reflector. We will return to the relevance of the Brewster line for our device modeling shortly.

We now begin to refer to a Bragg Reflector by its synonymous name, Photonic Crystal. If we interrupt the periodicity of the Photonic Crystal with an anomalous layer whose refractive index n_g or thickness t_g differ from n_1, n_2 , or t_1, t_2 , then this layer can be thought of as a ‘defect’ within the otherwise periodic structure. Further, if n_g and t_g are chosen appropriately, this defect layer may confine a mode of light that would otherwise be evanescent (complex β) within the Photonic Crystal. Thus, the defect layer becomes a waveguiding core for this highly confined mode of light. This propagating state of light is represented on the Projection Band Diagram as a dispersion relation between ω and β , lying within one of the Photonic Band Gaps.

The intuition we build on is to realize that for a finite-sized structure grown in the real world, the finite number of Bragg Reflectors (surrounding a defect layer) will still allow for some finite propagation of light (i.e. β is complex) that would otherwise be purely evanescent in an ideal Photonic Crystal (for which β is purely imaginary). Thus, light slowly escapes from the defect layer during propagation; the defect layer is a resonant cavity, confined by Bragg Reflectors inhibiting transmission of a wavelength designed to integrally fit into the cavity length,

$$t_g = m \frac{\lambda_o}{2n_g} \quad m = 1,2,3,\dots$$

(6.5)

where the ‘g’ subscript we have been using in t_g and n_g refer to the thickness of refractive index of this defect layer. (The ‘g’ denotes this cavity to ultimately be our Er-doped Gain

medium.) Equation (6.5) integrally fits half wavelengths (normalized with respect to the cavity refractive index, λ_0/n_g) into the cavity, assuming field magnitude to be zero at the cavity boundaries. In practice this is only true for metal-clad cavities, however (6.5) provides a good starting point from which to design the defect layer thickness that resonantly confines and guides a mode of light otherwise prohibited by the surrounding Photonic Crystal.

If the refractive index of the defect layer is less than the first layer of the surrounding Photonic Crystal (which we'll refer for example here, as n_2), then an accompanying π -phase shift between cavity and layer n_2 results in a resonantly confined field profile with power maximum in the cavity center (see Fig. 6.3.a), for t_g =integral half-wavelengths $\lambda_0/2n_g$. However, for a cavity with refractive index higher than n_2 , such a film thickness results in resonantly confined field profiles with power maximum at the

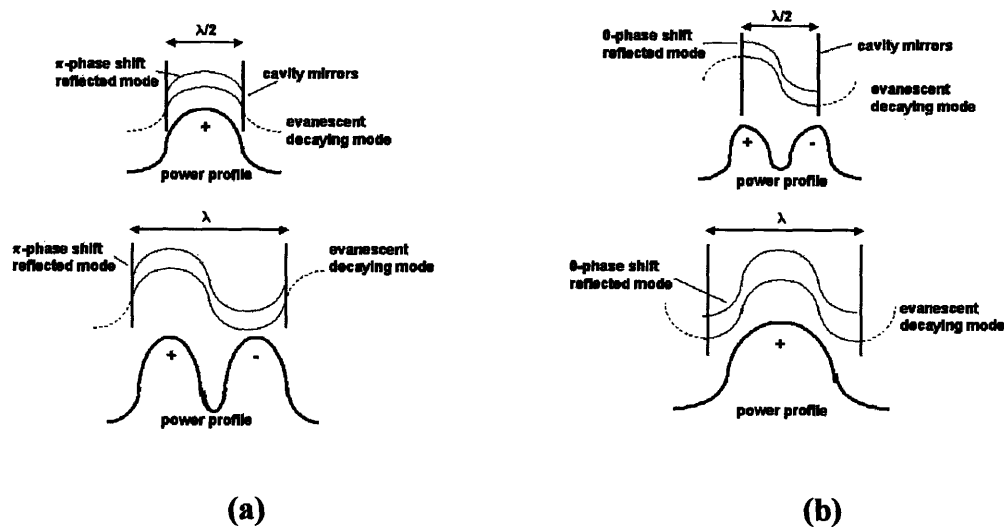


Fig. 6.3. Confinement inside a resonant cavity (a) with refractive index less than Photonic Crystal layer n_2 , and (b) with refractive index greater than Photonic Crystal layer n_2 .

cavity boundaries (Fig. 6.3.b). In this case, film thickness t_g =integral wavelengths λ_o/n_g confines the field profile power maximum within the cavity center. For the case study device we studied and grew in this chapter, $n_g=1.445 < n_2=3.5$; thus, we chose $t_g \sim \lambda_o/2n_g$.

The solution to the dispersion relation for these resonantly confined defect layer propagating modes was acquired in analogy to the scalar field mode solution for total internal reflection-confined waveguides[3], by taking an ansatz odd mode

$$E_g(x) = C_1 \sin k_g x$$

and even mode solution

$$E_g(x) = C_2 \cos k_g x.$$

(C_1 and C_2 are arbitrary constants.) (i) Equating the two solutions to (6.2), evaluated at the defect layer- n_2 interface (field continuity condition), and (ii) equating the derivatives of the two solutions to the derivative of (6.2), evaluated at the defect layer- n_2 interface (field differentiability condition). The resulting transcendental equation, when solved for numerically by computer simulation, yields the defect dispersion relation.

The most notable characteristic of such a resonant confinement-based dispersion relation, in contrast to a total internal reflection confinement-based dispersion relation (such as in Fig. 6.14.a), is the slope $d\omega/d\beta \rightarrow 0$ for $\beta \rightarrow 0$. This slope is the physical definition of photon group velocity v_g ($v_g=c/n_g$, where n_g is defined as the group refractive index), hence at $\beta=0$, the resonant mode is a genuine standing wave, consistent with our intuitive treatment of the defect layer as a Bragg Reflector confined resonant cavity.

For $\beta > 0$, recent work [130,131] has demonstrated the experimental viability of processing resonantly confined waveguides. We explore the potential application of this novel form of waveguide confinement in order to alter pump power profile and study the effect of pump resonance on device gain efficiency. We investigate the effect of resonantly coupling the pump wavelength λ_p from the outside ambient free space, through the Photonic Crystal and into the defect layer. The reflectivity of this finite-sized Photonic Crystal, i.e. this Bragg Reflector with a given number of Si/SiO₂ pairs, determines the external quality factor Q_e (see chapter 5 for Q_e definition) for this resonant coupling of λ_p .

As we'll see in the Results and Discussion section, the pump wavelength λ_p will couple into the defect layer not as a standing wave, but as a transverse-resonantly confined (PBG-confined) traveling wave. The propagation constant of this traveling wave β can be expressed in terms of an effective refractive index n_{eff} (recall $\beta = k_o(n_g \cos \theta_m) = k_o n_{eff}$), which can be related to any arbitrary ambient medium n_a above the Photonic Crystal, through Snell's Law: $n_g \cos \theta_m = n_g \sin \theta = n_a \sin \theta_a$. We thus solve for the angle at which the pump wavelength λ_p will couple into the PBG-confined propagating mode:

$$\theta_a = \sin^{-1} \left(\frac{n_{eff}}{n_a} \right).$$

(6.6)

We conclude with a comment concerning our Photonic Crystal-based WOA (PC-WOA) design. Fig. 6.4-Fig. 6.6 shows the TM and TE Projection Band Diagram for a Photonic Crystal composed of (i) Si₃N₄/SiO₂ Bragg pairs (Fig. 6.4), (ii) Si/Si₃N₄ Bragg pairs (Fig. 6.5), and (iii) Si/SiO₂ Bragg pairs (Fig. 6.6). Our device design (Fig. 6.7) is

made up of an SiO₂:Er defect layer, within which we want to PBG-confine a propagating mode at $\lambda_s=1.537$ nm. Treating this layer as the ambient medium which attempts transmission through its Photonic Crystal cladding, we work from the interpretation presented in [131] to conclude that λ_s will not be able to transmit into the Photonic Crystal cladding, if a complete band gap exists for λ_s (or, on such projection plots, ω_s) within the range of β values bounded by the confinement line of the ambient medium—in this case, that ambient medium being SiO₂:Er. The confinement line will have slope $1/n_1=1/n_{\text{SiO}_2}$ (note: the doping of ~ 1 atomic % Er does not observably change the measured refractive index of SiO₂, see chapter 4 for more details).

We observe that for case (i) and (iii) there is no complete band gap at λ_s , however there is one for case (ii), Si/Si₃N₄ Bragg pairs, where the slope of the confinement line lies above the Brewster line for the TM modes. However, $\lambda_p=980$ nm has no PBG-confined propagating state for case (ii) within the SiO₂ confinement line. There is a simultaneous λ_s and $\lambda_p=980$ nm propagating state for case (i) and (iii), in TE mode only. Therefore, we designed our PC-WOA using the case (iii) Si/SiO₂ Photonic Crystal, whose maximal Δn ensures a broadband gap (securely ensuring λ_s remain an evanescent state, despite any red/blue shift in its dispersion relation, occurring from sputtering thickness variation). Secondly, case (iii)'s high Δn implies we can sputter a minimal number of Bragg pairs to experimentally test the device. Our restriction then, is that we must do TE mode testing, of the PC-WOA properties.

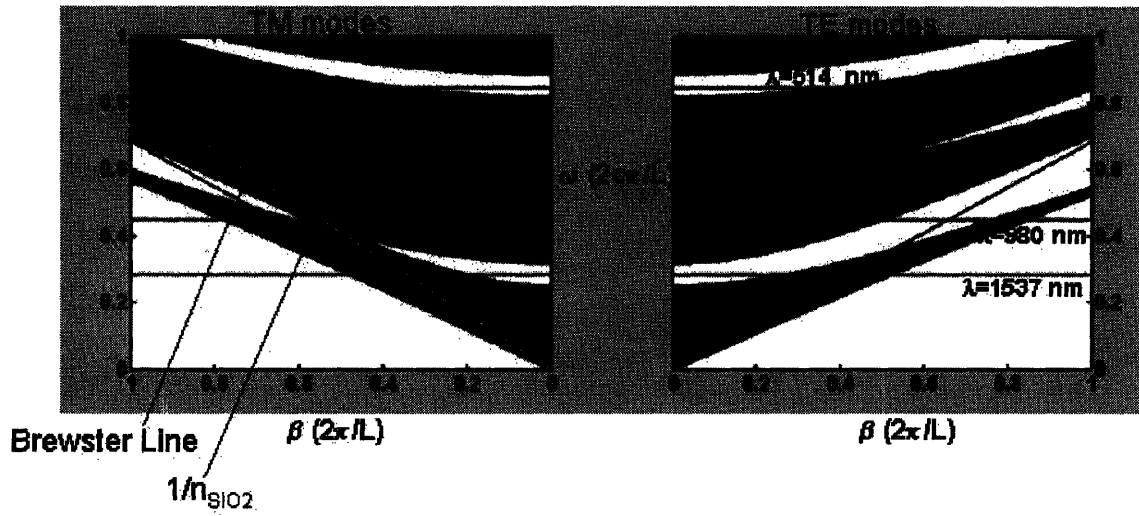


Fig. 6.4. Case (i): TM and TE mode projection band diagram for $\text{Si}_3\text{N}_4/\text{SiO}_2$ Photonic Crystal.

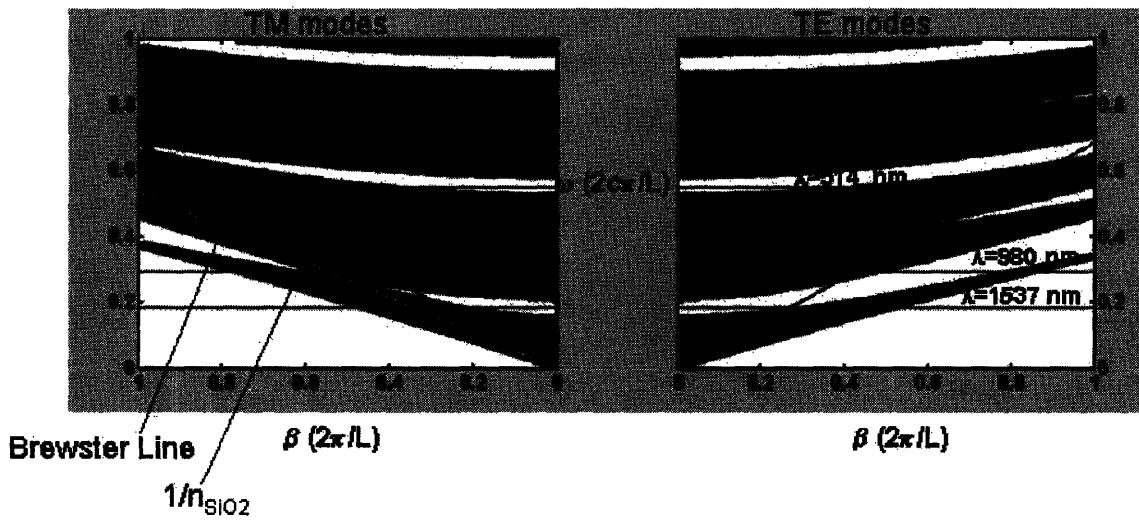


Fig. 6.5. Case (ii): TM and TE mode projection band diagram for $\text{Si}/\text{Si}_3\text{N}_4$ Photonic Crystal.

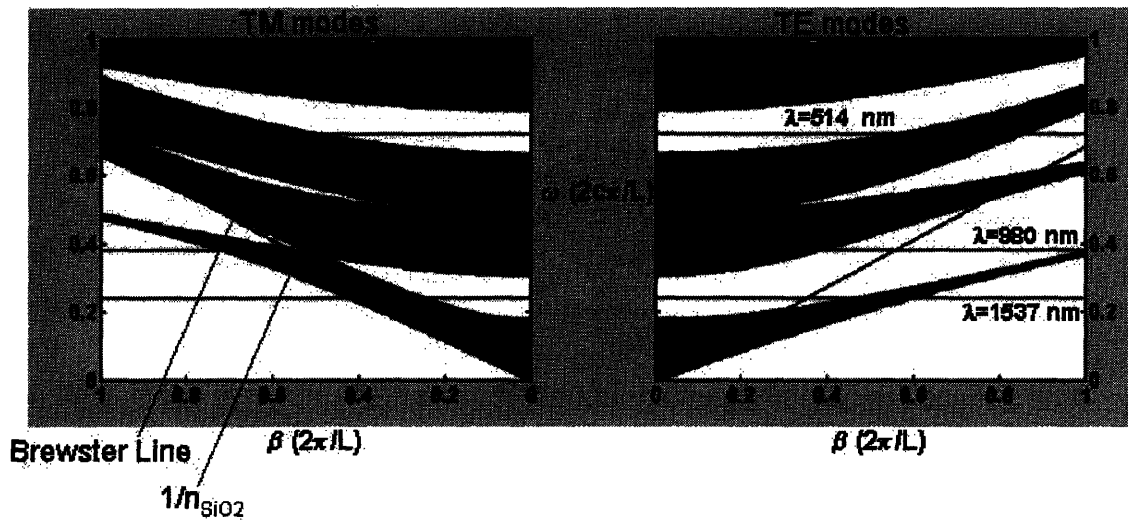


Fig. 6.6. Case (iii): TM and TE mode projection band diagram for Si/SiO₂ Photonic Crystal.

We conclude this section with two relevant equations derived in [129], concerning the dependence on Δn of Photonic Band Gap frequency width,

$$\Delta\omega \cong \omega_o \frac{2}{\pi} \frac{\Delta n}{n_{av}}$$

(6.7)

and the evanescent decay length x (of a PBG-confined propagating mode) into the Photonic Crystal,

$$\frac{1}{x} \cong \frac{1}{L} \frac{\Delta n}{n_{av}}$$

(6.8)

where $n_{av}=(n_1+n_2)/2$ and $L=t_1+t_2$.

6.4 Results

Our study of the Photonic Band Gap confined WOA (PC-WOA) will (i) focus on the device physics of such confinement and its influence on WDM signal transmission; and (ii) focus on the gain efficiency and areal footprint of such a device.

6.4.1 Device Physics and WDM Applicability

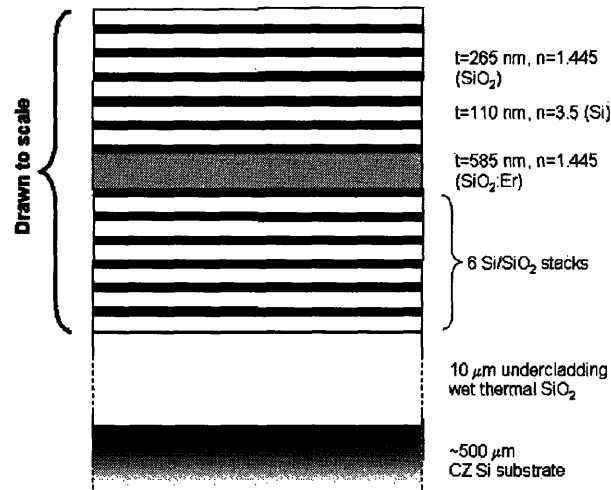


Fig. 6.7. Schematic diagram of 1-D PBG with an SiO₂:Er defect layer. The structure was grown with 6 Bragg reflector Si/SiO₂ pairs of thickness $\lambda_s/4n$, in order to minimize λ_s transmission loss in the propagation direction.

Fig. 6.7 shows a schematic diagram of the structure we grew by sputtering. The film thickness of the two materials comprising the Bragg Reflector, SiO₂ ($n_1=1.445$) and Si ($n_2=3.5$), were chosen to meet the quarter wavelength condition (i.e. $t_1=\lambda_s/n_1$, $t_2=\lambda_s/n_2$), for the which the reflectivity stopband (i.e. the Photonic Band Gap) is centered about $\lambda_s=1.537$ nm. We modeled our device around a 1.537 nm signal wavelength for Er-doped SiO₂ (see Fig. 6.8 for spectral overlay of SiO₂:Er PL emission and PC-WOA propagating states).

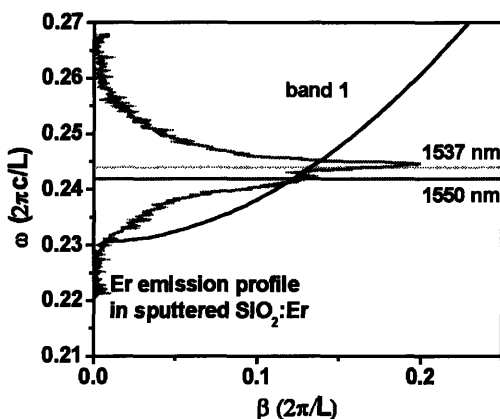


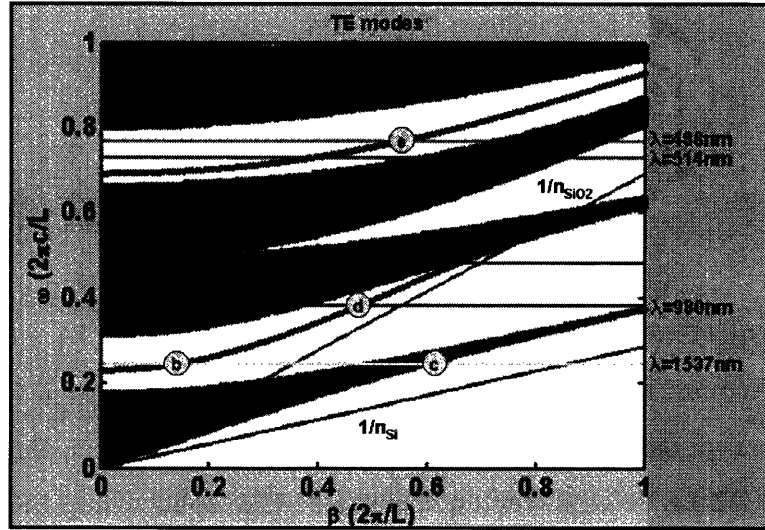
Fig. 6.8. Spectral profile of Er emission overlaid with PBG defect state band structure. ω and β variables are plotted in units normalized to $2\pi c/L$ and $2\pi/L$, respectively.

(i) in-plane coupling of λ_s

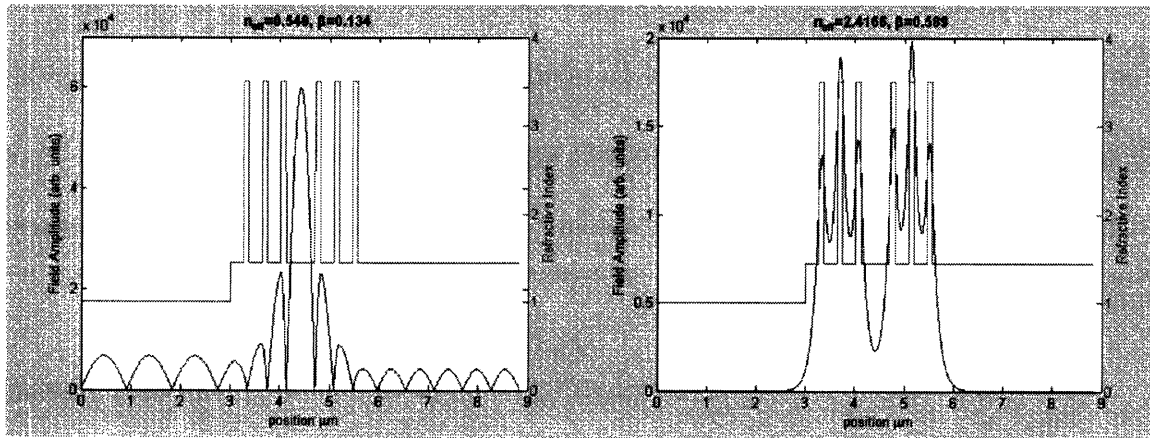
The structure is composed of Si and SiO₂ (refractive index labels n_2 and n_1) materials; the ~1% atomic concentration of Er in the doped defect layer negligibly modifies n_1 . The operation of this PC-WOA will be based on the in-plane input waveguide coupling of signal λ_s and the out-of-plane resonant coupling of optical pump λ_p , schematically detailed in Fig. 6.1.

The TE mode Projection Band Diagram of this device is shown in Fig. 6.9.a. Constant energy lines depicting signal wavelength $\lambda_s=1.537 \mu\text{m}$ and pump wavelengths $\lambda_p=0.98, 0.514$ and $0.488 \mu\text{m}$ are shown. As stated at the end of the Theoretical Background section, our interest is to study the amplifier as a TE-mode device. The spatial distribution of 1-D optical mode confinement was plotted, using the Finite Difference Method[60], to study mode profiles (for a PC-WOA clad with 3 Bragg Reflector pairs on either side, see Fig. 6.9.b-e) for propagating states corresponding to solutions on the Projection Band Diagram.

Given that Si is the material with the highest refractive index (n_2) in this structure, the $1/n_2$ slope confinement line defines, for all light frequencies ω , the maximum value



(a)



(b)

(c)

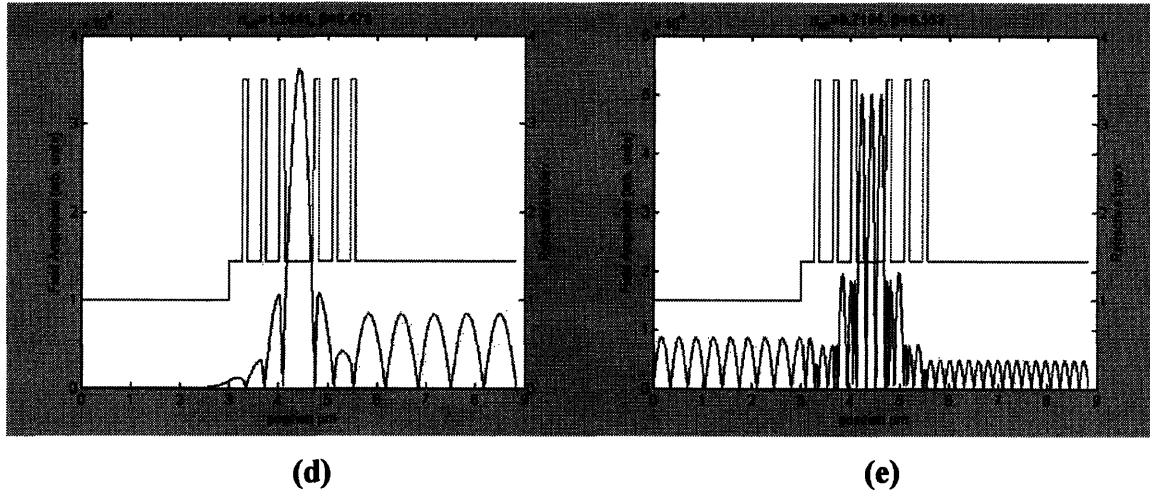


Fig. 6.9. (a) Projection Band Diagram for the designed PC-WOA structure. (b)-(e) plot spatial distribution of TE modes as labeled for given (ω, β) values from (a). Plots (b)-(e) were computed for a finite PC-WOA composed of 3 Bragg Reflectors cladding the SiO₂:Er defect layer on either side (the sputter-deposited structure is composed of 6 Bragg Reflectors cladding either side). The fraction of power confined within the PC-WOA core for these spatial modes are listed in Table 6.1.

for a propagating state's propagation constant β . Solutions (b),(d),(e) correspond to propagating states confined to the defect layer and solution (c) corresponds to a propagating state extended over the photonic crystal periodic regions (with intensity maxima in the Si Bragg Reflector layers).

We observe that when in-plane coupling λ_s into the PC-WOA, it will be important to mode-match the transverse spatial extent of the incoming mode to the defect layer propagating mode. Poor mode match may result in some fraction of the signal energy coupling to the dielectric band, resulting in minimal overlap with the Er-doped defect layer (i.e. Fig. 6.9.c) and thus negligible device gain. Integration of the Fig. 6.9.b mode profile within defect layer shows that $\Gamma_s=0.82$ of the mode is confined within (for a two dimensional confinement structure, we approximate $0.82^2=0.68$ of the mode to be

confined within the defect core). It is thus important to optimally insert as much of the input signal power into the $t_g=585$ nm defect layer as possible.

(ii) Out-of-Plane Coupling of λ_p

Fig. 6.9.d and Fig. 6.9.e show the modal profile of pump wavelengths $\lambda_p=0.98$ μm and $\lambda_p=0.488$ μm , respectively. The $\beta>0$ value for their propagation constants imply these are propagating states (re: a standing wave will have $\beta=0$), which we also observe from the slope >0 of defect dispersion bands 1 and 3 (dispersion slope=group velocity). Out-of-plane coupling to these propagating states, from an over-head pump uniformly illuminating the PC-WOA, requires a matching of propagating states β between the ambient air and the defect layer. However, as we saw in the Theoretical Background section, at a given frequency, the β values for light range from 0 to an upper limit defined by the confinement line. For ambient air, β -values less than the light-line are only possible, and these values are all less than the $\beta=0.476$ value for the $\lambda_p=0.98$ μm defect layer propagating state. Thus, we see from Fig. 6.9.a that it is not possible to couple from ambient air into the 980 μm propagating state. We explored various optical pump layer thicknesses, but for a defect layer made of SiO_2 , surrounded by an Si/SiO_2 based PBG, it isn't possible to engineer a defect-layer propagating state at $\lambda_p=0.98$ μm , with a β value $<$ the light line.

We can still couple from air into the 0.488 μm propagating state. $\lambda_p=488$ nm corresponds to pump excitation from an Ar-ion laser, and we have such a 0-2 W power output laser. It will be used for our preliminary studies to measure gain. However, as we can see in Fig. 6.9.e, the 488 nm propagating state is multi-mode, with an overlap fraction

of $\Gamma_p=0.66$ (re: 2-D confinement approximation= $(1\text{-D confinement})^2$) within the defect core. It is still preferable to work with a 980 nm pump, due to its better mode overlap with λ_s .

We can achieve coupling of the 980 nm pump by means of a prism coupler with refractive index higher than $n_d=1.445$. Fig. 6.10.a show the schematic of how a prism coupler works. The angular faceting of a prism coupler helps to re-direct light transmitted into the coupler (through the primary surface), into incident angles on the secondary surface, which lie outside the critical angle (with respect to air) of the high refractive index coupler. I.e., the faceting ensures that the surfaces of the prism coupler in Fig. 6.10.a are not parallel, and the β -value of light seen by the coupler surface abutting the PC-WOA, now lies outside the critical angle, thus trapping light and keeping it from transmitting back out to air. Faceting is the principle that ensures diamonds trap light from ambient air (and leak light back out to evanescently—creating the illusion of a glimmer at facet boundaries). This effect of faceting can be more generally understood on a Projection Band Diagram (Fig. 6.10.b) as the projecting of β -values outside the light-line. The range of incident λ_p ray angles from ambient air onto the prism coupler, correspond to the range of $\beta < \beta_{\text{air}}$, both in ambient air and within an Si_3N_4 prism coupler. However, the faceting angle maps the β -values within this range to a larger range of $\beta < \beta_{\text{SiON}}$, by ensuring that the angle of incidence on the secondary surface is greater than the angle of refraction through the primary surface. Integrating an Si_3N_4 coupler onto the PC-WOA with engineered adds significantly to design complexity. This is therefore not an optimal solution, we present a more efficient solution for coupling $\lambda_p=980$ nm in our second PC-WOA design, presented shortly.

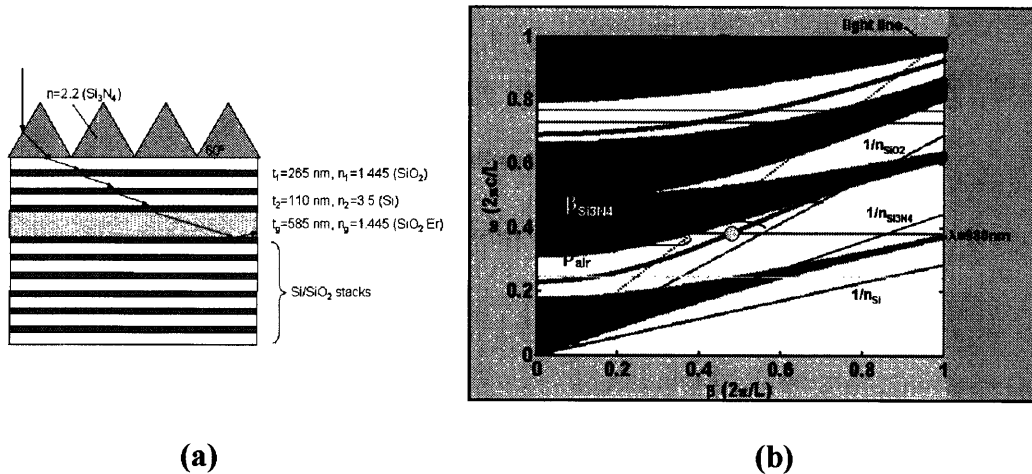


Fig. 6.10. (a) Schematic diagram of a Si_3N_4 60° prism coupler atop the PC-WOA. (b) The coupling effect of a Si_3N_4 prism coupler, as understood on the Projection Band Diagram.

Table 6.1 lists the required angles of incidence from ambient air at $\lambda_p=488$ nm and at $\lambda_p=980$ nm + a Si_3N_4 60° prism coupler.

	n_g	n_{eff}	Γ	θ_m	θ_{air}	$\theta_{\text{Si}_3\text{N}_4}$
1537 nm	5.147	0.546	0.68	67.8°	33.1°	7.8°
980 nm	1.915	1.246	0.82	30.4°	--	18.1°
488 nm	3.474	0.716	0.66	60.3°	45.7°	10.3°

Table 6.1. Summary of transverse-resonant propagating mode group and effect refractive indices, and mode angle θ_m ; coupling angle into the resonant states from ambient free space (θ_{air}) and an ambient Si_3N_4 prism coupler ($\theta_{\text{Si}_3\text{N}_4}$).

Our design goal with over-head pumping is to create a uniform pump power profile along the amplifier. We observed from Fig. 6.9.a that the defect layer confined modes are propagating states and not standing wave resonant states. As we can see from this figure, the resonant state for $\lambda_p=980$ nm comes from the same band as λ_s , as such it isn't possible to optically engineer a $v_g=0$ resonant for λ_p . Blue-shifting band 1 upward in

energy could achieve this, but at the loss of having a resonant state for λ_s . For the two high power wavelengths available from an Ar-ion laser, a standing wave state can be approached for $\lambda_p=514$ nm, but not $\lambda_p=488$ nm. As we will see in the transmission loss section, it is imperative to have signal group velocity $v_g \gg 0$. This requirement forces a red-shift in all the bands, resulting in $v_g \gg 0$ at $\lambda_p=488$ nm. Table 6.3 lists the group index n_g and group velocity v_g at these wavelengths.

However, whether the pump wavelength resonant state is a standing wave or propagating has no bearing on the designing of a uniform pump profile by over-head pumping. As schematically depicted in Fig. 6.1, our proposed design to us a cylindrical lens to deform a ~ 400 μm diameter pump excitation beam spot into a rectangular $10 \mu\text{m} \times 1$ cm stripe length. A constant pump flux is input along the entire device length $L_g=2$ cm, at the required coupling angles dictated by Table 6.1. Regardless of coupling to a propagating state, the same steady state resonantly confined pump intensity will be present, per unit length z within the defect layer, as predicted by the Finite Difference simulations of Fig. 6.9.d-e.

(iii) Thickness Variation of Defect Layer

The one dimensional confinement structure we have grown to test out-of-plane pump coupling and the influence of uniform optical pumping, was grown entirely by sputtering. Sputtering deposition rates have shown (see chapter 4) a film thickness variation across a 6" Si wafer substrate, of $\pm 5-10\%$. Given the sensitivity of transmission loss on group velocities $v_g \rightarrow 0$ (discussed later in this section), it was of paramount importance to design the PC-WOA with a nominally chosen defect layer thickness which

safely budgets, within a ± 5 -10% range, group velocities $\gg 0$, at λ_s . The sensitivity of this problem is unique to the physics of transmission loss for PBG-confined light propagation within a defect core; with conventional total internal based refractive index guiding (chapter 2 and 5), this was not a topic to address.

At $\lambda_s = 1.537 \mu\text{m}$, a defect layer clad above and below by Bragg reflectors beginning with a higher refractive index Si layer (see Fig. 6.7), and a film thickness of $t_g = \lambda_s / 2n_1 = 532 \text{ nm}$ will produce a transverse resonantly confined mode of light with intensity maxima in the center of the layer. With a potential deposition variation in a $\sim 500 \text{ nm}$ film as high as 10% ($\sim 50 \text{ nm}$), we selected a nominal (i.e. target value) film thickness of $t_g = 585 \text{ nm} \pm 50 \text{ nm}$. The above expression relating t_g to λ is directly proportional: decreasing t_g will decrease the λ -value of the standing wave wavelength inside the defect layer, and thus blue-shift both dispersion band 1 and its y-axis intercept frequency $\omega(\beta=0)$ (see Fig. 6.11.a,b). Since $v_g(\beta=0)=0$, we wanted to ensure that (i) the film wasn't too thin, which could result in no overlap of band 1 with the high luminescence (i.e. high gain) spectral emission range of Er lying between $\omega=0.23$ -0.26 ($2\pi c/L$ units) in Fig. 6.8; and (ii) we wanted to avoid having the $\omega(\beta=0)$ value of band 1—i.e. the y-axis intercept of band 1—occur at a frequency below the Er peak emission (occurring at wavelength 1537 nm).

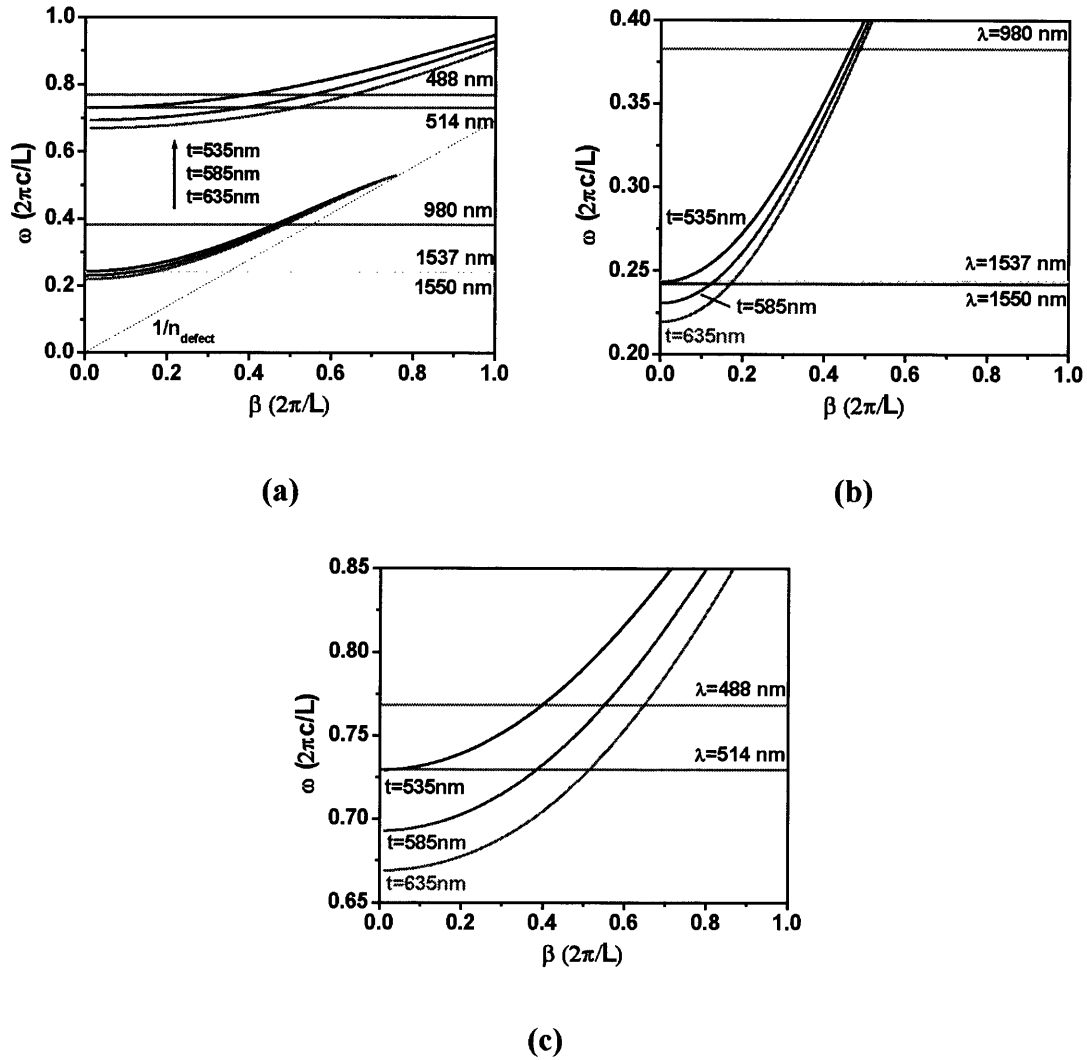


Fig. 6.11. (a) Plot of defect layer dispersion bands at λ_s and λ_p for the choice of three different defect layer thicknesses. (b) and (c) are magnifications of (a) around the λ_s and λ_p frequency regions, respectively.

Our minimal possible film thickness value (535 nm) lies at the boundary of the 1537 nm propagating state having $v_g \rightarrow 0$, while our maximum possible film thickness value (635 nm) results in a relatively large value for v_g at $\lambda_p = 514, 488$ nm (see Fig. 6.11.c). The approximate film thickness equation used to relate t_g and λ can be written for all three bands presented in our ω versus β plot:

$$t = \frac{1}{2} \frac{\lambda_1}{2n_{SiO_2}} = \frac{\lambda_2}{n_{SiO_2}} = \frac{3}{2} \frac{\lambda_3}{n_{SiO_2}}$$

(6.9)

where λ_i corresponds to the ω -axis frequency values at $\beta=0$ for band i (most of band 2 is subsumed within transmissive propagating states referred to as low dielectric bands, or air bands in [14]). We thus see from this expression that red-shifting band 1 will also red-shift band 3. Thus, we chose $t_g=585 \text{ nm} \pm 50$ as a balanced trade-off between ensuring a high v_g for λ_s while trying to not arbitrarily increase the v_g of at least one λ_p .

(iv) Transmission Loss

The confinement principle within a PC-WOA defect core is transverse resonant confinement, i.e. using the large angular reflectivity of two Bragg Reflectors to trap light within a defect core at angles corresponding to coherent wavefront propagation in the propagation direction: light stays trapped between the two reflectors and travels along the defect layer. The advantage of this photonic crystal confinement effect[131,15] is the ability to confine propagating light at arbitrary angles (with respect with to the Bragg Reflector normal). But unlike the confinement principle of total internal reflection, which fundamentally asserts zero power transmission of a propagating state out of the waveguide core, confinement from a finite-sized photonic crystal is a form of resonant confinement (which by definition couples propagating light out of the defect layer through weakly transmissive reflectors). The physics of transverse resonant confinement thus implies signal power P_s must leak out of the defect core as the signal propagates along the z -direction: we call this leakage of power the propagation loss of a PCWOA, α_p .

We study here the minimum number of Bragg pairs required to make this resonance transmission loss less than the Er gain, per unit cm.

We derive an expression for the propagation loss due to finite-sized Bragg reflector confinement, for a propagating state with effective index n_{eff} (corresponding to an angular incidence on the Bragg Reflectors of $\theta_{\text{eff}} = \cos^{-1}(n_d/n_{\text{eff}})$):

$$\alpha_p = \frac{1}{t_d} \sqrt{\left(\frac{n_d}{n_{\text{eff}}}\right)^2 - 1} \cdot \ln\left(\frac{1}{R_{\theta_{\text{eff}}}}\right).$$

(6.10)

The results are summarized in Table 6.2. We see that even the incremental improvement in an Si/SiO₂ Bragg Reflector's reflectivity for > 3 Bragg pairs (see Fig. 6.12.b) still results in vast decreases in propagation loss per unit cm. This is because of the sensitive exponential dependence of a resonant cavity's loss (what we called external coupling loss α_e in chapter 5) on reflectivity. As Table 6.2 shows, it is critical to clad the defect core with *at least* 8 Si/SiO₂ Bragg pairs in order to bring propagation loss $\alpha_p \sim 0.3$ dB/cm. For an Er doping concentration of $2 \times 10^{20} \text{ cm}^{-3}$, uniform pumping will ensure a uniform gain coefficient of $\gamma_0 \cong \sigma_{21} \Delta N \approx \sigma_{21} N = 5.22$ dB/cm. For our preliminary 1-D study, we decided to deposit 6 Bragg pairs below and above the defect layer for testing the basic principles of over-head power coupling. 6 pairs was considered a reasonable trade-off for a preliminary exploration of the pump coupling physics to a PC-WOA, if not for delivering a device with net gain.

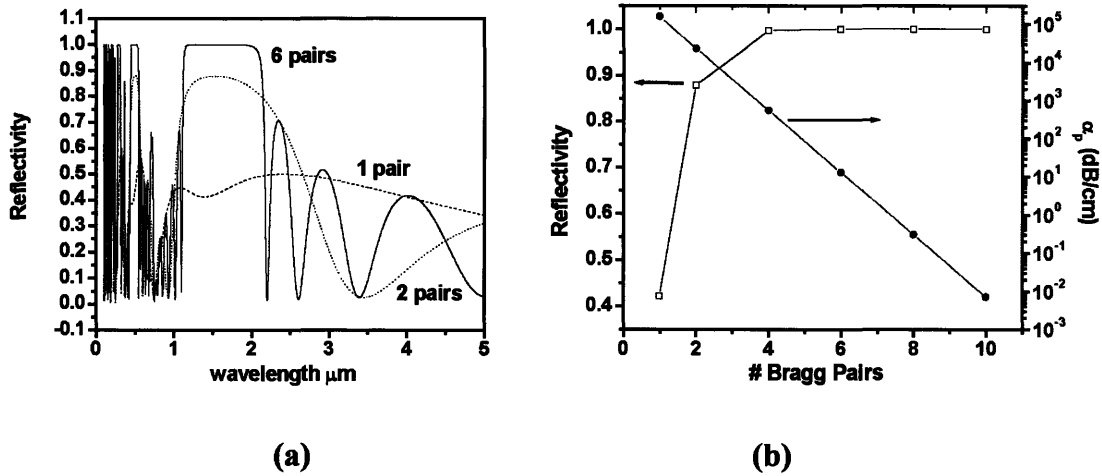


Fig. 6.12. (a) Spectral Reflectivity at angle corresponding to λ_s propagation, for different number Si/SiO₂ Bragg Reflector stacks. (b) Reflectivity and propagation loss α_p versus number Si/SiO₂ Bragg Reflector stacks, at λ_s .

	6 Si/SiO ₂ pairs		8 Si/SiO ₂ pairs	
	α_p (dB/cm)	Q_e	α_p (dB/cm)	Q_e
$\lambda_s=1.537 \mu\text{m}$	12.93	9.37×10^4	0.304	4×10^6
$\lambda_p=0.98 \mu\text{m}$	8.73×10^{-2}	3.55×10^6	6.18×10^{-4}	5.01×10^8
$\lambda_p=0.488 \mu\text{m}$	8.06	2.44×10^5	0.2	9.78×10^6

Table 6.2. Summary of propagation loss as a function of the number of Bragg Reflector pairs (cladding a defect layer below and above) reveals that the exponential sensitivity of α_p on R requires a minimum of 8 Si/SiO₂ Bragg Reflector pairs in order to decrease propagation loss to ~ 0.3 dB/cm.

(v) Free Spectral Range and WDM Applicability

λ_o (nm)	n_{eff}	n_g	v_g ($\times 10^8$ m/s)	FSR_λ (nm)
488	0.716	3.474	0.86	0.16
980	1.246	1.915	1.57	0.12
1537	0.546	5.147	0.58	4.07

Table 6.3. Summary of effective refractive index, group refractive index and Free Spectral Range at two pump wavelengths $\lambda_p=488, 980$ nm and signal wavelength $\lambda_s=1537$ nm.

Table 6.3 summarizes the effective index and group index of λ_s, λ_p within the Photonic Crystal WOA. For total internal reflection based index guided WOAs we observed a 25% discrepancy between effective refractive index n_{eff} and group refractive index n_g values (see table in ring laser section, chapter 5). We observe a much larger 89% discrepancy between n_{eff} and n_g at λ_s in the PC-WOA, and similarly large discrepancies for λ_p . This is indicative of the PC-WOA being a highly dispersive medium, i.e. a waveguiding medium within with a carrier signal's group velocity dramatically changes with wavelength.

Dispersion affects both (i) the WDM applicability and (ii) individual channel transmission rate of the PC-WOA. We evaluate (i) by examining the Free Spectral Range, i.e. the spacing between frequencies of light which maximally transmit through a *finite*-sized medium (more generally referred to as a Fabry-Perot cavity), of length $L_g=2$ cm.

We derive the general expression for a cavity's Free Spectral Range (FSR) to be

$$\text{FSR}_\lambda = \left(\frac{\lambda_o n_{\text{group}}}{n_{\text{eff}}^2} \right) \frac{1}{2L}$$

(6.11)

where the λ subscript on FSR denotes our expression to be in units of wavelength, and not the typically reported FSR units of frequency. We observe the expression has a dependence on both effective refractive index and group refractive index, representing the optical effect effective index dependence on λ (re: the FSR is quantifying the spectral gap between neighboring peaks of maximal transmission). We calculated the FSR for the transversely resonant confined propagating state from the first derivative of band 1 (see Fig. 6.13). Table 6.3 summarizes the results: we observe an $\text{FSR}_\lambda = 4.1$ nm at λ_s , corresponding to a ~ 510 GHz line spacing between WDM channels. We conclude the PC-WOA can accommodate moderate WDM amplification, but not the Dense-level D-WDM signals of a fiber optic link (100-200 GHz line-spacing).

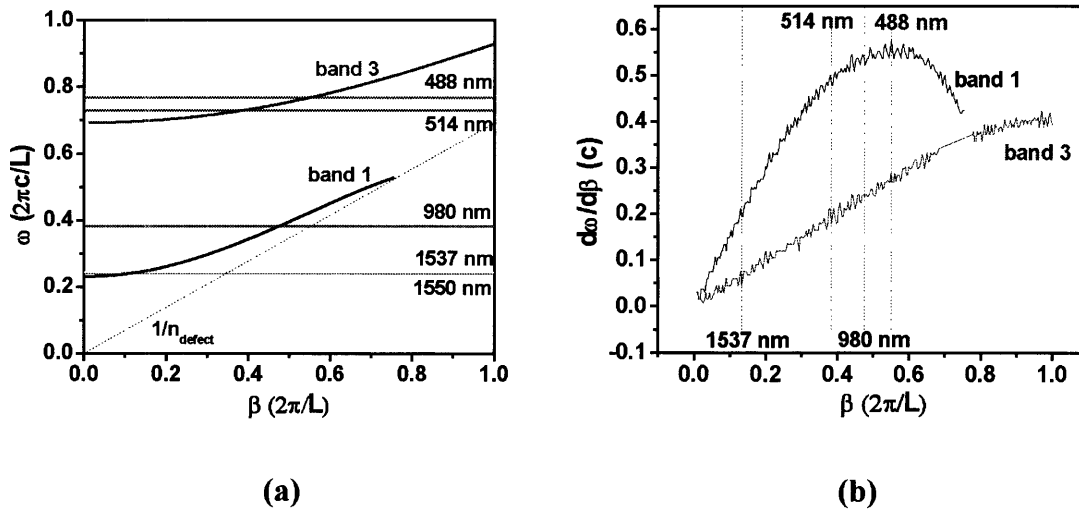


Fig. 6.13. (a) Re-plotting of defect bands 1 and 3 from Fig. 6.9.a (without low/high dielectric bands) and (b) the first derivative of (a), defined as the group velocity.

(vi) Dispersion and Transmission Rates

The encoding of digital bits of information as optical pulses in time, on carrier wavelength λ_s , is equivalent to adding a spectral bandwidth of frequencies $\Delta\nu$, about

carrier frequency ν_s (see [23] for reference on the Bandwidth Theorem). The drastic change in the ω versus β slope of band 1 indicates the PC-WOA is a highly dispersive gain medium, i.e. the group velocity may vary considerably amongst the range of frequencies $\Delta\nu$ used to temporally shape the pulse-encoded signal. This effect of changing group velocity is quantified as a modal dispersion coefficient[3]; it is proportional to the curvature ($d^2/d\omega^2$) of the band structure:

$$D_{\text{modal}} = \frac{d}{d\lambda_o} \left(\frac{1}{v_{\text{group}}} \right) = \frac{2\pi c}{\lambda_o^2} \frac{d^2 \beta}{d\omega^2} \quad \left(\frac{\text{ps}}{\text{km} \cdot \text{nm}} \right)$$

(6.12)

where the time delay in ps for a $\Delta\nu$ (or equivalently $\Delta\lambda$) nm-bandwidth in a medium of km-length L_g , is

$$\Delta t = D_{\text{modal}} \Delta\lambda_o L_g.$$

(6.13)

We looked at the band curvature of the propagating state at λ_s in the PC-WOA, and compared it to a total internal reflection index-guided WOA (such as the devices of chapter 2). Fig. 6.14.a shows the computed dispersion relation for our index-guided WOA reference: the SiON case study from the end of chapter 2. The computation is done for 1-D TE mode confinement, using an SiON layer thickness of 1.87 μm , corresponding to index-guiding at λ_s just below single-mode cut-off.

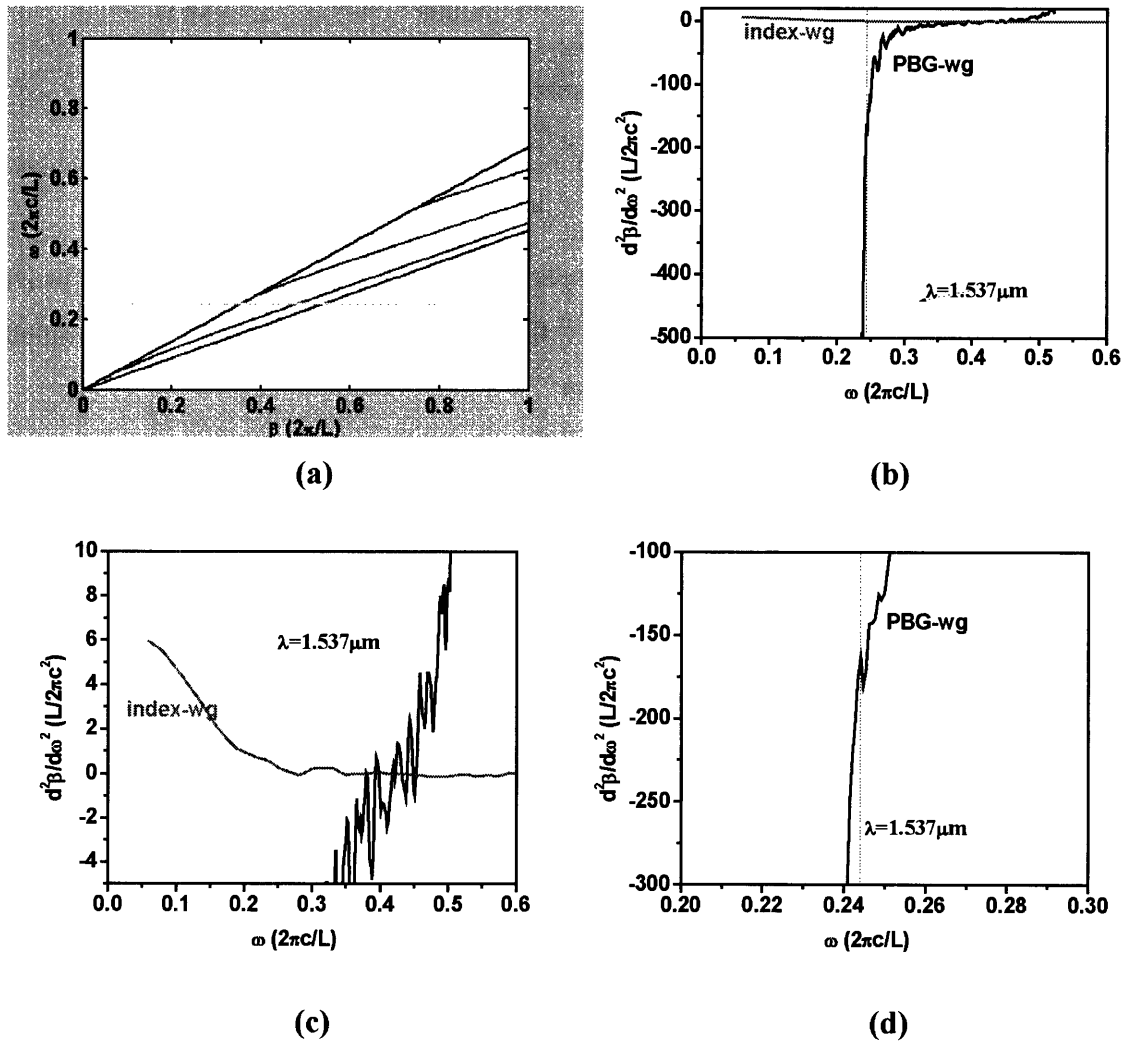


Fig. 6.14. (a) Dispersion relation for SiON case study (end of chapter 2) in one-dimension, show band structure for index-guided propagating modes. (b) Band structure curvature versus frequency ω for index-guided and PBG-guided propagating modes. Magnification of two local regions shows the curvature at frequency corresponding to λ_s for (c) index-guided band structure and (d) PBG-guided bandstructure.

Fig. 6.14.b-d plots the bandstructure curvature versus frequency ω , with magnification of particular regions showing the curvature value for index-guided and PBG-guided propagating states, at λ_s . We observe a $\sim 490\times$ larger curvature for the PBG-guided versus index-guided state. The results are summarized in Table 6.4: we see that

	$d\beta^2/d\omega^2$	D (ps/km·nm)	(100 Gbit/s) D·(1.57nm) ·(1cm)	(10 Gbit/s) D·(0.16nm) ·(1cm)
Index-wg	0.36	190	3×10^{-3} ps	3×10^{-4} ps
PBG-wg	-176	9.3×10^4	1.46 ps	0.15 ps

Table 6.4. List of band curvature, dispersion coefficient, and temporal pulse broadening Δt at 100 Gbit/s and 10 Gbit/s, for an index-guided versus PBG-guided WOA (Microphotonic length scale $L_g=1$ cm).

for a transmission rate of 100 Gbit/s, a wavelength bandwidth of $\Delta\lambda=1.57$ nm is required, and for a microphotonic scale 1 cm propagation length, this imparts $\Delta t=1.46$ ps temporal broadening to the pulse-encoded signal. For a 100 Gbit/s transmission with a 50/50 duty cycle, the time duration of one digital pulse is 5 ps; thus dispersion will contribute a significant intersymbol interference at 100 Gbit/s. At 10 Gbit/s, corresponding to a pulse time duration of 50 ps, less bandwidth is needed and thus a lower temporal broadening of $\Delta t=0.15$ ps is observed. This is safely within the margin of error (0.15 ps \ll 50 ps), assuring no intersymbol interference for a pulse-encoded signal.

Note that for a 1-10 m length fiber optic link length scale, the temporal broadening will be $\Delta t=146$ -1460 ps at 100 Gbit/s and $\Delta t=15$ -150 ps at 10 Gbit/s. We conclude the Photonic Crystal-WOA produces too high a dispersion for the 25-30 dB amplification requirements of fiber optic links. The PC-WOA is a device design suited to Microphotonic length scales at data rates < 10 Gbit/s.

We make a brief comment concerning the materials dispersion, i.e. the wavelength dependence of materials refractive index, for WOAs. Table 6.5 shows that the refractive index of Si and SiO₂, the two materials making up the Bragg Reflector for

the PC-WOA, increases with decreasing wavelength. With relation $t_i=m\lambda/4n_i$ ($i=1,2$) defining the center of the m -th stop band ($m=1,2,3,\dots$), we see the effect of increasing n_1 and n_2 is to red-shift (decrease in frequency) the m -th stop band. More importantly, the 3rd band, corresponding to propagating states at $\lambda_p=514, 488$ nm, similarly red-shifts. We see in Table 6.5 that the refractive index of (insulator) SiO_2 does not increase with decreasing λ as quickly as the refractive index for Si. We conclude the red-shifting of band 3 will not be a significant deviation from our calculations in Fig. 6.9.a.

λ_o (nm)	n_{Si}	n_{SiO_2}
488	4.367	1.462
633	3.875	1.46
830	3.67	1.453
1550	3.5	1.445

Table 6.5. Materials dispersion: the decrease in refractive index for both Si and SiO_2 with increasing wavelength. We observe a larger change in refractive index for Si over this wavelength range, than for SiO_2 .

(vi) PC-WOA Grown by Sputtering

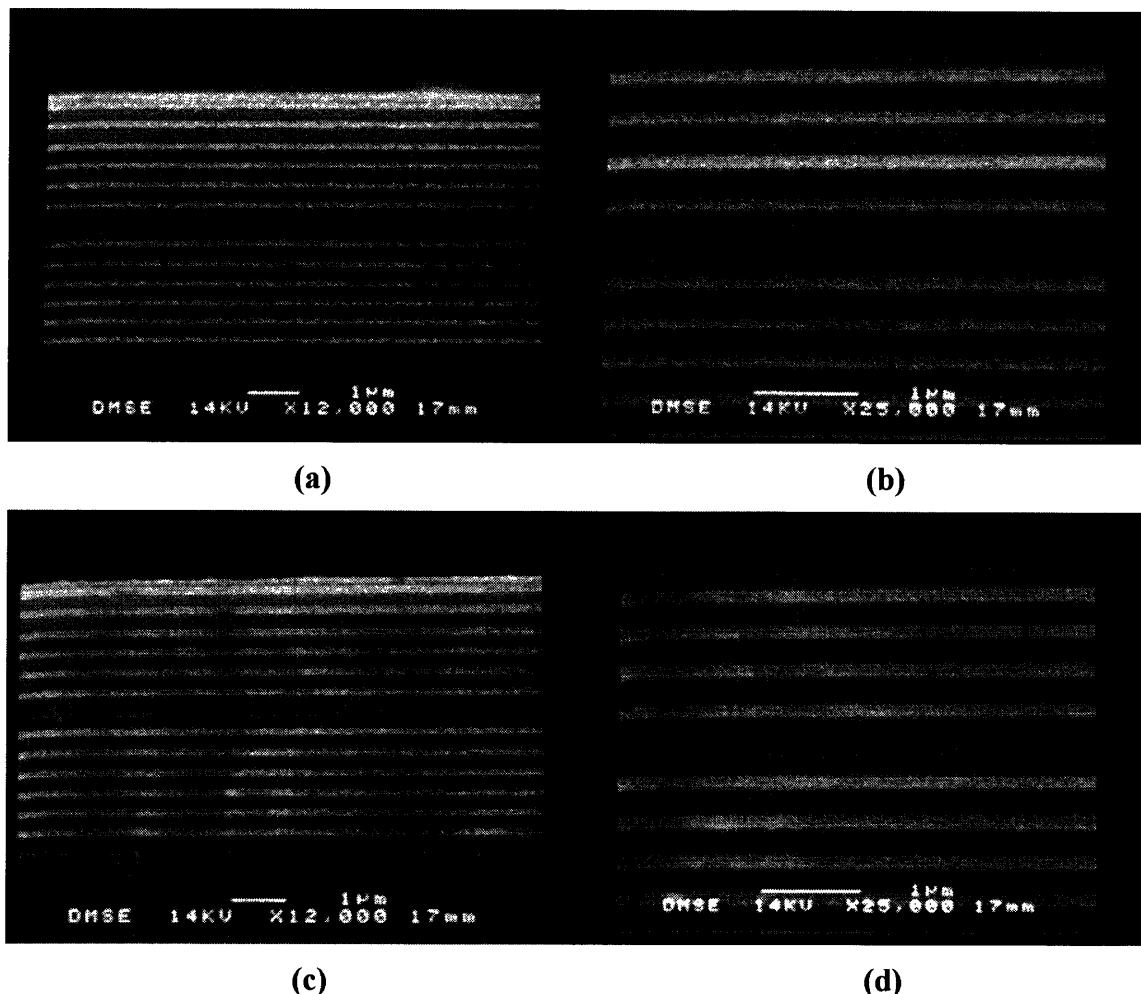


Fig. 6.15. Secondary Electron Mass (SEM) micrographs of the sputtered 1-D PC-WOA test structure, (a) as-deposited and (b) with magnification; (c) after $t=1$ hour, $T=1000^{\circ}\text{C}$ anneal and (d) with magnification.

We grew the 1-D Photonic Crystal-WOA preliminary test structure by Ar gas magnetron sputtering (see chapter 4 for experimental details) using a Si, SiO₂ and Er target to deposit 6 Si/SiO₂ Bragg pairs, an SiO₂:Er defect layer (nominal thickness 585 nm), followed by another 6 Si/SiO₂ Bragg pairs. The structure was grown under an Ultra-High Vacuum base pressure of 7×10^{-8} torr, with Ar gas chamber pressure of 4×10^{-4} torr during deposition (pressures measured by an Edwards AGD wide-range gauge).

Fig. 6.15 shows cross-section SEM micrographs of the structure as-deposited (Fig. 6.15.a and with magnification in Fig. 6.15.b) and after a $t=1$ hour, $T=1000^{\circ}\text{C}$ anneal (Fig. 6.15.c and with magnification in Fig. 6.15.d) under nitrogen gas overpressure (see chapter 4 for annealing details) to order to optimized Er light emission/optical gain within the defect layer. Profilometry measurements of calibration growths just before deposition of this structure showed 5% film thickness variation across 6" Si wafers. The deposited layer thickness measured from the SEM images give film thickness values of $t_d=606$ nm for the defect layer (within 3.5% of our nominal 585 nm value), $t_2=236$ nm for the Bragg Reflector's SiO_2 layer (within 11% of our nominal 265 nm value), and $t_1=151.5$ nm for the Bragg Reflector's Si layer (within 38% of our nominal 110 nm value). The enormous discrepancy for the Si measured layer thickness appears to an artifact of Si imaging in the SEM. Reflectivity measurements (see Fig. 6.16) confirm that the PC-WOA defect layer standing state and location of stop-band are in good agreement with our nominally chosen values for t_g , t_1 and t_2 . Annealing is observed to improve this agreement, possibly due to consolidation of the as-sputtered layers into denser thin films.

Experimental measurements of out-of-plane pump coupling into this structure is pending the construction of a new optical gain measurement set-up at MIT that includes an over-head pump coupling apparatus with an adjustable angular stage. By observing the intensity of output propagating spontaneous emission from the PC-WOA, as a function of the over-head optical pump angle of orientation (i.e. by scanning the angles of orientation about the free space coupling angle listed in Table 6.1), we will experimentally demonstrate the angular coupling of the optical pump through the Bragg Reflector cladding. The construction of this angular-adjustable gain-measurement optical stage, and

subsequent angular coupling and device gain measurements will be followed in the Ph.D. thesis work of fellow colleagues in this research group

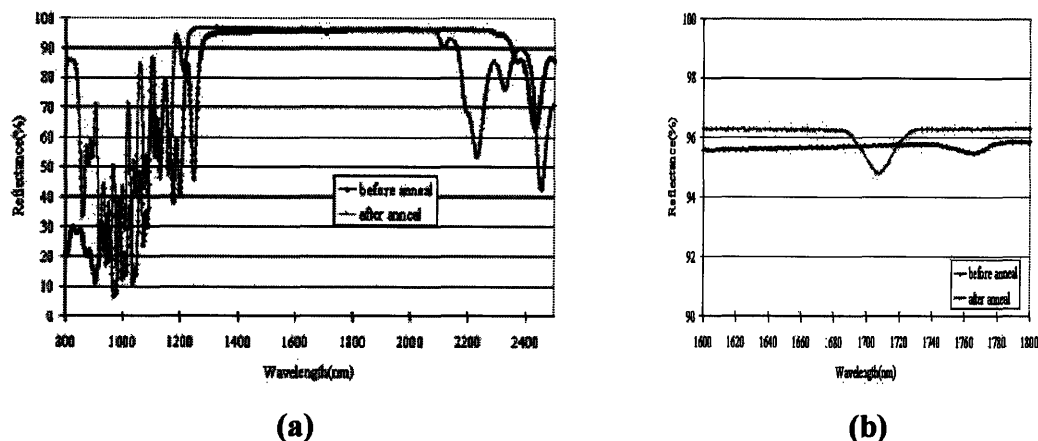


Fig. 6.16. (a) Reflectivity plot of sputtered PC-WOA, showing good agreement between experimental structure versus theoretical design, for both defect layer standing wave state (shown as higher spectral resolution in (b)) and Bragg Reflector stop-band.

We conclude our study on the PC-WOA with a theoretical evaluation of its gain efficiency and areal footprint. These two performance metrics are then compared with our HIC-WOA (chapter 2) and R-WOA (chapter 5) studies.

6.4.2 Device Performance

To model the effect of a transverse-resonant confinement based uniform pump profile on device gain efficiency, we worked with the coupled optical power and E_r excitation equations (2.1) and (2.2) of chapter 2, subject to the fixed condition of constant pump power profile across the device gain medium $0 < z < L_g$ (see Fig. 6.17.a).

This constant power profile $P_{p(in)}$, propagating within the resonantly confined PC-WOA, corresponds to an overhead input power $P_{p,overhead}$

$$P_{p,overhead} = P_{p(in)} \frac{L_g \times w_g}{t_g \times W_g}$$

(6.14)

where w_g is the width of the PC-WOA (for the particular case of our test sample, $w_g \gg 1$ μm would be the size of the cleaved sample orthogonal to the direction of experimentally measured propagation). Equation (6.14) relates the pump photon number required for optical gain (as determined by our simulation in Fig. 6.17.a), within the resonant cavity of the PC-WOA, to an overhead pump power which must be shaped (by use of a cylindrical lens) into a uniform rectangular beamspot of dimensions $w_g \times L_g$.

This overhead pump power must then be related to the pump power outside the PC-WOA, i.e. above the structure in free-space, by the equation (5.9) from chapter 5,

$$P_{p,overhead} = \frac{Q}{Q_e} \frac{Q}{t_g} \frac{4v_g}{\omega} P_{p,(out)}$$

(6.15)

which we have slightly modified (replacing the $2\pi r$ factor with t_g).

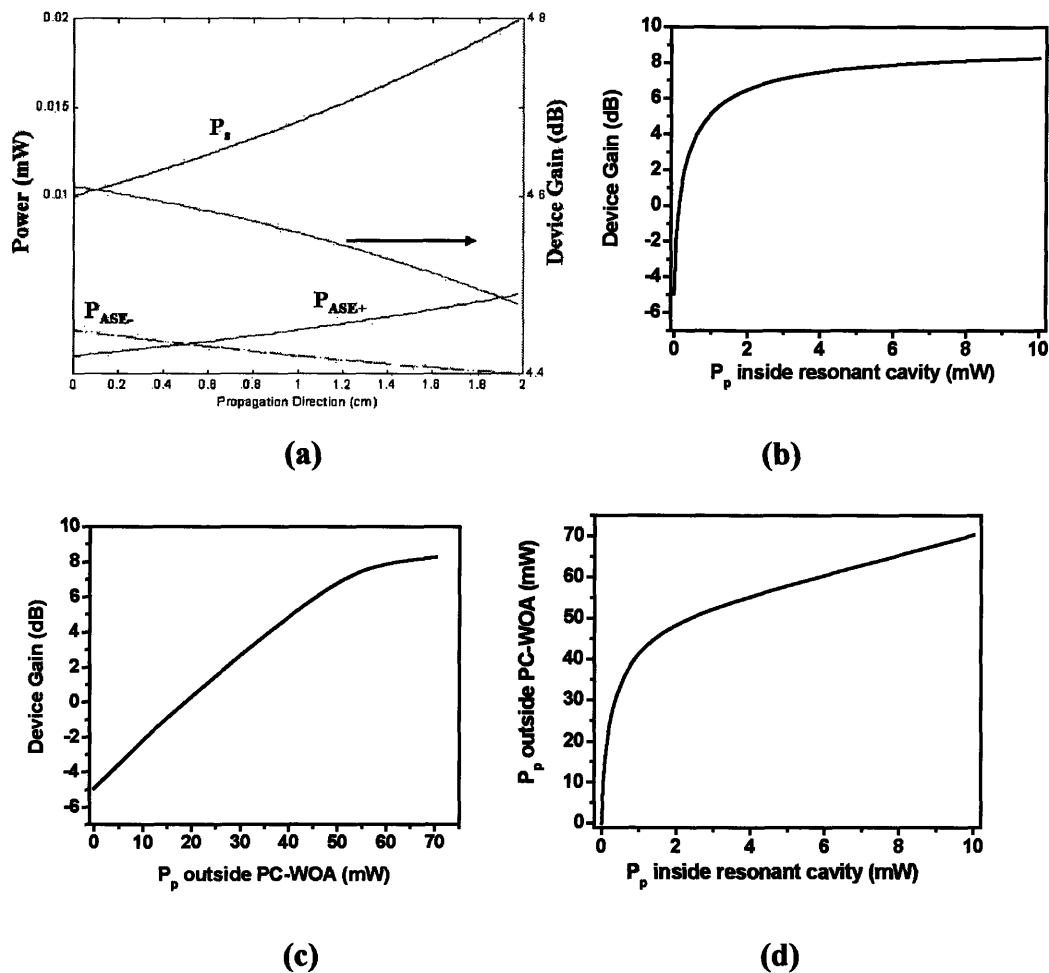


Fig. 6.17. (a) Plot of optical powers (left axis) and gain profile (right axis) versus position z within the $L_g=2$ cm PC-WOA, yielding an output device gain of 3 dB for $P_s=10 \mu\text{W}$ input signal power (constant pump power profile within the resonant cavity, $P_{p(\text{in})}=0.425$ mW). For the same device, plot of device gain versus pump power (b) inside the PC-WOA, $P_{p(\text{in})}$ and (c) outside the PC-WOA, $P_{p(\text{out})}$. We observe that $P_{p(\text{out})}=32$ mW corresponds to the $P_{p(\text{in})}=0.425$ mW cavity pump power profile. (d) Plot of $P_{p(\text{in})}$ versus $P_{p(\text{out})}$, demonstrating the PC-WOA to be a highly under-coupled device.

It is due to equation (6.15), that we discover a critical limitation in the design of a high gain efficiency PC-WOA. As the transmission loss section made clear, a minimum of eight Si/SiO₂ Bragg Reflector pairs are required above and below the defect layer, in

order to have propagation losses $\alpha_p < 0.3$ dB/cm. Having an equal number of Bragg reflector pairs above and below the defect layer or resonant cavity, ensures that coupling at resonant frequencies to the defect layer, is done under the *critical coupling* condition defined in chapter 5: the coupling rate from the outside to the defect layer, through the upper Bragg Reflector, is equal to the coupling from the defect back to the outside, through the lower Bragg Reflector. This critical match condition results in the large reflectivity dip (down to $R=0$ at λ_s), observed in Fig. 6.2.a. However, the doping of Er within the defect layer has now introduced a damping term (see chapter 5 for definitions) within the resonant cavity: pump photons entering the defect layer through the upper Bragg reflector, may escape the layer either by absorbing into the Er atoms or by coupling through the lower Bragg reflector.

	α_{Er} (dB/cm)	Q_{Er}	Q_e (6 Si/SiO ₂ pairs)	Q_e (8 Si/SiO ₂ pairs)
$\lambda_p=0.98 \mu\text{m}$	0.28	9.5×10^5	3.55×10^6	5.01×10^8
$\lambda_p=0.488 \mu\text{m}$	0.53	1.83×10^6	2.44×10^5	9.78×10^6

Table 6.6. Summary of Er absorption Q_{Er} versus external coupling Q_e . α_{Er} has been taken at $z=L_g$, the location in the PC-WOA at which population inversion ΔN is lowest (for a constant pump $P_{p(in)}=0.425$ mW power profile), and thus absorption at $\lambda_p=980, 488$ nm is highest.

The < 0.3 dB/cm propagation loss condition within the defect layer requires 8 or more Bragg Reflector pairs above and below the layer, and this in turn results in an external coupling $Q_e \gg$ the absorption Q_{Er} from Er: the resonant cavity is grossly under-coupled, to the point that the required pump power to couple overhead from free space, $P_{p(out)}$, is comparable to $P_{p(overhead)}$. Resonant confinement advantageously builds up pump power

only at critical coupling for λ_p , and the low propagation requirements for λ_s combined with the absorption coefficient of Er (for λ_p), results in the PC-WOA being highly under-coupled at λ_p . This limitation occurs for both $\lambda_p=980, 488$ nm (summarized in Table 6.6); the 3 dB gain efficiency (using $\lambda_p=488$ nm) of 0.19 dB/mW ($\lambda_p=980$ nm). In comparison, the 3 dB gain efficiency of the SiON HIC-WOA ($\Delta n=0.155$) from chapter 2, is 0.35 dB/cm. We conclude the uniform-pumped PC-WOA is a poor gain efficiency device.

While the device performance efficiency of a PC-WOA can not improve upon the HIC-WOA by means for uniform pumping, it can be comparable by use of a pump co-propagation scheme. Secondly, the results of chapter 2 for HIC-WOAs were contingent on the design of high Δn waveguides with Er-doped cores, where the default choice of cladding was SiO₂, in order to hermetically seal the PLC structure and allow for the potential design of multi-level PLCs. The results of this chapter provide an additional materials processing flexibility: low refractive index host materials can now be used for the Er-doped defect core, while the Si/SiO₂ Bragg Reflector produces an optimal exponential confinement[129]

$$\frac{1}{x} = \frac{1}{L} \frac{\Delta n}{n_{av}} = \frac{1}{0.365 \mu m} \frac{(3.5 - 1.445)}{(3.5 + 1.445) / 2} = \frac{1}{0.44 \mu m}$$

Si/SiO₂ PBG-confinement based waveguides can be spaced approximately within $3x=1.32 \mu m$ of each other, approximately *independent* of the refractive index of the defect core. This implies an $L_g=2$ cm long PC-WOA can be compactly packed within an areal footprint of $F=185 \times 185 \mu m^2$, using an SiO₂-based cladding materials system and arbitrary defect core host material for Er. In comparison, the footprint of the SiON case study from the end of chapter 2, is $425 \times 425 \mu m^2$.

Therefore, we conclude the performance and size advantages of a PC-WOA are comparable to the HIC-WOA, while opening up a materials processing degree of freedom in choice of defect core material.

We conclude this work with a suggestion for a device structure that will incorporate the benefits of a transverse-resonantly confined pump profile while avoiding the conflicting problem of critical coupling. Consider a PC-WOA with an SiON:Er defect core, clad with Si/SiO₂ Bragg Reflectors that terminate against the defect core, with an SiO₂ spacer layer of thickness $m \times \lambda_o / 2n_2$. m is an integer, chosen so that $m \times \lambda_o / 2n_2 > 3x_{\Delta n}$, where $x_{\Delta n}$ is the decay length of single mode (λ_s) light into this SiO₂ spacer layer, due to the confinement effect of total internal reflection (between this SiO₂ spacer layer and the Si₃N₄:Er higher refractive index defect layer). Such a structure will exhibit both PBG-confined and total internal reflection confined modes of propagating light. If the fundamental band gap is designed around $\lambda_p=980$ nm, a transverse resonant state will exist which lies above the light line, and thus $\lambda_p=980$ nm can couple to ambient free-space without the use of a prism coupler. By blue-shifting the fundamental band gap from a λ_s -centerpoint to a λ_p -centerpoint, there is no longer a PBG confinement mode that concentrates the λ_s field profile within the defect core—but there *is* such a total internal reflection confinement mode. In such a hybrid confinement design, total internal reflection fundamentally ensures no propagation loss ($\alpha_p=0$) at λ_s ; this allows us to flexibly alter the number of Bragg Reflector pairs so that there are fewer Si/SiO₂ pairs in the upper Bragg Reflector versus the lower Bragg Reflector, designed to ensure the critical coupling condition at $\lambda_p=980$ nm:

$$\left[\begin{array}{c} \text{Rate of Coupling from} \\ \text{Upper Bragg Reflector} \\ \text{into Defect Core} \end{array} \right] = \left[\begin{array}{c} \text{Rate of } \sigma_{13} \text{ Absorption} \\ \text{by Er atoms inside} \\ \text{Defect Core} \end{array} \right] + \left[\begin{array}{c} \text{Rate of Coupling to} \\ \text{Lower Bragg Reflector} \\ \text{out of Defect Core} \end{array} \right].$$

Under this condition, we will be able to take full advantage of resonant confinement in such a *hybrid PC-WOA*. Our simulations show the optimal 3-dB gain efficiency of such a uniform-pumped hybrid PC-WOA will be 0.31 dB/mW, still slightly less than the SiON HIC-WOA case study.

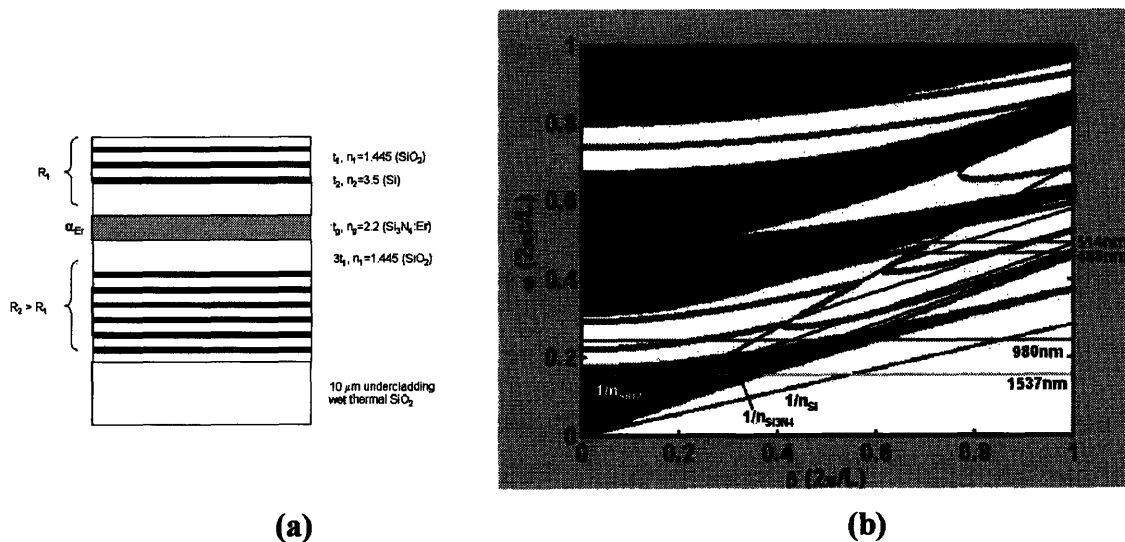


Fig. 6.18. (a) Schematic for hybrid PC-WOA, comprised of a higher refractive index defect layer which guides propagating modes of λ_s by total internal reflection confinement, and λ_p by both total internal reflection confinement and PBG resonant confinement. (b) Projection Band Diagram for this structure

We conclude the hybrid design brings us close to HIC-WOA gain efficiency performance, but it doesn't lead to further enhancement.

6.5 Conclusion

Taking inspiration from the resonance study of chapter 5, we studied in this chapter the influence of transverse-resonant confinement on pump power profile, by

designing (and growing by sputter deposition) a WOA whose optical confinement is based on the Photonic Band Gap principle, and not the total internal reflection principle. The question we sought to answer was whether such a device might provide an additional improvement on the HIC-WOA device performance properties observed in chapter 2. We concluded that in order to ensure net gain at λ_s , the PC-WOA design required >8 Bragg Reflector Si/SiO₂ pairs both above and below the defect core. But for such a high Bragg Reflectivity, we found the Er absorption at λ_p within the defect core resulted in severe under-coupling of $\lambda_p=980$ or 488 nm from the outside world into the defect core. Thus, in an over-head pump coupling scheme, this design could not take advantage of resonant confinement in order to pump the Er atoms at higher optical flux rates, using a small λ_p power source. In fact, 3 dB gain efficiency for the PC-WOA was found to be $\sim 1.84\times$ smaller than the SiON case study from the end of chapter 2, for 3 dB gain output ($L_g=2$ cm).

We conclude that despite a $\sim 1.84\times$ lower 3 dB gain efficiency and comparable Noise Figure (at 3 dB device gain), PC-WOAs have a valuable Microphotonic impact: PC-WOAs open up an extra degree of processing freedom by permitting arbitrary choice of defect core host material, while retaining the size scaling advantage of HIC-WOAs. The high Δn Si/SiO₂ pairs enables the creation of $185\times 185 \mu\text{m}^2$ footprints for $L_g=2$ cm long PC-WOAs with SiO₂:Er defect cores; this is a $5.2\times$ smaller areal footprint than the SiON HIC-WOA case study.

The WDM applicability of such PC-WOAs is compatible with moderate WDM transmission rates (500 GHz channel-to-channel spacing), but not Dense-WDM rates (50-100 GHz channel-to-channel spacing). Similarly, severe dispersion limits the relevance of

PC-WOAs to 1 cm-scale Microphotonics with transmission rates < 0.3 Gbit/s. Such optical amplifiers are not useful for high bit-rate densely multiplexed fiber-optic link transmissions.

Our sputtered PC-WOA is comprised of 6 Bragg Reflector pairs above and below the defect core. While this device will not show net gain at λ_s , it will experimentally confirm our angular coupling design for $\lambda_p=488$ nm from free space overhead pump coupling. Further, gain measurements can be extracted by measurement of loss modulation as a function of overhead pump power $P_{p(out)}$. These results are pending the construction of a new gain measurement stage for measuring λ_p overhead angular coupling.

We conclude with a device design that tries to sever the trade-off between low λ_s propagation loss versus λ_p under-coupling, by separating the confinement physics that governs mode propagation (in the defect core) at these two wavelengths. Our combined PC-WOA guides the signal λ_s by total internal reflection while confining the pump λ_p using transverse-resonant confinement. Such a device promises comparable WDM applicability as the HIC-WOA, but with a still $\sim 1.13\times$ lower gain efficiency.

Chapter 7:

Looking to the Light: Si Microphotonic Amplifier

Conclusions and Suggestions for Future Work



(Internet reproduction of character from Bloom County newspaper comic-strip, © Berkeley Breathed.)

“Stress is due to the difference between expectation and accomplishment.” –Prof. L.C. Kimerling, Fearless Leader, EMAT.

“No this is actually very good... it’s like we go through these moments in life, when these external pressures occur... they’re like milestones that make us go through the change... deadlines are a really good thing.” –Dave Danielson (Graduate Student, EMAT).

“Sajan... you can write much better than this!”-Mindy Baughman (Administrative Assistant, EMAT).

7.1 Er Waveguide Optical Amplifiers for Microphotronics

This thesis presented a (i) materials science experimental study of sputtered materials for Er-based optical amplification in Si Microphotronics, and (ii) an optics engineering theory study for optimizing amplifier pump power requirements by three different methods, within a densely integrated Si Microphotonic Planar Lightwave Circuit.

The materials and circuit design constraints this thesis adhered to, stem from a continuity of semiconductor industry research concerns and a convergence of both telecommunications and integrated circuit development. Silicon and oxygen are two of the most abundant elements in the earth's crust, and their synchronous combination as high quality thermal oxidized Si/SiO₂ interface has resulted in the electronics industry. The resulting ability to grow high purity SiO₂ has given rise to the long-distance telecommunication industry, centered about a carrier wavelength of 1.55 μm, corresponding to minimum loss transmission.

7.2 Future Work in the SiON–Si₃N₄:Er Systems

Si Microphotronics develops micron-scale planar waveguiding devices using Si industry materials processes, for single-mode propagation of at 1.55 μm range carrier frequencies. We thus focused on the 1.55 μm gain center, Er. While Er-doped waveguide amplifiers in low index difference systems have been developed and commercialized, our research looked at Er-doping in higher index difference systems, specifically waveguide cores made up of Er₂O₃, SiON and Si₃N₄. While the Er₂O₃ system showed highly power inefficient potential for optical gain, our measurements in SiON:Er and Si₃N₄:Er gave

very promising results, showing gain modulation which indicates small signal gain values of 14 dB/cm and 23 dB/cm, respectively.

The nitride environment indicates a reduction of both Er-Er clustering and Er-Er cooperative upconversion, enabling these high measurements of gain per unit length. The SiON:Er and Si₃N₄:Er systems may be excellent candidates for WOAs in Si Microphotonics, ($\Delta n=0.1-0.7$) provided background losses can be reduced to achieve net gain. While this goal appears feasible for SiON:Er, the background loss mechanism in Si₃N₄ must be further explored. CVD-grown Si₃N₄ does not show such high background losses. We recommend PL studies of CVD-grown versus sputtered Si₃N₄, as a function of heat treatment, be done in order to establish whether the Si₃N₄ sensitizer is related to background loss in sputtered Si₃N₄ or not. If CVD Si₄N₄ can yield these sensitizers while preserving low background, we recommend CVD co-doping of Er for future ring laser work.

7.3 The Impact of Optical Shrink

Our study on the influence of higher Δn confinement for gain efficiency enhancement extrapolated this confinement effect, first observed and studied by EDFA designers, to the high Δn limit of microphotonic systems. The physical phenomena behind this principle was observed by computer simulation to be the extension along the propagation direction of the gain saturation regime, or equivalently, the shrinking of the bleached absorption regime. Optical Shrink is a design methodology optimizing signal gain across the device length of a co-propagation pumped WOA. While the dependence of device gain on amplifier length has been exhaustively documented for EDFAs, our Optical Shrink analysis presented this dependence as a function of Δn , summarizing the

results in term of gain efficiency and device footprint. The results show that planar strip waveguides can produce 3 dB amplifiers for dense PLCs or 30 dB amplifiers for a new generation low cost EDWAs. Current commercial 30 dB gain ridge waveguide EDWAs have 10 cm length scale footprints. Implementing recent advances in strip waveguide loss, our study shows 30 dB WOAs can be coiled and fitted into compact footprints on the order of $3 \times 3 \text{ mm}^2$, dramatically leveraging parallel planar processing in order to reduce production cost per device.

The low power impact of high gain efficiency devices is relevant for microphotonic systems, which don't require a high saturation $\sim 10 \text{ mW}$ output signal powers, but rather require a modest amplification on the order of 2-10 \times (for input signals ranging from $P_s = 1-10 \text{ }\mu\text{W}$).

7.4 The Influence of Resonance on Gain Enhancement

Our design analysis for sub-threshold gain enhancement by ring resonator confinement is the Er-doped ring resonator analog of VCISOAs, a recently developing research activity. Our results show a very promising 120 \times increase in gain efficiency and 18 \times decrease in footprint. However, the SiON-based ring laser design is a highly multi-mode laser, thereby reducing the amount of power available to each lasing mode. In order to decrease the number of lasing modes we must work with smaller radius rings, and radiative turning loss constraints thus require a higher Δn waveguide, composed of an $\text{Si}_3\text{N}_4:\text{Er}$ core. If the loss mechanisms within sputtered Si_3N_4 can not be reduced further, a shift to Er co-doped CVD-grown Si_3N_4 should be adopted by our group within the next two years at MIT.

Our optical pumping design for ring lasers and R-WOAs relies on single mode propagation of λ_p . Given the lithographic constraints of the I-line stepper available through MIT's MTL laboratories, we must work with a pump wavelength of $\lambda_p=980$ nm and not $\lambda_p=488$ nm (the available high-power pump laser used for VSL measurements in chapter 4). If the sensitizers experimentally observed within SiON and Si₃N₄ are indeed Si nanocrystals, then we hypothesize that $\sim 10^6\times$ in pump absorption cross-section will also be observed at $\lambda_p=980$ nm (because this 980 nm pump energy is greater than the 1.12 eV bandgap of Si), identical to our experimental observations at $\lambda_p=488$ nm. We conservatively did not make this a priori assumption in our design work in chapter 5, and relied on the literature-reported values for 980 nm absorption cross-section by SiO₂:Er, as summarized in Table 4.1.

We therefore recommend absorption cross-section studies be done at $\lambda_p=980$ nm, and if similar $\sim 10^6\times$ absorption cross-section enhancement is confirmed, the ring laser differential slope and R-WOA gain efficiency will increase dramatically.

Our conservative theoretical prediction ring lasers show them to be low output (20 μ W) light sources more useful for microphotonic application than for long-haul telecom. Similarly R-WOAs are limited by experimentally achievable external Q_e values to deliver 3-5 dB amplification. However, given the impressive 23 dB/cm small signal gain measure in Si₃N₄:Er (due to the fast radiative lifetime of Er in combination with a low upconversion coefficient), Si₃N₄:Er ring lasers and R-WOAs will be able to meet the 10 mW light source and 30 dB device gain requirements of long-haul communications.

7.5 Photonic Crystal Methods

Our theoretical study into the influence of Photonic Crystal confinement on Er-based optical gain does not show better gain efficiency performance than the Δn effect of Optical Shrink, however our study opens up the possibility for new methods of vertical mode coupling optical pump excitation. The greater value of a PC waveguide for microphotonics may be as a high efficiency coupler to freespace and off-PLC communications.

In addition, the PC-WOA can be optically pumped by co-propagation, thus recovering the high gain efficiency principle of Optical Shrink, while the (Si/SiO₂ comprised) Photonic Crystal cladding's exponential reduction of cladding field intensity still allows us to reduce the WOA footprint by 5.3 \times , versus the footprint of the total internal reflection confined SiON case study.

7.6 Light Sources at Wavelengths $\neq 1.55 \mu\text{m}$

We conclude with some suggestions about future potential PLC designs that try to take advantage of the sensitizers discovered in SiON and Si₃N₄.

The 1.55 μm wavelength in Si Microphotonics is a choice in carrier frequency initiated by fiber-optic materials constraints, and not microphotonics. Given the short length scales of microphotonic circuits, the choice of carrier wavelengths need not be based on the optimal transmission properties of the waveguide material, but rather should be based on the optimal available choice of light emitter, amplifier, or photo-detector.

Our work has shown the existence of a sensitizer within annealed SiON:Er and Si₃N₄:Er, which increases the absorption cross-section at $\lambda_p=488 \text{ nm}$ by 10⁶ \times , relative to

Er. In samples doped without Er, light emission has been observed from this sensitizer in the spectral range 900-1050 nm, with a sub-ms lifetime below our current experimental resolution. We suggest further work be done to resolve and measure the 4 K versus room temperature lifetime of this sensitizer. If the sensitizer's sub-ms lifetime is a radiative lifetime, then these sensitizers are an ideal optical center for generating on-chip 900-1050 nm lasers, doped inside resonant cavities with required quality factors potentially as low as $Q_e=200-500$.

If such sensitizer-based light emitters are feasible, further studies should be done to study their absorption (at this same emission wavelength) as a function of refractive index. Our results suggest the nitride environment shifts sensitizer light emission to longer wavelengths. Hence a proposed microphotonic circuit may be comprised of an annealed Si_3N_4 sensitizer-based laser light source at ~ 1050 nm, propagating in an unannealed SiON waveguide (sensitizers within the SiON waveguide will be minimal without an anneal treatment, and their emission/absorption will be at a wavelength less than ~ 1050 nm, implying no absorption loss).

If such a shift in carrier wavelength from $1.55 \mu\text{m}$ to $\sim 1.05 \mu\text{m}$ is deemed appropriate, SiON waveguides naturally form the best waveguiding option from a lithography standpoint as well: single mode waveguide dimensions for $\lambda_s \sim 1.05 \mu\text{m}$ will be lithographically more feasible (with current I-line stepper resolution) for lower Δn waveguides (lower Δn implies larger single-mode waveguide dimensions) such as the SiON/SiO₂ system.

The question remains as to what this sensitizer is, and whether it is something different in a pure nitride environment, versus an oxide environment. As mentioned in chapter 4, recent work in Si-rich SiO₂ has confirmed the identity of such sensitizers to be Si nanocrystals. While refractive index measurements of sputter deposited Si₃N₄ show a higher index than stoichiometric Si₃N₄, Si nanocrystals have not been unambiguously confirmed as the source of sensitization. We suggest Transmission Electron Microscopy studies of annealed versus unannealed samples of both SiON and Si₃N₄, to confirm whether or not a nano-scale structure is precipitating from the host matrix after anneal. If a precipitate is observed, Selected Area Diffraction should be done to confirm whether it is indeed a Si nanocrystal or not.

In conclusion, the competitive relevance of SiON and Si₃N₄ sensitizers may only be as a higher mW power light source (due to a potentially faster radiative lifetime) than Er. The high small signal gains observed in this work, at high Er concentrations in sputtered SiON and Si₃N₄, have shown to us that the Er optical center has tremendous ongoing potential in optically pumped amplifier and light source applications for Si Microphotonics. 1.55 μm signal transmission continues to be the dominant guiding principle for microphotonic design.

Appendix 1: Modal Confinement & Turning Loss

Waveguides below single mode cut-off confine approximately 64% of the modal volume within the waveguiding core, *independent of index difference*. As a function of Δn , Fig. A1 presents single mode cut-off square waveguide cross-section width (at $\lambda=1.55\mu\text{m}$), and a turning radius value that corresponds to 0.042 dB/cm turning loss[19].

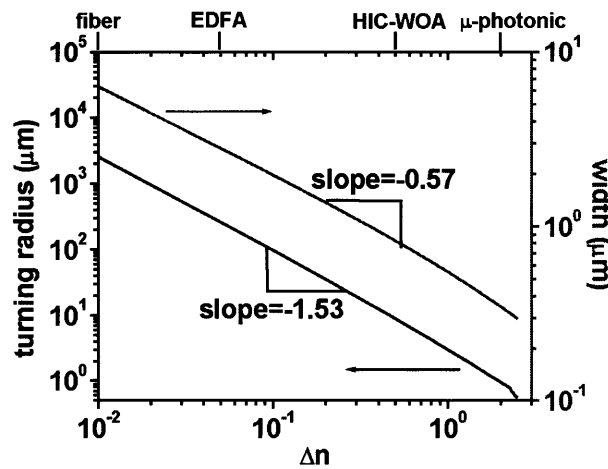


Fig. A1. Waveguide turning radius (for $\alpha_{\text{turn}}=0.042$ dB/cm) and width dimension for high gain efficiency amplifiers.

-
- [1] P.C. Becker, N.A. Olsson and J.R. Simpson, *Erbium-Doped Fiber Amplifiers: Fundamentals and Technology*, Academic Press, 1999.
- [2] C. J. Koester and E. Snitzer, *Appl. Opt.* **3**, 1182 (1964).
- [3] B.E.A. Saleh and M.C. Teich, *Fundamentals of Photonics*, (John Wiley & Sons Inc, 1991), ch 7.
- [4] E. Desurvire, *Erbium-Doped Fiber Amplifiers: Principles and Applications* (John Wiley & Sons, Inc, 1994).
- [5] D. Barbier, "Erbium-doped waveguide amplifiers promote optical-networking evolution," *Lightwave*, 2000.
- [6] R.G. Hunsperger, *Integrated Optics* (Springer-Verlag, 5th ed., 2002).
- [7] G.N. van den Hoven, E. Snoeks, A. Polman, C. van Dam, J.W.M van Uffelen and M.K. Smit, "Upconversion in Er-implanted Al₂O₃ waveguides," *J. Appl. Phys.* **79**(3), 1258-1266, 1996.
- [8] C. Strohhofer, P.G. Kik and A. Polman, "Selective modification of the Er³⁺ ⁴I_{11/2} branching ratio by energy transfer to Eu³⁺," *J. Appl. Phys.* **88**, 4486-4490 (2000).
- [9] S. Akiyama, M.A. Popovic, P.T. Rakich, K. Wada, J. Michel, H.A. Haus, E.P. Ippen and L.C. Kimerling, "Air Trench Bends and Splitters for Dense Optical Integration in Low Index Contrast," submitted to *IEEE J. Lightwave Tech.*, April 2004.
- [10] M. Morse, Ph.D. Thesis, MIT, 1997.
- [11] A. Polman, D.C. Jacobson, D.J. Eaglesham, R.C. Kistler and J.M. Poate, "Optical doping of waveguide materials by MeV Er implantation," *J. Appl. Phys.*, **70**(7), 3778-3784 (1991).
- [12] G. van den Hoven, Ph.D. Thesis, FOM (Institute for Atomic and Molecular Physics, Netherlands), 1997.
- [13] P.G. Kik, Ph.D. Thesis, FOM (Institute for Atomic and Molecular Physics, Netherlands), 2000.
- [14] J.D. Joannopoulos, R.D. Meade, J.N. Winn, *Photonic Crystals: Molding the Flow of Light*, (Princeton University Press, 1995).
- [15] M. Ibanescu, Y. Fink, S. Fan, E.L. Thomas, J.D. Joannopoulos, "The Coaxial Omniguide - An All-Dielectric Waveguide," *Science*, **21** (2000).
- [16] E. Hecht and A. Zajac, *Optics* (Addison-Wesley, 1974, 2nd Ed. 1987).
- [17] D.J. Griffiths, *Introduction to Electrodynamics*, (Prentice-Hall, Inc., Englewood Cliffs, NJ, 1981, 2nd Ed. 1989).
- [18] B.E.A. Saleh and M.C. Teich, *Fundamentals of Photonics*, (John Wiley & Sons Inc, 1991), ch 7.
- [19] K.C. Kao and G.A. Hockham, "Dielectric-fibre Surface Waveguides for Optical Frequencies," *Proc. IEE*, **113**(7), 1151-1158, 1966.
- [20] MIT class 3.46 lecture notes of Prof. L.C. Kimerling.
- [21] Modified from from MIT class 3.42 lecture notes of Prof. H. Tuller.
- [22] R.D. Maurer, D.B. Keck and P.C. Schultz, "Optical Waveguide Fibers," U.S. Patent #3,711,262.
- [23] G. Keiser, *Optical Communications Essentials* (McGraw-Hill Professional, 1st ed., 2003).
- [24] C.H. Fine and L.C. Kimerling, "Biography of a Killer Technology: Optoelectronics Drives Industrial Growth with the Speed of Light," in *OIDA Future Vision Program*, July 1997 (Optoelectronics Industry Development Association, Washington D.C.), 1-22, 1997.

-
- [25] Kimerling, L.C., Dal Negro L., Saini S., Yi Y., Ahn D., Akiyama S., Cannon D., Liu J., Sandland J., Sparacin D. and Watts M., "Monolithic Silicon Microphotonics," chapter 3 in *Si Photonics* (Springer-Verlag, 2004).
- [26] J.E. Geusic and H.E.D Scovil, *Bell. Syst. Tech. J.*, **41**, 1371 (1962).
- [27] J. Hecht, *City of Light: The Story of Fiber Optics* (Oxford Univ. Press, 1999).
- [28] G.H. Dieke, *Spectra and energy levels of rare earth ions in crystals*, Eds. H.M. Crosswhite and H. Crosswhite (Interscience Publishers, New York, 1968).
- [29] E. Desurvire, J.R. Simpson and P.C. Becker, *Opt. Lett.*, **12**, 888 (1987).
- [30] R.J. Mears, L. Reekie, S.B. Poole and D.N. Payne, *Elect. Lett.*, **LT-4**, 870 (1986).
- [31] P.C. Becker, N.A. Olsson and J.R. Simpson, *Erbium-Doped Fiber Amplifiers: Fundamentals and Technology*, (Academic Press, 1999), p. 2. (Modified reproduction from The AT&T Technical Journal ©1995).
- [32] M.J.F. Digonnet, *Fiber Amplifiers and Lasers for Lightwave System Applications*, SPIE's Photonic's East 2000 Short Course SC228, SPIE- The International Society for Optical Engineering, November 2000.
- [33] C.R. Giles, *Opt. Lett.* **14**(16), 880-882, 1989.
- [34] A.S. Sedra and K.C. Smith, *Microelectronic Circuits* (Oxford University Press, 4th ed., 1997).
- [35] "The TR100," MIT Technology Review, 2001.
- [36] Graph acquired from MIT class 6.720 lecture notes of Prof. J. del Alamo.
- [37] ITRS (2001), International Technology Roadmap for Semiconductors: 2001, <http://public.itrs.net/>.
- [38] S.K. Tewksbury and L.A. Hornak, "Optical Clock Distribution in Electronic Systems," *J. VLSI Signal Proc.* **16**, 225-246 (1997).
- [39] C. Debaes, A. Bhatnagar, D. Agarwal, R. Chen, G.A. Keeler, N.C. Helman, H. Thienpont, D.A.B. Miller, "Receiver-less Optical Clock Injection for Clock Distribution Networks," in *IEEE J. Selected Topics Quant. Electr.*, **9**(2), 400-409 (2003).
- [40] Ling Liao, Desmond Lim, Anuradha M. Agarwal, Kevin K. Lee and Lionel C. Kimerling, "Optical transmission losses in polycrystalline strip waveguides: Effects of waveguide dimensions, thermal treatment, hydrogen passivation, and wavelength," *J. Electr. Mat.*, **29**(12), pp. 1380-1386, December 2000.
- [41] A.M. Agarwal, L. Liao, J.S. Foresi, M.R. Black, X. Duan and L. C. Kimerling, "Low-loss polycrystalline silicon waveguides for silicon photonics," *J. Appl. Phys.*, **80**(11), pp. 6120-6123, 1 December 1996.
- [42] K.K. Lee, D.R. Lim, H.-C. Luan, A. Agarwal, J. Foresi and L.C. Kimerling, "The effect of size and roughness on light transmission in a Si/SiO₂ waveguide: Experiments and model," *Appl. Phys. Lett.* **77**, 2258 (2000).
- [43] S. Saini, J.G. Sandland, A. Eshed, D.K. Sparacin, L. Dal Negro, J. Michel and L.C. Kimerling. "A High Index Contrast Silicon Oxynitride Materials Platform for Er-doped Microphotonic Amplifiers," *New Materials for Microphotonics (MRS)*, Materials Research Society Spring Meeting 2004, Conference Proceedings.
- [44] K.K. Lee, D.R. Lim, L.C. Kimerling, J. Shin, F. Cerrina, "Fabrication of ultralow-loss Si/SiO₂ waveguides by roughness reduction," *Opt. Lett.*, **26**(23), 1888-1890 (2002).
- [45] V.R. Almeida, R. Panepucci and M. Lipson, "Compact mode conversion for highly-confined waveguides," in *Integrated Photonics Research*, OSA Technical Digest, (Optical Society of America, Washington DC, 2003), 230-233.

-
- [46] M. Dejneka, B. Samson, "Rare-Earth-Doped Fibers for Telecommunications Applications," *MRS Bull.*, **24**(9), 39-45(1999).
- [47] M. Dignonnet, ed., *Selected Papers on Rare-Earth-Doped Fiber Laser Sources and Amplifiers*, SPIE Milestone Series (Marcel Dekker, 2001).
- [48] C. Strohhofer and A. Polman, "Relationship between gain and Yb³⁺ concentration in Er³⁺-Yb³⁺ doped waveguide amplifiers," *J. Appl. Phys.*, **90**(9), 4314-4320 (2001).
- [49] K. Hattori, T. Kitagawa, M. Oguma, Y. Ohmori, M. Horiguchi, "Erbium-doped silica-based waveguide amplifier integrated with a 980/1530 nm WDM coupler," *Elect. Lett.*, **30**, 856 (1994).
- [50] G. Nykolak, M. Haner, P.C. 1, J. Shmulovich, Y.H. Wong, "Systems evaluation of an Er³⁺-doped planar waveguide amplifier," *IEEE Phot. Tech. Lett.* **5**, 1185 (1993).
- [51] A.V. Chelnokov, J.-M. Lourtioz, Ph. Boucard, H. Bernas, J. Chaumont and T. Plowman, "Deep erbium-ytterbium implantation codoping of low-loss silicon oxynitride waveguides," *Elect. Lett.*, **31**(8), 636-638(1995).
- [52] M. Krishnaswamy, J.N. McMullin, B.P. Keyworth and J.S. Hayden, "Optical properties of strip-loaded Er-doped waveguides," *Opt. Mat.*, **6**, 287-292(1996).
- [53] Y.C. Yan, A.J. Faber, H. de Waal, A. Polman and P.G. Kik, "Erbium-doped phosphate glass waveguide on silicon with 4.1 dB/cm gain at 1.535 μm ," *Appl. Phys. Lett.*, **71**(20), 2922-2944 (1997).
- [54] P.G. Kik and A. Polman, "Gain limiting processes in Er-doped Si nanocrystal waveguides in SiO₂," *J. Appl. Phys.*, **91**(1), 534-536 (2002).
- [55] D.M. Gill, G.M. Ford, B.A. Block, S. Kim, B.W. Wessels and S.T. Ho, "Guided wave absorption and fluorescence in epitaxial Er:BaTiO₃," *Thin Sol. Films*, **365**, 126-128 (2000).
- [56] S.F. Wong, E.Y.B. Pun, P.S. Chung, "Er³⁺-Yb³⁺ Codoped Phosphate Glass Waveguide Amplifier Using Ag⁺-Li⁺ Ion Exchange," *IEEE Phot. Tech. Lett.* **14**(1), 80-82 (2002).
- [57] G.N. van den Hoven, R.J.I.M. Koper, A. Polman, C. van Dam, J.W.M. van Uffelen, and M.K. Smit, "Net optical gain at 1.53 μm in Er-doped Al₂O₃ waveguides on silicon," *Appl. Phys. Lett.*, **68**(14), 1886-1888 (1996).
- [58] D. Barbier and R.L. Hyde, "Erbium-Doped Glass Waveguide Devices" in *Integrated Optical Circuits and Components: Design and Applications*, E.J. Murphy, ed. (Marcel Dekker Inc., NY, 1999); Teem Photonics website, Product Information, http://www.teemphotonics.com/pages/product/f_product.html.
- [59] G.B. Arfken, H.-J. Weber, *Mathematical Methods for Physicists* (Academic Press, 5th ed., 2000).
- [60] L.A. Coldren and S.W. Corzine, *Diode Lasers and Photonic Integrated Circuits* (John Wiley & Sons, Inc., 1995).
- [61] S. Saini, J. Michel and L.C. Kimerling, "Index Scaling for Optical Amplifiers," *IEEE J. Lightwave Tech.*, **21**(10), 2368-2376 (2003).
- [62] B.E.A. Saleh and M.C. Teich, *Fundamentals of Photonics*, (John Wiley & Sons Inc, 1991) pp.253, 488-489.
- [63] J. Hecht, "The Evolution of Optical Amplifiers," *Optics & Phot. News*, **13**(8), 36-39(2002).
- [64] K.K. Lee, Ph.D. Thesis, MIT, 2002.
- [65] D.K. Sparacin, K. Wada and L.C. Kimerling, "Oxidation kinetics of waveguide roughness minimization in silicon microphotronics," in *OSA Topical Meeting: Integrated Photonics Research*, OSA Technical Digest, Postconference Edition (Optical Society of America, Washington DC), 129 (2003).

-
- [66] K. Chen, S. Saini, M. Lipson, X. Duan and L.C. Kimerling, "Growth, crystallization, and room temperature photoluminescence of Er/sub 2/O/sub 3/ thin films" Proc. SPIE – Inter. Soc. Opt. Eng., **4282**, 168-173 (2001).
- [67] R.L. Liboff, *Introductory Quantum Mechanics* (Addison-Wesley Publishing Company, 1980).
- [68] B.E.A. Saleh and M.C. Teich, *Fundamentals of Photonics*, (John Wiley & Sons Inc, 1991) p.439.
- [69] M.A. Green, *Solar cells : operating principles, technology, and system applications* (Prentice-Hall, Inc., Englewood Cliffs, NJ, 1982) .
- [70] L.C. Kimerling, "Si Microphotonics," Appl. Surf. Sci., **159-160**, 8-13 (2000).
- [71] A. Kasuya, M. Suezawa, "Resonant excitation of visible photoluminescence from an erbium-oxide overlayer on Si," Appl. Phys. Lett., **71**(19), 2728-2730 (1997).
- [72] S. Saini, K. Chen, X. Duan, J. Michel, L.C. Kimerling and M. Lipson, "Er₂O₃ for high gain waveguide amplifiers," J. Electr. Mat., **33**(7), 809-814 (2004).
- [73] F.Y.G. Ren, Ph.D. Thesis, MIT, 1994.
- [74] L.E. Murr, "Study of Erbium Thin Film Oxidation in the Electron Microscope," Phys. Stat. Sol., **24**, 135-148 (1967).
- [75] J.R. Dean, D. Bloor, "Spectroscopy of rare earth oxide systems. II. Spectroscopic properties of erbium oxide (at antiferromagnetic transition)," **5**(20), 2921-2940 (1972).
- [76] R.S. Quimby, W.J. Miniscalco and B. Thompson, "Clustering in erbium-doped silica glass fibers analyzed using 980 nm excited-state absorption," J. Appl. Phys., **76**(8), 4472-4478 (1994).
- [77] W. O. Milligan, D.F. Mullica, H.O. Perkins and C.K.C. Lok, "Short-Range-Order Structure of Amorphous Hydrated Erbium Oxide," Acta. Cryst., **A40**, 264-269 (1984).
- [78] O. Lumholt, H. Bernas, A. Chabli, J. Chaumont, G. Grand and S. Valette, "Low-Energy Erbium Implanted Si₃N₄/SiO₂/Si Waveguides," Electr. Lett., **28**(24), 2242-2243, 1992.
- [79] A. V. Chelnokov, J.M. Lourtioz, Ph. Boucaud, H. Bernas, J. Chaumont and T. Plowman, "Deep erbium-ytterbium implantation codoping of low-loss silicon oxynitride waveguides," Electr. Lett., **31**(8), 636-638, 1995.
- [80] A.V. Chelnokov, J.M. Lourtioz, Ph. Boucaud, H. Bernas, J. Chaumont and T. Plowman, "Deep high-dose erbium implantation of low-loss silicon oxynitride waveguides," Electr. Lett., **30**(22), 1850-1852.
- [81] A.R. Zanatta, M. Bell and L. Nunes, "Visible photoluminescence from Er⁺³ ions in a-SiN alloys," Phys. Rev. B **59**(15), 10091-10098, 1999.
- [82] M. Bell, L. Nunes and A.R. Zanatta, "Optical excitation of Er⁺³ ions in a-SiN alloys," J. Appl. Physics, **86**(1), 338-341, 1999.
- [83] A.R. Zanatta, C.T.M. Ribeiro and U. Jahn, "Visible luminescence from a-SiN films doped with Er and Sm," Appl. Phys. Lett. **79**(4), 488-490, 2001.
- [84] A.R. Zanatta, C.T.M. Ribeiro and F. Alvarez, "X-ray photoelectron spectroscopic study of rare-earth doped amorphous silicon-nitrogen films," J. Appl. Phys., **93**(4), 1948-1953, 2003.
- [85] M.S. Sercheli, C. Rettori and A.R. Zanatta, "Neutral dangling bond depletion in amorphous SiN films induced by magnetic rare-earth elements," Solid State Communications, **128**, 47-50, 2003.
- [86] L. Pavesi, L. Dal Negro, C. Mazzoleni, G. Franzo and F. Priolo, "Optical gain in Si nanocrystals," Nature **408**, 440 (2000).
- [87] H.K. Kim, C.C. Li, X.M. Fang, Y. Li, D.W. Langer, J. Solomon, "Photoluminescence of highly Er-doped silica films and Er-doped gallium arsenide," J. of Lumines. **60&61**, 220-222, 1994.

-
- [88] H.S. Han, S.Y. Seo, J.H. Shin, "Optical gain at 1.54 μm in erbium-doped silicon nanocluster sensitized waveguide," *Appl. Phys. Lett.* **79**(27), 4568-4570, 2001.
- [89] M. Fujii, M. Yoshida, S. Hayashi and K. Yamamoto, "Photoluminescence from SiO₂ films containing Si nanocrystals and Er: Effects of nanocrystalline size on the photoluminescence efficiency of Er⁺³," *J. Appl. Phys.* **84**(8), 4525-4531, 1998.
- [90] F. Gourbilleau, C. Dufour, M. Levalois, J. Vicens, R. Rizk, C. Sada, F. Enrichi and G. Battaglin, "Room-temperature 1.54 μm photoluminescence from Er-doped Si-rich silica layers obtained by reactive magnetron sputtering," *J. Appl. Physics* **94**(6), 3869-3874, 2003.
- [91] F. Gourbilleau, P. Choppinet, C. Dufour, M. Levalois, R. Madelon, C. Sada, G. Battaglin and R. Rizk, "Er emission from Er-doped Si-rich silicon oxide layers synthesized by hydrogen reactive magnetron co-sputtering," *Physica E* **16**, 341-346, 2003.
- [92] F.C. Yuan, G.Z. Ran, Y. Chen, L. Dai, Y.P. Qiao, Z.C. Ma, W.H. Zong and G.G. Qin, "Room-temperature 1.54 μm electroluminescence from Er-doped Si-rich SiO₂ films deposited on p-Si by magnetron sputtering," *Thin Solid Films* **409**, 194-197, 2002.
- [93] W.J. Miniscalco, "Erbium-Doped Glasses for Fiber Amplifiers at 1500 nm," invited paper, *IEEE J. Lightwave Tech.*, **9**(2), 234-250 (1991).
- [94] B.S. Sahu, O.P. Agnihotri, S.C. Jain, R. Mertens and I. Kato, "Influence of hydrogen on losses in silicon oxynitride planar optical waveguides," *Semicond. Sci. & Technol.*, **15**, L11-L14, (2000).
- [95] R. Germann, H.W.M. Salemink, R. Beyeler, G.L. Bona, F. Horst and B.J. Offrein, "Silicon-Oxynitride Layers for Optical Waveguide Applications," *J. Electrochem. Soc.*, **147**(6), 2237-2241 (2000).
- [96] S. Saini, J. Sandland, A. Eshed, D. Sparacin, J. Michel, and L.C. Kimerling, "High index contrast silicon oxynitride materials platform for Er-doped microphotonic amplifiers," *Proceedings of the MRS Spring Meeting, San Francisco, CA* (2004).
- [97] A. J. Steckl and J. M. Zavada, "Optoelectronic Properties and Applications of Rare-Earth-Doped GaN," *MRS Bulletin*, **24**(9), 33-38, 1999.
- [98] S.K. Ghandhi, *VLSI Fabrication Principles: Silicon and Gallium Arsenide* (Wiley-Interscience, 2nd ed., 1994).
- [99] J.G. Sandland, Ph.D. Thesis, MIT, 2004.
- [100] L. Dal Negro, P. Bettotti, M. Cazzanelli, D. Pacifici and L. Pavesi, "Applicability conditions and experimental analysis of the variable stripe length method for gain measurements," *Optics Comm.*, **229**, 337-348 (2004).
- [101] http://www.jdsu.com/index2.cfm/NAVCID/5/CID/5/ACT/Default/G_ID/10/C_ID/219/S_ID/321/?page=Arrayed%20Waveguide%20Gratings.
- [102] T. E. Murphy, J. T. Hastings and H.I. Smith, "Fabrication and Characterization of Narrow-Band Bragg-Reflection Filters in Silicon-on-Insulator Ridge Waveguides", *J. Lightwave Tech.*, **19**(12) 1938-1942, (2001).
- [103] B.E. Little, S.T. Chu, "Estimating surface-roughness loss and output coupling in microdisk resonators," *Opt. Lett.*, **21**(17), 1390-1392, 1996.
- [104] B.E. Little, S.T. Chu, H.A. Haus, J. Foresi and J.-P. Laine, "Microring Resonator Channel Dropping Filters," *J. Lightwave Tech.*, **15**(6), 998-1005, 1997.
- [105] <http://www.littleoptics.com/>.
- [106] G.P. Agrawal, *Long-Wavelength Semiconductor Lasers* (Van Nostrand Reinhold, 1986).

-
- [107] B.E. Little, J.-P. Laine and S.T. Chu, "Surface-roughness-induced contradirectional coupling in ring and disk resonators," *Opt. Lett.*, **22**(1), 4-6, 1997.
- [108] D.W. Vernooy, V.S. Ilchenko, H. Mabuchi, E.W. Streed and H.J. Kimble, "High-Q measurements of fused-silica microspheres in the near infrared," *Opt. Lett.*, **23**(4), 247-249, 1998.
- [109] D.K. Armani, T.J. Kippenberg, S.M. Spillane and K.J. Vahalla, "Ultra-high-Q toroid microcavity on a chip," *Nature*, **421**, 925-928, 2003.
- [110] H. A. Haus, *Waves and Fields in Optoelectronics* (Prentice-Hall, Inc., Englewood Cliffs, NJ, 1984).
- [111] S.T. Chu, B.E. Little, W. Pan, T. Kaneko, S. Sato and Y. Kokubun, "An Eight-Channel Add-Drop Filter Using Vertically Coupled Microring Resonators over a Cross Grid," *IEEE*
- [112] K. Djordjev, S.-J. Choi, S.-J. Choi and P.D. Dapkus, "High-Q Vertically Coupled InP Microdisk Resonators," *IEEE Phot. Tech. Lett.*, **14**(3), 331-333, 2002.
- [113] T. Barwicz, M.A. Popovic, P.T. Rakich, M.R. Watts, H.A. Haus, E.P. Ippen and H.I. Smith, "Fabrication and analysis of add-drop filters based on microring resonators in SiN," in *The 2004 Optical Fiber Communication Conference (OFC:04)*, Los Angeles, California, February 22-27, TuL4 (2004).
- [114] S. J. Choi, Z. Peng, Q. Yang, S. J. Choi and P. D. Dapkus, "8-Channel microdisk CW laser arrays vertically coupled to common output bus waveguides," in *OSA Integrated Photonics Research Conference (IPR 2004)*, San Francisco (CA), IWC-1 (2004).
- [115] S. J. Choi, Z. Peng, Q. Yang, S. J. Choi and P. D. Dapkus, "8-Channel tunable MUX/DEMUX using vertically coupled active microdisk resonators," in *IEEE 16th Annual LEOS 2003 Meeting*, Tucson (AZ), TuM-4 (2003).
- [116] A. Polman, B. Min, J. Kalkman, T.J. Kippenberg and K.J. Vahala, "Ultra-low-threshold erbium-implanted toroidal microlaser on silicon," *Appl. Phys. Lett.*, **84**(7), 1037-1039 (2004).
- [117] E.S. Bjorlin, P. Abraham, D. Pasquariello, J. Piprek, Y.J. Chiu and J.E. Bowers, "High Gain, High Efficiency Vertical-Cavity Semiconductor Optical Amplifiers," *Proceedings from 14th International Conf. on Indium Phosphide and Related Materials*, 2002.
- [118] E.S. Bjorlin, J.E. Bowers, "Noise Figure of Vertical-Cavity Semiconductor Optical Amplifiers," *IEEE J. Quant. Electr.*, **38**(1), 61-66, 2002.
- [119] E.S. Bjorlin, "Long-wavelength vertical-cavity semiconductor optical amplifiers," *SPIE ITCOM02, Semiconductor Lasers and Optical Amplifiers for Lightwave Communication Systems*, 2002.
- [120] http://www.nature.com/nature/journal/v424/n6950/box/nature01939_bx2.html.
- [121] D.K. Cheng, *Field and Wave Electromagnetics* (Prentice Hall, 2nd ed., 1989).
- [122] Y.A. Vlasov and S.J. McNab, "Losses in single-mode silicon-on-insulator strip waveguides and bends," *Optics Express*, **12**(8), 1622 (2004).
- [123] Desmond Lim, Ph.D. Thesis, MIT, 2001.
- [124] B.E.A. Saleh and M.C. Teich, *Fundamentals of Photonics*, (John Wiley & Sons Inc, 1991), p.615.
- [125] L. Colace, G. Masini, G. Assanto, H.-C. Luan, K. Wada and L.C. Kimerling, "Efficient high-speed near-infrared Ge photodetectors integrated on Si substrates," *Appl. Phys. Lett.*, **76**(10), 1231 (2000).
- [126] D.D. Cannon, J. Liu, Y. Ishikawa, K. Wada, D.T. Danielson, S. Jongthammanurak, J. Michel and L.C. Kimerling, "Tensile strained epitaxial Ge films on Si(100) substrates with potential application in L-band telecommunications," *Appl. Phys. Lett.*, **84**(6), 906 (2004).
- [127] S. M. Sze, *Physics of Semiconductor Devices*, (Wiley, New York, 2nd ed., 1981) p 750.
- [128] H.-C. Luan, L. Giovane, L. Colace, G. Masini, G. Assanto, K. Chen, K. Wada, and L.C. Kimerling, "Germanium photodetectors for silicon microphotronics," *Proceedings of the MRS*, **637** E5.6.1 (2001).

[129] P. Yeh, *Optical Waves in Layered Media* (Wiley-Interscience, 1988).

[130] J.G. Fleming, S.Y. Lin, I. El-Kady, R. Biswas and K. M. Ho, "All-metallic three-dimensional photonic crystals with a large infrared bandgap," *Nature* **417**(6884), 52-55 (2002).

[131] Y. Fink, J.N. Winn, S. Fan, J. Michel, C. Chen, J.D. Joannopoulos, E.L. Thomas, "A Dielectric Omnidirectional Reflector," *Science* **282**, 1679–1682, (1998).